



HAL
open science

Suspensions concentrées et compaction des milieux granulaires

Maxime Nicolas

► **To cite this version:**

Maxime Nicolas. Suspensions concentrées et compaction des milieux granulaires. Mécanique des fluides [physics.class-ph]. Université de provence - Aix-Marseille I, 2005. tel-01442486

HAL Id: tel-01442486

<https://hal.science/tel-01442486>

Submitted on 25 Jan 2017

HAL is a multi-disciplinary open access archive for the deposit and dissemination of scientific research documents, whether they are published or not. The documents may come from teaching and research institutions in France or abroad, or from public or private research centers.

L'archive ouverte pluridisciplinaire **HAL**, est destinée au dépôt et à la diffusion de documents scientifiques de niveau recherche, publiés ou non, émanant des établissements d'enseignement et de recherche français ou étrangers, des laboratoires publics ou privés.

UNIVERSITÉ DE PROVENCE — Aix-Marseille I
Laboratoire IUSTI UMR 6595

Mémoire présenté pour l'obtention de
L'HABILITATION À DIRIGER LES RECHERCHES

Par

Maxime NICOLAS

Maître de Conférences à Polytech Marseille, Université de Provence

SUSPENSIONS CONCENTRÉES
ET
COMPACTION DES MILIEUX GRANULAIRES

Soutenu le 6 décembre 2005 devant le jury composé de

D.	Clausse	Univ. Technologique de Compiègne
O.	Dauchot	CEA, Gif sur Yvette
J.-P.	Hulin (rapporteur)	FAST, Orsay
J. F.	Morris (rapporteur)	City College, New York
J.	Quinard (rapporteur)	IRPHE, Marseille
R.	Saurel	IUSTI, Université de Provence

Table des matières

1	Introduction	4
1.1	Parcours personnel	4
1.2	Contexte scientifique	5
2	Fluidisation	8
2.1	Description diphasique	8
2.2	Résultats	9
2.3	Références	11
3	Compaction	13
3.1	Introduction	13
3.2	Compaction sous vibration horizontale	14
3.3	Compaction sous cisaillement	16
3.4	Dynamique microscopique des particules	17
3.5	Références	19
4	Avalanches sous-marines	21
4.1	Introduction	21
4.2	Des écoulement granulaires aux avalanches sous-marines	22
4.3	Comparaison avec les résultats expérimentaux	24
4.4	Instabilité de surface	25
4.5	Approche macroscopique	26
4.6	Perspectives	27
4.7	Références	27
5	Dispersion de suspensions concentrées	29
5.1	Sédimentation hétérogène	29
5.2	Jets de suspension	30
5.3	Modes de dispersion	31
5.4	Évolution de gouttes de suspension	33
5.5	Références	34

6	Impact de gouttes chargées en particules	35
6.1	Étalement ou fragmentation	36
6.2	Effet des particules sur l'étalement : théorie	37
6.3	Effet des particules sur l'étalement : résultats	39
6.4	Perspectives	40
6.5	Références	40
7	Perspectives	42
A	Curriculum vitae – Activités – Liste des travaux	46
A.1	État civil & statut	46
A.2	Poste précédent	46
A.3	Formation et diplômes	46
A.4	Activités d'enseignement	47
A.4.1	Dans le cadre de Polytech Marseille	47
A.4.2	Dans le cadre du Master Mécanique, Physique et Modélisation (DEA)	48
A.4.3	Enseignements abandonnés	48
A.4.4	Production de photocopies	48
A.4.5	Participation à des jurys	49
A.4.6	Responsabilités pédagogiques	49
A.5	Activités de recherche	49
A.5.1	Encadrement de stages	49
A.5.2	Encadrement de thèse	49
A.5.3	Rayonnement scientifique	49
A.6	Publications et communications	51
A.6.1	Publications dans des journaux à comité de lecture	51
A.6.2	Colloques et congrès avec actes	52
A.6.3	Séminaires	52
A.6.4	Communications à des colloques sans actes	52
A.7	Résumé des activités	54
B	Publications	55
B.1	Crystallisation under horizontal shaking	55
B.2	De l'ordre dans les billes !	60
B.3	Wavy instability in liquid-fluidized beds	62
B.4	Compaction under cyclic shear	67
B.5	A minimal model for slow dynamics	74
B.6	Compaction of hard spheres	83
B.7	Constitutive laws of liquid-fluidized beds	87
B.8	Dense suspension jets	122
B.9	Fluctuating particle motion during granular compaction	131
B.10	Pore pressure relaxation during granular compaction	136

B.11 Spreading of a drop of neutrally buoyant suspension	139
B.12 Submarine granular flows down inclined planes	150
B.13 Dynamics of a sliding porous block	162

Chapitre 1

Introduction

1.1 Parcours personnel

Ce mémoire d'habilitation présente les travaux de recherche que j'ai menés durant mon Service National comme Scientifique du Contingent (novembre 1996-octobre 1997) au Laboratoire d'Hydrodynamique de l'École Polytechnique (LadHyX), comme Attaché Temporaire d'Enseignement et de Recherche (octobre 1998-septembre 1999) puis comme Maître de Conférences au sein du Laboratoire IUSTI, unité mixte de recherche Université de Provence/CNRS.

Après une formation en physique et un DEA de physique des liquides, j'ai effectué une thèse de 1994 à 1997 au Laboratoire de Physique et Mécanique des Milieux Hétérogènes (ESPCI, Paris) sous la direction d'Élisabeth Guazzelli portant sur les instabilités de concentration en particules dans les lits fluidisés.

En parallèle avec la thèse, j'ai entamé en 1996 des recherches sur les milieux granulaires secs, en particulier sur le problème de la compaction. Ces travaux, en collaboration avec O. Pouliquen au LADHYX (Ecole Polytechnique), ont permis d'établir une collaboration durable entre O. Pouliquen, E. Guazzelli et moi-même. Cette collaboration a donné naissance en 1998 au Groupe Écoulements de Particules, installé au sein du laboratoire IUSTI¹ de Polytech Marseille. Regroupant des études sur les suspensions, les écoulements de particules en milieu aérien ou immergé, l'équipe compte à l'heure actuelle 8 chercheurs et enseignants-chercheurs permanents, un technicien et quatre étudiants en thèse.

À la suite de ma thèse, je n'ai pas effectué de changement thématique brusque. Lors de l'installation du GEP à Marseille, j'ai continué à travailler sur la fluidisation et la compaction, deux thématiques déjà entamées. Ces travaux sont présentés dans les chapitres 2 et 3. Pendant mon année d'ATER, j'ai également commencé une étude sur la dispersion d'un jet de particules solides dans un liquide, une forme de sédimentation hétérogène. Cette expérience est née par l'observation des particules sortant d'une pipette en voulant remplir un récipient. Le jet ne semblait pas vouloir garder sa forme cylindrique mais se

1. Institut Universitaire des Systèmes Thermiques Industriels, UMR 6595 CNRS/Université de Provence.

brisait en paquets de particules. L'expérience initialement prévue (la fluidisation brutale d'un sédiment) a été abandonnée au profit d'une expérience de sédimentation hétérogène fort simple mais riche en résultats, présentée dans le chapitre 5.

Les recherches que je présente dans ce mémoire ont particulièrement profité du dynamisme du Groupe Écoulements de Particules. Dans ce contexte favorable, je m'intéresse depuis 2001 aux écoulements granulaires immergés. Transposition des travaux d'O. Pouliquen sur les écoulements granulaires secs, cette expérience de modélisation d'une avalanche sous-marine a établi un lien durable entre les descriptions des granulaires secs et celles des suspensions très concentrées. Sur ce sujet, j'ai encadré la thèse de Cyril Cassar d'octobre 2002 à novembre 2005. Sa thèse doit être soutenue en novembre 2005. Les principaux résultats sont présentés dans le chapitre 4.

La forte imbrication de l'école d'ingénieurs Polytech Marseille et du laboratoire IUSTI m'a permis d'accueillir régulièrement des étudiants dans le cadre de projets expérimentaux, longues séances de travaux pratiques dont le résultat n'est pas connu à l'avance. Ce fut souvent l'occasion de débroussailler des sujets nouveaux à partir d'expériences « de table ». Certains de ces sujets ont été abandonnés, certains sont en attente de temps disponible, d'autres ont initié une recherche à long terme.

Parmi ces sujets, j'ai commencé depuis 2004 l'étude de l'impact et l'étalement de gouttes liquides chargées en particules. Issu de discussions avec des industriels de la microélectronique, ce sujet de recherche a donné des résultats surprenant lors d'une étude préliminaire. Surtout, j'ai pu aborder une nouvelle thématique : l'interaction de particules avec une interface liquide/gaz. Les résultats obtenus jusqu'à aujourd'hui sont présentés dans le chapitre 6.

1.2 Contexte scientifique

En ce début de XXI^e siècle, la physique macroscopique présente encore des mystères et des surprises. Situés sur une échelle de taille entre les atomes et les planètes, les matériaux divisés sont facilement visibles à l'œil nu et pourtant leur description présente encore des lacunes. De façon générique, ces matériaux sont constitués de particules solides — grains, poussières, fragments — dispersées dans un fluide. Le fluide est facilement caractérisé par sa densité, sa viscosité ou sa rhéologie s'il est non newtonien. Les particules sont caractérisées par leur densité, leurs formes et tailles. Le tableau des caractéristiques est donc complet. Du mélange de ces deux constituants, on peut déduire facilement quelques quantités, comme la densité moyenne ou la distance moyenne entre particules.

Mais la description d'un écoulement d'un milieu divisé reste un défi. Induit par une force extérieure (gravité, force électrique ou magnétique), des contraintes locales (mouvement d'une paroi par exemple) ou encore par une différence de pression, l'écoulement résulte d'un équilibre entre les énergies cinétique et potentielle et le travail des forces de dissipation. C'est cette dernière contribution à l'équilibre qui pose le plus de difficultés.

Une première approche consiste à remplacer le mélange fluide+particules par un liquide dont les propriétés vont dépendre des caractéristiques du mélange.

Auteur	Viscosité relative
Einstein (1905)	$1 + 2.5\phi$
Leighton & Acrivos (1967)	$[1 + 1.5\phi/(1/\phi/\phi_m)]^2$
Krieger (1972)	$1/(1 - \phi/\phi_m)^{1.87}$

TAB. 1.1 – Expressions classiques de viscosité effective des suspensions. ϕ_m est la fraction volumique maximum.

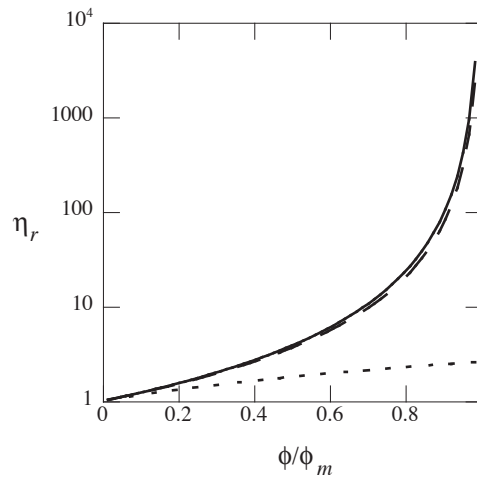


FIG. 1.1 – Comparaison des viscosités effectives : modèles d'Einstein (traits pointillés), modèle de Krieger (courbe discontinue) et modèle d'Acrivos (courbe continue).

La modélisation de la viscosité des fluides complexes tels que les suspensions ou les émulsions est un problème qui a attiré un grand nombre de chercheurs depuis les travaux précurseurs d'Einstein (1905) puis de Taylor (1934). Mais ces approches sont limitées aux très faibles concentrations (Kynch en 1954 a montré que le calcul d'Einstein est limité aux fractions volumiques de moins de 1 %). D'autres approches sont donc nécessaires pour obtenir une valeur prédictive pour toute la gamme de fraction volumique.

Ainsi des approches empiriques prennent le relais pour des concentrations élevées, avec comme horizon une divergence de la viscosité effective lorsque les particules forment un empilement compact, avec création de chaînes de forces en percolation sur la taille du système. On note ϕ_m la fraction volumique maximum. Le tableau 1.1 résume quelques expressions classiques utilisées pour calculer la viscosité d'une suspension de sphères non browniennes.

La figure 1.1 montre la comparaison entre les expressions obtenues par Einstein, dans la limite des faibles concentrations, Leighton & Acrivos (1967) et Krieger (1972). On peut voir que les deux expressions empiriques sont très proches. Ces courbes montrent que la viscosité relative vaut 10 pour $\tilde{\phi} = \phi/\phi_m = 0.69$, 100 pour $\tilde{\phi} = 0.90$ et 1000 pour $\tilde{\phi} = 0.97$.

Une lacune importante de cette approche est le manque de prédictibilité pour les

suspensions très concentrées $\phi \rightarrow \phi_m$. Une faible variation de la fraction volumique induit une très grande variation de la viscosité effective. Cette approche ne semble pas apte à caractériser précisément une suspension dont les particules sont en contact ou proches du contact.

Pourtant, les occurrences des suspensions concentrées sont nombreuses dans la nature ou dans les processus industriels. Quelques exemples :

- géophysique : avalanches sous-marines, écoulement de débris, coulées de boues ;
- génie chimique : lit fluidisé, filtration ;
- génie civil : rhéologie des ciments et bétons ;
- géotechnique : stabilité des sols saturés en eau, transport de sédiments ;
- liquides complexes : pâtes granulaires, encres conductrices.

La grande variété des applications et utilisations des suspensions concentrées ne doit pas occulter qu'une description universelle est possible, si toutefois les interactions entre les particules solides sont de même nature. Mes recherches ont porté sur des suspensions formées de « grosses » particules — typiquement d'un diamètre supérieur à $50 \mu\text{m}$ — pour lesquelles les interactions de surface et le mouvement brownien sont négligeables. Seuls deux types d'interaction seront pris en compte : les interactions hydrodynamiques et les interactions de contact.

Malgré la diversité apparente des thématiques abordées dans ce mémoire, j'apporterai dans le chapitre 7 une vision fédératrice de tous ces sujets. Cette vision est la source des perspectives de recherche que je me fixe pour les prochaines années. Ce mémoire est complété par deux annexes contenant mon CV (annexe A), le résumé de mes différentes activités, et la reproduction des articles et communications écrites (annexe B).

Chapitre 2

Fluidisation

*En collaboration avec P. Duru (doctorant 1999-2002),
E.J. Hinch (Université de Cambridge) et É. Guazzelli (DR).*

J'ai commencé à travailler sur la fluidisation dans le cadre de ma thèse. À l'issue de celle-ci, la démarche était mise au point mais des données précises manquaient pour terminer l'étude. L'expérience que j'avais développée a été reprise par Paul Duru pendant la première partie de son doctorat, et ses travaux nous ont permis d'apporter une conclusion importante sur le problème de la description de la rhéologie des lits fluidisés. Cette partie est essentiellement un résumé d'un article publié dans *J. Fluid Mech.*

2.1 Description diphasique

Un lit fluidisé est un procédé au départ développé par le génie chimique et pétrolier pour réaliser des réactions chimiques à haut rendement par catalyse. Des particules solides (le catalyseur) sont maintenues en lévitation par un écoulement de fluide contraire à la gravité. Les particules offrent alors une grande surface de contact avec le fluide, permettant de maximiser la cinétique de la réaction. Mais cette configuration se révèle être très souvent instable. En effet, la fluidisation homogène est difficilement réalisable, sauf à utiliser un fluide très visqueux et/ou des très petites particules. Les instabilités observées prennent la forme d'ondes de concentration en particules solides, ces ondes devenant elles-mêmes instables pour donner naissance à des bulles, zones de l'écoulement dépourvues en particules.

Les descriptions de ce procédé de fluidisation sont longtemps restées empiriques. Développés à partir des années 1960, les modèles diphasiques ont été particulièrement appliqués à la fluidisation (Jackson 1963, Anderson & Jackson 1967, 1968). La description diphasique des lits fluidisés propose un mélange de deux phases continues — une phase fluide et une phase solide — toutes deux décrites par une rhéologie newtonienne.

Si cette modélisation permet de simplifier le problème, elle apporte également son lot de questions, en particulier pour la phase solide :

- cette rhéologie est-elle valide ?

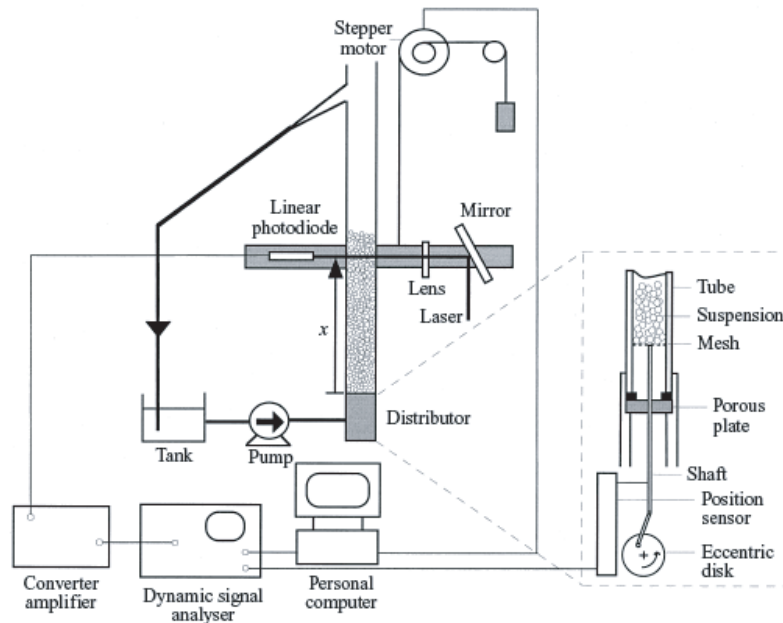


FIG. 2.1 – Dispositif expérimental utilisé pour la mesure de l'onde de concentration.

- quelle est la viscosité $\mu_s(\phi)$ de la phase solide ?
- quelle est la pression $p_s(\phi)$ de la phase solide ?

La confrontation de ce modèle avec des expériences bien choisies nous a permis d'apporter toutes les réponses nécessaires à ces questions.

2.2 Résultats

Comme la fluidisation homogène est difficile à mettre en œuvre, nous avons utilisé la première instabilité, qui prend la forme d'une onde plane générée par des fluctuations de fraction volumique au niveau de l'injecteur du lit fluidisé (Nicolas *et al.* 1994, 1996). De nature convective, cette instabilité est fortement non linéaire, ce qui rend impossible la mesure de son taux de croissance. Par contre, l'onde linéaire sature en amplitude lors de son évolution spatiale. La mesure précise de cette onde non linéaire saturée donne accès à de nombreuses informations

Le dispositif expérimental utilisé (figure 2.1) était un lit fluidisé confiné, un tube d'environ 1 cm de diamètre, rempli par des particules de 100 à 300 μm . On s'assure ainsi que seule une onde plane peut se développer. Nous avons mesuré les fluctuations de concentration par une technique d'atténuation de lumière. L'instabilité était forcée harmoniquement par un piston poreux qui faisait office d'injecteur. La figure 2.2 donne un exemple d'une onde saturée.

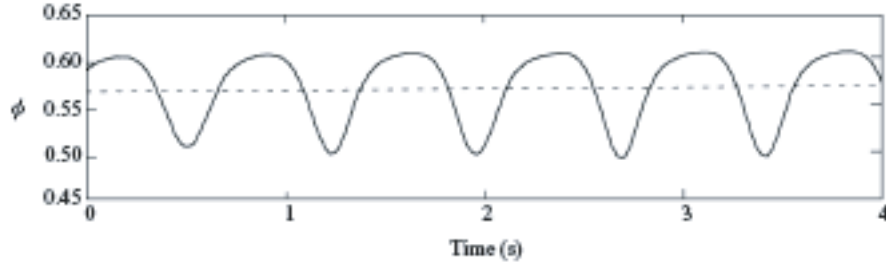


FIG. 2.2 – Exemple de mesure de la fraction volumique, obtenue pour une fréquence de forçage de 1.4 Hz. La courbe est une moyenne sur 100 enregistrements. Particules de verre lourd, 685 μm , fluidisés par de l'eau.

À partir du modèle diphasique établi par Anderson & Jackson, il est possible d'obtenir pour la fraction volumique une équation unique décrivant l'onde plane saturée :

$$\frac{4}{3}c\phi_0 \frac{d}{dX} \left[\mu_s(\phi) \frac{d\phi}{dX} \frac{1}{\phi^2} \right] + F_1(\phi) + \left[F_2(\phi) - \frac{dp_s}{d\phi} \right] \frac{d\phi}{dX} = 0, \quad (2.1)$$

où la fonction F_1 est la différence entre la traînée et le poids, et la fonction F_2 regroupe les termes d'inertie et de masse ajoutée (voir l'article A7 pour plus de détails). La confrontation de cette équation avec les mesures de la forme de l'onde saturée nous a permis d'avoir accès aux deux fonctions jamais mesurées jusque là $\mu_s(\phi)$ et $p_s(\phi)$.

En ce qui concerne la viscosité de la phase solide, la meilleure corrélation obtenue avec les données expérimentales (Figure 2.3) est

$$\mu_s(\phi) = 0.18 \frac{\rho_s d v_t}{\phi_{rlp} - \phi}, \quad (2.2)$$

où v_t est la vitesse de chute d'une particule, d son diamètre et ϕ_{rlp} la fraction volumique *random loose packing*. C'est une fonction qui diverge quand la concentration est proche de celle d'un empilement aléatoire lâche, c'est-à-dire quand les premières chaînes de contact se forment au sein de la suspension.

L'équation (2.1) donne accès à la dérivée de la pression solide $dp_s/d\phi$, et les principaux résultats sur ce terme sont montrés sur la figure 2.4. Cette dérivée semble être constante pour les concentrations inférieures à la concentration maximum, puis semble diverger négativement à l'approche de ϕ_{rlp} . On peut donc proposer une expression de la forme

$$\frac{dp_s}{d\phi} \approx 0.2\rho_s v_t^2 + \frac{K}{\phi - \phi_{rlp}} \quad \text{ou} \quad \frac{dp_s}{d\phi} \approx 0.7\rho_f v_t^2 + \frac{K}{\phi - \phi_{rlp}}, \quad (2.3)$$

soit

$$p_s \approx 0.2\rho_s v_t^2 \phi + K \log(\phi - \phi_{rlp}) \quad \text{ou} \quad p_s \approx 0.7\rho_f v_t^2 \phi + K \log(\phi - \phi_{rlp}), \quad (2.4)$$

Ce résultat montre que, aux faibles fractions volumiques, la pression solide est une fonction linéaire de la concentration, comme proposé par Needham & Merkin (1983). À l'approche

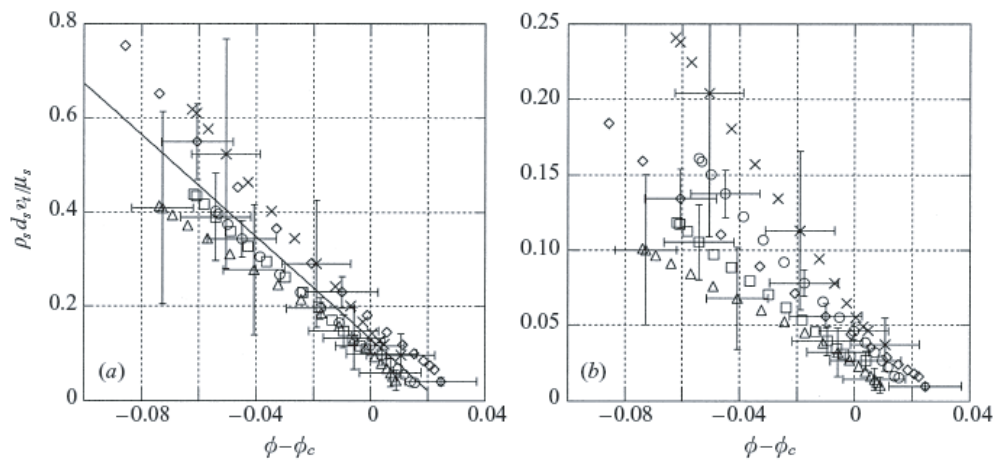


FIG. 2.3 – Viscosité de la phase solide dans un lit fluidisé liquide-solide. Voir la légende de la figure 20 de l'article A7 (Duru et al. 2002).

de la fraction volumique maximale, la pression décroît rapidement, et $dp_s/d\phi$ montre de fortes valeurs négatives.

Ces résultats, publiés en 2002 dans le *J. Fluid Mech.* (Duru et al. 2002) ont apporté une conclusion à trente ans de spéculations et d'hypothèses sur la description de la phase solide. Ces résultats sont à l'heure actuelle utilisés par des modèles numériques continus, et confrontés à des simulations numériques discrète. En particulier, les recherches s'orientent actuellement sur la formation de bulles dans les lits fluidisés, zones dépourvues en particules et modifiant considérablement la structure globale de l'écoulement.

2.3 Références

ANDERSON T. B. & JACKSON R. 1967 Fluid mechanical description of fluidized beds. Equation of motion. *Ind. Engng Chem. Fundam.* **6**, 527–539.

ANDERSON T. B. & JACKSON R. 1968 Fluid mechanical description of fluidized beds. Stability of the state of uniform fluidization. *Ind. Engng Chem. Fundam.* **7**, 12–21.

[A7] P. DURU, M. NICOLAS, E.J. HINCH & É. GUAZZELLI 2002, Constitutive laws of liquid-fluidized beds. *J. Fluid Mech.* **452**, 371–404.

JACKSON R. 1963 The mechanics of fluidized beds. I: the stability of the state of uniform fluidization. *Trans. Inst. Chem. Engrs* **41**, 13–21.

– NEEDHAM, D. J. & MERKIN, J. H. 1983 The propagation of voidage disturbances in a uniform fluidized bed. *J. Fluid Mech.* **131**, 427–454.

[A1] M. NICOLAS, J.-M. CHOMAZ & É. GUAZZELLI 1994, Absolute and convective instabilities of fluidized beds. *Physics of Fluids* **6** (12), 3936–3944.

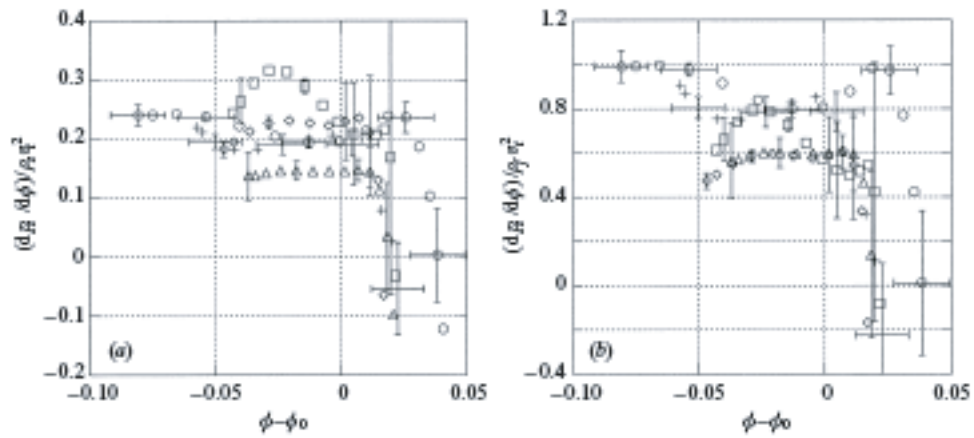


FIG. 2.4 – Dérivée de la pression de la phase solide en fonction de la fraction volumique. Voir la légende de la figure 27 de l'article A7 (Duru et al. 2002).

- A2 M. NICOLAS, J.-M. CHOMAZ, D. VALLET & É. GUAZZELLI 1996, Experimental investigations on the nature of the first wavy instability in liquid-fluidized beds. *Physics of Fluids* **8** (8), 1987–1989.
- A5 M. NICOLAS, E.J. HINCH & É. GUAZZELLI 1999, Wavy instability in liquid-fluidized beds. *Ind. Eng. Chem. Res.*, **38**, 799–802.

Chapitre 3

Compaction

*En collaboration avec P. Duru, P. Weidman (Univ. of Colorado),
M. Belzons (MCF) et O. Pouliquen (DR).*

3.1 Introduction

D'apparence banale, les empilements de particules solides ont depuis longtemps attiré le regard des physiciens. En 1611, Képler pose comme une évidence que l'empilement de sphères identiques le plus compact montre une fraction volumique — également appelée compacité — $\phi = \pi/\sqrt{18} \approx 0.74048$ (Figure 3.1a). Cette assertion faisait suite à une discussion scientifique et épistolaire avec Harriot sur la nature atomique de la matière. Cette conjecture, étudiée par Newton, Hilbert (en 1900), Fejes Tóth (en 1953) fut enfin démontrée à partir de 1994 par Hales (Hales 1997, 2000). Un tel empilement de compacité maximale a une énergie potentielle minimale et constitue donc l'aboutissement d'un processus de compaction sous l'effet de la gravité. Toutefois, un empilement réel montre souvent un caractère désordonné, avec une fraction volumique qui peut varier de 0.55 à 0.64 (Scott 1960, Cumberland & Crawford 1987) pour les empilements aléatoires, et de 0.64 à $\pi/\sqrt{18}$ pour les empilements partiellement ou parfaitement ordonnés.

La répartition hétérogène des contraintes de contact entre particules (chaînes de forces, voûtes) permet de former des empilements stables dont l'énergie potentielle n'est pas minimale. Seule une action extérieure permet à l'empilement de changer de configuration, d'évoluer pour éventuellement diminuer son énergie. La taille importante des particules souvent utilisées (sable, gravier, billes) ne permet pas aux fluctuations thermiques de jouer ce rôle. C'est pourquoi les empilements granulaires désordonnés sont des bons modèles de systèmes désordonnés athermiques. Ils ont donc de fortes analogies avec d'autres systèmes métastables tels que les verres.

Une première façon de solliciter un empilement est la vibration verticale. Soumis à une accélération supérieure ou égale à celle de la gravité, l'empilement est décompacté puis se recompacte par gravité dans une autre configuration. Étudiée expérimentalement par Knight *et al.* (1995) et Nowak *et al.* (1998), la vibration verticale assure une compaction lente dont l'évolution de la compacité est décrite par une fonction en inverse du logarithme

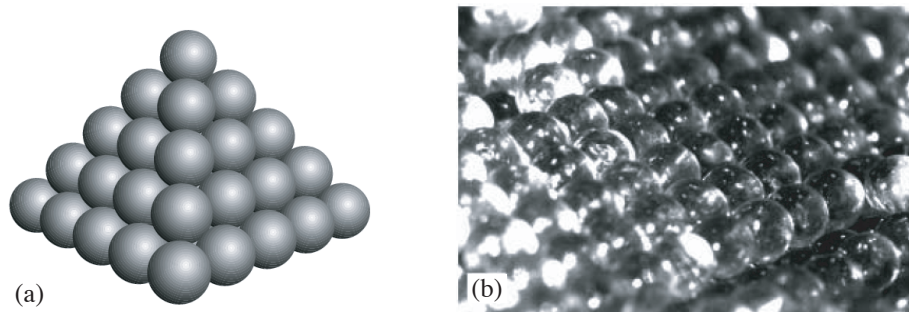


FIG. 3.1 – (a) Empilement cubique à face centrée, (b) photo d'un empilement de billes de verre obtenu par cisaillement quasi-statique.

du nombre de secousses. À partir d'un empilement aléatoire lâche, on peut ainsi obtenir un empilement aléatoire compact avec une compacité proche de 0.64. Le changement d'amplitude de l'accélération en cours d'expérience montre que la dynamique comporte des effets de mémoire (Josserand *et al.* 2000) : deux empilements de la même fraction volumique mais avec des histoires différentes n'auront pas la même évolution malgré une sollicitation identique.

La vibration verticale sous forme de secousses n'est pas le seul moyen de perturber un empilement. Nous avons étudié successivement l'effet d'une vibration horizontale continue puis l'effet d'un cisaillement quasi-statique.

3.2 Compaction sous vibration horizontale

L'observation d'un empilement granulaire vibré horizontalement montre que seules les couches superficielles sont mobiles, dans un référentiel lié au mouvement du récipient. Les couches profondes sont maintenues immobiles par le poids du matériau au dessus. Une fois la vibration arrêtée, il est facile d'observer que les particules des couches superficielles sont organisées pour former une structure cristalline. Nous avons donc développé un dispositif expérimental qui permet d'alimenter en continu un récipient soumis à une vibration horizontale (Figure 3.2a). Le contrôle du débit d'alimentation Q et de l'accélération horizontale $\Gamma = A\omega^2/g$ donne accès à différentes configurations de l'empilement, caractérisée par la fraction volumique finale ϕ . Comme le montre la figure 3.2b, extraite d'une publication dans *Phys. Rev. Lett.* (Pouliquen *et al.* 1997), la fraction volumique finale peut varier de 0.625 (empilement aléatoire compact) à 0.665, ce qui traduit la présence de zones cristallisées.

La variation du débit d'alimentation donne accès à des informations sur le processus de cristallisation. Comme le montre la figure 3.2c, l'efficacité de la compaction est moindre quand le débit est élevé. Ceci indique que la formation de zones cristallisées n'est pas

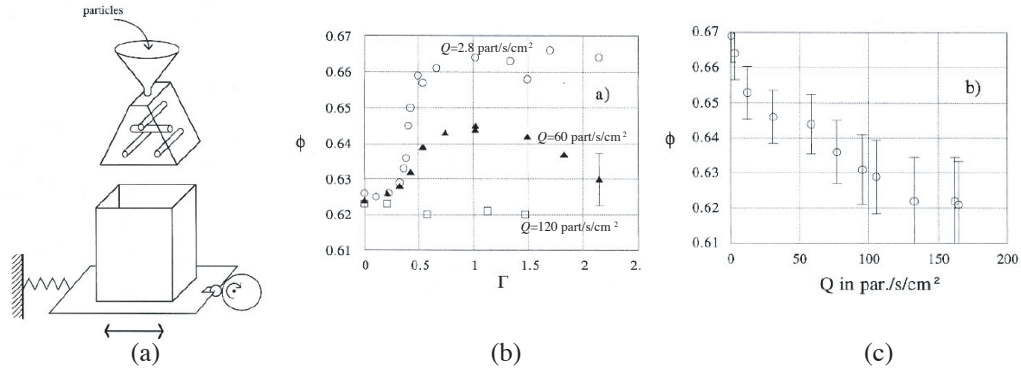


FIG. 3.2 – (a) Schéma de l'expérience de compaction par vibration horizontale. Le récipient est animé par un moteur et une came excentrée. L'alimentation en particules se fait par un diffuseur. (b) Compacité finale de l'empilement en fonction de l'accélération $\Gamma = A\omega^2/g$ pour trois débits d'alimentation. (c) Compacité finale en fonction du débit d'alimentation Q pour une accélération $\Gamma = 1$.

immédiate lors de la déposition des particules. L'assemblage des particules sous la forme d'un empilement cubique à faces centrées ou hexagonal compact nécessite un certain temps. La déposition de particules en continu impose un poids qui va « figer » l'empilement et l'empêcher de continuer à évoluer. Ainsi cette expérience met en lumière la compétition entre un apport d'énergie — la vibration horizontale — et une contrainte qui limite les mouvements des particules, « refroidissement » imposé sur la face supérieure de l'empilement. Ce système composé de « grosses » particules, donc insensibles au mouvement brownien, est pourtant analogue aux empilements de particules colloïdales. Si le liquide dispersant a le même indice de réfraction que celui des particules, les forces d'attraction de Van der Waals sont minimisées, et les particules ont des interactions de sphères dures. D'un diamètre d'environ $1 \mu\text{m}$, ces particules en sédimentation forment au fond du récipient un empilement cristallin aux propriétés optiques remarquables (Pusey & van Megen 1986, Pusey *et al.* 1989, Davis *et al.* 1989, van Blaaderen *et al.* 1997). La vibration horizontale imposée aux particules granulaires est analogue au mouvement brownien des colloïdes tandis que le rôle de l'alimentation continue des particules est joué par la gravité dans le cas des colloïdes pour « figer » l'ensemble dans un état métastable proche d'un réseau cristallin.

Entre la couche supérieure formée des particules les plus mobiles et les couches proches du fond du récipient, la variation de mobilité des particules incite à introduire une description en terme de cisaillement. Mais un tel dispositif expérimental ne garantit pas le contrôle de l'homogénéité et de l'amplitude du cisaillement. De plus l'apport continu de particules empêche d'étudier en détail le rôle de ce cisaillement dans le processus de cristallisation. A la suite de cette première expérience, nous avons développé un dispositif pour étudier la compaction d'un empilement soumis à une cisaillement seul.

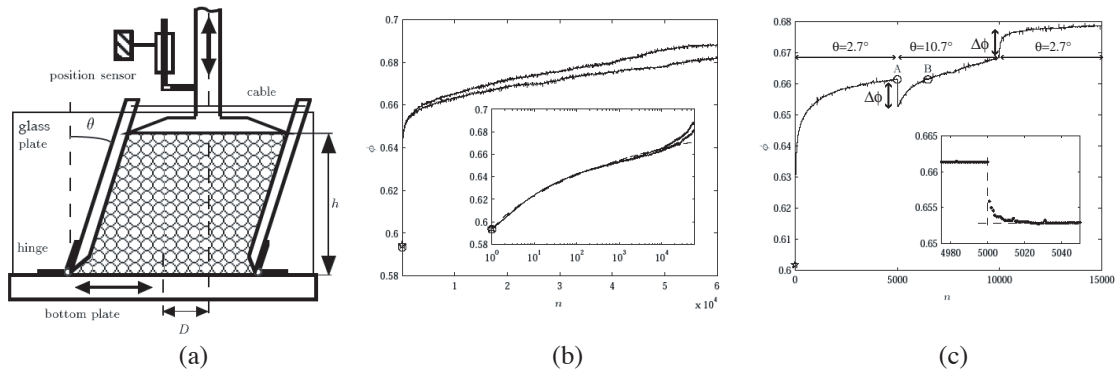


FIG. 3.3 – (a) Schéma de l'expérience de cisaillement cyclique d'un empilement granulaire. (b) Evolution de la fraction volumique pour un angle de cisaillement $\theta = 5.4^\circ$. Les deux courbes illustrent la difficile reproductibilité de l'empilement initial. L'insert présente les mêmes courbes en coordonnées semi-logarithmique, et la comparaison avec un modèle proposé par Knight *et al.* (1995). (c) Effet d'un changement d'amplitude de cisaillement sur la courbe de compaction. En insert, on peut observer la rapidité de la dynamique lors du changement de paramètre d'angle.

3.3 Compaction sous cisaillement

Le dispositif expérimental est basé sur un cisaillement cyclique du matériau granulaire. Le cisaillement est imposé par l'inclinaison alternative de deux plaques parallèles formant la cellule. Les deux autres plaques sont fixes. La base de la cellule est montée sur un banc de translation et la face supérieure est maintenue sur un guidage vertical uniquement. Un capteur de déplacement associé à la face supérieure donne accès à la fraction volumique durant tout le cours de l'expérience (Figure 3.3a). En imposant une faible vitesse de déplacement, on assure une déformation quasi-statique à l'empilement. Le seul paramètre est donc l'angle maximum d'inclinaison.

Chaque cycle de cisaillement est composé d'une inclinaison à $-\theta$ suivie d'une inclinaison à $+\theta$ puis d'un retour à la verticale. L'enregistrement de la fraction volumique au cours d'un cycle montre une alternance de déformation dilatante et de déformation contractante. Sur le long terme, seule la fraction volumique lors du retour à la verticale des plaques est mesurée. À partir d'un empilement aléatoire lâche, les 1000 premiers cycles d'oscillation montrent une compaction rapide, suivie d'une évolution lente, jusqu'à des temps de l'ordre de 60 000 cycles. Ceci est illustré sur la figure 3.3b.

La comparaison des données expérimentales avec les modèles proposés dans la littérature n'est pas satisfaisante (Barker & Mehta 1993, Knight *et al.* 1995). La présence de zones cristallines — attestée par une fraction volumique bien supérieure à 0.64 — explique cet écart avec des modèles issus de la physique statistique et basé sur le caractère aléatoire de l'empilement. Le caractère ordonné de l'empilement est vérifié par des observations en surface et à cœur. La photo de la figure 3.1b montre un exemple de 'une telle structure

pour des billes de verre de 2 mm de diamètre.

Ce dispositif expérimental est adapté à l'étude d'un changement de paramètre de contrôle. Lorsqu'une variation d'angle d'inclinaison est imposée au cours de l'expérience, la courbe de compaction subit une brusque évolution (Figure 3.3c). Alors que l'évolution « naturelle » de l'empilement nécessite de 1000 à 10 000 cycles, cette évolution ne prend qu'une dizaine de cycles pour avoir un effet considérable sur la fraction volumique. Nous avons pu montrer que ce saut $\Delta\Phi$ est linéairement opposé à la variation d'angle $\Delta\theta$ (Nicolas *et al.* 2000). La courbe de la figure 3.3c a été obtenue par une compaction avec un angle $\theta = 2.7^\circ$, suivie par une compaction avec $\theta = 10.7^\circ$ et enfin suivie d'une compaction avec $\theta = 2.7^\circ$ à nouveau. Les points A et B sur la courbe correspondent à la même fraction volumique mais montrent que l'évolution est très différente à partir de ces deux points, pourtant soumis à la même déformation de 10.7° . Il faut en conclure que la fraction volumique macroscopique est largement insuffisante pour décrire un empilement.

L'autre conclusion de cette étude est la mise en évidence de deux temps caractéristiques pour l'évolution de la fraction volumique : un temps long associé à une dynamique irréversible, et un temps court associé à des fluctuations réversibles. Tous ces résultats ont été publiés dans *Eur. Phys. J. E* (Nicolas *et al.* 2000) et présentés au congrès Powder and Grains 2001 (Nicolas *et al.* 2001).

3.4 Dynamique microscopique des particules

La coexistence de deux temps caractéristiques d'évolution de la compaction a été à la source de nombreuses études théoriques et numériques (Barker & Mehta 1992, Coniglio & Herrmann 1996, Barrat & Loreta 2001) mais la question du lien entre la compacité macroscopique et la structure microscopique des particules reste ouverte. Le dispositif expérimental de cisaillement a été adapté pour pouvoir contenir un liquide du même indice de réfraction que celui des billes de verre utilisées. L'empilement ainsi rendu translucide, nous avons suivi le mouvement de quelques particules rendues opaques par un dépôt de peinture (figure 3.4a). La fraction volumique globale est mesurée simultanément.

Des exemples de trajectoires sont montrés sur la figure 3.4b. Le mouvement de descente est rapide lors des premiers cycles de cisaillement puis les particules semblent stagner et fluctuer autour d'une position d'évolution très lente. Une analyse plus détaillée de ces mouvements fluctuants indique que les particules tracent des trajectoires en forme de pelotes connectées par des mouvements rapides de changement de pelotes (Figure 3.5a). Si la difficulté de l'expérience a limité la statistique sur les changements de pelote, nous disposons de bonnes informations sur les mouvements fluctuants au sein d'une pelote. En particulier, le déplacement moyen $\langle \Delta r \rangle$ est relié à l'amplitude du cisaillement macroscopique (Figure 3.5b).

Lors d'un changement décroissant du paramètre de cisaillement, le volume exploré par une particule diminue. La taille des pelotes de trajectoire évolue rapidement et permet une variation rapide de la fraction volumique globale. Nous pensons qu'il est donc possible de relier la dynamique lente de compaction aux changements occasionnels de pelotes,

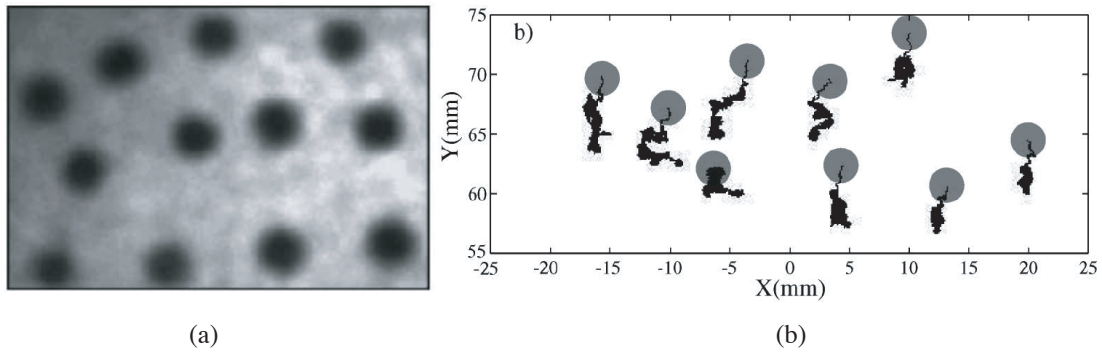


FIG. 3.4 – (a) Exemple de visualisation de particules opaques dans le milieu iso-indice. (b) Exemples de trajectoires de particules marquées durant 15 000 cycles à $\theta = 5.4^\circ$.

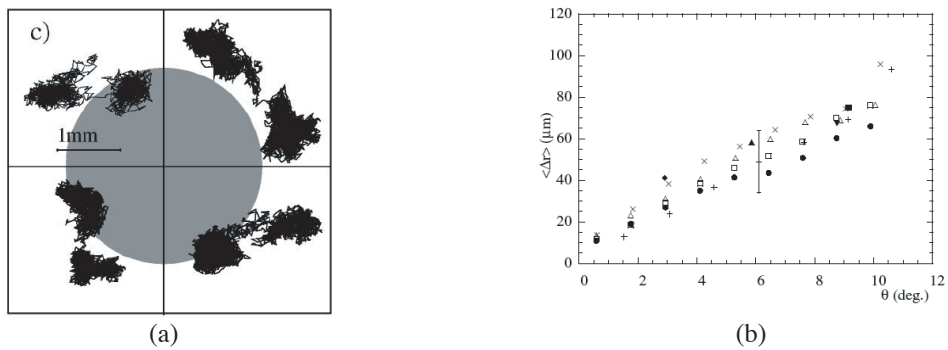


FIG. 3.5 – (a) Exemples de mouvement de cages de particules marquées. (b) Corrélation entre le déplacement moyen $\langle \Delta r \rangle$ et le paramètre de cisaillement macroscopique θ .

les sauts de cage, et de relier la dynamique rapide observée lors d'un changement de paramètre à la variation de taille des pelotes. Ce dernier phénomène est réversible car entièrement contrôlé par le paramètre de cisaillement. Les résultats de cette étude sur les mouvements microscopiques des particules ont été publiés dans *Phys. Rev. Lett.* (Pouliquen *et al.* 2003).

3.5 Références

- BARKER G. C. & MEHTA A. 1992 Vibrated powders: Structure, correlations, and dynamics. *Phys. Rev. A* **45**, 3435–3446.
- BARKER G. C. & MEHTA A. 1993 Transient phenomena, self-diffusion, and orientational effects in vibrated powders. *Phys. Rev. E* **47**, 184–188.
- BARRAT A. & LORETO V. 2001 Memory in aged granular media. *Europhys. Lett.* **53**, 297–303.
- CONIGLIO A. & HERRMANN H. J. 1996 Phase transitions in granular packings. *Physica* **225A** 1–6.
- CUMBERLAND D. J. & CRAWFORD R. J. 1987 The packing of particles. Handbook of powder technology, Elsevier, Amsterdam.
- DAVIS K. E., RUSSEL W. B., & GLANTSCHING W. J. 1989 Disorder to order transition in settling suspensions of colloidal silica: x-ray measurements. *Science* **245**, 507.
- HALES T. C. 1997 Sphere Packings I, *Discrete Comput. Geom.* **17** 1–51.
- HALES T. C. 1997 Sphere Packings II, *Discrete Comput. Geom.* **18** 135–149.
- HALES T. C. 2000 Cannonballs and honeycombs, *Notices of the AMS* **47**(4) 440–449.
- JOSSERAND C., TKATCHENKO A., MUETH D. & JAEGER H. M. 2000 Memory effects in shaken granular material. *Phys. Rev. Lett.* **85**, 6362.
- KNIGHT J.B., FANDRICH C. G., LAU C. N., JAEGER H. M. & NAGEL S. 1995 Density relaxation in a vibrated granular material. *Phys. Rev. E* **51**, 3957.
- [C4] LUDING S., NICOLAS M. & POULIQUEN O., 2000 A minimal model for slow dynamics: compaction of granular media under vibration or shear. , In "Compaction of soils, granulates and powders", D. Kolymbas and W. Follin (eds) A. A. Balkema, Rotterdam, p. 241.
- [A6] NICOLAS M., DURU P. & POULIQUEN E. 2000, Compaction of a granular material under cyclic shear. *Eur. Phys. J. E* **3**, 309–314.
- [C5] NICOLAS M., DURU P. & POULIQUEN O. 2001 Compaction of a packing of hard spheres under horizontal shear. In "Powder and grains 2001", Y. Kishino éditeur, A.A. Balkema, Tokyo.
- NOWAK E.R., KNIGHT J.B., BEN-NAIM E., JAEGER H. M. & NAGEL S. 1998 Reversibility and irreversibility in the packing of vibrated granular material. *Phys. Rev. E* **57**, 1971.

- A3 POULIQUEN O., NICOLAS M. & WEIDMAN P. 1997 Crystallisation of non-Brownian spheres under horizontal shaking. *Phys. Rev. Lett.* **79**(19), 3640–3643.
- A9 POULIQUEN O., BELZONS M. & NICOLAS M. 2003, Fluctuating particle motion during shear induced granular compaction. *Phys. Rev. Lett.* **91** (1) 014301.
- PUSEY P. N. & VAN MEGEN W. 1986 Phase-behavior of concentrated suspensions of nearly hard colloidal spheres. *Nature* **320** 340–342.
- PUSEY P. N., VAN MEGEN W., BARTLETT P., ACKERSON B. J., RARITY J. G., & UNDERWOOD S. M. 1989 Structure of crystals of hard colloidal spheres. *Phys. Rev. Lett.* **63**, 2753–2756.
- SCOTT D. G. 1960 *Nature* **188**, 908.
- VAN BLAADEREN A., RUEL R. & WILTZIUS P. 1997 Template-directed colloidal crystallisation. *Nature* **385**, 321.

Chapitre 4

Écoulements granulaires immergés : application aux avalanches sous-marines

En collaboration avec C. Cassar (doctorant 2002-2005) et O. Pouliquen (DR).

4.1 Introduction

La littérature géophysique rapporte de nombreux événements où des particules solides dévalent une pente en milieu sous-marin ou saturé en eau. C'est le cas des avalanches sous-marines, souvent consécutives à des tremblements de terre, quelques fois dues à l'activité humaine. Deux exemples célèbres. Le 18 novembre 1929 à la pointe sud des *Grand Banks*, au Canada, un séisme déclenche une coulée sous-marine de 200 km³ de débris, parourant 100 km à une vitesse de 60 à 100 km/h. Douze câbles télégraphiques sont sectionnés et un tsunami tue 28 personnes. Les vagues générées par une telle coulée sont ressenties de l'autre côté de l'océan, au Portugal (Fine *et al.* 2005). Plus récemment, en 1979 au large de Nice, une coulée sédimentaire de 150 millions de m³ a lieu à l'embouchure du Var, emportant une digue, une partie des remblais de l'aéroport et causant un tsunami sur Antibes. Encore plus récemment, le 24 août 2004, une avalanche à 15 km des côtes de Marseille a provoqué le retrait des eaux de la plage de la Pointe Rouge sur une vingtaine de mètres. L'onde de retour a été bénigne.

Toutes les avalanches sous-marines n'ont pas de conséquence dramatiques, ce qui fait que la plupart passent inaperçues. Pour celles dont le dépôt a pu être observé, les distances sur lesquelles les avalanches se déplacent sont souvent considérables, malgré une faible pente du fond océanique. La géophysique fait alors état de *long run-out avalanches* (Legros 2002). Ces grandes distances de déplacement ne peuvent être expliquées avec des modèles purement granulaires. Le rôle de l'eau semble donc avoir une importance particulière. Certains auteurs évoquent un phénomène d'*hydroplaning* quand une fine couche d'eau se place entre le fond et la coulée, créant un « coussin » qui diminue la

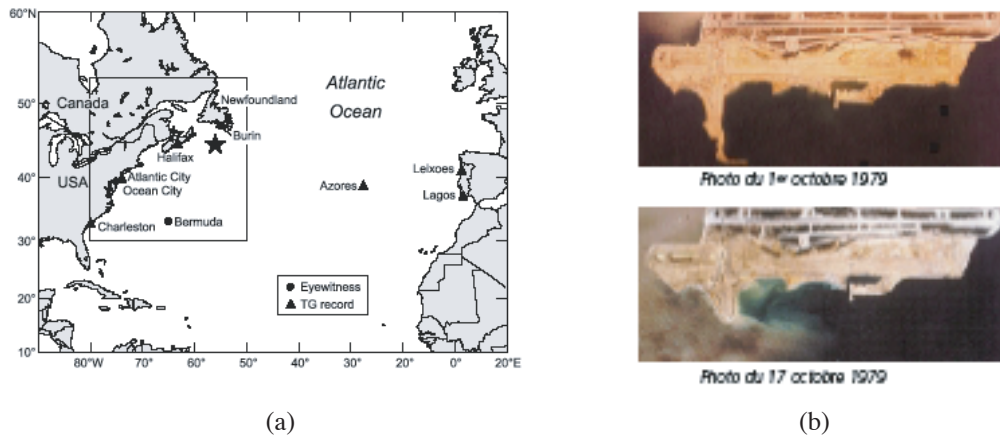


FIG. 4.1 – (a) Carte situant l’avalanche sous-marine de 1929 au Canada. L’étoile précise l’épicentre du séisme. D’après Fine *et al.* (2005). (b) Deux photos aériennes de l’aéroport de Nice avant et après l’avalanche d’octobre 1979.

coefficient de friction du matériau (Mohrig *et al.* 1998).

La modélisation des avalanches sous-marines repose souvent sur une description de la coulée par un fluide non newtonien avec une rhéologie de Bingham comportant un seuil de contrainte (Assier Rzadkiewicz *et al.* 1996). Le choix ad-hoc de cette rhéologie permet de reproduire la rhéologie des écoulements réels, composés d’un liquide porteur et de nombreux composants solides (rocs, graviers, sables, argiles, etc.). Mais cette description empêche d’aborder le lien entre la structure microscopique du matériau (taille, densité des particules) et son comportement en écoulement.

Nous avons donc choisi deux approches complémentaires pour tenter de modéliser de tels écoulements. La première est une approche expérimentale, couplée à une description théorique issue des développements récents de la rhéologie des écoulements granulaires. La deuxième approche est un calcul de la dynamique d’un bloc poreux indéformable en mouvement le long d’un plan rugueux. L’effet du fluide interstitiel peut ainsi être isolé.

4.2 Des écoulement granulaires aux avalanches sous-marines

Une des configurations simples pour étudier les milieux granulaires est l’écoulement sur plan incliné. À partir d’un réservoir à ouverture fixée, on peut observer selon l’inclinaison θ du fond des écoulements stationnaires et uniformes. Il existe alors une relation entre l’épaisseur h , la vitesse u et l’angle. O. Pouliquen (1999) a montré que la relation entre ces quantités nécessite de connaître l’épaisseur du dépôt h_{stop} : $u/\sqrt{gh} = \beta h/h_{stop}$.

Dans un article récent issu d’un Groupe de Recherches sur les milieux divisés (GDR Midi 2004), il a été montré que le coefficient de friction d’un milieu granulaire est une fonction d’un unique nombre sans dimension I (nombre inertiel), rapport de deux temps

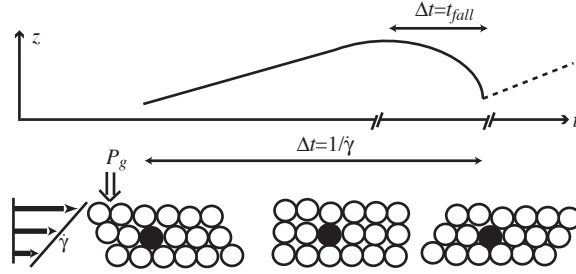


FIG. 4.2 – Description graphique du mouvement d'une particule au sein d'un écoulement de particules cisailé et soumis à une pression de confinement P_g .

caractéristiques, l'un microscopique, l'autre macroscopique. Ce dernier est le temps de déformation de la structure des grains. Dans le cadre d'un écoulement sur un plan incliné, ce temps est l'inverse du taux de cisaillement défini par $\dot{\gamma} = u/h$, où u est la vitesse de l'écoulement et h l'épaisseur de la coulée. Le temps microscopique est le temps nécessaire à une particule pour retrouver une position énergétiquement favorable après la déformation macroscopique (voir Figure 4.2). Ce temps dépend des forces qui s'appliquent à une particule, force de pesanteur ou force de confinement P_g liée à la présence de particules au dessus.

Nous avons modélisé une avalanche sous-marine par un écoulement granulaire immergé. Notre approche consiste donc à adapter et généraliser la rhéologie des écoulements granulaires en tenant compte de la présence d'un fluide interstitiel. Le temps microscopique est lié à la chute d'un grain dans un interstice formé par la déformation du milieu. En présence d'un fluide dense (un liquide), la particule subit donc une force de traînée proportionnelle à sa vitesse dans un régime visqueux, ou proportionnelle au carré de sa vitesse en régime inertiel. De plus, le déplacement de cette particule se fait dans un environnement confiné, un milieu poreux formé par toutes les particules voisines. Le mouvement de la particule peut être décrit par trois nombres sans dimension, un nombre de Stokes, un nombre de Reynolds et le rapport des densités :

$$St = \left(\frac{2}{3}\right)^{1/2} \frac{\alpha d \sqrt{\rho_p P_g}}{\eta_f}, \quad Re = \frac{St}{r} = \frac{\alpha d}{\eta_f} \sqrt{\frac{2\rho_f C_d P_g}{3}}, \quad r = \sqrt{\frac{\rho_p}{\rho_f C_d}}, \quad (4.1)$$

avec C_d le coefficient de frottement et α le coefficient sans dimension intervenant dans la perméabilité $k = \alpha d^2$ du milieu poreux formé par un assemblage de particules de diamètre d .

Dans le cas d'une avalanche sous-marine, la pression de confinement est simplement un pression de type hydrostatique : $P_g = \Delta\rho gh \cos\theta$. Avec tous ces éléments, il est possible de définir plusieurs nombres I en fonction de la nature du fluide et du régime de déplacement

d'une particule.

- régime granulaire sec ($St \gg 1$ and $r \gg 1$),

$$I = I_{ff} = \frac{5}{2} \frac{ud}{h^{3/2}} \sqrt{\frac{2\rho_p}{3\Delta\rho g \cos \theta}}; \quad (4.2)$$

- régime visqueux ($St \ll 1$ and $r \gg St$),

$$I = I_v = \frac{3u}{h^2} \frac{\eta_f}{\alpha\Delta\rho g \cos \theta}; \quad (4.3)$$

- régime inertiel ($St \gg r$ and $r \ll 1$),

$$I = I_i = \frac{5}{2} \frac{ud}{h^{3/2}} \sqrt{\frac{2\rho_f C_d}{3\Delta\rho g \cos \theta}}. \quad (4.4)$$

Pour le régime visqueux il est intéressant de remarquer que le nombre I_v est le rapport entre un nombre de Reynolds interstitiel (basé sur la taille des interstices αh) $Re_i = \alpha h u \rho_f / \eta_f$ et un nombre de Froude $Fr = u^2 / \phi((\rho_p / \rho_f - 1)gh \cos \theta)$:

$$I_v = \frac{3Fr}{Re_i}.$$

4.3 Comparaison avec les résultats expérimentaux

Le dispositif expérimental est un plan incliné rugueux immergé dans une cuve en verre. Deux types d'expériences ont été réalisées : des écoulements aériens et des écoulements immergés. Ces deux fluides (air et eau) sont suffisamment différents pour tester la rhéologie proposée. La rugosité du fond est fabriquée avec les mêmes particules que l'écoulement. Deux tailles de billes de verre ont été utilisées, environ 100 et 200 μm . Les détails expérimentaux sont reportés dans l'article B11 (Cassar, Nicolas & Pouliquen 2005). Les expériences ont été effectuées dans l'air et dans l'eau.

Nous avons observé trois régimes d'écoulement :

- peu après l'ouverture du réservoir, l'écoulement s'arrête ;
- écoulement stationnaire et uniforme ;
- écoulement instable avec formation d'ondes de surface.

Le régime inertiel de chute d'une particule n'a pu être observé dans nos expériences. Seuls les régimes visqueux et granulaires ont été observés. L'effet de l'eau induit une baisse de la vitesse d'écoulement d'un facteur 10 environ, à angle et épaisseur de coulée constants.

La figure 4.3(a) montre la corrélation entre le nombre I et le coefficient de friction $\mu = \tan \theta$ pour la plupart des expériences effectuées. Les données expérimentales se rassemblent

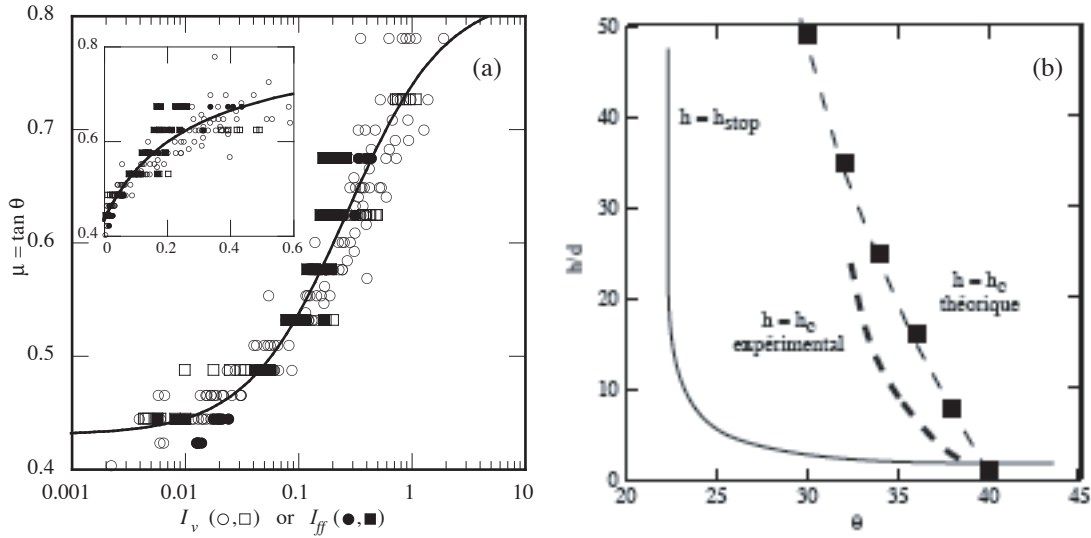


FIG. 4.3 – (a) Correlation entre le nombre I calculé pour les écoulements aériens (symboles noirs) et immergés (symboles clairs) et le coefficient de friction μ . La courbe est la représentation de l'expression (4.5) avec $\mu_1 = 0.43$, $\mu_2 = 0.82$ et $I_0 = 0.27$. (b) Régimes d'écoulement dans le plan (θ, h) . La courbe continue est la limite $h_{stop}(\theta)$, la courbe discontinue est la limite entre les écoulements stationnaires uniformes et les écoulements instables. La courbe discontinue rehaussée de carrés noirs est le seuil d'instabilité calculé par l'approximation linéaire.

relativement bien autour d'une courbe maîtresse qui peut être décrite par une fonction du type

$$\mu(I) = \mu_1 + \frac{\mu_2 - \mu_1}{I_0/I + 1}, \quad (4.5)$$

où μ_1 , μ_2 et I_0 sont des constantes.

Ces résultats montrent que malgré la simplicité du modèle, une fonction $\mu(I)$ permet de décrire aussi bien des écoulements granulaires secs que des écoulements immergés. La dispersion des points expérimentaux incite néanmoins à penser que cette description est imprécise.

4.4 Instabilité de surface

Connaissant la loi de friction, il est possible de s'intéresser à la stabilité d'un écoulement stationnaire et uniforme. En utilisant le formalisme des équations moyennées dans l'épaisseur (Savage & Hutter 1989, Forterre & Pouliquen 2003), on peut obtenir une relation de dispersion de la forme

$$-\Omega^2 + 2\beta\Omega K + \frac{i}{Fr^2}(a-b)\Omega K + \left(\frac{1}{Fr^2} - \beta\right)K^2 = 0 \quad (4.6)$$

avec $Fr = u_0/\sqrt{gh_0 \cos \theta}$ et β le coefficient indicateur du profil de vitesse ($\beta = 6/5$ pour un profil semi-parabolique).

L'analyse spatiale de cette équation montre que tous les nombres d'ondes sont instables si

$$Fr^2 > Fr_c = \frac{1}{9 - 5\beta}.$$

Avec l'hypothèse d'un profil de vitesse semi-parabolique ($\beta = 6/5$), on obtient un critère d'instabilité de la forme $Fr > 0.58$. La comparaison entre le critère d'instabilité linéaire et les observations montre un accord qualitatif (Figure 4.3b) mais le critère théorique est décalé. Le comportement réel de l'écoulement est sans doute non linéaire, ce qui peut expliquer l'écart avec les prédictions théoriques.

4.5 Approche macroscopique

Dans une vision macroscopique, une coulée de particules solides peut être modélisée comme un bloc poreux glissant le long d'une pente rugueuse. Ce modèle est dérivé des travaux de Iverson (1989, 1993), et de Musso *et al.* (2004). Dans une première approche, le caractère déformable de ce bloc n'est pas pris en compte. Pour simplifier encore le problème, la rugosité $R(X)$ est remplacée par une modulation sinusoïdale du fond imperméable. Le bas du bloc poreux présente cette même modulation dont la longueur d'onde est représentative de la taille d'une particule. Le glissement du bloc le long du fond — si glissement il y a — produit périodiquement un mouvement de fluide au sein du poreux, mouvement régi par une loi de Darcy. En prenant en compte une force de pesanteur, une force de friction et une force d'origine Darcienne, l'équation du mouvement du bloc poreux en contact avec le substrat est

$$\begin{aligned} \ddot{X} \left(1 + \mu(X) \frac{dR}{dX} \right) &= \sin \theta - \mu(X) \cos \theta \\ &\quad - \mu(X) \left(\dot{X}^2 \frac{d^2 R}{dX^2} + \frac{1}{St} \dot{X} \frac{dR}{dX} \right). \end{aligned} \quad (4.7)$$

avec le nombre de Stokes

$$St = \frac{k\phi}{\eta} \sqrt{\frac{g\rho_p \Delta\rho}{d}}. \quad (4.8)$$

Cette équation est résolue numériquement, et montre trois types de trajectoires : arrêt du mouvement, mouvement périodique à vitesse moyenne constante, et mouvement accéléré. La figure 4.4 montre les occurrences des écoulements stationnaires dans le plan (St, θ) . On peut ainsi voir que le rôle du fluide n'est pas unique. En effet, dans le cas d'une faible perméabilité, la force induite par l'écoulement de Darcy impose au bloc de rester en contact avec le plan. Mais le fluide joue également un rôle de lubrifiant dans les mouvements de descente du bloc. Il en résulte une courbe non monotone, traduction d'un rôle ambivalent du liquide interstitiel.

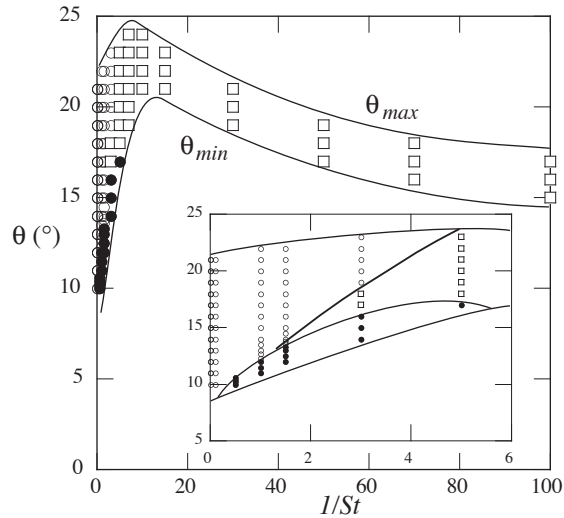


FIG. 4.4 – Angles minimum et maximum en fonction de St pour obtenir un écoulement moyen stationnaire. L'insert permet de mieux distinguer les trajectoires de contact (cercles noirs), les trajectoires ballistiques (cercles blancs) et les trajectoires lubrifiées (carrés).

4.6 Perspectives

La description par une rhéologie unique des écoulements aérien et immergés sur plan incliné constitue une étape importante. L'approche à deux temps caractéristiques semble être capable de décrire un certain nombre de configurations. Toutefois, le rôle de la pression interstitielle du liquide est encore mal compris. Il semble maintenant nécessaire de continuer l'étude pour des écoulements non stationnaires, en particulier lors des phases de démarrage et d'arrêt de l'écoulement. Une thèse sera prochainement proposée sur ce sujet.

4.7 Références

S. ASSIER RZADKIEWICZ, C. MARIOTTI, & P. HEINRICH 1996, Modeling of submarine landslides and generated water waves, *Phys. Chem. Earth*, **21**, 7.

A11 C. CASSAR, M. NICOLAS & O. POULIQUEN, 2005 Submarine granular flows down inclined planes, *Phys. Fluids*. **17**, 103301.

A12 C. CASSAR, O. POULIQUEN & NICOLAS, Dynamics of a sliding porous block down a non permeable rough substrate, soumis à *Eur. Phys. J. E*.

COURRECH DU PONT S., GONDRET P., B. PERRIN B. and RABAUD M. 2003 Granular avalanches in fluids *Phys. Rev. Lett.* **90**, 044301.

FINE I. V. ,RABINOVICH A. B., B.D. BORNHOLD B. D., THOMSON R. E. &

- KULIKOV E. A. 2005 The Grand Banks landslide-generated tsunami of November 18, 1929: preliminary analysis and numerical modeling. *Marine Geol.* **215** 45–57.
- FORTERRE Y. & POULIQUEN O. 2003 Long-surface-wave instability in dense granular flows, *J. Fluid. Mech.* , **486**, 21–50.
- GDR MIDI 2004 On dense granular flow *Eur. Phys. J. E* **14**, 341–365.
- IVERSON R.M., LAHUSEN R. G. 1989 Dynamic pore pressure fluctuations in rapidly shearing granular materials. *Science* **246**, 796-799.
- IVERSON R. M. 1993 Differential equations governing slip-induced pore pressure fluctuations in water saturated granular medium. *Math. Geol.* **25** (8), 1027–1048.
- LEGROS F. 2002 The mobility of long-runout landslides. *Engineering Geology* **63**, (3-4), 301–331.
- MOHRIG D., WHIPPLE K. X., HONDZO M., ELLIS C., PARKER G. 1998 Hydroplaning of subaqueous debris flows. *Geol. Soc. Am. Bull.* **110** (3), 387–394.
- MUSSO A., FEDERICO F. & TROIANO G. 2004, A mechanism of pore pressure accumulation in rapidly sliding submerged porous blocks. *Comp. and Geotech.* **31**, 209–226.
- POULIQUEN O. 1999 Scaling laws in granular flows down rough inclined planes. *Phys. Fluids* **11** (3), 542.
- SAVAGE S. B., HUTTER K. 1989, The motion of a finite mass of granular material down a rough incline. *J. Fluid. Mech.* **199**, 177–215.

Chapitre 5

Dispersion de suspensions concentrées : jets, gouttes, tores

5.1 Sédimentation hétérogène

La description de la sédimentation de particules solides non browniennes repose souvent sur une hypothèse d'homogénéité de la suspension (Figure 5.1a). La sédimentation est alors caractérisée par une vitesse moyenne, une distribution de fluctuations de vitesse et par l'évolution du front entre la suspension et le fluide clair. Le contre-écoulement induit par la sédimentation des particules a lieu dans le volume même de la suspension et conduit à un effet de freinage qui dépend uniquement de la fraction volumique.

Pour des faibles fractions volumiques, Batchelor (1972) a montré que la vitesse de sédimentation décroît linéairement avec la fraction volumique :

$$\langle v_p \rangle = v_s(1 - 6.55\phi) + O(\phi^2). \quad (5.1)$$

Aux concentrations plus élevées, on utilise généralement une description empirique due à Richardson & Zaki (1954) :

$$\langle v_p \rangle = v_s(1 - \phi)^n + O(\phi^2). \quad (5.2)$$

où l'exposant n dépend du nombre de Reynolds particulaire. Cet exposant est proche de 5 pour les faibles nombres de Reynolds.

La situation est très différente quand le contre-écoulement peut emprunter un chemin préférentiel. C'est le cas de la sédimentation en récipient incliné, avec une vitesse moyenne de sédimentation augmentée par l'inclinaison du récipient — phénomène appelé effet Boycott du nom du biologiste qui l'a mis en évidence dans les années 1920. En effet, une couche de fluide clair apparaît le long de la paroi supérieure et permet au liquide déplacé par les particules de s'écouler plus librement qu'au travers de la suspension (Figure 5.1b).

L'augmentation de la vitesse de sédimentation est encore amplifiée dans la configuration de jet que nous avons étudié. La suspension sédimente au centre d'un grand volume de fluide clair, et le contre-écoulement induit une force de cisaillement sur le contour du jet.

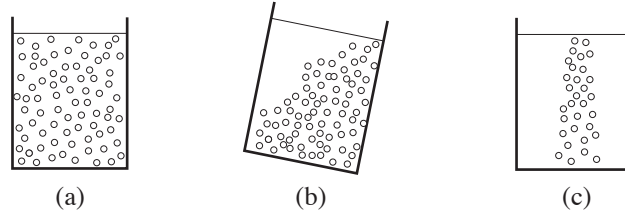


FIG. 5.1 – (a) *Sédimentation homogène* ; (b) *Effet Boycott dans un récipient incliné* ; (c) *Sédimentation hétérogène : jet de suspension*.

Cette configuration a déjà été largement étudiée quand un liquide est injecté dans un autre liquide (qui peut être de même nature), mais la nature granulaire induit toute une gamme de comportements jamais observé auparavant.

De plus, le grand volume disponible permet à la suspension de changer de fraction volumique au cours de la sédimentation. Partant de la fraction volumique maximale, on peut observer suivant les conditions différentes formes de dispersion du jet : formation de gouttes, dispersion par instabilité spirale, atomisation.

5.2 Jets de suspension

Le dispositif expérimental est présenté sur la figure 5.2. Le réservoir qui contient la suspension est un tube en verre complètement immergé dans une cuve remplie de liquide. Le jet est filmé à partir de l'ouverture d'une trappe qui ferme le fond du tube. Initialement assemblées en empilement compact, les particules quittent le tube sous forme d'un jet concentré de particules qui peut prendre différentes formes en fonction de l'accélération, des forces visqueuses et des interactions hydrodynamiques entre particules.

L'écoulement des particules dans le tube est analogue à un écoulement de liquide dans un viscosimètre capillaire. L'écoulement est induit par la gravité uniquement, la différence de pression étant nulle. L'équilibre des contraintes à la paroi avec la force de gravité permet de relier la vitesse d'écoulement à la viscosité du matériau. Si on note v_0 la vitesse moyenne de l'écoulement et r_0 le rayon interne du tube, cet équilibre s'écrit sous la forme

$$F_0 = \left(\frac{R_0}{32\alpha\eta_r} \right)^{1/2}, \quad (5.3)$$

avec

$$\alpha = \frac{\rho_f}{\rho}, \quad F_0 = \frac{v_0}{\sqrt{2gr_0(1-\alpha)}}, \quad R_0 = \frac{2v_0r_0\rho_f}{\eta_f}. \quad (5.4)$$

La pertinence de ces nombres sans dimension est validée par les résultats expérimentaux montrés sur la figure 5.3. On peut vérifier que l'écoulement se fait à vitesse constante, une fois un temps d'accélération passé. La corrélation entre F_0 et R_0/α est bien vérifiée, avec toutefois une incertitude assez grande sur la viscosité relative η_r . En effet, tous

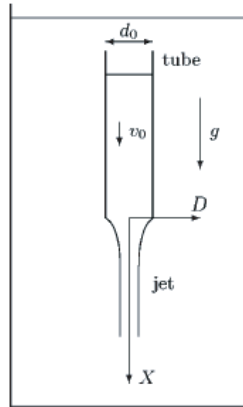


FIG. 5.2 – Schéma d'une expérience de jet de suspension. Le tube contient les particules qui s'écoulent dans la cuve par gravité.

les modèles de viscosité effective montrent une divergence de la viscosité à l'approche de la fraction volumique maximum, ce qui rend ces modèles délicats à utiliser pour les suspensions concentrées.

Malgré la simplicité du dispositif expérimental, de nombreuses configurations de jets peuvent être explorées. La vitesse de sortie du jet dépend principalement de la densité des particules ainsi que de la viscosité du liquide.

5.3 Modes de dispersion

Dans le cas d'une forte viscosité du liquide ou d'une très faible différence de densité, le jet se comporte comme un écoulement laminaire, avec une variation de diamètre due à son accélération de la vitesse de décharge dans le tube à la vitesse d'écoulement dans le liquide clair.

Pour des jets plus rapides, une première instabilité apparaît. Cette instabilité du jet montre une modulation du diamètre du jet analogue — visuellement — à l'instabilité de Rayleigh d'une colonne liquide soumise aux forces capillaires. Funada *et al.* (2004) ont montré qu'en l'absence de tension de surface, un jet cylindrique ne présente pas de mode instable, quel que soit les viscosités et densités relatives entre le jet et le fluide environnant. Ceci confirme les hypothèses avancées dans Nicolas (2002) : l'instabilité du jet de suspension est d'origine particulaire. Cette question est source de perspectives de recherche.

Le développement de cette instabilité conduit à la formation de « gouttes » de suspension qui vont avoir une dynamique individuelle (figure 5.4a). Ultérieurement, ces gouttes subissent elles-mêmes une instabilité pour donner naissance à des tores, eux-mêmes instables etc. Cette cascade d'instabilité est présentée dans la section §5.4.

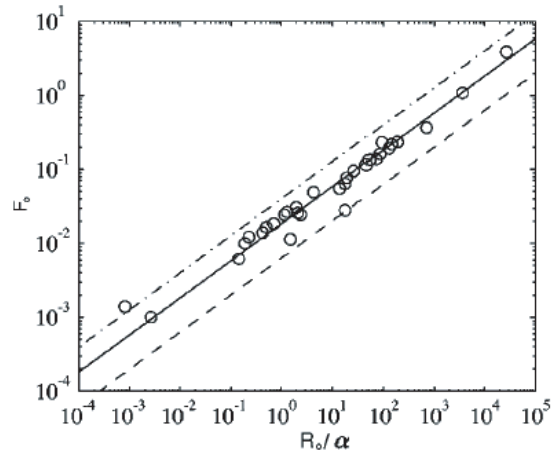


FIG. 5.3 – Corrélation entre R_0/α et F_0 . Le trait pointillé supérieur est tracé pour $\eta_r = 20$ tandis que le trait pointillé inférieur est tracé pour $\eta_r = 800$.

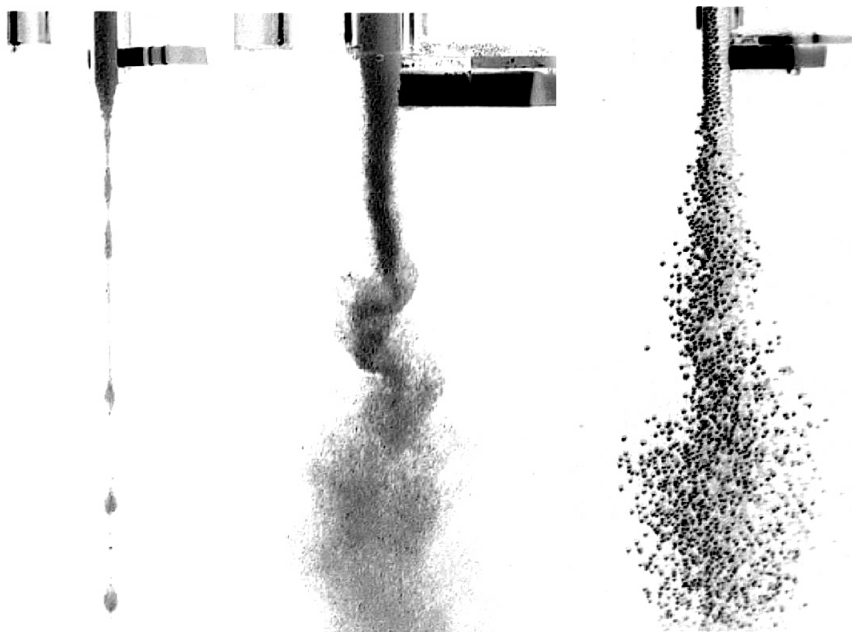


FIG. 5.4 – Différents modes de dispersion d'un jet de particules. Instabilité en gouttes (gauche), jet spiral (milieu) et jet atomisé (droite).

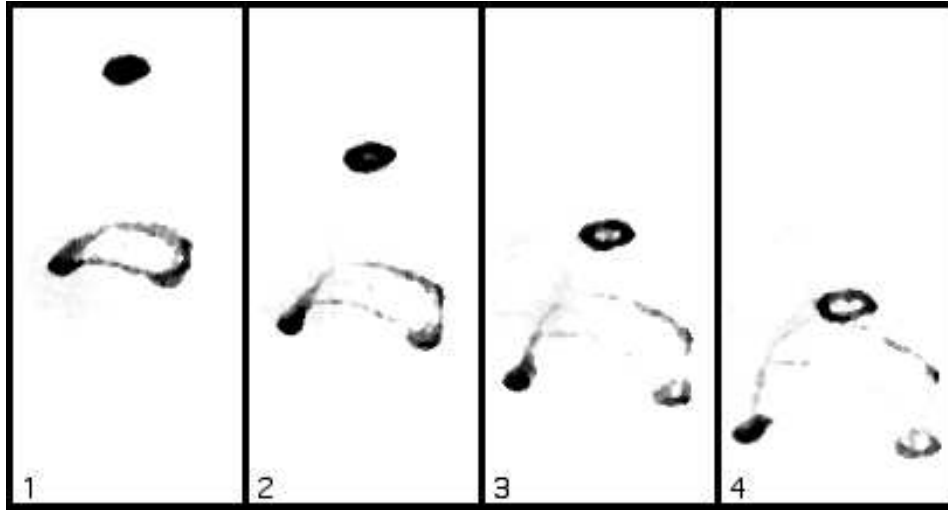


FIG. 5.5 – Evolution d'une goutte de suspension de particules sphériques.

Lors de ces expériences, quelques essais ont été réalisés avec un liquide interstitiel coloré par de la fluoresceine. Lors de l'écoulement du jet, nous avons pu observer que le colorant restait « piégé » au sein de la suspension, montrant que les échanges entre le liquide interstitiel et le liquide clair sont très faibles.

Pour des vitesses de jet plus importantes, on retrouve avec la suspension les mêmes comportements que pour des jets liquide/liquide. On peut ainsi observer un jet spiral (figure 5.4b) ou un jet atomisé (figure 5.4c). On a dans ces deux cas une forte dispersion des particules, avec une augmentation statistique de la distance inter-particules.

5.4 Évolution de gouttes de suspension

La fragmentation d'une colonne de particules en différentes gouttes isolées donne lieu à une cascade d'instabilité. Au départ d'une forme quasi-sphérique, une goutte de suspension va évoluer sous la forme d'un anneau. Cet anneau sera lui-même instable et peut se briser en 2, 3 ou 4 fragments qui vont avoir la même dynamique. Ce phénomène est analogue à l'évolution inertielle d'une goutte de liquide miscible (par exemple une goutte de lait dans de l'eau). Toutefois, les nombres de Reynolds calculés sur l'échelle de la goutte et sur l'échelle de la particules montrent que l'inertie ne joue pas de rôle.

Ceci a été confirmé par des expériences et des simulations numériques effectuées par B. Metzger et E. Guazzelli. La simulation est basée sur l'évolution temporelle d'un nuage de Stokeslets (points forces) au cours de la sédimentation. Même à nombre de Reynolds nul, la goutte finit par former un anneau, lui-même instable sous l'effet d'une instabilité de type Rayleigh-Taylor (Figure 5.5).

Des expériences préliminaires effectuées avec des fibres ont montré le même type de déformation d'un amas de fibres (Figure 5.6). Ces expériences montrent que ce sont les

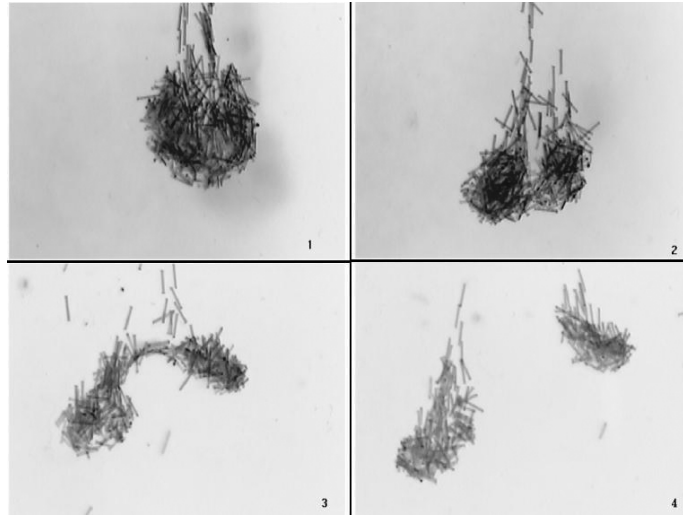


FIG. 5.6 – Evolution d'un amas de fibres de nylon.

interactions hydrodynamiques seules qui sont responsables de la dynamique complexe des amas d'objets solides en sédimentation.

Les expériences sur les gouttes isolées ont été reprises dans le cadre de la thèse de B. Metzger. Des comparaisons quantitatives avec les simulations numériques sont envisagées.

5.5 Références

FUNADA T., JOSEPH D. D. & YAMASHITA S. 2004 Stability of a liquid jet into incompressible gases and liquids. *Int. J. Multiphase Flow* **30**, 1279–1310.

MACHU G., MEILE W., NITSCHKE L. C. & SCHAFLINGER U. 2001 Coalescence, torus formation and breakup of sedimenting drops: experiments and computer simulations. *J. Fluid. Mech.* **447**, 299–336.

A8 M. NICOLAS 2002, Experimental study of gravity-driven dense suspension jets. *Phys. Fluids* **14** (10), 3570–3576.

POWELL R. L. & MASON S. G. 1982 Dispersion by laminar flow. *AIChE Journal* **28**(2) 286–293.

SCHAFLINGER U. & MACHU G. 1999 Interfacial phenomena in suspensions. *Chem. Eng. Technol.* **22**, 617–619.

Chapitre 6

Impact de gouttes chargées en particules

L'impact et l'étalement d'une goutte liquide sur une surface solide ou une nappe liquide est un sujet ancien aux nombreuses applications (l'article de revue de Rein, 1993, donne une bonne vue d'ensemble). La déposition de gouttes sur des surfaces est un sujet qui intéresse de nombreux domaines d'applications : déposition de peinture, d'encres, d'engrais, de métaux liquides avant solidification (Bhloa & Chandra 1999). Alors que la littérature ne mentionne que les impacts de goutte de liquide pur, des applications émergentes nécessitent de connaître l'impact et l'étalement de gouttes de fluides plus complexes.

J'ai commencé en mars 2004 à m'intéresser au rôle des particules solides sur l'impact de gouttes de suspension. Ce sujet m'a été inspiré par des discussions avec des industriels de la microélectronique. En effet, des technologies d'imprimante à jet d'encre conductrice se développent actuellement. Cette technologie vise à s'affranchir de la traditionnelle gravure sur silicium pour les connections entre puces et processeurs. Toutefois les encres conductrices ne se révèlent suffisamment conductrices que si elles sont fortement chargées en particules métalliques. Se posent alors les questions des propriétés rhéologiques d'un tel mélange, du comportement en écoulement et surtout de la répartition des particules solides lors de l'impact de la goutte sur un substrat. Il m'a semblé intéressant de monter une expérience de déposition de suspension sur une plaque plane. Les questions suivantes sont abordées :

- quel est l'effet des particules sur la nature de l'impact : étalement ou éclatement de la goutte ?
- quel est l'effet des particules sur la forme finale de la goutte étalée ?
- quelle est la répartition des particules au sein de la goutte étalée ?

Considérons une goutte sphérique venant s'étaler sur une surface. On note β le rapport entre le diamètre de la goutte étalée et son diamètre initial. Les nombres sans dimension pertinents pour ce problème sont le nombre de Reynolds $Re_0 = \rho d_0 U / \eta$ et le nombre de Weber $We = \rho d_0 U^2 / \sigma$ (ρ est la masse volumique, η est la viscosité dynamique et σ is la tension de surface du liquide avec l'air).

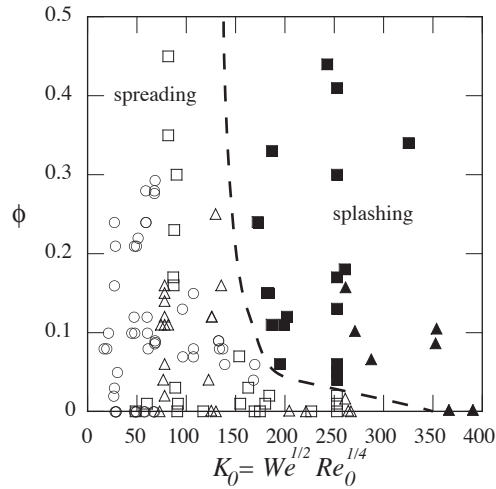


FIG. 6.1 – Diagramme d'impact : les symboles creux représentent des étalements et les symboles pleins représentent des impacts avec fragmentation.

6.1 Étalement ou fragmentation

Pour une goutte de liquide pur en impact sur une surface plane, le fait qu'une particule s'étale ou se fragmente dépend de la rugosité de la surface (Range & Feuillebois 1998, Stow & Hadfield 1981). Pour des grands nombres d'Ohnesorge, $Oh = \sqrt{We}/Re_0$, la limite de fragmentation est écrite sous la forme $We^{0.5} Re_0^{0.25} > K_c$. L'augmentation du Reynolds ou l'augmentation du Weber au delà d'un seuil favorise donc la fragmentation de la goutte. Le seuil K_c dépend de la rugosité de la surface.

Le dispositif expérimental détaillé dans l'article A10 (B.11) propose d'observer l'impact de gouttes de suspension formées d'un liquide et de particules de même densité. Cette configuration est éloignée d'une éventuelle application à des particules métalliques mais est en accord avec la configuration théorique : les particules n'ont d'effet que sur la viscosité effective de la suspension.

Un des principaux résultats de ce travail est l'observation suivante : le fait de rajouter des particules isodensité à un liquide ne limite pas forcément la fragmentation. Si l'ajout de particules permet d'augmenter la viscosité effective, on peut également favoriser la fragmentation. En effet, la figure 6.1 montre qu'à nombre $K = We^{0.5} Re_0^{0.25}$ constant, l'augmentation de la fraction volumique induit une transition vers la fragmentation de la goutte. Ce phénomène apparaît pour des nombres $K > 150$. En dessous de cette limite, aucune fragmentation n'a été observée.

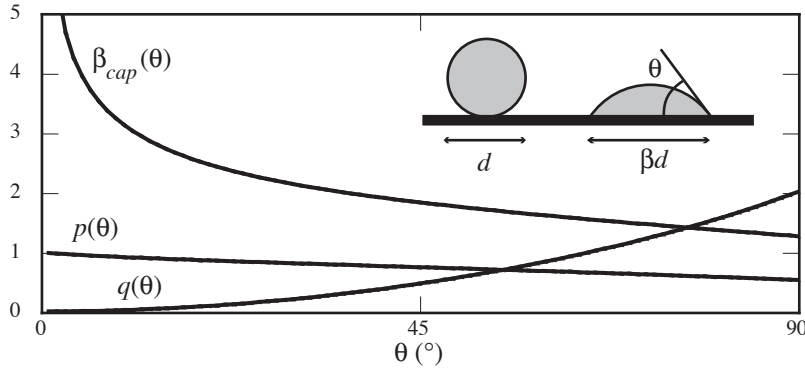


FIG. 6.2 – Relation entre le facteur d'étalement β_{cap} et l'angle de contact θ pour une calotte sphérique. Sont également tracées les fonctions $p(\theta)$ (Eq. 6.3) and $q(\theta)$ (Eq. 6.4).

6.2 Effet des particules sur l'étalement : théorie

La première équation est une équation de conservation de la masse. Quelle que soit la forme de la goutte étalée, son volume doit être égal à son volume initial $\pi d_0^3/6$. Ford & Furmidge (1967) et Park *et al.* (2003) ont montré que, si on suppose que la goutte étalée est une calotte sphérique avec un angle de contact statique θ , le facteur d'étalement β_{cap} est

$$\beta_{cap}(\theta) = \sin \theta \left(\frac{4}{2 - 3 \cos \theta + \cos^3 \theta} \right)^{1/3}. \quad (6.1)$$

La fonction $\beta_{cap}(\theta)$ est tracée sur la figure 6.2 et atteint un minimum (1.26) pour $\theta = 90^\circ$. De plus, Shikhmurzaev (1997) a montré que la goutte étalée est une calotte sphérique uniquement si le nombre de Bond $Bo = \rho_f g d_0^2 / \sigma$ est petit devant l'unité. Pour $Bo \approx 5$, la goutte n'est plus une calotte mais plutôt une mare aplatie par la gravité.

Selon le principe de conservation d'énergie, si la goutte étalée est à l'arrêt, le facteur d'étalement doit vérifier une équation du type

$$E_k + E_p + E_s = E'_k + E'_p + E'_s + W_d \quad (6.2)$$

où le membre de gauche est la somme des énergies de la goutte avant l'impact (cinétique, potentielle et de surface), le membre de droite la somme des énergies après l'étalement.

Quand la goutte entre en contact avec le plan, l'énergie potentielle est $E_p = mgd_0/2$ après l'étalement — en supposant une calotte sphérique —, elle vaut $E'_p = mgh_{CM}$, où h_{CM} est la hauteur du centre de masse. La différence d'énergie potentielle est donc $E_p - E'_p = \frac{\pi}{12} \rho g d_0^4 p(\theta)$ avec une fonction

$$p(\theta) = 1 - \frac{\beta_{cap}(\theta)}{\sin \theta} \left(\frac{3}{4} \frac{(1 - \cos^2 \theta)^2}{(2 - 3 \cos \theta + \cos^3 \theta)} - \cos \theta \right). \quad (6.3)$$

La fonction $p(\theta)$ est de l'ordre de 0.5 à 1 (voir figure 6.2).

La variation d'énergie de surface est due à la variation de l'interface liquide/gaz et à la variation de l'aire de contact liquide/solide. En utilisant l'équation de Young, la différence d'énergie de surface est $E_s - E'_s = \sigma_{LV} (A_{LV} - A'_{LV} + A'_{SL} \cos \theta)$ où A_{LV} est l'aire de contact liquide/air avant l'impact, A'_{LV} et A'_{SL} sont les aires de contact liquide/air et solide/liquide après l'impact. En supposant une calotte sphérique, cette différence est

$$E_s - E'_s = \frac{\pi \sigma d_0^2}{4} [4 - \beta^2 q(\theta)] \text{ avec } q(\theta) = \frac{2(1 - \cos \theta)}{\sin^2 \theta} - \cos \theta. \quad (6.4)$$

La fonction $q(\theta)$ est tracée sur la figure 6.2.

L'énergie dissipée par viscosité est formellement écrite comme

$$\int_0^{t_s} \int_{\Omega} \Phi d\Omega dt \quad (6.5)$$

où t_s est le temps d'étalement et Ω le volume de la goutte. Le temps t_s est de l'ordre de d_0/U et Pasandideh-Fard *et al.* (1996) ont suggéré $t_s = (8/3)(d_0/U)$. Le taux volumique d'énergie dissipée Φ est écrit comme $\alpha \eta (U/L)^2$ avec L l'échelle de longueur de variation de la vitesse et α un préfacteur sans dimension de l'ordre de l'unité.

Dans le cas d'une forte viscosité, la dissipation visqueuse a lieu dans tout le volume de la goutte et l'épaisseur moyenne de la goutte est $L = h = 2d_0/3\beta^2$ (Chandra & Avedisian 1991, Mao *et al.* 1997, Park *et al.* 2003). L'énergie dissipée est donc $W_d = \alpha \pi \eta U d_0^2 \beta^4$ le bilan énergétique (6.2) conduit à

$$We + 12 + p(\theta)Bo - 3\beta^2 q(\theta) = 12\alpha \frac{We}{Re} \beta^4. \quad (6.6)$$

Pour des liquides faiblement visqueux ($Re > 81\beta^4$), la dissipation n'a lieu que dans une couche limite d'épaisseur $L = 2d/\sqrt{Re}$ proche du plan, et le travail des forces visqueuses est $W_{BL} = \frac{\pi}{3} \rho U^2 d^3 \beta^2 / \sqrt{Re}$. Le bilan énergétique (6.2) donne alors une expression explicite pour le facteur d'étalement :

$$\beta = \left(\frac{12 + We + p(\theta)Bo}{3q(\theta) + 4 \frac{We}{\sqrt{Re}}} \right)^{1/2}. \quad (6.7)$$

Une expression très proche a été obtenue par Pasandideh-Fard *et al.* (1996) sans le terme d'énergie potentielle et en supposant un disque plat au lieu d'une calotte sphérique : $\beta = [(12 + We)/(3(1 - \cos \theta) + 4We/\sqrt{Re})]^{1/2}$.

Quand la vitesse d'impact est faible, en étalement quasi-statique, les nombres Re et We tendent vers zéro. Le facteur d'étalement est donc $\beta_{U \rightarrow 0} = [(12 + p(\theta)Bo)/(3q(\theta))]^{1/2}$. Au contraire, pour une grande vitesse d'impact, le membre de gauche de (6.6) se réduit à We , et le facteur d'étalement dépend seulement de la viscosité :

$$\beta_{U \rightarrow \infty} = \left(\frac{Re}{12\alpha} \right)^{1/4}. \quad (6.8)$$

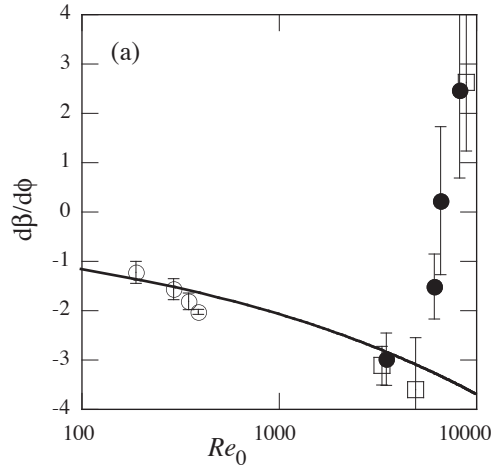


FIG. 6.3 – Taux de réduction du facteur d'étalement en fonction du nombre de Reynolds. La courbe continue est la fonction théorique $d\beta/d\phi = -0.37Re_0^{1/4}$ calculée d'après un bilan énergétique.

Si la goutte contient des particules solides, sa viscosité va être modifiée par la présence des particules. Pour des fractions volumiques « raisonnables », cette viscosité peut être évaluée par un modèle de viscosité effective tel que présenté dans l'introduction (chapitre 1). L'équilibre entre ces termes permet de prédire que le facteur d'étalement varie comme le nombre de Reynolds à la puissance 1/4. En choisissant pour la viscosité effective une relation empirique proposée par Krieger et Dougherty $\eta_r = (1 - \phi/\phi_m)^{-n}$, l'effet des particules sur l'étalement est prédit par

$$\frac{d\beta}{d\phi} = -\frac{n}{4\phi_m} \left(\frac{Re_0}{12\alpha} \right)^{1/4}. \quad (6.9)$$

6.3 Effet des particules sur l'étalement : résultats

Pour des faibles vitesses d'impact, l'étalement de la goutte est comme prévu limité par la présence des particules. En effet, la viscosité effective de la suspension augmente avec la fraction volumique ϕ et donc augmente la dissipation d'énergie lors de l'impact. La figure 6.3 montre le bon accord quantitatif entre les mesures et la prédiction théorique de l'équation 6.9. Cet effet a été vérifié quantitativement jusqu'à une valeur limite du nombre de Reynolds d'impact. Au delà ($Re \gtrsim 5000$), la présence des particules joue le rôle inverse. Au lieu de limiter l'étalement, elle le favorise au point d'induire une fragmentation de la goutte. Cet effet apparaît même pour des très faibles fractions volumiques.

Dans les régimes d'étalement, la répartition des particules dans la surface de la goutte étalée dépend du nombre de Reynolds. La répartition est homogène pour des nombres de Reynolds inférieurs à 800. Au delà, une distribution annulaire des particules est observée

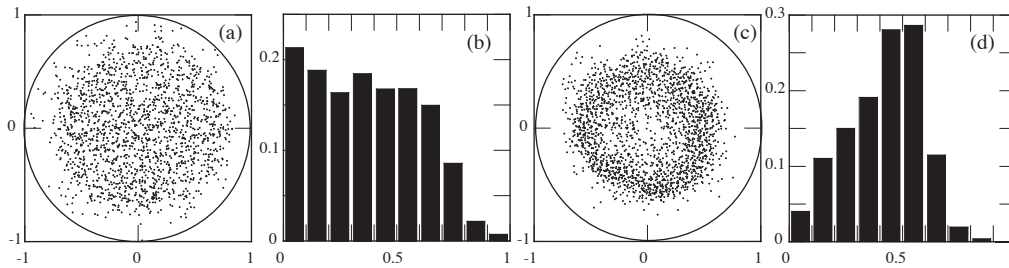


FIG. 6.4 – (a,b) Positions des particules et distribution radiale pour des faibles nombres de Reynolds d’impact, $Re_0 < 807$. (c,d) Positions des particules et distribution radiale pour des nombres de Reynolds d’impact $3184 < Re_0 < 3513$.

(Figure 6.4). Cette distribution résulte de l’interaction entre l’interface gaz/liquide et les particules au cours de la phase d’étalement, qui dure de l’ordre de 20 ms.

6.4 Perspectives

Ces premiers travaux ont été limités à des fractions volumiques inférieures à 45 %. Pourtant, même à des faibles fractions volumiques, les particules ont tendance à s’organiser sous forme de chaîne et à créer des contacts. Les photos de la figure 6.5a illustrent l’interaction entre les particules et l’interface liquide/gaz. Comme le film liquide a une épaisseur comparable voire inférieure à la taille des particules, l’interface déformée donne naissance à des forces attractives entre particules. Bien qu’étudiées en détail pour des particules ou des bulles en flottaison (Nicolson 1949, Fortes 1982, Joseph *et al.* 2003), ces forces sont modifiées par la présence d’un fond solide (figure 6.5b).

Ces expériences montrent que l’interaction entre les particules et une interface liquide/gaz mobile est complexe. Une des surprises de cette expériences a été la robustesse de l’hypothèse de milieu effectif utilisée pour prédire la réduction de l’étalement. Pourtant, lors de l’étalement, l’épaisseur du film de liquide est du même ordre de grandeur que la taille des particules. Cet effet de confinement influe certainement sur le comportement étalement/fragmentation de la goutte et mérite de plus amples recherches.

6.5 Références

- BHOLA R. & CHANDRA S. 1999 Parameters controlling solidification of molten wax droplets falling on a solid surface. *J. Mater. Sci.* **34** 4883–4894.
 CHANDRA S. & AVEDISIAN C. T. 1991 *Proc. R. Soc. London* **432** 13.
 FORD R. E. & FURMIDGE C.G.L. 1967 *Wetting Soc. Chem. Industry Monograph*, 417.

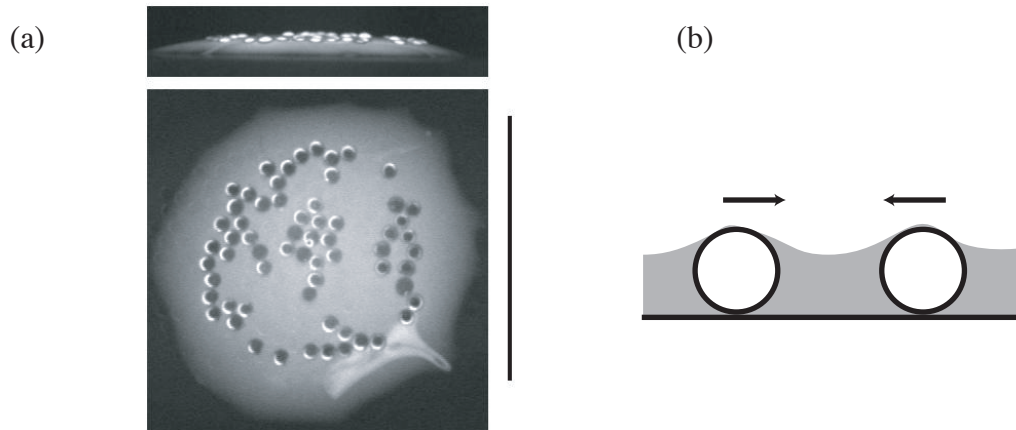


FIG. 6.5 – (a) Photographies de côté et de dessus d'une goutte étalée contenant des particules ($\phi = 0.15$). La formation d'amas traduit l'interaction attractive entre les particules. (b) Interaction attractive entre deux particules confinées dans un film liquide. La minimisation de l'énergie de surface de l'interface liquide/air induit une force attractive entre les particules.

FORTES , M. A. 1982 Attraction and repulsion of floating particles. *Can. J. Chem.* **60**, 2889.

JOSEPH D. D., WANG J., BAI R., YANG B.H. & HU H. H. 2003 *J. Fluid Mech.* **496** 139.

MAO T., KUHN D.C. S. & HONGHI T. 1997 *AIChE J.* **43**, 2169.

A10 M. NICOLAS, Spreading of a drop of neutrally buoyant suspension, accepté à *J. of Fluid Mech.*

NICOLSON, M. M. 1949 The interaction between floating particles. *Proc. Camb. Phil. Soc.* **45**, 288.

PARK H., CARR W. W. , ZHU J. & MORRIS J. F. 2003 *AIChE J.* **49** (10), 2461.

PASANDIDEH-FARD M., QIAO Y. M., CHANDRA S. & MOSTAGHIMI I. 1996 *Phys. Fluids* **8**, 650.

RANGE K. & FEUILLEBOIS F. 1998 *J. Coll. Interface Sci.* **203** 16.

REIN M. 1993 Phenomena of liquid drop impact on solid and liquid surfaces. *Fluid Dyn. Res.* **12**, 61–93

SHIKHMURZAEV Y.D. 1997, Spreading of drops on solid surfaces in a quasi-static regime. *Phys. Fluids* **9** (2) 266–275.

STOW C. D. & HADFIELD M. G. 1981 *Proc. Roy. Soc. A* **373** 419.

Chapitre 7

Perspectives

Parmi les perspectives déjà présentées à la fin de chaque chapitre, je souhaite mettre l'accent sur deux thématiques.

- **Interaction pression/écoulements de particules.** Lorsqu'un empilement granulaire saturé de liquide est mis en écoulement, sous l'effet d'une contrainte, d'une déstabilisation, de la gravité, la structure de l'empilement est modifiée. Cette déformation est fortement couplée à l'écoulement du liquide interstitiel. Si l'empilement se compacte, le liquide doit être expulsé et au contraire pour une dilatation, du liquide doit être aspiré dans les interstices. Une suspension concentrée est alors décrite comme un milieu poreux déformable. Cette interaction entre l'écoulement de liquide interstitiel et la déformation e la structure granulaire semble être un des points clés de la compréhension des avalanches sous-marines ou de la stabilité des sols saturés en eau.

Lors d'un tremblement de terre, déformation rapide d'un sol, on observe parfois une perte de solidité du sol. Les constructions s'enfoncent alors comme dans un liquide visqueux (figure 7.1). Cette liquéfaction est souvent expliquée par la différence des échelles temporelles entre le temps de sollicitation du sol et le temps d'écoulement du liquide. Si ce dernier est beaucoup plus long que le temps de déformation, il en résulte une forte augmentation de la pression interstitielle, et consécutivement une perte des contacts entre les particules granulaires.

Une analyse physique basée sur des temps caractéristiques a déjà montré son efficacité dans le cas des écoulements granulaires immergés (chapitre 4). Cette approche doit être maintenant transposée à des systèmes traditionnellement étudiés par des relations contraintes/déformation. Le premier dispositif expérimental envisagé est un empilement immergé soumis à une vibration verticale, brusque ou continue. La mesure du profil de pression le long de la verticale permettra de mesurer le taux de particules en suspension et d'appréhender les fronts de compaction/décompaction. On peut ainsi avoir accès aux temps de réponse de l'empilement, en fonction de la nature des particules formant l'empilement.

Une seconde étude expérimentale sera l'extension du montage utilisé par Cyril Cassar lors de sa thèse sur les écoulements granulaires immergés et stationnaires. Le



FIG. 7.1 – *Photo illustrant la liquéfaction d'un sol lors d'un tremblement de terre, Niigata, Japon 1964. Photo extraite du site web www.ce.washington.edu/~liquefaction/*

dispositif sera adapté à des écoulements instationnaires, avec une attention particulière portée aux phases de démarrage et d'arrêt de l'écoulement. Les mesures de pression dans ces systèmes sont fondamentales car elles seules permettent de savoir si les particules sont en contact ou non. En effet, les mesures d'épaisseur ou de fraction volumique d'un écoulement ne sont jamais suffisamment précises.

- **Particules et interfaces.** L'influence importante des particules solides sur la transition étalement/fragmentation d'une goutte impactée a été démontrée, mais le rôle exact des particules n'est pas compris. De manière générale, les connaissances sur les interfaces chargées en particules sont peu nombreuses.

Des particules solides en suspension dans un liquide modifient la dissipation d'énergie, représentée par une augmentation de la viscosité effective. De la même manière on peut se demander quelle est l'influence de particules placées à l'interface entre un liquide et un gaz. C'est une situation courante dans un procédé utilisant un mélange gaz/liquide/solide. Dans cette configuration, l'angle de contact entre les particules et le liquide est sans doute un des paramètres prépondérants qui influe sur la tension de surface effective.

On peut envisager des configurations simples. La première est une surface plane recouverte de particules en flottaison ou hydrophobes. L'excitation de cette surface par des vagues ou des vibrations verticales donne accès à la nature de l'interface en terme de viscosité et de tension de surface effectives. Une deuxième configuration est une bulle de gaz dont la surface est recouverte de particules (voir figure 7.2).

L'utilisation des forces interfaciales pour créer des micro-assemblages de particules est actuellement en plein développement. Toutefois, la physique des interactions à l'échelle des particules est parfois mise de côté au profit des progrès technologiques.

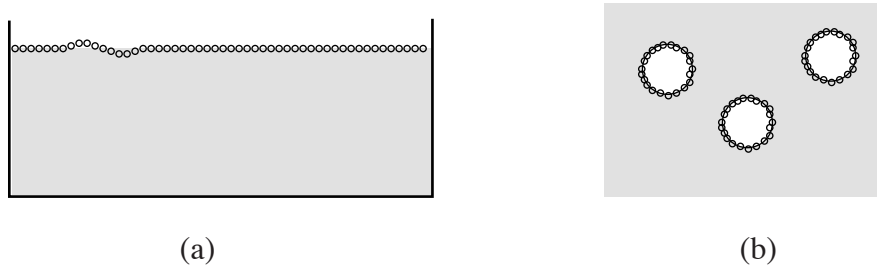


FIG. 7.2 – Deux exemples de surfaces recouvertes de particules solides : surface plane (a) et bulles (b).

C'est pourquoi je souhaite mettre en place dans les prochaines années une activités centrée sur cette thématique.

Mes travaux de recherche passés et présents ont particulièrement profité du dynamisme du Groupe Écoulements de Particules. La présence dans un même laboratoire d'expériences sur les milieux granulaires secs, les suspensions très visqueuses, les écoulements de particules solide où l'inertie est importante peut paraître anecdotique mais me semble au contraire très propice à de nouveaux développements. Les résultats obtenus sur les écoulements granulaires immergés forment un exemple marquant : une « boîte à outils » commune aux écoulements aériens et immergés a été mise en place, et sa portée générale a été démontrée. Elle sera prochainement appliquée à d'autres problèmes, comme la formation de rides sous-marines.

Les connaissances sur les milieux divisés sont traditionnellement fractionnées dans différentes zones d'influence. Les premiers travaux sur la fluidisation sont issus du génie chimique et pétrolier. Les travaux fondateurs sur les milieux granulaires sont issus de la mécanique des sols, du génie civil et de la géotechnique. Les écoulements de particules ont été d'abord étudiés par la géophysique, et les dépôts formés par ces écoulements par la géologie. Le cloisonnement parfois très marqué entre ces différents domaines semble être parfois un obstacle. Pour un même phénomène, les réponses du géophysicien ne satisfont pas le mécanicien, de la même manière les réponses du mécanicien ne satisfont pas le physicien.

Au delà des prolongements naturels des travaux déjà menés, une perspective générale de ce travail réside dans la « réconciliation » entre les différentes approches d'un même système. Un travail de traduction sera parfois nécessaire. La mise en place à Polytech Marseille d'un cours introductif sur les milieux divisés m'a permis d'engager ce travail

et d'évaluer les difficultés. Surmonter ces difficultés signifie apporter les outils récents à tous les domaines qui s'intéressent aux milieux divisés : la mécanique des sols, la géotechnique, le génie civil, la conception de matériaux et de liquides complexes. Un défi qui mérite d'être relevé.

Annexe A

Curriculum vitae – Activités – Liste des travaux

A.1 État civil & statut

Nom	NICOLAS
Prénom	Maxime
Né le	19 septembre 1971 à Commercy (55)
Nationalité	Française
Service National	Scientifique du contingent du 1/11/1996 au 30/10/1997
Situation de famille	Marié, deux enfants
Adresse personnelle	27 Boulevard Ludovic 13010 Marseille
Téléphone personnel	04 95 08 23 96
Situation professionnelle	Maître de Conférences Polytech Marseille, Université de Provence Titulaire depuis le 1/9/1999, section 62 du CNU.
Téléphone professionnel	04 91 10 68 97
Laboratoire	IUSTI, UMR 6595
email	maxime.nicolas@polytech.univ-mrs.fr

A.2 Poste précédent

Attaché Temporaire d'Enseignement et de Recherche, IUSTI, Université de Provence, de Septembre 1998 à Août 1999.

A.3 Formation et diplômes

1997 Doctorat de l'Université Paris VI, attribué avec la mention Très Honorable avec les félicitations du jury (spécialité : Physique des Liquides) : « Instabilités en onde

plane dans un lit fluidisé liquide-solide ». Jury composé de P.-G. de Gennes, D. Lhuillier, E. J. Hinch, D. Salin, S. Fauve, J. Pantaloni et E. Guazzelli.

- 1995 Advanced school : *Flow of particles in suspension*, Udine (Italie).
- 1994 DEA de Physique des Liquides, Université Paris VI.
Magistère de Physique, Université Paris VI et École Normale Supérieure.
Ecole d'été : *Mobile Particulate Systems*, Cargèse (Advanced Science Institute, OTAN)
- 1992 Licence de Physique, Université Paris VI.
Maîtrise de Physique, Université Paris VI.
- 1991 DEUG A, Université de Metz.
- 1989 Baccalauréat section E.

A.4 Activités d'enseignement

A.4.1 Dans le cadre de Polytech Marseille

Première année

- Ondes et vibrations, cours (10h), TD (20h), depuis 2002. *Notion d'oscillateur. Amortissement et forçage. Couplage de deux oscillateurs. Couplage de N oscillateurs, passage au continu. Vibration des cordes, membranes et poutres. Acoustique linéaire. Introduction aux systèmes non linéaires.*
- Optique, cours (14h), depuis 2003. *Éléments d'histoire de l'optique. Optique géométrique, réfraction. Optique ondulatoire. Sources et détecteurs. Applications aux techniques de visualisation en mécanique des fluides : ombroscopie, vélocimétrie laser.*
- Mécanique de fluides, TP (72h), depuis 2004.

Deuxième année

- Milieux divisés, cours (14h), depuis 2004. *Paramètres et caractérisation. Microhydrodynamique. Suspensions et rhéologie. Milieux granulaires secs.*
- Veille technologique, projet (12h), depuis 2005. *Recherche documentaire sur bases de données de brevets, suivi de technologies.*
- Caractérisation, TP (36h), depuis 2004.
- Projets expérimentaux, projet (36h), depuis 2004. Quelques exemples de sujets : *Analyse d'un fluide rhéopépaississant, impact de gouttes chargées en particules, comportement d'un fluide viscoélastique, effet Weissenberg, liquéfaction des sols.*

A.4.2 Dans le cadre du Master Mécanique, Physique et Modélisation (DEA)

- Milieux poreux, cours (16h), depuis 2000. *Aspects géométriques, structures. Modélisation de la perméabilité, modèle de Saffman. Déplacement miscible et non miscible. Ecoulement à l'interface d'un poreux.*

A.4.3 Enseignements abandonnés

- tutorat pédagogique en physique, Université Paris 6 (1994-96) ;
- travaux pratiques d'hydrodynamique, École des Mines de Paris (1994-98) ;
- travaux dirigés de mécanique des fluides compressibles, ENSTA (1995-96) ;
- travaux expérimentaux de mécanique des fluides, École Polytechnique (1996-97) ;
- cours et TD de propagation des ondes électromagnétiques (1ere année), Polytech Marseille 1998-2001 ;
- cours et TD de mécanique des vibrations (1ere année), Polytech Marseille, 1999.

A.4.4 Production de photocopiés

Notes de cours

- Ondes et vibrations (87 pages) ;
- Milieux poreux (34 pages) ;
- Optique, notes de cours (55 pages).

Photocopiés de travaux pratiques

- Modèle de structure cristalline : *Reproduction de l'expérience de L. Bragg (1947) sur la formation d'une structure cristalline par des bulles en flottaison à la surface d'un liquide savonneux. Défauts à 2D. Analyse d'image, détection de défauts.* ;
- Panache thermique : *convection naturelle et instationnaire au dessus d'une résistance chauffant à $t = 0$. Analyse d'image et nombres sans dimension.* ;
- Convection et rayonnement : *mesures de l'émissivité d'un barreau chauffant. Mesures des coefficients de convection pour une atmosphère gazeuse à pression contrôlée* ;
- Canal à houle : *Ondes à la surface d'un liquide. Ondes progressives et stationnaires. Mesures des vitesses de phase et de groupe. Utilisation des capteurs à ultrasons.* ;
- Propriétés électriques des matériaux : *Mesures des paramètres RLC de matériaux diélectriques simples et composés.* ;
- Résistance des matériaux : *bancs d'essais de traction et flexion sur des matériaux homogènes et composites.* ;
- Analyse rhéologique des huiles moteur : *effet de la température sur la viscosité. Effets des additifs sur le comportement.*

A.4.5 Participation à des jurys

- jurys de stage de fin d'étude de Polytech (depuis 1999) ;
- jurys d'admission au concours Archimède pour Polytech (depuis 1999) ;
- jurys d'admission à la Prépa Ingénieur Polytech (niveau bac), depuis 2005.

A.4.6 Responsabilités pédagogiques

- Coordination des travaux pratiques de 2002 à 2005 (avec J. Duplat).
- Évaluation des enseignements au département Mécanique-Energétique de Polytech, depuis 2002 ;
- Responsabilité du Parcours Intégré Polytech depuis 2005 : recrutement des étudiants niveau bac, tutorat, organisation des enseignements complémentaires. Communication et diffusion de l'information vers les établissements secondaires.

A.5 Activités de recherche

A.5.1 Encadrement de stages

- Matthias Piot, maîtrise de Mécanique (université Paris XI), mai-juillet 2000 ;
- Cyril Cassar, DEA Phénomènes Complexes (Université de Provence), mars-juillet 2002 ;
- Mickaël Villar, Polytech' Marseille (2eme année), juillet-août 2002.
- Stanislav Simonenko, Master Mécanique, physique et modélisation (1ere année), juin-juillet 2005.

A.5.2 Encadrement de thèse

- Cyril Cassar, thèse : « *Écoulements granulaires immergés : application aux avalanches sous-marines*, » 2002-2005, encadrement à 80 %. Thèse soutenue le 7 novembre 2005 devant le jury composé de M. Rabaud (rapporteur), M. Naaim (rapporteur), E. Clément, L. Tadriss, O. Pouliquen et M. Nicolas.

A.5.3 Rayonnement scientifique

Rapporteur pour des revues scientifiques

J'ai depuis 1999 une activité régulière de *referee* pour les journaux suivants :

- Chaos (1999) ;
- Europhysics letters (2000) ;
- Physical Review Letters (2001, 2002, 2003-2005) ;
- Physical Review E (2001, 2003-2005) ;

- Physics of Fluids (2001, 2003).

Expertise

- Membre du Groupe de travail « Sciences de la Matière en Microgravité » du CNES, depuis 2003.
- Membre du comité d'experts "Fluid and combustion" de l'ESA, en 2005.

Diffusion de la recherche

- Participation à Science en Fête, IUSTI, Marseille (1998).
- Collaboration à un article de Science et Vie (*Les piles d'oranges défient la physique*, numéro 993, juin 2000)
- Accueil et visites de laboratoire pour des professeurs du secondaire, 2002.
- Secrétaire de la section locale (Marseille) de la Société Française de Physique depuis mars 2002.

Distinctions

- Prix Jean Langlois de la recherche 1994 (École Supérieure de Physique et Chimie Industrielles de la Ville de Paris).
- F. N. Frenkiel Award 2003, American Physical Society, Division of Fluid Dynamics.

Fonctions électives

- membre titulaire de la Commission de Spécialistes section 62 de l'université Aix-Marseille 1, depuis 2001 ;
- membre suppléant de la Commission de Spécialistes section 62 de l'université Aix-Marseille 3 (2001-2004) ;
- membre élu du Conseil de Laboratoire de l'UMR 6595 (IUSTI) ;
- membre élu du Conseil de Département Mécanique-Energétique de Polytech (2001-2004);
- membre élu du Conseil d'École de Polytech Marseille (2005-2008);

Contrat

- Partenaire du consortium MaJE (Material Jet for Electronics) pour le développement d'un procédé d'impression à jet d'encre conductrice. Projet validé en juillet 2003 par PIDEA et conduit par la Sté SPS, Rousset.
- Étude rhéologique du glaçage de calissons (Sté Calissons du Roy René), en collaboration avec Lounès Tardist (DR, IUSTI). *Caractérisation de la pâte sucrée recouvrant les calissons avant cuisson. Conception, développement et suivi de fabrication d'un consistomètre adapté à une manipulation quotidienne.*

Organisation de réunions et colloques

- Organisation de la journée « Suspensions » du GDR Physique des Milieux Hétérogènes Complexes (avec P. Gondret et J. Martin, mars 1998) ;
- Organisation du mini-colloque « Mélange dans les liquides et milieux granulaires » aux JMC7 (Poitiers, 2000) ;
- participation à l’organisation des 5emes journée sur les milieux poreux, Marseille 2001.
- Participation à l’organisation de la journée ”Physique en 13” de la SFP Marseille, 2002 ;
- Organisation du mini-colloque « Instabilités et formation de structures dans les fluides complexes » aux JMC8 (Marseille, 2002).

A.6 Publications et communications

A.6.1 Publications dans des journaux à comité de lecture

- A1 M. NICOLAS, J.-M. CHOMAZ & É. GUAZZELLI 1994, Absolute and convective instabilities of fluidized beds. *Physics of Fluids* **6** (12), 3936–3944.
- A2 M. NICOLAS, J.-M. CHOMAZ, D. VALLET & É. GUAZZELLI 1996, Experimental investigations on the nature of the first wavy instability in liquid-fluidized beds. *Physics of Fluids* **8** (8), 1987–1989.
- A3 O. POULIQUEN, M. NICOLAS & P. WEIDMAN 1997, Crystallisation of non-Brownian spheres under horizontal shaking. *Physics Review Letters* **79** (19), 3640–3643.
- A4 M. NICOLAS & O. POULIQUEN 1998, De l’ordre dans les billes ! *Bulletin de la Société Française de Physique*, n°117, p. 8.
- A5 M. NICOLAS, E.J. HINCH & É. GUAZZELLI 1999, Wavy instability in liquid-fluidized beds. *Ind. Eng. Chem. Res.*, **38**, 799–802.
- A6 M. NICOLAS, P. DURU & O. POULIQUEN 2000, Compaction of a granular material under cyclic shear. *Eur. Phys. J. E* **3**, 309–314.
- A7 P. DURU, M. NICOLAS, E.J. HINCH & É. GUAZZELLI 2002, Constitutive laws of liquid-fluidized beds. *J. Fluid Mech.* **452**, 371–404.
- A8 M. NICOLAS 2002, Experimental study of gravity-driven dense suspension jets. *Phys. Fluids* **14** (10), 3570–3576.
- A9 O. POULIQUEN, M. BELZONS & M. NICOLAS 2003, Fluctuating particle motion during shear induced granular compaction. *Phys. Rev. Lett.* **91** (1) 014301.
- A10 M. NICOLAS, 2005 Spreading of a drop of neutrally buoyant suspension, accepté à *J. of Fluid Mech.* Sous presse.
- A11 C. CASSAR, M. NICOLAS & O. POULIQUEN, 2005 Submarine granular flows down inclined planes, *Phys. Fluids*. **17**, 103301.
- A12 C. CASSAR, O. POULIQUEN & NICOLAS, Dynamics of a sliding porous block down a non permeable rough substrate, en préparation pour *Eur. Phys. J. E*.

A.6.2 Colloques et congrès avec actes

- [C1] M. NICOLAS, J.-M. CHOMAZ, D. VALLET & É. GUAZZELLI 1996, Wave instability in liquid-fluidized beds. Proceedings of the workshop on *Traffic and Granular Flows*, D.E. Wolf, M. Schreckenberg et A. Bachem eds, World Scientific, Singapour, 267–277.
- [C2] M. NICOLAS, J.-M. CHOMAZ, D. VALLET & É. GUAZZELLI, 1996 Wave instabilities of a liquid-fluidized bed. Proceedings of the 5th World Congress of Chemical Engineering, San Diego.
- [C3] M. NICOLAS, E.J. HINCH & É. GUAZZELLI, 1998 Questioning two-phase model of fluidization. Actes du 3^e congrès international sur les écoulements multiphasiques ICMF' 98, Lyon.
- [C4] S. LUDING, M. NICOLAS & O. POULIQUEN, 2000 A minimal model for slow dynamics: compaction of granular media under vibration or shear. , In "Compaction of soils, granulates and powders", D. Kolymbas and W. Follin (eds) A. A. Balkema, Rotterdam, p. 241.
- [C5] M. NICOLAS, P. DURU & O. POULIQUEN 2001 Compaction of a packing of hard spheres under horizontal shear. In "Powder and grains 2001", Y. Kishino éditeur, A.A. Balkema, Tokyo.
- [C6] M. NICOLAS, M. BELZONS & O. POULIQUEN 2004 Pore Pressure Relaxation During Granular Compaction. In "XXI International Conference on Theoretical and Applied Mechanics" ICTAM'04, Varsovie.

A.6.3 Séminaires

- [S1] *Instabilités dans les lits fluidisés*, Laboratoire PMMH, Paris (1996).
- [S2] *Instabilités dans les lits fluidisés*, Laboratoire de Modélisation en Mécanique, Paris (1997).
- [S3] *Une instabilité convective dans un lit-fluidisé liquide-solide*, LADHYX, école Polytechnique, Palaiseau (1997).
- [S4] *Cristaux de billes*, LADHYX, école Polytechnique, Palaiseau (1997).
- [S5] *Évolution non linéaire de l'instabilité des lits fluidisés*, IUSTI, Marseille (1998).
- [S6] *Spreading and splashing of droplets of suspension*, The Textile Institute, Georgia Tech, Atlanta (2004).
- [S7] *Experimental study of a submarine granular flow*, Dept of Physics, Emory University, Atlanta (2004).

A.6.4 Communications à des colloques sans actes

- *Instabilités dans les lits fluidisés*, M. Nicolas & É. Guazzelli, affiche aux Journées d'Hydrodynamique de la Montagne Sainte-Geneviève (Paris, 1993).

- *Instabilités dans les lits fluidisés*, M. Nicolas, J.-M. Chomaz & É. Guazzelli, GDR Ordre et Désordre dans la Matière (Palaiseau, 1993).
- *Instabilités dans les lits fluidisés*, M. Nicolas, J.-M. Chomaz & É. Guazzelli, Colloque de Physique Statistique (Paris, 1994).
- *Instabilités dans les lits fluidisés*, M. Nicolas, J.-M. Chomaz & É. Guazzelli, GDR Physique des Milieux Hétérogènes Complexes (Paris, 1994).
- *Absolute and convective instabilities of fluidized beds*, M. Nicolas, J.-M. Chomaz & É. Guazzelli, École d'été Mobile Particulate Systems (Cargèse, 1994).
- *Absolute and convective instabilities of fluidized beds*, M. Nicolas, J.-M. Chomaz & É. Guazzelli, congrès de l'American Physical Society - Division of Fluid Dynamics (Atlanta, USA, 1994).
- *évolution non linéaire de l'instabilité en onde plane dans les lits fluidisés*, M. Nicolas & É. Guazzelli, GDR Physique des Milieux Hétérogènes Complexes (Orsay, 1995).
- *Instabilités absolue et convective dans les lits fluidisés*, M. Nicolas, J.-M. Chomaz & É. Guazzelli, congrès de la Société Française de Physique (Marseille, 1995).
- *Instabilité convective dans un lit fluidisé liquide-solide*, M. Nicolas, J.-M. Chomaz, D. Vallet & É. Guazzelli, Colloque de Physique Statistique (Paris, 1996).
- *Instabilité convective dans un lit fluidisé liquide-solide*, M. Nicolas, J.-M. Chomaz, D. Vallet & É. Guazzelli, GDR Physique des Milieux Hétérogènes Complexes (Paris, 1996).
- *Wave instabilities of a liquid-fluidized bed*, M. Nicolas, J.-M. Chomaz, D. Vallet & É. Guazzelli, 5th World Congress of Chemical Engineering, (San Diego, USA, 1996).
- *Observations of instabilities in a liquid-fluidized bed*, M. Nicolas, J.-M. Chomaz, D. Vallet & É. Guazzelli, conférence Cooperative Phenomena in Complex Media (Cambridge, UK, 1996).
- *Crystallisation of beads*, M. Nicolas, O. Pouliquen & P. Weidman, GDR Physique des Milieux Hétérogènes Complexes (Paris, 1997).
- *Crystallisation of spherical particles under horizontal shaking*, P. Weidman, O. Pouliquen & M. Nicolas, congrès de l'American Physical Society - Division of Fluid Dynamics (San Francisco, USA, 1997).
- *Questioning two-phase model of fluidization*, M. Nicolas, E.J. Hinch & É. Guazzelli, 3^e congrès international sur les écoulements multiphasiques ICMF' 98 (Lyon, 1998).
- *Cristallisation de billes*, M. Nicolas & O. Pouliquen, 23^{es} journées sur les Milieux Aléatoires Macroscopiques (Carré-le-Rouet, 1998).
- *Compaction d'un empilement sous cisaillement périodique*, M. Nicolas & O. Pouliquen, 14^e congrès de l'Association Universitaire de Mécanique (Toulouse, 1999).
- *Dispersion d'un jet de suspension dense*, M. Nicolas & M. Piot 7^{es} journées de la Matière Condensée (Poitiers 2000).
- *Avalanches sous-marines*, GDR Milieux Divisés (Carré-le-rouet, 2002).

- *Submarine granular flow down a rough plane*, M. Nicolas, C. Cassar & O. Pouliquen, congrès de l'American Physical Society - Division of Fluid Dynamics (Meadowlands, USA, 2003).
- *2003 Francois Frankiel Award: Experimental study of gravity-driven dense suspension jets*, M. Nicolas, congrès de l'American Physical Society - Division of Fluid Dynamics (Meadowlands, USA, 2003).
- *Spreading and splashing of droplets of suspensions*, Studies on splashes, Euromech 450, Marseille (2004).

A.7 Résumé des activités

Renseignements divers

Maxime NICOLAS, 34 ans, de nationalité Française. Docteur de l'Université Paris 6 (1997), Maître de conférences depuis le 1^{er} septembre 1999. Chercheur à l'IUSTI, UMR 6595.

Principales activités d'enseignement

- Polytech Marseille : travaux pratiques de caractérisation, de mécanique des fluides, cours d'optique, d'ondes et vibrations, de milieux divisés
- Master Mécanique, Physique et Modélisation : cours sur les milieux poreux.
- Mise en place et suivi des évaluations des enseignements, liaison avec le Parcours intégré Polytech.

Activités de recherche

Production scientifique :

- Articles : 9 publiés, 2 sous presse, 1 soumis.
- Conférences avec actes : 6
- Séminaires : 7
- Communications : 22.

Annexe B

Publications

Les publications apparaissent dans l'ordre chronologique.

B.1 Crystallisation of non-Brownian spheres under horizontal shaking

O. POULIQUEN, M. NICOLAS & P. WEIDMAN
Physics Review Letters **79** (19), 3640–3643 (1997).

Crystallization of non-Brownian Spheres under Horizontal Shaking

O. Pouliquen, M. Nicolas, and P. D. Weidman*

LadHyX, CNRS UMR 156, École Polytechnique, 91128 Palaiseau Cedex, France

(Received 31 July 1997)

Until now, it has been observed that a collective handling of uniform spheres could only lead to a random close packing of 0.64 maximum volume fraction. In this Letter, we show that denser crystalline arrangements can be obtained when beads are poured at low flow rates into a horizontally shaken container. A parallel is suggested between this process and that of colloidal sedimentation which also yields crystalline structure. [S0031-9007(97)04421-9]

PACS numbers: 46.10.+z, 61.50.-f, 81.20.Ev, 83.70.Fn

Packings of uniform spheres have been extensively studied both by the powder technology community [1,2] and by physicists who consider hard spheres systems as a model for simple liquids [3]. It is well known (although not rigorously demonstrated [4,5]) that the volume fraction of the packing, defined as the ratio of the volume occupied by the spheres to the total volume, cannot exceed 0.74, corresponding to the regular crystal arrangements (for example, hexagonal or face-centered cubic). However, spheres simply released in a box do not spontaneously arrange into a crystalline formation. Even when vibrations are imposed to compact the arrangement, the maximum volume fraction obtained is 0.64 (in the limit of large boxes) [6–9]. This is called the random close packing limit and is commonly considered as the maximum density that can be reached by collectively handling the particles as reported by an anonymous author [10]: “ball bearings and similar objects have been shaken, settled in oil, stuck with paint, kneaded inside rubber balloons and all with no better result than a density of about 0.636.”

Although this limit seems to be well defined, some studies in the literature report that higher densities corresponding to regular arrangements can be obtained. Scott *et al.* observed in a short note [11] that cyclic shear motion can induce packing with a density higher than 0.64. Owe Berg *et al.* [12] carried out experiments on the packing of spheres obtained under different shaking processes and concluded that “three dimensional shaking” (shaking with an horizontal component) can lead to a crystallization. More recently, Vanel *et al.* [13] obtained a regular packing of steel beads by vertically vibrating the container. However, all these experiments deal with a very small number of particles and the thickness of the crystal does not exceed 20 particles. Under such conditions, the packings are certainly dramatically influenced by the boundaries. To our knowledge, no process has been reported for creating large crystals of non-Brownian spheres.

On the other hand, in the case of Brownian hard spheres sensitive to thermal fluctuations, spontaneous crystallization can occur [14–17]. The slow sedimentation of colloidal spherical particles in a fluid with the same index of refraction (in order to minimize the van der Waals forces)

yields a dense crystalline sediment of density around 0.67 [15]. The crystallization is in this case controlled by the temperature: as a result of Brownian motion, the spheres reaching the free surface of the sediment rearrange spontaneously into an equilibrium ordered state.

In this paper we present a method inspired by the colloidal crystallization for creating crystalline arrangements of non-Brownian spheres. The method consists in continuously pouring the spheres into a box subjected to horizontal vibrations. The vibrations allow the particles to rearrange and play a role similar to the temperature in the colloidal sedimentation. Whereas many reports have been devoted to the dynamics of a granular media [18,19] and its compaction [1,20,21] under vertical vibrations, few have been concerned with horizontal vibrations [22,23] and to our knowledge no crystallization results have been reported.

The experimental setup is presented in Fig. 1. A glass box 12 cm × 12 cm × 25 cm is fixed on a table which can horizontally move on linear bearings. A

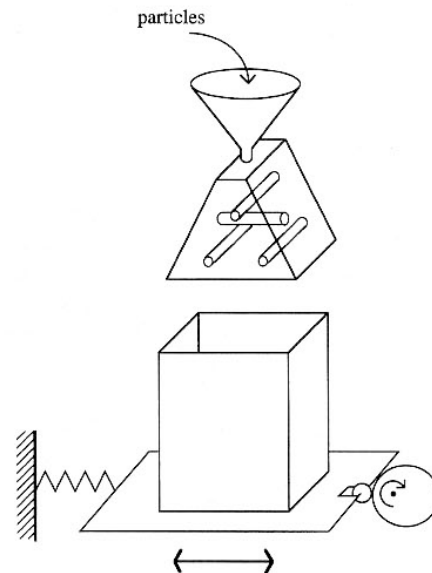


FIG. 1. Experimental setup.

quasisinusoidal motion $A \sin(\omega t)$ is induced to the table by the mean of an eccentric wheel driven by a motor. The particles fall from a glass funnel into the box through a set of horizontal cylindrical bars: the chaotic motion of the particles induced by the multiple collisions with the bars provides a uniform distribution of the particles over the surface of the box. The particle flow rate can be varied by using funnels having different outlet diameters. The particles we used were spherical glass beads 1.98 ± 0.06 mm in diameter, with a density $\rho = 2.64$ g/cm³. Many parameters can influence the granular dynamics, but in this paper we focus on the three major control parameters:

(i) The relative acceleration of the vibration $\Gamma = A\omega^2/g$ where A and ω are the amplitude and the pulsation of the vibration, and g the gravitational acceleration.

(ii) The filling rate Q , number of particles falling in the box per second per unit surface area [in (particle/s)/cm²].

(iii) The relative amplitude of vibration A/d , where d is the particle diameter.

The influence of other important effects like the surface properties of the particles, the density of the beads, and the falling height of the particles has not yet been studied systematically.

To characterize the crystallization, we computed the final volume fraction ϕ of the packing simply by measuring the height and the weight of the final packing. This method takes into account the boundary effects and thus gives densities lower than in the infinite container limit [6].

Before each experiment, the walls of the box are cleaned with an antistatic agent in order to minimize the electrostatic interaction. Horizontal vibration is then imposed to the empty box before the particles are poured into the funnel. The experiment is stopped when the height of the packing reaches at least 20 cm (~ 100 particle diameters). When the particle flow rate is low and the relative acceleration is sufficiently strong, a very dense and ordered packing is obtained. Figure 2 shows the free surface of such a packing. We have

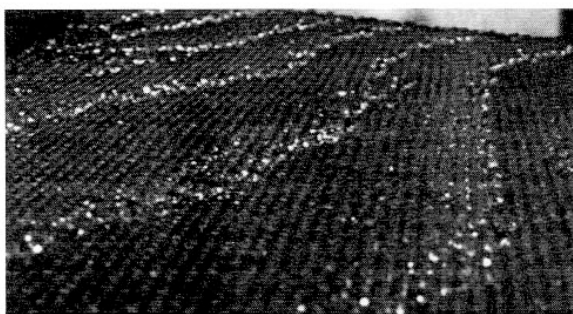


FIG. 2. The free surface of a packing obtained for $\Gamma = 1$, $Q = 2$ (particle/s)/cm², $A/d = 1.1$. In order to enhance the crystal-like structure, we have artificially created steps on the free surface by slightly inclining the box from horizontal.

verified that the organized structure observed at the free surface in Fig. 2 is the signature of an internal organized structure by using the elegant method proposed by Berg *et al.* [12]: at the end of the experiment, water is poured into the container and frozen. The ice block then can be carefully cut apart to reveal the internal packing structure. As in colloidal crystallization, the packings we observed are regular but consist of a superposition of randomly stacked hexagonal layers perpendicular to gravity [24]. We return to a discussion of this point later in the paper.

Careful observation of the system during the filling reveals that the crystallization process is entirely controlled by the dynamics of the free surface. The vibrations serve to fluidize the uppermost layers of the packing (between 0 and 6 layers, depending on the acceleration) [23], while the rest of the particles remain fixed in the frame of the accelerating box. In this fluidized layer, the particles experience both horizontal random motion and shearing. The arrangement taken by the particles seems to result from the combination of these two factors. The active zone being restricted to the free surface, the only method for creating a large crystalline arrangement is to continuously supply new particles to the free surface. A horizontal shaking applied to a randomly filled box leads to a thin layer of crystal phase at the free surface, but the rest of the material below remains in the initial random state. It should be noted that convective particle motion was not observed at the low values of Γ covered in the present experiments.

The two necessary ingredients for creating a crystal are thus an acceleration sufficiently large to fluidize the free surface, and a moderately low flow rate to allow time for the free surface particles to organize in a regular pattern before being covered by the new particles showered from above. We have systematically studied the influence of the acceleration, Γ , and of the flow rate, Q , by measuring the final volume fraction of the packings. The results are presented in Fig. 3. For low accelerations, $\Gamma \lesssim 0.4$, the packings are random with a density 0.625, independent of the filling rate. This value is compatible with the random close packing density measured by Scott [6] in containers having the same relative size (box length/particle diameter) as in our experiment. For higher acceleration, crystallization is observed but strongly depends on the filling rate. For very low filling rates [$Q \lesssim 2$ (particle/s)/cm²] the final volume fraction ϕ is equal to 0.67, the maximum we were able to obtain. This value is independent of Γ in the range allowed with our experimental setup. For intermediate flow rates, $2 \lesssim Q \lesssim 120$ (particle/s)/cm², the volume fraction decreases with increasing Q [Fig. 3(b)] at constant acceleration. This tendency is a direct consequence of the creation of more and more defects in the crystal. In this range of flow rate, a decrease of the volume fraction is also observed when the relative acceleration rises above one, in which case the fluctuating motion induced by the horizontal

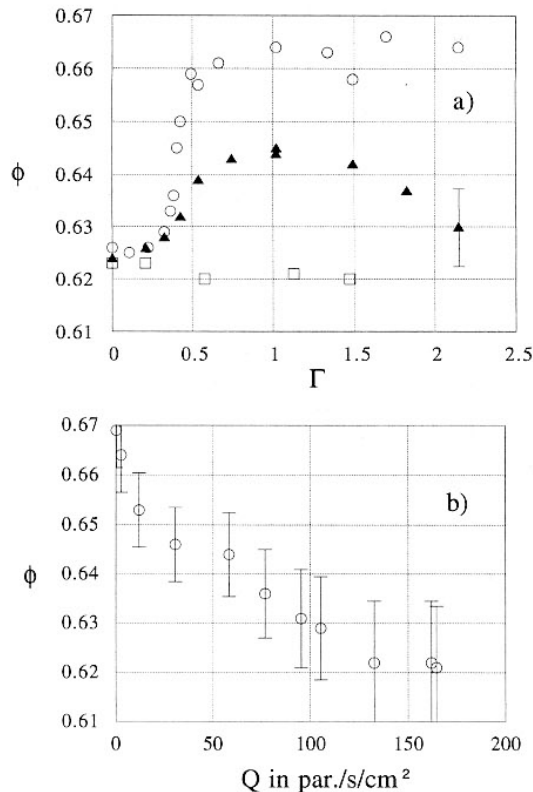


FIG. 3. (a) Final volume fraction as a function of the relative acceleration Γ for $A/d = 1.1$ and for different filling rates. \circ : $Q = 2.8$ (particle/s)/cm²; \blacktriangle : $Q = 60$; \square : $Q = 120$. (b) Final volume fraction as a function of the filling rate for $\Gamma = 1$ and $A/d = 1.1$.

vibration becomes increasingly important. Finally, for high filling rates $Q \geq 120$ (particle/s)/cm² crystallization is no longer observed.

We have also investigated the influence of the dimensionless vibration amplitude A/d varied over the range 0.35–10 at $\Gamma = 0.66$ and a flow rate $Q = 12$ (particle/s)/cm². In this range the final density does not depend on A/d as long as $A/d > 1$, the density being $\phi = 0.655$. For vibration amplitudes less than the particle diameter, $A/d < 1$, a slight decrease in the compacity seems to appear, the final value $\phi = 0.645$ attained at $A/d = 0.35$.

The experiments presented here were carried out in a square section box with flat walls. One can legitimately wonder to what extent the crystallization is initiated by the flat boundary conditions. We thus performed a control experiment using irregular boundaries made of glass beads 4 mm in diameter randomly glued to the bottom surface and on the four lateral walls of the glass box. The volume fraction of the random packing obtained when the beads are poured in this roughened box at $Q = 3$ (particle/s)/cm² with no external vibration

is $\phi = 0.615$. When a horizontal acceleration $\Gamma = 1$ is imposed, the final density is $\phi = 0.645$. The study of the internal structure of the packing exhibits a crystal-like structure everywhere except in a layer of 8 particle diameters adjacent to the walls, showing that sphere crystallization is an intrinsic behavior of the system, and not the result of flat boundaries. We conclude that ordered nature of the packings is insensitive to wall roughness conditions.

However, some specific boundaries can dramatically influence the precise structure of a crystalline arrangement. For the flat or irregular boundaries considered above, the crystalline packings we have created are formed by the superposition of hexagonal-patterned layers [Fig. 4(a)]. However, there exist two ways of forming a new hexagonal layer on top of a previous one. The final arrangement is thus, strictly speaking, not a crystal, but a sequence of randomly stacked hexagonal packings perpendicular to gravity. This vertical, one-dimensional disorder is well known in colloidal sedimentation [24]. The crystalline sediment is not a perfect crystal, and this leads to some difficulties for technological applications. Recently, van Blaaderen *et al.* [17] have proposed a method for controlling the crystal orientation and producing large single colloidal crystals. Their idea is to create the sediment starting with a square-patterned substrate. When the mesh of the substrate is exactly equal to the particle diameter, the square pattern corresponds to the (100) plane of a face-centered-cubic (fcc) packing. Since there is only one way for the beads to arrange themselves on the square pattern, a perfect fcc crystal can be formed. We have applied the same method in our system of non-Brownian spheres, by placing a square wire netting on the bottom surface before filling the box under horizontal vibrations. The mesh was 2 mm and oriented parallel to the vibration direction (otherwise the square pattern is lost after a few

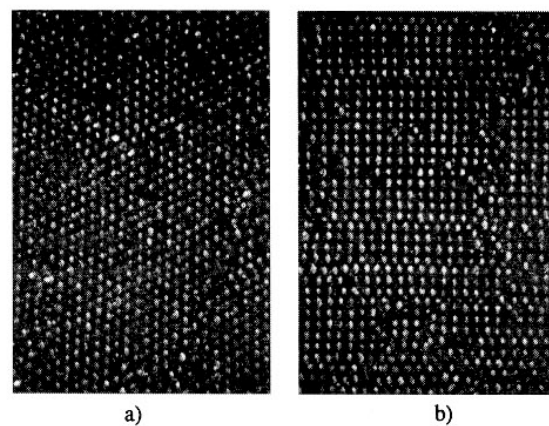


FIG. 4. The free surface structure of packings 40 layers thick obtained in a box with: (a) flat bottom wall; (b) square-patterned bottom wall.

layers). Under such conditions, we obtained a fcc crystal exhibiting a square pattern at the free surface [Fig. 4(b)]. The efficiency of the method seems to be only limited by boundary effects: some zones of hexagonal packing nucleate close to the walls parallel to the direction of oscillation. Their size grows as the height of the packing increases, invading finally the entire box. The maximum height of the fcc crystal that can be created (50 particle diameters in our box) is thus controlled by the width of the container.

In conclusion, we have shown that crystalline packings denser than random close packing can be obtained by collectively handling the particles. The method of filling under horizontal vibration presents strong analogies with colloidal crystallization. However, the particle dynamics are different, since horizontal vibration under a vertical gravitational field is not *a priori* equivalent to thermal fluctuations. Further investigations are thus necessary in order to precisely understand how the horizontal vibrations lead to the spontaneous arrangement of quasi-crystalline particle structures.

This work has benefited from stimulating discussions with P. Gondret and R. Monasson. We thank A. Garcia, T. Lescuyer, and J. Webert for technical assistance and R. T. Goodwin for a critical reading of the manuscript.

*Permanent address: Department of Mechanical Engineering, University of Colorado, Boulder, CO 80309.

- [1] H.H. Hausner, K.H. Roll, and P.K. Johnson, *Vibratory Compacting*, Principles and Methods Vol. 2 (Plenum Press, New York, 1967).
- [2] D.J. Cumberland and R.J. Crawford, *Packing of Particles*, Handbook of Powder Technology Vol. 6 (Elsevier, Amsterdam, 1987).
- [3] J.D. Bernal, Proc. R. Soc. London A **280**, 299 (1964).
- [4] N.J.A. Sloane, Sci. Am. **250**, 92 (1984).
- [5] J.H. Conway and N.J.A. Sloane, *Sphere Packing, Lattices and Groups*, Series of Comprehensive Studies in Mathematics Vol. 290 (Springer, Berlin, 1988).
- [6] D.G. Scott, Nature (London) **188**, 908 (1960).
- [7] M.A. Slifkin, Nature (London) **193**, 465 (1962).
- [8] H. Susskind and W. Becker, Nature (London) **212**, 1564 (1966).
- [9] J.G. Berryman, Phys. Rev. A **27**, 1053 (1983).
- [10] Anonymous, Nature (London) **239**, 488 (1972).
- [11] D.G. Scott, J. Chem. Phys. **40**, 611 (1964).
- [12] T.G. Owe Berg, R.L. McDonald, and R.J. Trainor, Jr., Powder Technol. **3**, 183 (1969).
- [13] L. Vanel, A.D. Rosato, and R.N. Dave, Phys. Rev. Lett. **78**, 1255 (1997).
- [14] P.N. Pusey and W. van Meegen, Nature (London) **320**, 340 (1986).
- [15] K.E. Davis, W.B. Russel, and W.J. Glantschnig, Science **245**, 507 (1989).
- [16] P.N. Pusey *et al.*, Phys. Rev. Lett. **63**, 2753 (1989).
- [17] A. van Blaaderen, R. Ruel, and P. Wiltzius, Nature (London) **385**, 321 (1997).
- [18] S. Douady, S. Fauve, and C. Laroche, Europhys. Lett. **8**, 621 (1989).
- [19] F. Melo, P.B. Umbanhowar, and H.L. Swinney, Phys. Rev. Lett. **75**, 3838 (1995).
- [20] J.E. Ayer and F.E. Soppet, J. Am. Ceram. Soc. **48**, 180 (1965).
- [21] J.B. Knight, *et al.*, Phys. Rev. E **51**, 3957 (1995).
- [22] P. Evesque, P. Alfonsi, C. Stefani, and B. Barbe, C. R. Acad. Sci. Paris Serie II **311**, 393 (1990).
- [23] S.G.K. Tennakoon and R.P. Behringer (to be published).
- [24] M.S. Elliot, B.T.F. Bristol, and W.C.K. Poon, Physica (Amsterdam) **235A**, 216 (1997).

B.2 De l'ordre dans les billes !

M. NICOLAS & O. POULIQUEN

Bulletin de la Société Française de Physique, n° 117, p. 8 (1998).

De l'ordre dans les billes

Maxime Nicolas et Olivier Pouliquen

Groupe écoulements de particules, IUSTI, Technopôle de Château-Gombert,
5 rue Enrico Fermi 13453 Marseille Cédex 13, maxime@iusti.univ-mrs.fr

La modélisation simple d'un liquide, de la structure atomique d'un solide ou d'un matériau granulaire (sable, poudre) amène à s'intéresser au problème d'empilement de sphères dures. Inévitablement se pose alors la question de la meilleure façon d'empiler des sphères de même taille.

Si on cherche à minimiser le volume occupé par l'empilement (donc à augmenter au maximum sa densité), la réponse est connue : il faut réaliser une structure cubique à faces centrées (cfc). On obtient alors une fraction volumique égale à $\pi/\sqrt{18} \approx 0,74048$. Derrière l'évidence de la réponse se cache un mystère mathématique car

de la conjecture de Kepler. Ce n'est que quatre siècles plus tard que la preuve complète est enfin trouvée par Thomas Hales, un mathématicien de l'université du Michigan (2). La démonstration de Hales est basée sur l'étude cas par cas des contre-exemples possibles de la conjecture et semble convaincre tous les spécialistes de la question.

Mais si mathématiquement l'empilement cristallin de sphères dures a livré ses secrets, sa réalisation expérimentale est loin d'être évidente. Le remplissage sans précaution d'un récipient avec des sphères dures ne produit pas d'arrange-

ment maximale pour une accélération horizontale induite par vibration de l'ordre de 10 ms^{-2} et pour une alimentation en billes de l'ordre de quelques billes par cm^2 et par seconde. L'empilement obtenu est alors très organisé comme le montre la figure 1, image de la surface libre de l'empilement. Nous avons vérifié que la cristallisation induite par vibration horizontale n'est pas limitée à la surface mais s'étend en volume en utilisant la méthode dite « du glaçon » : après formation de l'empilement dans un récipient étanche, les pores sont comblés par de l'eau puis le tout est congelé. On obtient ainsi une structure solide qui, découpée à cœur, montre une organisation des billes en structure cfc. La fraction volumique atteint 0,68.

Le cristal parfait n'est pas formé à cause de la présence des bords, de nombreux défauts dans la structure ainsi que d'une polydispersité des billes (faible mais néanmoins présente).

Nous ne comprenons pas encore très bien comment la vibration horizontale permet d'atteindre l'empilement cristallin. Les premières études semblent montrer que la dynamique de cristallisation est dominée par la « liquéfaction » des couches supérieures de l'empilement, lieu d'un fort cisaillement. Une étude plus précise de l'influence du cisaillement sur l'empilement de sphères dures est en cours, et devrait nous livrer plus d'informations.

La démonstration de la conjecture de Kepler vient donc confirmer l'actualité de la recherche sur les empilements, en particulier dans le domaine toujours plus actif des milieux granulaires.

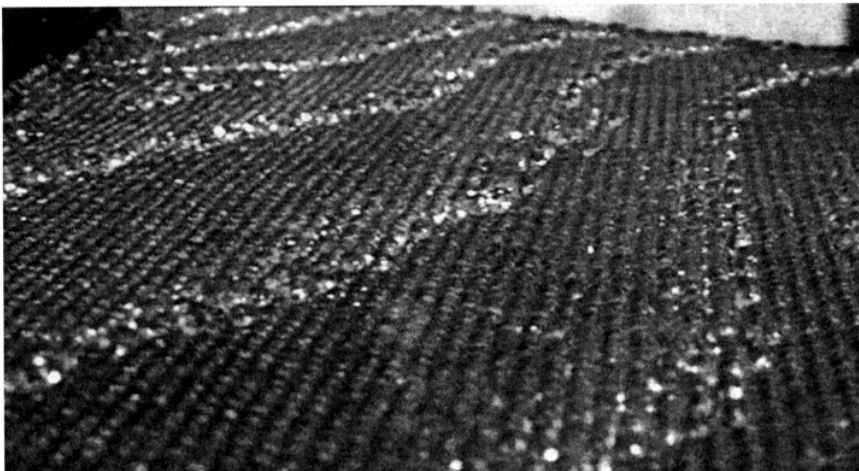


Figure 1 : Photographie de la surface libre d'un empilement réalisé sous vibration horizontale. Le récipient a été légèrement incliné pour montrer la structure stratifiée de l'empilement. On peut également noter l'organisation à longue portée sur chaque strate.

la preuve que cette fraction volumique est la plus élevée possible s'est fait longuement attendre.

A la suite d'une correspondance avec Thomas Harriot, qui s'était penché sur le problème du dénombrement de boulets de canon empilés, le problème a été posé par Johannes Kepler en 1611. Après une description de l'empilement cfc, Kepler écrit : « L'assemblage sera très serré, de sorte qu'ensuite aucune disposition ne permettra d'entasser un plus grand nombre de sphères dans le même récipient » (1).

Sans preuve mathématique, cette assertion est restée connue sous le nom

ment ordonné. Imposer des vibrations pour compacter l'empilement ne semble pas suffire non plus, la fraction volumique pouvant atteindre au mieux 0,64, celle de l'empilement aléatoire le plus compact (3). Le système reste bloqué dans un état métastable ne correspondant pas à l'état d'énergie le plus bas. La seule méthode pour créer l'empilement cristallin serait-elle de ranger les billes une à une ?

Une expérience récente a montré qu'un état organisé peut être atteint avec une manipulation collective des sphères (4). Dans cette expérience, le récipient est rempli tout en étant soumis à une vibration horizontale. L'efficacité de la méthode est

Références

- 1- Traduction de Robert Halleux, C.N.R.S., 1975.
- 2- *Science*, **281**, 1267 (1998). Voir également sur le web le site de T. Hales : <http://www.math.lsa.umich.edu>.
- 3- D.G. Scott, *Nature* **188**, 908 (1960).
- 4- O. Pouliquen, M. Nicolas et P. Weidman, *Phys. Rev. Letters* **79**, 19 (1997).

B.3 Wavy instability in liquid-fluidized beds

M. NICOLAS, E.J. HINCH & É. GUAZZELLI
Ind. Eng. Chem. Res., **38**, 799–802 (1999).

Wavy Instability in Liquid-Fluidized Beds

Maxime Nicolas,[†] John Hinch,[‡] and Élisabeth Guazzelli*[†]

Laboratoire de Physique et Mécanique des Milieux Hétérogènes, CNRS UMR 7636, ESPCI, 10 rue Vauquelin, 75231 Paris Cedex 05, France, and Department of Applied Mathematics and Theoretical Physics, University of Cambridge, Silver Street, Cambridge CB3 9EW, U.K.

Experiments on the primary wavy instability in a liquid-fluidized bed are designed to test the two-phase flow governing equations. The wave is shown to saturate along the bed. The saturated wave can be well described as a cnoidal wave. The solid-phase viscosity and pressure which are unknown in the two-phase model are deduced from the shape of the saturated wave. The validity of the two-phase Newtonian model is then questioned.

1. Introduction

To fluidize a bed of particles, a fluid is pumped upward at the bottom of the bed through a porous plate. At low flow rates (below minimum fluidization), the bed is packed. As the flow is increased, the drag force on the particles increases until it is sufficient to balance their buoyant weight. The particles then become free to move, and the bed is said to be fluidized. When the flow is increased above minimum fluidization, the bed expands to accommodate the upward flow.

Uniform and homogeneous fluidized beds are rarely realized in practice. Fluidized beds present usually a variety of complex flow regimes above minimum fluidization. Gas-fluidized beds are very unstable and rapidly attain a bubbling regime. In this regime, bubbles, which are regions essentially devoid of particles, rise through the bed.^{1–3} Liquid-fluidized beds exhibit voidage instability waves.^{4–7} The instability remains one-dimensional only in narrow beds. The measured disturbances were shown to grow exponentially upward along the bed height and eventually to lead to a saturated finite amplitude.^{4,5} In wider beds, there is a secondary gravitational overturning instability. A conjecture is that bubbles originate from the later evolution of this secondary instability.^{8,9}

Most of what is known about fluidized beds comes from experiments. A complete theory for fluidized beds is not yet fully established. Two-phase modeling has been used extensively over the past 2 decades with some success; see, in particular, the pioneering work of Anderson and Jackson.^{10,11} The fluidized bed is assumed to be one-dimensional and infinite, and the conservation equations for the mass and the momentum are written for the two phases, the particles and the fluid. To close these equations, it is then necessary to postulate expressions for the interphase force and the stress tensors associated with the fluid and particle phases. An empirical correlation, the Richardson–Zaki law, can be used for the drag force in terms of the relative motion between the phases. This law depends on the particle volume fraction, ϕ . A Newtonian fluid form is usually adopted for the stress tensors. It is not clear, however, how to describe the pressure, p_s , and the viscosity, μ_s ,

of the solid phase. These parameters may increase with an increase of the particle volume fraction.

One of the most pressing problems in the fundamental understanding of fluidized beds is the uncertainties in the governing equations. The objective of the present paper is to test the individual terms by using an experimental investigation of the primary wavy instability of fluidized beds. This primary wavy instability is an interesting problem in itself and is also the first step in the understanding of bubble formation.

2. Convective Nature of the Instability

From a hydrodynamic point of view, a fluidized bed is an open flow; i.e., fluid particles are not confined in the fluidization column. Instabilities evolving in such flows can be classified in two categories. If the instability is sensitive to external perturbations (noise), it is said to be *convective*. Perturbations are then amplified while convected by the mean flow, and the flow can be described as a noise amplifier. On the contrary, if the instability has an intrinsic behavior, it is said to be *absolute*. The flow then behaves as an oscillator.¹²

Experimentally, the behavior of the fluidized bed can be determined by investigating the response of the suspension to a localized and controlled perturbation. The nature of the wavy instability was examined experimentally for a liquid-fluidized bed. A fluidized suspension of glass spheres (with diameter $d = 685 \pm 28 \mu\text{m}$ and density $\rho_s = 4.0 \pm 0.1 \text{ g cm}^{-3}$) in water was contained in a thin vertical glass tube with a minimum fluidization velocity of $q_{mf} = 0.82 \pm 0.07 \text{ cm s}^{-1}$ (see Figure 1). The typical Froude number of the present experiment was 0.06. The suspension was held by a porous piston which can be moved with a sinusoidal motion at a given frequency and with an amplitude of $1.5d$. This piston-type distributor was used to study the response of the suspension to a local harmonic forcing.

Above this special distributor, the wave propagation can be visualized by backlighting the column with a neon light. A CCD camera captures a one-dimensional image of the tube, and a digital imaging system is able to construct spatiotemporal plots from successive 1D images. Figure 2 shows such plots and demonstrates the convective nature of the instability. When a sinusoidal perturbation (larger than the “natural noise” of the distributor) is applied, the waves are periodic and follow the forcing, as can be seen for two different frequencies in Figure 2. Further details on the spatial

[†] ESPCI. Present address: IUSTI, CNRS UMR 6595, Université de Provence, Technopôle de Château Gombert, 5 rue Enrico Fermi, 13453 Marseille Cedex 13, France.

[‡] University of Cambridge.

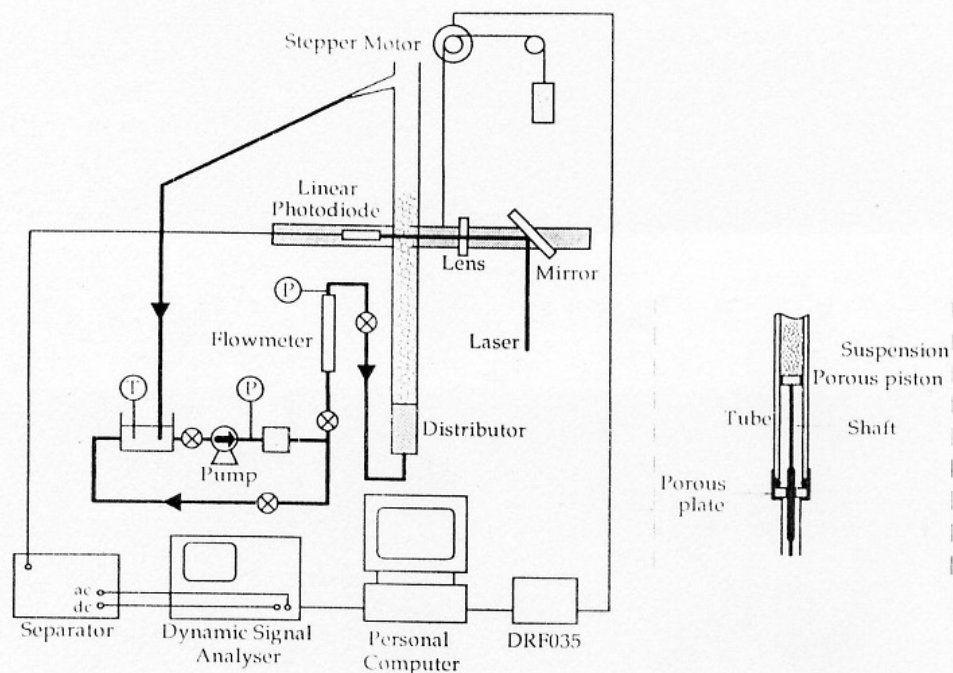


Figure 1. Schematic of the fluidized bed.

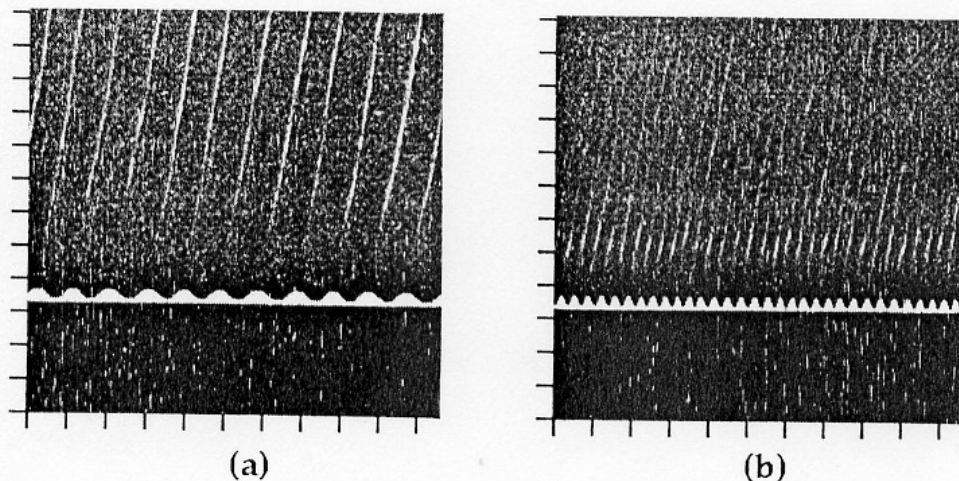


Figure 2. Spatiotemporal plots: waves forced at 0.5 (a) and 1.5 Hz (b). The mean particle volume fraction is 0.500 ± 0.001 . The inclined white lines in these plots correspond to low concentration regions of the suspension moving upward with nearly constant velocity. The sinusoidal motion of the porous piston can also be seen.

stability of the two-phase equations as well as on the experimental results may be found in refs 13 and 14.

Though not formulated in the absolute/convective framework, the spatial evolution of the wave was noted in the early work of Anderson and Jackson.⁴ The power spectra of the waves were found to be very broad (without forcing). There was clear evidence, however, of a dominant low-frequency mode. Its amplitude was found to increase along the bed and eventually to saturate.⁵⁻⁷

3. Nonlinear Saturation of the Wave

Because the instability is convective in nature, any perturbation at the bottom of the bed (natural noise or controlled perturbation) is amplified up the suspension. It is then fundamental to investigate the spatial evolution of each mode independently. To this end, a more quantitative experiment was designed in which the particle volume fraction was measured with a light attenuation technique, using a He-Ne laser beam as a light source. A synchronized average method was used to separate the forcing mode from other modes (noise), using the moving piston as a reference signal.

The amplitudes of the unstable modes were found to saturate. As can be seen in Figure 3, which is typically of many further observations, the saturated wave can be described as a succession of concentration dips and plateaus. Within experimental errors, the wave seems to be symmetric about the minimum of concentration. It can be well fitted by a cnoidal wave (a periodic solution of the Korteweg-de Vries equation¹⁵):

$$\phi(t) = \phi_{\max} - (\phi_{\max} - \phi_{\min}) \text{cn}^2[\tilde{\omega}(t-t_0)|m] \quad (1)$$

where ϕ_{\max} and ϕ_{\min} are maximum and minimum concentrations, $\tilde{\omega}$ is the frequency, and t is time. The parameter m (≈ 0.99 in the present case) is a hidden parameter of the cnoidal function cn (a Jacobian elliptic function¹⁶). It is interesting to mention that such a cnoidal solution has been found in weakly nonlinear analysis of the two-phase equations.¹⁷

4. Questioning the Two-Phase Model

Using the experimental measurement of the shape of the saturated wave, it is then possible to estimate the

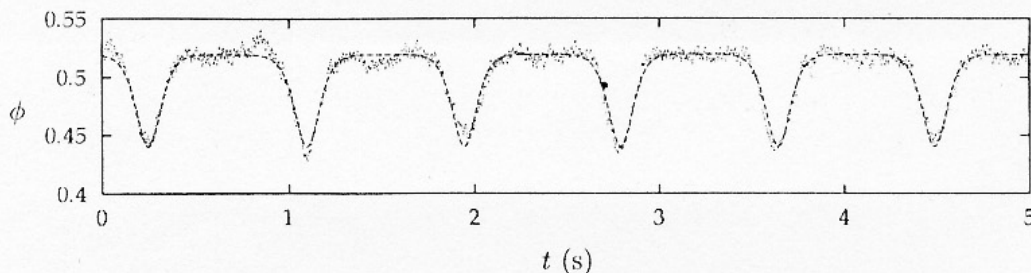


Figure 3. Example of a saturated wave (points) fitted by a cnoidal function (dashed line) measured 5 cm above the distributor. The coefficients of (1) are $\phi_0 = 0.503 \pm 0.02$, $f_0 = 1.17 \pm 0.03$ Hz, $\phi_{\max} = 0.5199$, $\phi_{\min} = 0.44$, $\bar{\omega} = 11.30$ s $^{-1}$, $m = 0.9989$, and $t_0 = 1.0968$ s.

viscous and pressure terms (μ_s and p_s), which are unknown parameters in the two-phase model. For the purpose of the present work, we choose to consider the model of Anderson and Jackson.^{10,11} The fluidized bed is assumed to be one-dimensional and infinite, and the conservation equations for the mass and the momentum are written for the two phases in the following forms:

$$\frac{\partial \phi}{\partial t} + \frac{\partial}{\partial x}(\phi v) = 0 \quad (2)$$

$$u = \frac{q - \phi v}{1 - \phi} \quad (3)$$

$$\begin{aligned} \rho_s \phi \left(\frac{\partial v}{\partial t} + v \frac{\partial v}{\partial x} \right) = & - \frac{\partial p_s}{\partial x} + \beta(u - v) - \phi(\rho_s - \rho_f)g + \\ & \frac{4}{3} \frac{\partial}{\partial x} \left(\mu_s \frac{\partial v}{\partial x} \right) + \rho_f \phi \tilde{C} \left(\frac{\partial u}{\partial t} + u \frac{\partial u}{\partial x} - \frac{\partial v}{\partial t} - v \frac{\partial v}{\partial x} \right) + \\ & \rho_f \phi \left(\frac{\partial u}{\partial t} + u \frac{\partial u}{\partial x} \right) \quad (4) \end{aligned}$$

In this formulation, u and v are the fluid and particle velocities, q is a constant mixture velocity (equivalent to fluidizing flow rate), and ρ_f and ρ_s are the fluid and solid densities, respectively. The parameter \tilde{C} is the added-mass coefficient, which cannot be neglected in liquid fluidization and depends a priori on the particle volume fraction ϕ . The drag on the solid phase is represented by the coefficient β , which can be related to the useful Richardson-Zaki law.⁹

These equations are rewritten in a reference frame moving with the saturated wave at velocity c_{sat} , where the spatial coordinate is $X = x - c_{\text{sat}}t$. After elimination of u and v with (2) and (3), a single equation can be derived from (4) which describes the shape of the saturated wave:

$$\frac{4}{3} \frac{c_{\text{sat}} \phi^*}{\phi^2} \left[\mu_s(\phi) \phi_{XX} + \left(\mu'_s(\phi) - 2 \frac{\mu_s(\phi)}{\phi} \right) \phi_X^2 \right] + F_1(\phi) + [F_2(\phi) - p'_s(\phi)] \phi_X = 0 \quad (5)$$

with

$$\begin{aligned} \mu'_s(\phi) = d\mu_s/d\phi, \quad p'_s(\phi) = dp_s/d\phi, \\ F_1(\phi) = \phi \rho_s \frac{g(\rho_s - \rho_f) \left[q - c_{\text{sat}}(1 - \phi^*/\phi) \right]}{\rho_s \left[\frac{q - c_{\text{sat}}(1 - \phi^*/\phi)}{v_t(1 - \phi)^n} - 1 \right]} \quad (6) \end{aligned}$$

$$\begin{aligned} F_2(\phi) = \rho_f \phi (1 + \tilde{C}) \frac{[q + c_{\text{sat}}(\phi^* - 1)]^2}{(1 - \phi)^3} + \\ (\rho_s + \rho_f \tilde{C}) \left(\frac{c_{\text{sat}} \phi^*}{\phi} \right)^2 \quad (7) \end{aligned}$$

The Richardson-Zaki parameters are v_t , the terminal

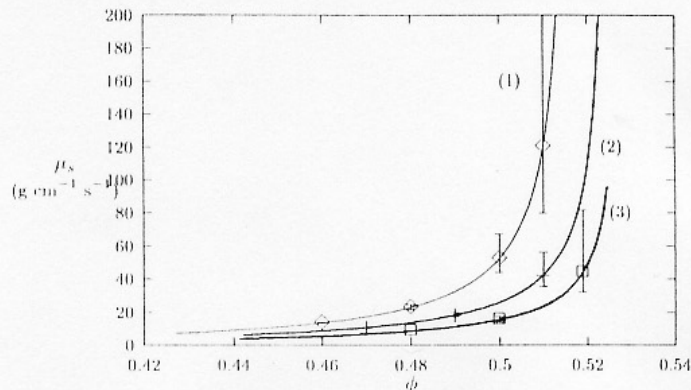


Figure 4. Solid-phase viscosity plotted against concentration for three different waves: $f_0 = 1$ (1), $f_0 = 1.4$ (2), and $f_0 = 2.1$ Hz (3). The volume fraction is the same ($\phi_0 = 0.5$) for these waves. The viscosity increases with decreasing frequencies.

velocity of a single particle, and n , an exponent depending on the Reynolds number. The volume fraction ϕ^* is theoretically equal to ϕ_0 , the mean particle volume fraction, but may differ slightly because of experimental errors in the measurement. The saturated wave velocity was observed not to vary much with the forcing frequency ($c_{\text{sat}} = 3.8 \pm 0.2$ cm s $^{-1}$).

Theoretical studies^{9,17} assume some expressions for the viscosity $\mu_s(\phi)$ and pressure $p_s(\phi)$ and then use (5) to solve for the shape of the steady wave of $\phi(X)$. Here we do the opposite. From the experimental observations of the shape of the wave, we solve (5) to find the unknown viscosity and pressure functions.

For a symmetric wave such as that found experimentally, the pressure term balances the inertial terms and therefore

$$p'_s = F_2(\phi) \quad (8)$$

The viscous term balances the gravity and drag terms [$F_1(\phi)$]. The solid viscosity can then be found numerically. Further details can be found in ref 18.

The deduced viscosity increases with increasing volume fraction and seems to diverge at large volume fractions as can be seen in Figure 4. The existence of the three separated curves means that the "viscosity" depends also upon the frequency of the forcing mode and of the mean volume fraction of the suspension. This assertion assumes that the quasi-static Richardson-Zaki drag law can still be applied, which we believe to be true because the fluid typically passes a particle in 10 ms, a time much shorter than the period of waves. This finding suggests that a Newtonian description of the stress tensor of the solid phase may not be valid. However, these results are strongly dependent on the assumed cnoidal form of the wave. Further work is necessary to confirm and fully understand these results.

Literature Cited

- (1) Clift, R.; Grace, J. R. Continuous bubbling and slugging. In *Fluidization*; Davidson, J. F., Clift, R., Harrison, D., Eds.; Academic: London, 1985.
- (2) Homsy, G. M. Aspects of flow and mixing behavior in fluidized beds. In *Disorder and Mixing*; Guyon, E., Nadal, J.-P., Pomeau, Y., Eds.; Kluwer Academic Publishers: Dordrecht, The Netherlands, 1988.
- (3) Davidson, J. F. Bubbles in fluidized beds. In *Mobile Particulate Systems*; Guazzelli, É., Oger, L. Eds.; Kluwer Academic Publishers: Dordrecht, The Netherlands, 1995.
- (4) Anderson, T. B.; Jackson, R. A fluid mechanical description of fluidized beds—Comparison of theory and experiment. *Ind. Eng. Chem. Fundam.* **1969**, *8*, 137.
- (5) El-Kaissy, M. M.; Homsy, G. M. Instability waves and the origin of bubbles in fluidized beds. Part I. Experiments. *Int. J. Multiphase Flow* **1976**, *2*, 379.
- (6) Didwania, A. K.; Homsy, G. M. Flow regime and flow transitions in liquid-fluidized beds. *Int. J. Multiphase Flow* **1981**, *7*, 563.
- (7) Ham, J. M.; Thomas, S.; Guazzelli, É.; Homsy, G. M.; Anselmet, M.-C. An experimental study of the stability of liquid-fluidized beds. *Int. J. Multiphase Flow* **1990**, *16*, 171.
- (8) Batchelor, G. K. Secondary instability of a gas-fluidized bed. *J. Fluid Mech.* **1993**, *257*, 359.
- (9) Anderson, K.; Sundaresan, S.; Jackson, R. Instabilities and the formation of bubbles in fluidized beds. *J. Fluid Mech.* **1995**, *303*, 327.
- (10) Anderson, T. B.; Jackson, R. A fluid mechanical description of fluidized beds—Equations of motion. *Ind. Eng. Chem. Fundam.* **1967**, *6*, 527.
- (11) Anderson, T. B.; Jackson, R. A fluid mechanical description of fluidized beds—Stability of the state of uniform fluidization. *Ind. Eng. Chem. Fundam.* **1968**, *7*, 12.
- (12) Huerre, P.; Monkewitz, P. A. Local and global instabilities in spatially developing flows. *Annu. Rev. Fluid Mech.* **1990**, *22*, 473.
- (13) Nicolas, M.; Chomaz, J.-M.; Guazzelli, É. Absolute and convective instabilities of fluidized beds. *Phys. Fluids* **1994**, *6*, 3936.
- (14) Nicolas, M.; Chomaz, J.-M.; Vallet, D.; Guazzelli, É. Experimental investigations on the nature of the first wavy instability in liquid-fluidized beds. *Phys. Fluids* **1996**, *8*, 1987.
- (15) Drazin, P. G.; Johnson, R. S. *Solitons: an introduction*; Cambridge University Press: Cambridge, U.K., 1989.
- (16) Abramowitz, M.; Stegun, I. A. *Handbook of mathematical functions*; National Bureau of Standards: Washington, DC, 1972.
- (17) Harris, S. E. The growth of periodic waves in gas-fluidized beds. *J. Fluid Mech.* **1996**, *325*, 261.
- (18) Nicolas, M. Instabilité en onde plane dans un lit fluidisé liquide-solide. Thèse de l'Université Paris 6, 1997.

Received for review June 23, 1998

Revised manuscript received September 17, 1998

Accepted September 22, 1998

IE980401B

B.4 Compaction of a granular material under cyclic shear

M. NICOLAS, P. DURU & O. POULIQUEN
Eur. Phys. J. E **3**, 309–314 (2000).

Compaction of a granular material under cyclic shear

M. Nicolas^a, P. Duru, and O. Pouliquen

Groupe Ecoulements de Particules, IUSTI Technopôle de Château-Gombert, 5 rue Fermi, 13453 Marseille cedex 13, France

Received 31 March 2000

Abstract. In this paper we present experimental results concerning the compaction of a granular assembly of spheres under periodic shear deformation. The dynamics of the system is slow and continuous when the amplitude of the shear is constant, but exhibits rapid evolution of the volume fraction when a sudden change in shear amplitude is imposed. This rapid response is shown to be uncorrelated with the slow compaction process.

PACS. 45.70.Cc Static sandpiles; granular compaction – 61.50.-f Crystalline state

1 Introduction

Powder compaction has recently attracted the attention of physicists as the prototype of a disordered system without thermal fluctuations. For millimetric grains, thermal energy is negligible compared to gravitational energy. Once poured in a box, the grain packing is trapped in a metastable configuration and stays in this state unless an external excitation such as vibrations is imposed. During such a process, the particles assembly exhibits a slow and complex evolution towards a more compact configuration. This evolution has been studied experimentally by Knight *et al.* [1] and Nowak *et al.* [2] in the case of a vertically vibrated packing of spheres.

Their experiment consisted in a vertical cylinder full of monodispersed beads submitted to successive distinct vertical taps of controlled acceleration. The mean volume fraction was recorded after each tap. The experiments were first performed with taps of constant amplitude [1]. They have shown that the increase in volume fraction is a very slow process well fitted by the inverse of a logarithm of the number of taps. The more energetic taps are the more efficient for compaction. Nowak *et al.* [2] have studied the compaction under taps of variable amplitude, and showed that irreversible processes occur during the compaction. Starting from a loose packing, the evolution of the volume fraction is not the same when increasing the amplitude of vibration as when decreasing. The first branch is irreversible, whereas the second is reversible. The highest volume fraction is obtained by first increasing the tap acceleration then decreasing it back to zero. Recently, Josserand *et al.* [3] have investigated the evolution of the packing to sudden change of tap amplitude. They showed that the response of the system depends on the history of compaction.

These experimental results have motivated numbers of theoretical and numerical studies trying to find a min-

imal model which could exhibit qualitatively similar features. Most of the models suggest that the rearrangement of particles in a more compact state needs more and more cooperative reorganization as the volume fraction increases. Absorption-desorption model [2, 4, 5], geometrically frustrated lattice model [6–8], random walk model [9] or excluded-volume model have been proposed [10, 11]. Most of these approaches aspire to describe the vertically vibrated system. To our knowledge the question of how the compaction dynamics depends on the method of excitation has not yet been raised. In the absence of thermal fluctuations, one can legitimately wonder how the compaction dynamic depends on the way the system is excited.

An alternative way of excitation is horizontal vibration. In a previous experiment we have shown that very compact and crystalline packings of monodispersed beads can be obtained this way [12] whereas vertical vibrations only yield random close packings. However, under horizontal vibration, only the top layers of the packing are affected and indeed submitted to a periodic horizontal shear. The goal of this paper is the study of the response to shear of the whole packing. A parallelepiped box full of beads is submitted to a horizontal shear through the periodic motion of two parallel walls. The resulting compaction is analyzed in detail in this paper.

Deformation of granular material under cyclic solicitation has been extensively studied in soil mechanics [13]. Cyclic loading in a triaxial test shows a compaction but no systematic study of the dynamic of compaction for long-time behavior has been investigated. Cyclic shear is also evoked by Scott *et al.* [14] in a short note where they show that this deformation applied to monodispersed beads packing could lead to a partially ordered structure. A shear apparatus has been also developed by Bridgwater and Scott [15, 16] in order to study the segregation dynamic during shear. Cyclic shear has been recently applied to thermally activated systems such as assembly of spherical colloidal particles. A periodic shear deformation

^a e-mail: maxime@iusti.univ-mrs.fr

applied to a colloidal hard spheres glass yields the formation of ordered regions [17, 18]. However, both the thermal excitation and the imposed deformation are in this case present. The experiments presented in this paper can be seen as the analog of the colloidal experiments at zero temperature. The paper is presented as follows. The experimental setup is described in Section 2. In Section 3 the compaction under constant shear amplitude is investigated and the crystallisation process and the slow relaxation are discussed. Section 4 reports the study of the response of the system to sudden change in the shear amplitude. Finally we discuss in Section 5 the analogies and differences between compaction under cyclic shear and vertically vibrated system before giving concluding remarks in Section 6.

2 Experimental setup

The experimental setup is sketched in Figure 1. The shear cell was parallelepiped, and the volume occupied by the beads was typically 10.5 cm high, 7.9 cm wide and 10.2 cm deep. The bottom of the cell was a flat PVC plate attached to a horizontal linear displacement device driven by a stepper motor. The two mobile lateral walls were aluminum plates linked with two hinges to the bottom plate. These plates were covered with a thin plastic sheet to insulate the packing from metallic dust due to particle/wall friction. The front and back sides were glass plates fixed on the bottom plate.

The granular packing was confined on the top by a rectangular plate mounted on a vertical displacement rail. This plate was independent of the rest of the shear cell and was free to move vertically only, no horizontal displacement being allowed. The periodic shear deformation was obtained by imposing a periodic horizontal displacement to the bottom plate, the two mobile lateral walls being constrained by two cables to remain in contact with the top plate.

The granular material we used were spherical glass beads. Experiments were performed with either monodispersed or bidispersed set of beads. For experiments with monodisperse particles, beads were 2.97 ± 0.06 mm in diameter with a density of 2.52 ± 0.02 g cm⁻³. The cell was filled with 1450 g of particles. The bidispersed set of particles was constituted of 725 g of the 3 mm beads and 725 g of 2 mm beads of the same density. In order to prevent the surface deterioration of the beads during long-time experiments, beads were coated with silicon oil Rhodorsil 47V100 (viscosity hundred times viscosity of water). Note that the same quantitative results were observed without lubrication, but lifetime of the beads was in this case quite shorter.

We measured the volume fraction during the compaction process by recording the vertical position of the top plate, which went down (respectively up) when compaction (respectively dilatation) occurred. Its position was accurately measured by a linear position sensor Novotechnik T50 (potentiometric transducer). The position resolution was $3 \cdot 10^{-3}$ cm corresponding to a $2 \cdot 10^{-4}$ resolution

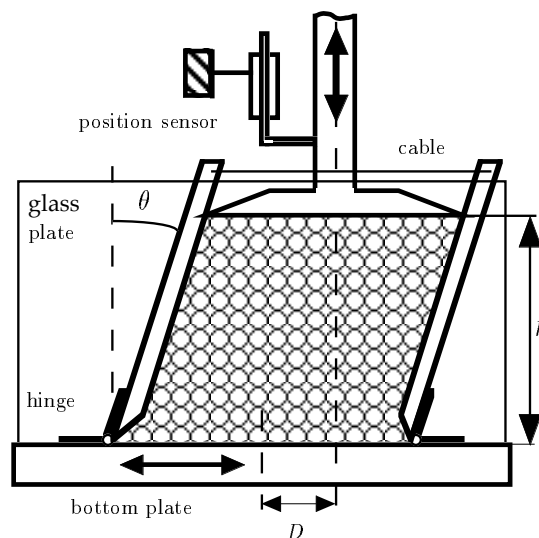


Fig. 1. Schematic of the shear cell and position sensor. D is the horizontal displacement of the bottom plate and h is the height of the packing. The angle of shear is $\theta = \arctan(D/h)$.

in volume fraction. Both the data acquisition and the horizontal displacement of the cell were controlled by the same PC computer. Data could be recorded continuously during the shear, or once every cycle for the study of the long time evolution.

The experimental procedure was the following. The top plate was removed, the mobile side walls were put in the vertical position and the particles were poured into the cell through a hopper. The mean initial volume fraction of the packing obtained by this procedure was $\phi_0 = 0.592 \pm 0.008$. The top plate was then slowly put into contact with the packing. Once the initial random packing was ready, the periodic shear deformation was imposed. The lateral plates were inclined to an angle $+\theta$, followed by an inclination to an angle $-\theta$. The plates were then put back in the vertical position and the volume fraction was recorded. A new cycle of shear was then applied and so on. The volume fraction could also be continuously recorded.

During the experiments, we have observed that the inclination angle θ was the only pertinent control parameter. Change in the velocity of the bottom plate (from 1.9 to 3.8 cm/s) or change in the weight exerted by the top plate on the packing (from 1.8 to 3.8 kg) did not affect any of the measurements. We also performed experiments using asymmetric motion of the lateral plates: the plates were oscillating between $\theta_{\text{medium}} + \theta$ and $\theta_{\text{medium}} - \theta$. In the range accessible by our setup ($\theta < 12^\circ$) no influence of the medium position has been observed. The compaction process was then only controlled by the amplitude of the cyclic shear.

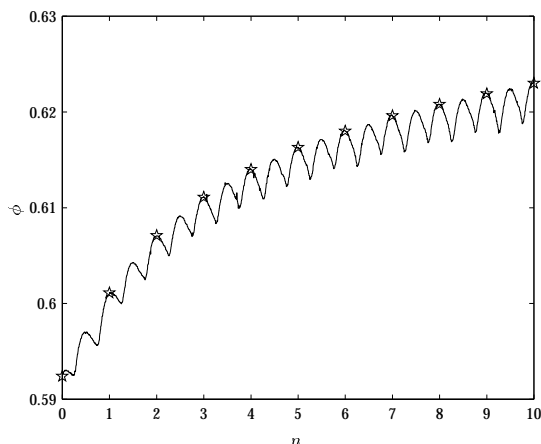


Fig. 2. Continuous evolution of volume fraction as a function of number of cycles; $\theta = 5.4^\circ$.

3 Cyclic shear of constant amplitude

We have first studied the evolution of a packing submitted to a periodic shear of constant amplitude θ . A typical evolution of the packing volume fraction is presented in Figure 2. In this figure the volume fraction ϕ was recorded with a resolution of 325 samples/cycle. This plot clearly shows a slow and continuous evolution from the initial random packing towards higher volume fraction. Superposed to this slow evolution, a quasi-periodic oscillation is observed, corresponding to the dilatation occurring during one cycle: the packing is denser in the vertical position and alternatively dilates when the walls are inclined at $+\theta$ and $-\theta$. This behavior is also observed when the medium position is not the vertical. In this case a local maximum of the volume fraction is measured at the medium position θ_{medium} whereas a local minimum is observed when the walls are inclined at $\theta_{\text{medium}} + \theta$ and $\theta_{\text{medium}} - \theta$.

In this paper we do not study the dilatancy properties in detail but rather focus on the long time evolution of the packing volume fraction. For this purpose, the volume fraction is recorded only once a cycle when the walls are brought back to the vertical position (stars in Fig. 2). A monotonous curve is then obtained, representing the evolution of the volume fraction ϕ as a function of the number of cycles n . The results for three different shear amplitudes $\theta = 2.7^\circ$, 5.4° , 10.7° are presented in Figure 3 for the case of 3 mm beads.

The first remark is that the compaction process is a very slow process. After $6 \cdot 10^4$ cycles (one week experiment), the volume fraction still slowly increases. This slow compaction appears to be more efficient for large shear amplitude than for small shear amplitude as shown by the insert in Figure 3 representing the volume fraction as a function of the shear amplitude θ after 10^4 (asterisks), $3 \cdot 10^4$ (crosses), and $6 \cdot 10^4$ cycles (triangles).

Although curves of Figure 3 present very small fluctuations for an individual run, the final volume fraction can vary significantly (approximately 10%) from one experi-

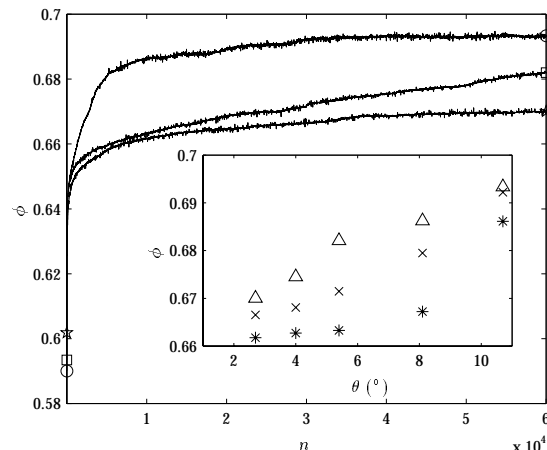


Fig. 3. Compaction under different shear angles : $\theta = 2.7^\circ$ (star), $\theta = 5.4^\circ$ (square), $\theta = 10.7^\circ$ (circle). Insert: volume fraction of the packing *versus* shear angle for increasing number of cycles: $n = 10^4$ cycles (asterisks), $n = 3 \cdot 10^4$ cycles (crosses), $n = 6 \cdot 10^4$ cycles (triangles).

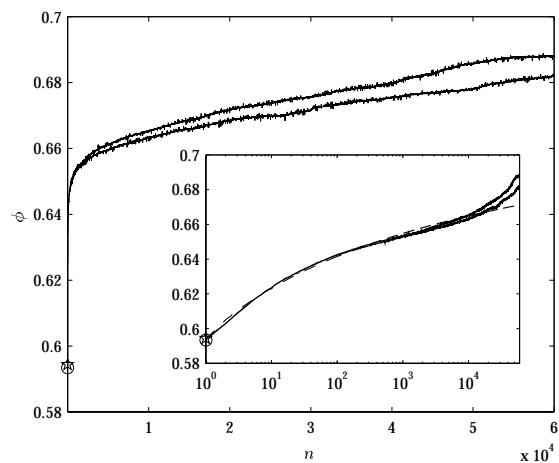


Fig. 4. Compaction curves for $\theta = 5.4^\circ$ for two different runs. Insert: semi-logarithmic scale. Dotted line is the inverse logarithmic fit $\phi = \phi_\infty - (\phi_\infty - \phi_0) / [1 + B \ln(1 + n/\tau)]$ with $\phi_\infty = 0.74$, $\phi_0 = 0.594$, $B = 0.1$ and $\tau = 0.8$.

ment to another carried out at the same shear angle. For example, Figure 4 shows two compaction curves obtained for $\theta = 5.4^\circ$ starting from almost the same initial volume fraction (0.594 ± 0.0008) prepared by the same procedure. Evolution of the packing thus seems to be rather sensitive to the initial random structure of the grains assembly. The insert of Figure 4 presents the same curves in semi-logarithmic scale. We have tried to fit our experimental results by the inverse logarithmic function proposed by Knight *et al.* for the compaction under vertical taps (Eq. (3) of [1]). However, no reasonable agreement with both the short and long time behavior could be found (Fig. 4). Other proposed fits like the two exponential function [19]

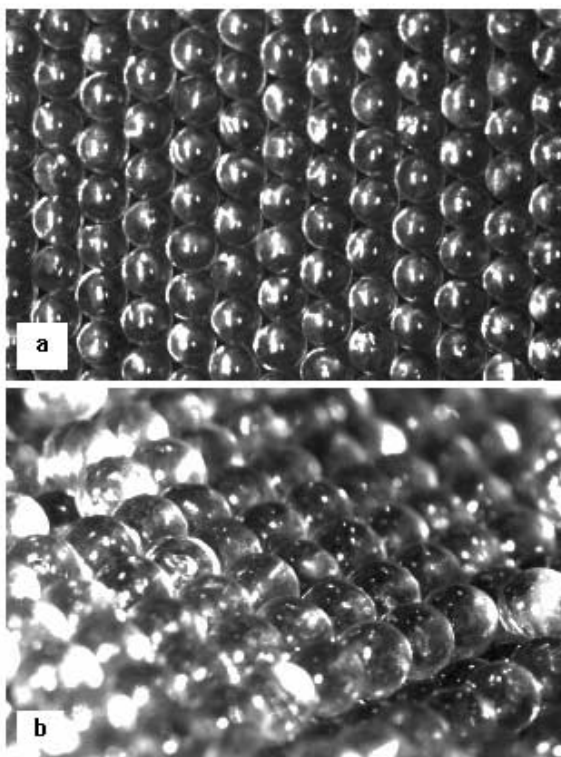


Fig. 5. Photographs of the 3 mm beads packing. (a) Front view of the packing. (b) Ordered structure in the bulk of the packing (upper layers of the packing were removed).

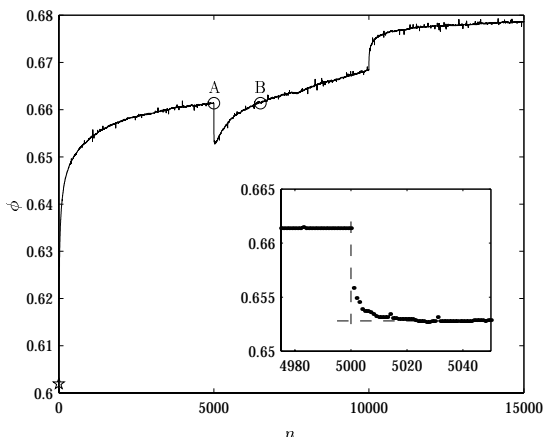


Fig. 6. Example of angle variation effect during the compaction process. The insert shows a close-up of the first jump (point A).

or the stretched exponential ([1] and references therein) do not provide more convincing agreements.

A major difference between the periodic shear compaction and the vertically vibrated system is the large volume fraction up to 0.693 that can be attained by the former. Such a value obtained for monodispersed particles is much larger than the volume fraction of a random close

packing, which is 0.63, according to Scott and Kilgour [20]. This means that crystalline arrangements are created during the compaction, which perhaps explains why the $\log t$ behavior is not observed in our system. The crystal structure of the packing is indeed observed at the wall of the cell as shown in Figure 5a. Moreover we checked that crystallisation is also present in the bulk by carefully removing the particles layer after layer at the end of an experiment. The picture in Figure 5b shows a structure observed in the bulk. The orientation of the crystal observed in the bulk is not always parallel to the walls, suggesting that the order is not only wall-induced but nucleates and grows in the bulk.

In contrast, no crystalline alloy structure has been observed with the bidispersed material made of mixture of 2 and 3 mm beads. However the evolution of the volume fraction as a function of number of cycles and shear amplitude presents the same trend using mono or bidispersed material. In this case, the maximum volume fraction obtained for $\theta = 10.7^\circ$ after $6 \cdot 10^4$ cycles is 0.65 to be compared with 0.693 for the monodispersed packing.

4 Response to a change in shear amplitude

After the study of compaction under constant shear angle, we investigated the effects of a sudden change of angle. A periodic shear with inclination angle θ_1 is first imposed to a random packing, and at a given time, the shear amplitude is suddenly changed to another value $\theta_2 = \theta_1 + \Delta\theta$. A typical experiment is presented in Figure 6. Starting with a shear amplitude $\theta_1 = 2.7^\circ$, the angle is switched to $\theta_2 = 10.7^\circ$ at $n = 5000$, and then switched back to θ_1 at $n = 10^4$. As can be seen, increasing the shear angle at $n = 5000$ produces a rapid fall of volume fraction ϕ followed by a slow and continuous increase. When shear angle is decreased back at $n = 10^4$, a rapid increase of ϕ occurs, followed by a slower one.

Such a response is non-trivial. It first shows that memory effects exist in the compaction process. Points A and B in Figure 6 correspond to packings having the same volume fraction. However, their responses to the same shear amplitude $\theta = 10.7^\circ$ are different: packing A becomes looser whereas packing B pursues its compaction. This means that knowing the volume fraction of the packing is not sufficient to predict the evolution of the system. Such memory effects have been recently brought to the fore in vertically shaken granular packings [3].

Another important observation is the rapid character of the packing response. Whereas the compaction from initial random state is a slow process (Sect. 3), a sudden variation of shear amplitude induces a rapid change of volume fraction, which can be regarded as a discontinuity or a jump. The amplitude $\Delta\phi$ of this jump can be accurately defined and measured with the help of the tangent lines as shown on the insert of Figure 6. This definition is also valid for positive jumps ($n = 10^4$ in Fig. 6). We have systematically studied how the volume fraction jumps depend on the different parameters.

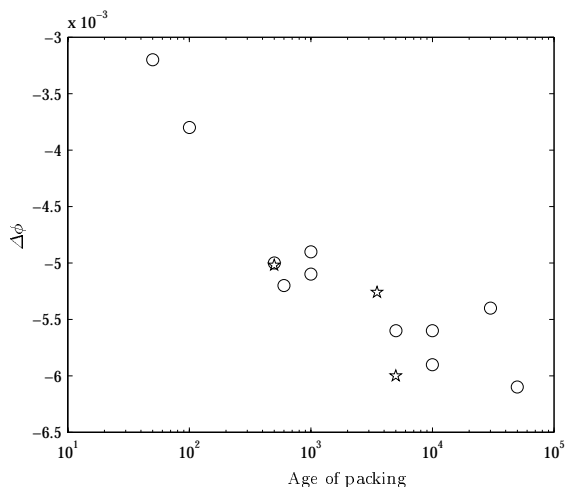


Fig. 7. Jump amplitude *versus* age of packing. $\Delta\theta = 5.4^\circ$ (circles), $\Delta\theta = -5.4^\circ$ (stars).

First, we have investigated how the discontinuity $\Delta\phi$ is influenced by the age of the packing, namely the time elapsed before the angle change is applied. Figure 7 shows the response $\Delta\phi$ to the same angle change $\Delta\theta = 5.4^\circ$ as a function of the elapsed time. The jump $|\Delta\phi|$ increases with age and eventually saturates for $n > 2000$. The same trend is observed for positive jumps ($\Delta\theta = -5.4^\circ$). After 2000 cycles, the response does not depend on the age any more.

Secondly, we have observed that the initial angle does not play any role. Changing the shear amplitude from θ_1 to $\theta_1 + \Delta\theta$ yield a response $\Delta\phi$ in volume fraction independent of θ_1 . *In fine*, the response of the system for sufficiently aged packings only depends on the shear change $\Delta\theta$.

Figure 8 summarizes jump measurements carried out for the number of cycles $n > 3 \cdot 10^4$. Data points align along a straight line crossing the origin:

$$\Delta\phi = -\alpha\Delta\theta \quad (1)$$

with $\alpha = 1.45 \cdot 10^{-3}$ and $\Delta\theta$ in degrees. In conclusion, the response of the packing to sudden change amplitude appears to be simpler than first thought. The rapid variation of the volume fraction induced by the change is simply proportional and opposite to the angle change.

5 Discussion

Two kinds of evolution are observed in the system of cyclic sheared packing: a slow and continuous compaction when the shear amplitude is constant and a rapid response when a change in shear amplitude is imposed. The striking feature is that the rapid dynamic is uncorrelated with the slow compaction: the variation of the volume fraction $\Delta\phi$ induced by a sudden change $\Delta\theta$ in shear amplitude is independent of the state ϕ of the system, and depends linearly

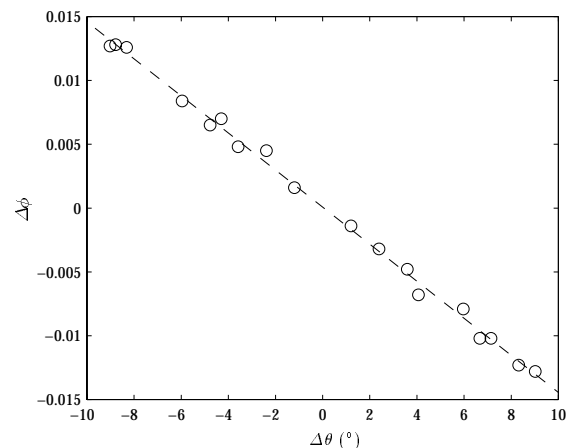


Fig. 8. Relation between volume fraction jumps and angle change for aged packings ($n > 3 \cdot 10^4$).

on $\Delta\theta$. This observation suggests to split the evolution of the volume fraction into two terms:

$$\phi(n) = \phi_{\text{slow}}(n) - \alpha\theta. \quad (2)$$

The first term $\phi_{\text{slow}}(n)$ corresponds to a slow and *continuous* evolution and the second term is proportional to angle θ . This description is compatible with Figure 8: when a sudden change in θ is imposed, one observes a corresponding jump $\alpha\Delta\theta$ in volume fraction, ϕ_{slow} being a continuous function.

One way of interpreting these results is to say that the periodic shear deformation plays two roles. On the one hand, it allows for the particles to slowly and continuously rearrange to form a more compact packing. It thus profoundly affects the structure of the packing in an irreversible way, by introducing more and more order. This contribution is ϕ_{slow} . On the other hand, it introduces an additional disorder superimposed to the ordered structure, represented in equation (2) by the negative contribution $-\alpha\theta$. These two contributions are uncorrelated. In this framework, the slow and rapid dynamics would then correspond to changes in the packing structure that are of complete different nature.

However, such interpretation remains speculative as long as we are not able to relate the macroscopic behavior of the volume fraction to local rearrangement of the particles. An important question is the discrimination between the rearrangements involved in the slow compaction process from those involved during the rapid compaction or dilatation subsequent to a sudden change in shear amplitude. Some numerical simulations suggest the existence of collective motion of cluster and of individual motion of particles which could perhaps be related to the slow and rapid dynamics [21, 19, 22].

At this stage, it is interesting to compare the results presented here about the compaction of a granular packing under cyclic shear with the results obtained previously in the case of a vertically vibrated packing. In order to do so, we have carried out the annealing experiment analog

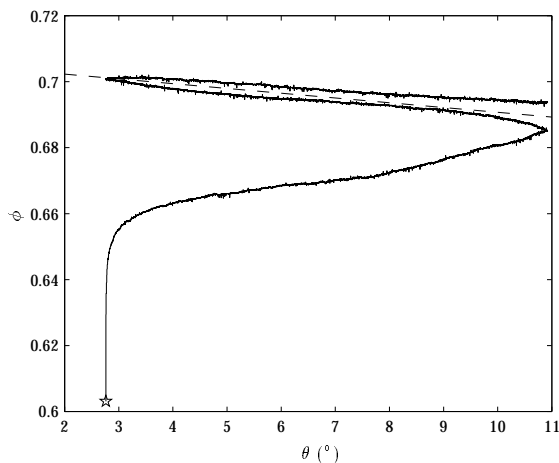


Fig. 9. Compaction under variable shear angle. θ is increased linearly from 2.7° to 10.7° then decreased to 2.7° and finally increased again up to 10.7° . The rate of increase or decrease is $\pm 2.7 \cdot 10^{-4} \text{ }^\circ/\text{cycle}$. The dashed line has a slope equals to $-\alpha$.

to the one described in [2] for the tap excitation: the amplitude of shear is continuously increased then decreased and increased again. The evolution of the volume fraction is plotted in Figure 9. As observed in the tap experiment, one gets an irreversible branch and a reversible one.

However, in our case, the reversible branch is simply a straight line parallel to $-\alpha\theta$. In the light of the above interpretation about the response of the system to sudden shear changes, this behavior can be explained as follows: slowly increasing the shear amplitude yields a quasi-saturated state, where $\phi_{\text{slow}}(n)$ does no longer vary with n . By then changing the angle θ , one explores the linear variation of ϕ with θ . The slight shift between the decreasing and increasing branches in the reversible regime comes from the slight evolution of $\phi_{\text{slow}}(n)$. Hence this shift increases (respectively decreases) when decreasing (respectively increasing) the rate of change in angle.

There thus exist several similarities between the two modes of compaction. However, some differences have to be noted. First, cyclic shear induces the crystallisation of an assembly of monodispersed beads, whereas such order is not reported in the experiments of vertical taps. The small aspect ratio (10 particles in a cross-section) of the tap experiment could perhaps inhibit the crystallisation. A second difference is the amplitude of the fluctuations. According to [2] vertical taps induce fluctuations from one cycle to another of the order of 0.8% of the mean volume fraction, whereas in our shear experiment the variation of volume fraction is less than 0.1%. Periodic shear is perhaps a less violent way of exploring the different packing configurations.

6 Conclusion

In this paper we have presented experiments about the compaction of a granular media under cyclic shear. First

we have put in evidence that this method of compaction leads to crystals when the material is made of monodispersed particles. By studying the response of the system to sudden change in shear amplitude we have shown that discontinuities in volume fraction are observed, with amplitudes proportional to the angle change. The evolution of the packing is thus composed of two dynamics: a slow, continuous and monotonous compaction and a rapid evolution occurring during the shear jump. This observation suggests that the rearrangement of the particles in the packing associated to the two dynamics are of different nature. However, the next important step would be to experimentally relate the compaction process with the evolution of the internal structure of the packing.

This work has benefited from fruitful discussions with R. Monasson, A. Lemaitre and S. Luding. It would not have been possible without the technical assistance of F. Ratouchniak.

References

1. J.B. Knight, C.G. Fandrich, C.N. Lau, H.M. Jaeger, S. Nagel, *Phys. Rev. E* **51**, 3957 (1995).
2. E.R. Nowak, J.B. Knight, E. Ben-Naim, H.M. Jaeger, S.R. Nagel, *Phys. Rev. E* **57**, 1971 (1998).
3. C. Josserand, A. Tkatchenko, D. Mueth, H. Jaeger, submitted to *Phys. Rev. Lett.*, 2000.
4. X. Jin, G. Tarjus, P. Viot, *J. Phys. A* **32**, 2997 (1994).
5. J. Talbot, G. Tarjus, P. Viot *Cond-mat/9910239* (1999).
6. A. Coniglio, H.J. Herrmann, *Physica A* **225**, 1 (1996).
7. M. Nicodemi, A. Coniglio, H.J. Hermann, *Phys. Rev. E* **55**, 1575 (1997).
8. M. Nicodemi, A. Coniglio, *Phys. Rev. Lett.* **82**, 916 (1999).
9. S. Luding, M. Nicolas, O. Pouliquen, in *Compaction of Soils, Granulates and Powders*, edited by D. Kolymbas, W. Fellin (A.A. Balkema, Rotterdam, 2000) p. 241.
10. R.B.S. Oakeshott, S.F. Edwards, *Physica A* **189**, 188 (1992).
11. T. Boutreux, P.G. de Gennes, *Physica A* **244**, 4758 (1997).
12. O. Pouliquen, M. Nicolas, P.D. Weidman *Phys. Rev. Lett.* **79**, 3640 (1997).
13. G.N. Pande, O.C. Zienkiewicz (Editors) *Proceedings of the International Symposium on Soils under Cyclic and Transient Loading, Swansea, 1980* (University College of Swansea, Swansea, 1980).
14. G.D. Scott, A.M. Charlesworth, M.K. Mak, *J. Chem. Phys.* **40**, 611 (1964).
15. A.M. Scott, J. Bridgwater, *Powder Technology* **14**, 177 (1976).
16. M.H. Cooke, J. Bridgwater, A.M. Scott, *Powder Technology* **21**, 183 (1978).
17. M.D. Haw, W.C.K. Poon, P.N. Pusey, *Phys. Rev. E* **57**, 6859 (1998).
18. M.D. Haw, W. C.K. Poon, P.N. Pusey, P. Hebraud, F. Lequeux, *Phys. Rev. E* **58**, 4673 (1998).
19. G.C. Barker, A. Mehta, *Phys. Rev. E* **47**, 184 (1993).
20. G.D. Scott, D. M. Kilgour, *Brit. J. Appl. Phys.* **2**, 863 (1969).
21. G.C. Barker, A. Mehta, *Phys. Rev. A* **45**, 3435 (1992).
22. D.A. Head, G. J. Rodgers, *J. Phys. A* **31**, 107 (1998).

B.5 A minimal model for slow dynamics: Compaction of granular media under vibration or shear

S. LUDING, M. NICOLAS & O. POULIQUEN

Proceedings of the International Workshop on Compaction of Soils, Granulates and Powders, Innsbruck, 241–248 (2000).

A minimal model for slow dynamics: Compaction of granular media under vibration or shear

Stefan Luding¹, Maxime Nicolas², Olivier Pouliquen²

¹ Institute for Computer Applications 1,
Pfaffenwaldring 27, 70569 Stuttgart, Germany
e-mail: lui@ica1.uni-stuttgart.de

² Groupe Ecoulement de Particules, IUSTI, Technopole de Chateau-Gombert,
5 rue Enrico Fermi, 13453 Marseille Cedex 13, France

Abstract: Based on experiments of the compaction of granular materials under periodic shear of a packing of glass beads, a minimal model for the dynamics of the packing density as a function of time is proposed. First, a random “energy landscape” is created by a random walk (RW) in energy. Second, an ensemble of RWs is performed for various temperatures in different temperature-time sequences. We identify the minimum (mean) of the energy landscape with the maximum (random) density. The temperature scaled by the step-size of the energy landscape determines the dynamics of the system and can be regarded as the agitation or shear amplitude. The model reproduces qualitatively both tapping and shear experiments.

Key-words: Compaction, crystallization, Sinai-diffusion, random walks, quenched disorder

1 Introduction

The issue of slow dynamics, rare events and anomalous diffusion is object to ongoing research in statistical physics [4, 7, 13, 21, 22]. One example for an experimental realization of slow dynamics is the compaction of granular materials, being of interest for both industrial applications and research. Many compaction experiments have been carried out in the last decades, see e.g. [1, 2, 6, 12], but the evolution of density with time is far from being well understood. Recent laboratory experiments concern pipes filled with granular media and periodically accelerated in order to allow for some reorganization [9, 17, 18]. The compaction dynamics was obtained to be logarithmically slow and could be reproduced with a simple parking model [3, 11]. Alternative experiments concern a sheared block of a granular material (monodisperse glass spheres) and display a similar dynamics [16]. Numerical model approaches, like a frustrated lattice gas (the so-called “Tetris” model) [5, 15, 20] also lead to this slow dynamic behavior, as well as some theory based on stochastic dynamics [14]. The fact that a peculiar dynamics is reproduced by so many models indicates that it is a basic and essential phenomenon.

Rather than modeling granular systems in all details, e.g. in the framework of molecular dynamics or lattice gas simulations [19, 20], we will propose a very simple

model based on the picture of a random walk in a random energy landscape, for a review see [4], and even simpler than recent, very detailed considerations in the same spirit [8]. Random walks have been examined, for example, on fractals and ultrametric spaces, where the continuous time random walk was introduced in order to allow a mathematical treatment [10]. If a random walker is situated in an uncorrelated, random, fractal energy landscape, the process is called Sinai-diffusion [4]. The aim of this study is to show that the Sinai model is in qualitative agreement with the compaction dynamics of granular media. An issue not addressed here is a quantitative adjustment which can be reached, for example, by introducing correlations in the EL.

2 Summary of the experimental results

The subject of compaction of granular material [1, 2, 6, 12] has been recently revisited through careful experiments carried out by Knight et al. and Nowak et al. [9, 17, 18]. The experiment consists of a vertical cylinder, full of monodisperse beads, which is submitted to successive distinct taps of controlled acceleration (vertical vibration). The measurement of the mean volume fraction after each tap gives a precise information about the evolution of the compaction. From the first experiments performed with taps of constant amplitude, the increase in volume fraction was found to be a very slow process well fitted by the inverse of a logarithm of the number of taps. Nowak et al. [17, 18] have then studied the compaction under taps of variable amplitude, and showed that irreversible processes occur during the compaction. Starting with a loose packing, the evolution of the volume fraction is not the same when increasing the amplitude of vibration as when decreasing. The first branch appears to be irreversible, whereas the second is reversible.

We have recently performed a compaction experiment based on cyclic shear applied to an initially loose granular packing [16]. A parallelepipedic box full of beads is submitted to a horizontal shear through the periodic motion of two parallel walls at amplitude θ_{\max} , see Fig. 1(a). Compaction occurs during this process, leading to crystallisation of the beads in the case of a monodisperse material. The control parameter in this configuration is the maximum amplitude of shear θ_{\max} (inclination angle of the walls). The measurement of the mean volume fraction ϕ shows that compaction under cyclic shear is a very slow process as in the vertical vibration experiments (typically 5×10^4 shear cycles or taps). The higher the shear amplitude the more efficient is the compaction (shear amplitudes up to $\theta_{\max} < 12.5^\circ$ were examined), when starting with a loose packing of the same initial volume fraction. More surprising results arise when the packing is submitted to a sudden change in shear amplitude. We have observed that a “jump” in volume fraction occurs which is opposite and proportional to the change in θ_{\max} . Sudden increase (resp. decrease)

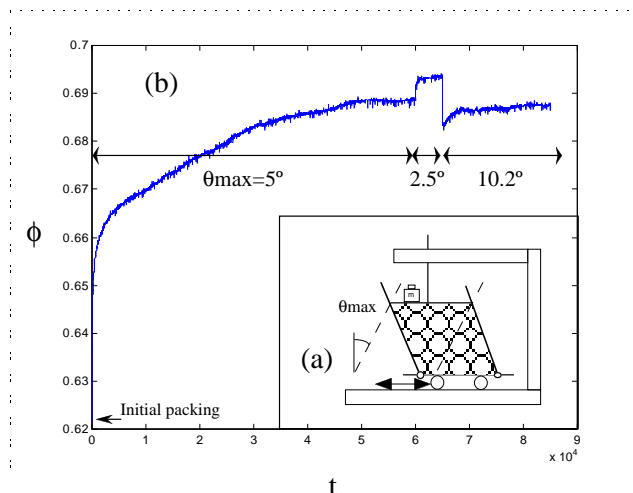


Figure 1: (a) Sketch of the experimental setup. (b) Evolution of the volume fraction as function of shear cycles n : a saturated state is seemingly reached after 6×10^4 cycles with an initial shear angle of 5 degrees; a positive jump in volume fraction is observed when the angle is decreased to 2.5 degrees and applied for 5×10^3 cycles; a negative jump is observed when the angle is increased to 10.2 degrees.

in the shear amplitude decreases (resp. increases) the volume fraction (Fig. 1). The response is very rapid (less than 20 cycles) and quasi-independent of the state before the angle change. For more detailed experimental results see [16].

3 The Model

A naive picture that evolves out from the experimental observations is the analogy between the packing of beads and a thermal system seeking for a minimum of energy in a very complex potential-energy landscape [4]. Due to some agitation (shear) compaction occurs and the total potential energy of the packing decreases. Starting from a loose packing at $n = 0$, the vibrational or shear excitation can be seen as the analog of the temperature in the sense that the excitation allows for an exploration of the phase space. In a granular packing of monodisperse spheres, the absolute minimum of the energy is obtained for a perfect (fcc) or (hc) crystal with volume fraction $\phi = 0.74$. If the energy landscape is complex with a lot of different scale valleys or hills, one can understand that an efficient, fast compaction will be obtained with high temperatures: the system is then able to escape the deep local valleys and find a valley with lower potential energy. A decrease of the temperature is then

needed to explore local fine-scale minima. The goal of this paper is simply to explore this idea by studying the dynamics of random walkers on a random landscape (the Sinai model), and to show that this very naive picture gives results in qualitative agreement with the experimental observations.

Our model is based on the assumption that all possible configurations of a granulate in a given geometry can be mapped onto an “energy landscape” (EL). Since a simple two-level system (as used to model the dynamics in simple glasses) does not lead to the experimentally observed phenomenology, we assume a fractal energy landscape created by a random walk in energy with phase space coordinate x . A typical EL with energy $V(x)$ is schematically shown in Fig. 2. The stepsize in energy is ΔV , the mean of the energy landscape is V_{mean} and its absolute minimum is V_{min} . Here, the EL is symmetric to its center, in order to allow for periodic boundary conditions in x . Given some EL, the granulate is now modeled as an ensemble of random walkers diffusing on the EL, with a temperature T_{RW} . The analog to the density of a granular packing is the rescaled energy of an ensemble of random walkers in the energy landscape

$$\nu = 1 - \frac{E - V_{\text{min}}}{V_{\text{mean}} - V_{\text{min}}}, \quad (1)$$

which we denote as *density* in the following. For the (random) initial configuration, the energy will be $E \approx V_{\text{mean}}$ so that $\nu = 0$; for the close-packing configuration, i.e. all RWs are in the absolute minimum, one has $E \approx V_{\text{min}}$ and thus $\nu = 1$. The energy landscape has the size L , the ensemble of RWs consists of R random walkers and S is the number of steps performed.

Since the energy of the RWs in the EL corresponds to the potential energy of the packing, we interpret the (constant) stepsize ΔV (used here as one possibility for the construction of the EL) as a typical activation energy barrier. The maximum of V corresponds to a random loose, local packing density, the mean to the (initial) random close packing, and the absolute minimum to the hexagonal close packing. For one RW, the probability to jump within time Δt from one site x_i to its neighbor-site $x_{i\pm 1}$ is

$$p_{\pm}(x_i) = \min [1, \exp(-\Delta_{\pm}(x_i)/T_{RW})], \quad (2)$$

with $\Delta_{\pm}(x_i) = V(x_{i\pm 1}) - V(x_i)$. Since ΔV is the only energy scale of the system, we define the dimensionless energy steps $\delta_{\pm}^i = \Delta_{\pm}(x_i)/\Delta V$ and the dimensionless temperature $T = T_{RW}/\Delta V$. Written in dimensionless parameters, the jump probabilities are thus $p_{\pm}^i = p_{\pm}(x_i) = \min [1, \exp(-\delta_{\pm}^i/T)]$, so that a particle always jumps downhill ($\delta_{\pm}^i \leq 0$), but jumps uphill only with a probability $e_0 = \exp(-1/T)$ (for $\delta_{\pm}^i > 0$), at finite temperature. The limits $T \rightarrow 0$ and $T \rightarrow \infty$ correspond thus to immobile particles or to a homogeneous RW, respectively. The discrete master equation for the probability density $n^i(t)$, to find a particle at time t at site i of the

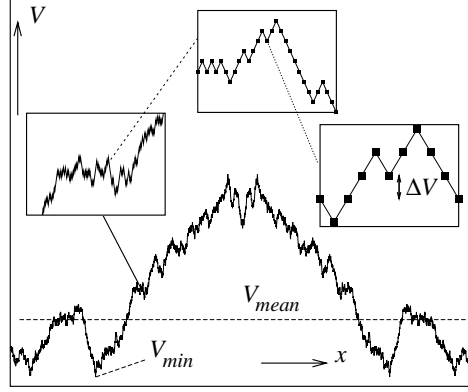


Figure 2: Schematic plot of a typical energy landscape as used for the simulations. The insets show different zoom levels, in order to get an idea of the local situation. For an explanation of the symbols, see the text.

EL, is

$$n^i(t + \Delta t) - n^i(t) = - [p_+^i + p_-^i] n^i(t) + p_-^{i+1} n^{i+1}(t) + p_+^{i-1} n^{i-1}(t) \quad (3)$$

and is (straightforwardly) simulated with $R = 200$ random walkers in an energy landscape with $L = 5000$ sites, if not explicitly mentioned. The time interval Δt corresponds to one Monte-Carlo step but *not* to one shear-cycle n . For the sake of simplicity, we measure x in units of the distance between neighboring sites $\Delta x = x_{i+1} - x_i = 1$, and time in units of Δt . The diffusion constant of a homogeneous random walk ($p_{\pm} = 1/2$ or $T \rightarrow \infty$) is thus $D = \Delta x^2 / \Delta t = 1$. For a constant occupation probability (initial density $n_c = n^i(t = 0) = R/L = \text{const.}$), one can extract the diffusion constant D_c as function of the temperature, since $p_{\pm} = 1/2$ and $p_{\pm} = e_0/2$ occur with equal probability, so that

$$D_c(T) = \frac{1 + e_0}{2} = \frac{1 + \exp(-1/T)}{2}. \quad (4)$$

In Fig. 3, $D_c = R_2(t)/\sqrt{t}$ is plotted against T after different times t , with $R_2(t) = \langle (x(t) - x_0)^2 \rangle$. For large T , the system does not feel the EL and behaves like an ensemble of homogeneous RWs, whereas its behavior becomes subdiffusive after several steps for small T when the EL is explored. In a situation with $T \approx 0$, after a rather short transient, all RW will occupy a local minimum, a valley (\vee), whereas the unstable local configurations hill (\wedge), or left- ($/$) and right-slope (\backslash) cannot be occupied. If T is small enough, the random walkers stay trapped. Note that this statement is strictly true for $T = 0$ or when a fixed number of shear-cycles or taps is implied. In the Sinai diffusion model, for a finite system, the RW will always find

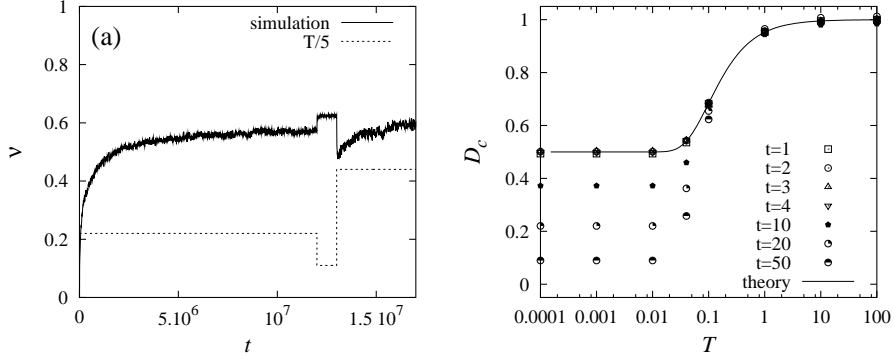


Figure 3: (a) Density plotted against time t (in units of Monte-Carlo steps) for a simulation with $T_0 = 1.1$, $L = 5000$ and $R = 200$. The temperature-sequence is indicated by the dashed line. (b) Diffusion constant $D_c = R_2(t)/\sqrt{t}$ at time t as function of temperature T for systems with constant (initial) density. The solid line shows Eq. (4).

the global minimum – the temperature only determines the time-scale of this process [4]. Since the duration of an experiment is limited, the global minimum cannot be found by all particles if the phase space volume L is large enough.

4 Results and Discussion

In parallel to the tapping experiments by Nowak et al. [18], we present simulations of our model using a periodic time series for the temperature. The temperature is kept constant for S steps and then increased by $\Delta T = 0.1$, where it is kept again constant for S steps. T is initially zero and then raised up to $T = 2$. From this state, T is decreased to zero and the loop is repeated seven times. In Fig. 4, the simulation results are displayed for different S as given in the inset. In the initial branch with increasing T , the density increases and slowly decreases for large T . This branch is irreversible, but the periodic loops show almost reversible behavior. For very short loops (small S), the density continuously increases, for longer loops the behavior of the system is reversible. Note that the system also shows hysteretic behavior, the density at decreasing T is below the density at increasing T .

In summary, we presented a very simple model for the dynamics of the compaction of granular media due to an external agitation. Our model is not as detailed as others (parking lot or frustrated lattice-gas models), but it is extremely simple and still shows qualitative agreement with two different types of experiment. Its simplicity allows for future analytical treatments. However, such a simple model arises, besides

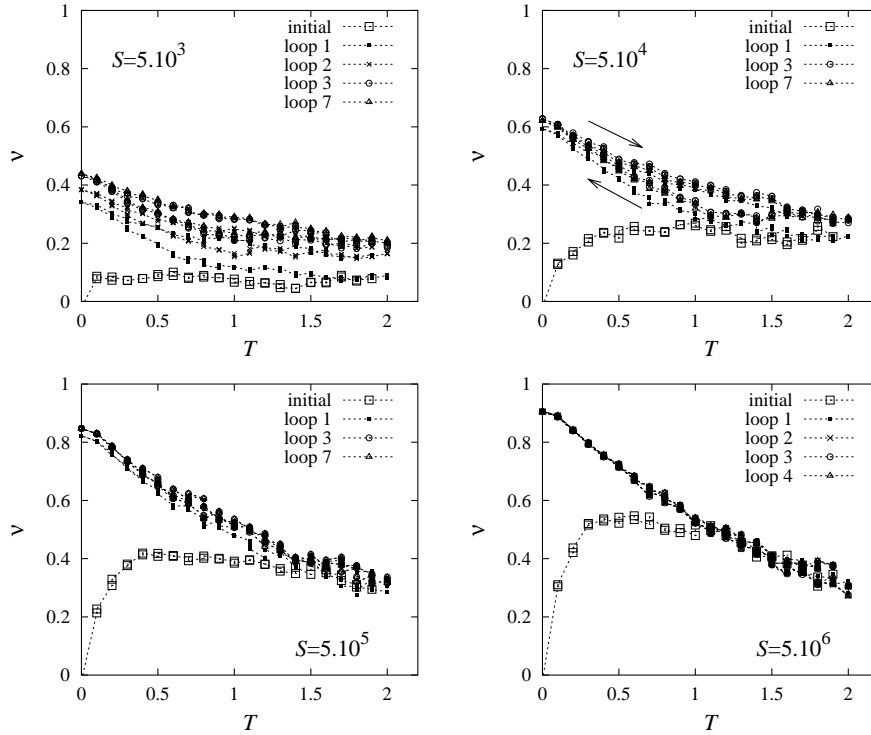


Figure 4: Rescaled density ν plotted as a function of the temperature T for a periodic temperature sequence. The arrows indicate the direction of the loops.

many others, two major questions: (i) Is it possible to link the real configuration phase space with the an energy landscape? (ii) Is it correct to do the analogy between the experimental external excitations like shear or tapping with a temperature?

Acknowledgements

S. L. acknowledges the support of the I.U.S.T.I., Marseille and thanks for the hospitality. Furthermore, helpful discussions with A. Blumen and I. Sokolov are appreciated.

References

- [1] I. Aydin, B. J. Briscoe, and N. Ozkan. Modeling of powder compaction: A review. *MRS Bulletin*, 22(12):1, 1997.

- [2] J. E. Ayer and F. E. Soppet. Vibratory compaction II: Compaction of angular shapes. *J. Am. Ceramic Soc.*, 49:207, 1966.
- [3] E. Ben-Naim, J. B. Knight, and E. R. Nowak. Slow relaxation in granular compaction. *J. Chem. Phys.*, 100:6778, 1996.
- [4] J.-P. Bouchaud and A. Georges. Anomalous diffusion in disordered media: Statistical mechanisms, models and physical applications. *Phys. Repts.*, 195:127–293, 1990. p. 194.
- [5] E. Caglioti, V. Loreto, H. J. Herrmann, and M. Nicodemi. A “Tetris-like” model for the compaction of dry granular media. *Phys. Rev. Lett.*, 79(8):1575–1578, 1997.
- [6] K. G. Ewsuk. Compaction science and technology. *MRS Bulletin*, 22(12):14–16, 1997.
- [7] D. S. Fisher, P. Le Doussal, and C. Monthus. Random walks, reaction-diffusion, and nonequilibrium dynamics of spin chains in one-dimensional random environments. *Phys. Rev. Lett.*, 80:3539, 1998.
- [8] D. A. Head and G. J. Rodgers. A coarse grained model for granular compaction and relaxation. *J. Phys. A*, 31(1):107, 1998.
- [9] J. B. Knight, C. G. Fandrich, C. N. Lau, H. M. Jaeger, and S. R. Nagel. Density relaxation in a vibrated granular material. *Phys. Rev. E*, 51(5):3957–3962, 1995.
- [10] G. Köhler and A. Blumen. Random walks on ultrametric spaces: Mean and variance of the range. *J. Phys. A*, 24:2807, 1991.
- [11] A. J. Kolan, E. R. Nowak, and A. V. Tkachenko. Glassy behavior of the parking lot model. *Phys. Rev. E*, 59:3094, 1999.
- [12] H. Kuno and J. Okada. The compaction process and deformability of granules. *Powder Technol.*, 33:73–79, 1982.
- [13] L. Laloux and P. Le Doussal. Aging and diffusion in low dimensional environments. *Phys. Rev. E*, 57:6296, 1998.
- [14] S. J. Linz and A. Dohle. Minimal relaxation law for compaction of tapped granular matter. *Phys. Rev. E*, 60(5):5737, 1999.
- [15] M. Nicodemi, A. Coniglio, and H. J. Herrmann. A model for the compaction of granular media. *Physica A*, 225:1–6, 1995.
- [16] M. Nicolas and O. Pouliquen. Compaction d’un empilement sous cisaillement périodique. In *14eme congres francais de mecanique*, Toulouse, Septembre, 1999. and in preparation 2000.
- [17] E. R. Nowak, J. B. Knight, E. Ben-Naim, H. M. Jaeger, and S. R. Nagel. Density fluctuations in vibrated granular materials. *Phys. Rev. E*, 57(2):1971–1982, 1998.
- [18] E. R. Nowak, M. Povinelli, H. M. Jaeger, S. R. Nagel, J. B. Knight, and E. Ben-Naim. Studies of granular compaction. In *Powders & Grains 97*, pages 377–380, Rotterdam, 1997. Balkema.
- [19] G. Peng and T. Ohta. Logarithmic density relaxation in compaction of granular materials. *Phys. Rev. E*, 57:829, 1997.
- [20] M. Piccioni, M. Nicodemi, and S. Galam. Logarithmic relaxations in a random-field lattice gas subject to gravity. *Phys. Rev. E*, 59:3858, 1999.
- [21] S. Rajasekar and K. P. N. Murthy. Dynamical evolution of escape probability in the presence of Sinai disorder. *Phys. Rev. E*, 57:1315, 1998.
- [22] H. Schiessel, I. Sokolov, and A. Blumen. Dynamics of a polyampholyte hooked around an obstacle. *Phys. Rev. E*, 57:2390, 1997.

B.6 Compaction of a packing of hard spheres under horizontal shear

M. NICOLAS, P. DURU & O. POULIQUEN

Proceedings of the Powder and Grains Conference, Sendai, Japon, 2001.

Compaction of a packing of hard spheres under horizontal shear

M. Nicolas, P. Duru & O. Pouliquen

IUSTI, Technopole de Chateau-Gombert, 5 rue Fermi 13453 MARSEILLE cedex 13 France

ABSTRACT: We present experimental results concerning the compaction of a granular assembly of glass spheres under periodic shear deformation. Results for a monodisperse set of spheres and a bidisperse set of spheres are presented

1 INTRODUCTION

It is well known that an assembly of identical rigid spheres poured in a box without caution arrange in a random packing with a volume fraction higher than 55 percent. The volume fraction of such a packing can be increased up to 63.66% (according to Scott 1969) with tapping or shaking of the box. This limiting value is known as the maximum volume fraction of a random packing. Denser packings are obtained only if spheres arrange in an ordered structure. The maximum volume fraction is then 74.05%, corresponding to the face-centered cubic packing.

The evolution of a random loose packing to a random close packing has been experimentally studied by Knight *et al* (1995) and Nowak *et al* (1998). In this experiment the packing of hard spheres was submitted to a vertical vibration made of constant amplitude taps. Another compaction experiment (Pouliquen *et al* 1997) suggested that a horizontal shear could be responsible for the compaction of an assembly of hard spheres. In that case, the compaction leads to crystalline arrangements of particles.

After a description of the experimental setup, we present results about the compaction of a monodisperse set of spheres (section 3). Section 4 presents the results for compaction of a two-sizes set of beads.

2 EXPERIMENTAL SETUP

Particles were spherical glass beads of 2 or 3 mm diameters. In order to prevent attrition effects between particles, beads were coated with viscous silicon oil. This coating did not affect the results for compaction but improved the lifetime of the glass beads.

The shear apparatus is drawn in figure 1. The shear cell was parallelepiped, and the volume occupied by the beads was 10.5 cm high, 7.9 cm wide and 10.2 cm deep. The bottom of the cell was a flat plate attached to a horizontal linear displacement device driven by a stepper motor. The two mobile lateral walls were aluminum plates linked with two hinges to the bottom plate. These plates were covered with a thin plastic sheet to insulate the packing from metallic dust due to particle/wall friction. The front and back sides were glass plates fixed on the bottom plate. The granular packing was confined on the top by a rectangular plate mounted on a vertical rail.

The volume fraction of the packing was measured by recording the vertical position of the top plate with a linear position sensor. The accuracy of the sensor corresponded of a 2×10^{-4} resolution in volume fraction.

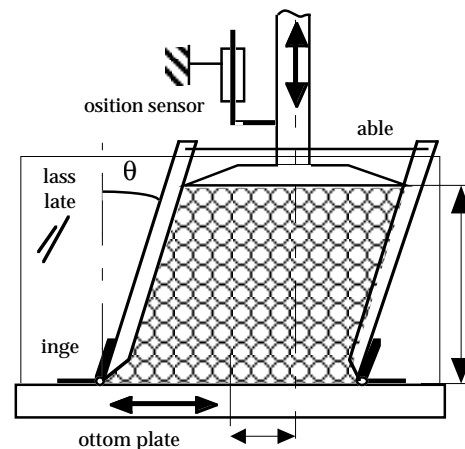


Figure 1. Sketch of the experimental setup.

Before each experiment, the shear cell was filled with the lateral walls kept vertical. Beads were poured down through a hopper designed to ensure a homogeneous filling of the box section. The mean initial volume fraction obtained with this procedure was $60 \pm 1\%$. The periodic shear was then imposed. First, the lateral plates were inclined to an angle $+\theta$, then to an angle $-\theta$, and finally were put back in the vertical position. The volume fraction after such a cycle was recorded. The volume fraction could also be continuously recorded with 325 measurements during a cycle.

3 COMPACTION OF MONODISPERSE PACKINGS

3.1 Dilatancy properties

A typical measurement of the volume fraction of the packing is shown in figure 2. This plot shows a superposition of two dynamics: a slow and monotonous increase of volume fraction ϕ and an oscillation corresponding to the dilatation of the packing during the shear cycle.

The oscillation amplitude $\delta\phi$ due to dilatation was observed to increase during the experiment. Figure 3 shows this amplitude plotted versus the average volume fraction (averaged over a cycle). Except for low volume fraction, a linear relation could be found between the dilatation amplitude and the volume fraction.

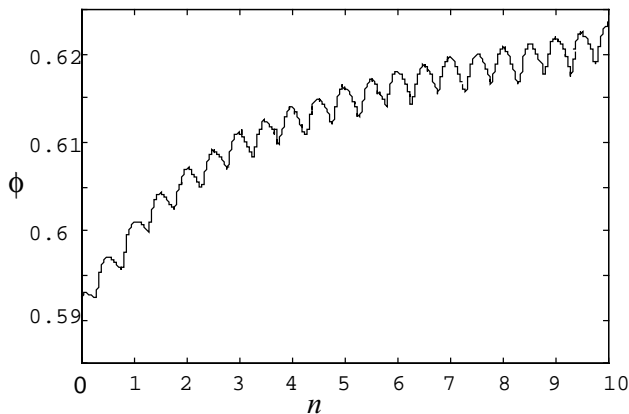


Figure 2. Volume fraction evolution from a random packing with a shear angle $\theta = 5.4^\circ$. n is the elapsed number of cycle from the beginning of the experiment.

1.2 Long-time evolution of volume fraction

The compaction by horizontal shear was observed to be a slow process. Figure 4 shows the volume fraction ϕ versus time for three different shear angles in semi-logarithmic scale. The volume fraction was still increasing even after a large number of cy-

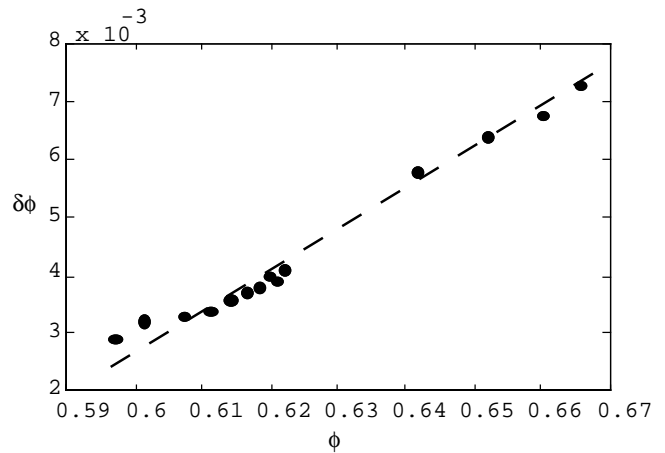


Figure 3. Amplitude of dilatation $\delta\phi$ versus volume fraction ϕ .

cles, 60 000 in that case (typically a one week experiment with our setup).

The long-time volume fraction was well above the random-close packing value. We obtained a maximum volume fraction of 69.3% to be compared to 63.66% for a random-close packing. This means that crystalline arrangements are created during the compaction. The crystal structure was observed at the wall of the shear apparatus, but we also checked that crystalline structures were present in the bulk of the packing by carefully removing the beads layer after layer at the end of an experiment. An example of crystalline structure is shown in figure 5, a photograph taken in the midst of the packing.

The time evolution $\phi(t)$ could not be fitted with an inverse logarithmic function as in Knight *et al* (1995) and the presence of ordered structure in our experiments may explain this difference.

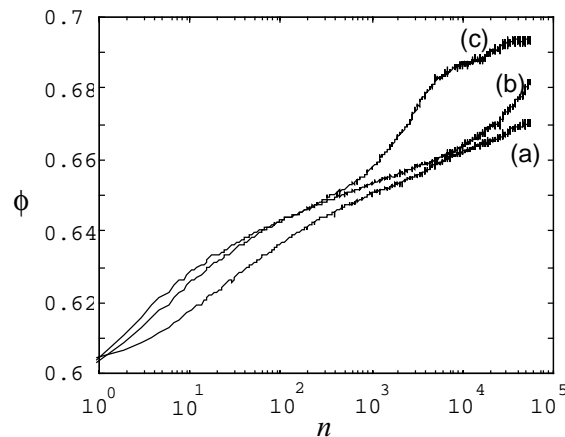


Figure 4. Long-time evolution for different shear angles : $\theta = 2.7^\circ$ (a), $\theta = 5.4^\circ$ (b), $\theta = 10.7^\circ$ (c).

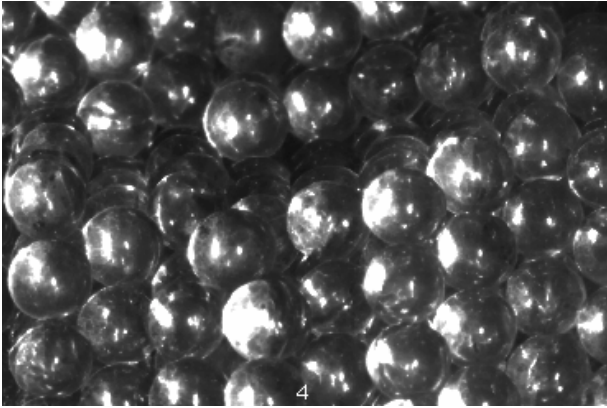


Figure 5. Photograph of the packing in the bulk for 3 mm beads. Crystalline planes appear clearly, and are not connected with the boundary planes of the shear cell. Local arrangements of particles are face-centered cubic.

The response of the packing to a change of shear amplitude was also investigated. Increasing the shear angle produced a sudden decrease of the volume fraction whereas a decrease of shear angle produced a sudden increase of ϕ . A linear relation between the angle change $\Delta\theta$ and the volume fraction jump $\Delta\phi$ was found (Nicolas *et al* 2000) : $\Delta\phi = -\alpha \Delta\theta$ with $\alpha = 1.45 \times 10^{-3}$ and $\Delta\theta$ in degrees.

Two kind of evolution have been observed: a slow and continuous compaction when the shear angle is constant and a rapid response when a change of angle is imposed. Moreover, the variation of the volume fraction $\Delta\phi$ induced by a sudden change $\Delta\theta$ of angle is independent of the state ϕ of the system. The rapid dynamic induced by an angle variation seems thus to be uncorrelated with the slow compaction dynamic.

2 COMPACTION OF BIDISPERSE PACKINGS

For these experiments, the granular matter was a mixture of 50% 2 mm diameter beads and 50% 3 mm diameter beads. The experimental procedure was the same as in the monodisperse experiments.

As in the monodisperse case, a rapid increase of volume fraction occurred for the first 100 cycles (see figure 6). But for the same shear angle, the maximum volume fraction (65.5%) is much lower in the bidisperse case. This lower volume fraction is easily explained by the fact that no order appeared during the shear process.

Compaction curves (M) and (B) are quite similar for the 1000 first cycles. After that time, the bidisperse curve does not evolve much, whereas the monodisperse curve increases up to 69%. It seems that the initial compaction ($n < 1000$) deals only with local re-arrangements of beads without creation of ordered structures. For later times, it seems that long-range arrangements of beads appear in the monodisperse case, and hence further compaction is

possible. These long-range structures do not appear in the bidisperse case, and the packing is thus stuck into a random-close packing state.

Despite this difference with the monodisperse case, the bidisperse packing submitted to a sudden change of shear angle exhibited also a rapid compaction dynamic with a linear relation between $\Delta\phi$ and $\Delta\theta$.

3 CONCLUSIONS

We have shown that horizontal shear is responsible for compaction of a granular matter constituted of hard spheres. In the case of monodisperse beads, the highest volume fraction was 69.3%, and corresponded to a crystalline arrangement of the beads. No higher value could be obtained because of numerous defects (grain boundary, dislocations) present in the bulk. In the case of a bidisperse medium (mixture of 2 and 3 mm beads), no crystalline structure was observed, but compaction occurred with a volume fraction up to 65.5%.

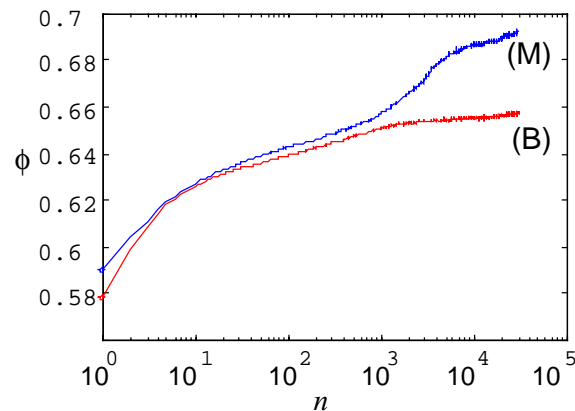


Figure 6. Volume fraction evolution for a monodisperse set of beads (M) and a bidisperse set of beads (B). Shear angle was $\theta = 10.2^\circ$.

REFERENCES

- Knight, J.B., Fandrich, C.G., Lau, C.N., Jaeger, H.M. & Nagel, S.R. 1995. Density relaxation in a vibrated granular material. *Phys. Rev. E* 51 (5):3957-3963.
- Nicolas, M., Duru, P. & Pouliquen, O. 2000. Compaction of a granular material under cyclic shear. *Eur. Phys. J. E* 3:309-314
- Nowak, E.R., Knight, J.B., Ben-Naim, E., Jaeger, H.M. & Nagel, S.R. 1998. Density fluctuations in vibrated granular materials. *Phys. Rev. E* 57 (2):1971-1982.
- Pouliquen, O., Nicolas, M. & Weidman, P.D. 1997. Crystallization of non-Brownian spheres under horizontal shaking. *Phys. Rev. Lett.* 79:3640-3643.
- Scott, G.D. & Kilgour, D.M. 1969. The density of random close packing of spheres. *Brit. J. Appl. Phys* 2:863-866.

B.7 Constitutive laws of liquid-fluidized beds

P. DURU, M. NICOLAS, E.J. HINCH & É. GUAZZELLI

J. Fluid Mech. **452**, 371–404 (2002)

Constitutive laws in liquid-fluidized beds

By PAUL DURU¹, MAXIME NICOLAS¹, JOHN HINCH²
AND ÉLISABETH GUAZZELLI¹

¹IUSTI, CNRS-UMR 6595, Technopôle Château-Gombert, 13453 Marseille cedex 13, France

²DAMTP, University of Cambridge, Silver Street, Cambridge CB3 9EW, UK

(Received 6 May 2001 and in revised form 10 September 2001)

The objective of the present work is to test experimentally the two-phase modelling approach which is widely used in fluidization. A difficulty of this way of modelling fluidized beds is the use of empirical relations in order to close the system of equations describing the fluidized bed as a two-phase continuum, especially concerning the description of the solid phase. We performed an experimental investigation of the primary wavy instability of liquid-fluidized beds. Experiments demonstrate that the wave amplitude saturates up the bed and we were able to measure the precise shape of this voidage wave. We then related this shape to the unknown solid phase viscosity and pressure functions of a simple two-phase model with a Newtonian stress-tensor for the solid phase. We found the scaling laws and the particle concentration dependence for these two quantities. It appears that this simplest model is quite satisfactory to describe the one-dimensional voidage waves in the limited range of parameters that we have studied. In our experimental conditions, the drag on the particles nearly balances their weight corrected for buoyancy, the small imbalance being mostly accounted for by solid phase viscous stress with a much smaller contribution from the solid phase pressure.

1. Introduction

Fluidized beds are widely used in many industrial fields and display a wide range of intriguing phenomena. To fluidize a bed of particles, a fluid is pumped upwards at the bottom of the bed through a porous plate. At low flow rates (below minimum fluidization), the bed is packed. As the flow is increased, the drag force on the particles increases until it is sufficient to balance their weight corrected for buoyancy. The particles then become free to move and the bed is said to be fluidized, and, indeed, the bed can be stirred and poured as if it were a fluid. Uniform and homogeneous fluidized beds are rarely realized in practice. Fluidized beds usually present a variety of complex flow regimes above minimum fluidization. On one hand, gas-fluidized beds are very unstable and rapidly attain a bubbling regime, see Davidson & Harrison (1971). On the other hand, liquid-fluidized beds exhibit a voidage-wave instability. The instability was shown to remain one-dimensional in narrow beds (Anderson & Jackson 1969; Ham *et al.* 1990; Nicolas *et al.* 1996) whereas in wider beds, transverse structures can develop (El-Kaissy & Homsy 1976; Didwania & Homsy 1981). Batchelor (1991) conjectured that bubbles evolve from this secondary instability.

The theoretical description of fluidized systems is an important challenge for physicists and engineers. Noting that the velocity of the particles is on average quite different from the velocity of the fluid, we rapidly conclude that a minimal description of a fluidized bed must be as two coexisting continua, a fluid phase

and a solid phase. Such a two-phase continuum description has been proposed by many before, for a review see Jackson (2001). Attempts have been made to derive two-phase governing equations by averaging separately the equations of motion for the fluid and the particles, for instance Anderson & Jackson (1967). These averaging procedures generate averaged quantities more numerous than the available equations and consequently there is a problem of closure, in particular for the drag force between the phases, for added mass effects, and for the stresses in the two phases. Under practical conditions, where the Reynolds number for the flow past the particle is 10 or more, we know theoretically that the stress at a point must depend on the strain rate at nearby points at previous times, and so a simple expression for the closures cannot exist; exactly the same conceptual problem occurs in turbulence where the eddy-viscosity theoretically cannot exist.

Thus, at best, we are searching for empirical expressions for the closures which are satisfactory within the narrow range of operating conditions of interest. For the drag force between the two phases we use the Richardson–Zaki law, which gives a drag proportional to the difference between the instantaneous values of the velocities of the two phases. The coefficient of proportionality depends on the concentration of the particles. The Richardson–Zaki law has been found over the years to work well. When the particles accelerate relative to the fluid, the fluid exerts a force on the particles proportional to the relative acceleration with a coefficient called the added mass. This added mass has not been studied in concentrated beds. Fortunately, it plays a minor role. We therefore will eventually adopt the value for an isolated sphere equal to half the displaced mass of fluid. The biggest closure problem comes with expressions for the stresses in the fluid and solid phases. We assume like many before that both phases behave as Newtonian viscous fluids. It is clear that the bed as a whole does have a fluid-like behaviour, but it is certainly not clear that both the fluid and solid phases are purely viscous; perhaps the solid phase should have an elastic part. The linearity of the Newtonian stresses in the strain rate is also an assumption whose only justification is that it is the simplest possible alternative.

We note that there are more complicated models introducing a granular temperature and thus a new equation for the ‘thermal’ energy conservation, for a review see Jackson (2001). It results in a great complexity when trying to derive exact closure relations linking unknown terms to the temperature and to the particle concentration and we think that it is very unlikely that this kind of model could be tested experimentally.

Despite the wide use of models using empirical closure relations, there is a lack of knowledge about the viscosity and the pressure appearing in the Newtonian stress tensor of the solid phase. Several speculative expressions have been proposed since Murray (1965) for the solid viscosity μ_s and the solid pressure p_s , some of them being presented in table 1. Most of these authors chose monotonic functions of the particle volume fraction ϕ which diverge when the particle volume fraction reaches the random close packing volume fraction ϕ_{cp} .

Rough estimates for the unknown solid viscosity and pressure were obtained by studying the voidage-wave instability occurring in narrow liquid-fluidized beds (Anderson & Jackson 1969; El-Kaissy & Homsy 1976). The voidage disturbances were found to grow exponentially up the bed and eventually to saturate at their finite amplitude. By measuring their propagation properties and the general growth and comparing with linear stability theory, these authors were able to estimate parameters appearing in the assumed constitutive equations. However, these measurements did not give any insight on the shape of the functions $\mu_s(\phi)$ and $p_s(\phi)$ as they only provided values for a few particle concentrations ϕ .

Authors	$p_s(\phi)$	$\mu_s(\phi)$
Murray (1965)	0	$\mu_f \frac{M\phi}{\phi_{cp} - \phi}$
Fanucci <i>et al.</i> (1981)	Not given	$M \exp \left[\frac{\phi_{cp} - \phi}{(1 - \phi_{cp})(1 - \phi)} \right]$
Needham & Merkin (1983)	$P\phi$	Constant
Harris & Crighton (1994)	$P\phi/(\phi_{cp} - \phi)$	Constant
Anderson <i>et al.</i> (1995)	$P\phi^3 \exp \left(\frac{r\phi}{\phi_{cp} - \phi} \right)$	$\frac{M\phi}{1 - (\phi/\phi_{cp})^{1/3}}$
Glasser <i>et al.</i> (1996)	$\left\{ \begin{array}{l} C_1 \phi^3 \exp \left(\frac{r\phi}{\phi_{cp} - \phi} \right) \\ C_2 \phi \\ C_2 \frac{\phi}{(\phi_{cp} - \phi)^2} \end{array} \right.$	$\frac{M\phi}{1 - (\phi/\phi_{cp})^{1/3}}$

TABLE 1. Various expressions for p_s and μ_s proposed in the literature.

The two-phase model has also been tested as a whole, by simulating the fully nonlinear two-phase equations with different closure relations for the solid viscosity and the solid pressure (Anderson *et al.* 1995; Glasser, Kevrekidis & Sundaresan 1996, 1997). Glasser *et al.* (1997) have notably shown that two-dimensional bubble-like solutions were stationary solutions of the two-phase equations in both liquid and gas cases. However, these structures could be reached only in this latter case, either by a two-dimensional destabilization of the uniform bed or by a two-dimensional destabilization of the fully developed one-dimensional plane wave, these mechanisms failing to produce bubbles in the liquid-fluidized case. The two-phase equations, along with these *ad hoc* closure relations seem to succeed in reproducing some important experimental facts. It should be noticed that the added mass term was omitted in their numerical simulations, even in the liquid-fluidized bed case.

The approach we adopt in this paper is different. We study experimentally the voidage-wave instability and show that the voidage disturbance, after its initial growth, reaches a nonlinearly saturated shape which we are able to measure with accuracy. We then relate this saturated shape to the unknown parameters of the two-phase model and are thus able to recover the viscosity and the pressure of the solid phase. Hence, we find the form and the scaling laws for the viscosity and the pressure. Our experiments can thus be viewed as a restricted test of the two-phase model of a fluidized bed.

This paper is organized as follows. First, we present the measurements of the accurate shape of the voidage wave propagating in a narrow liquid-fluidized bed. This is an important result since this wave shape has never been measured experimentally before, but was rather obtained by numerical simulations. Our experimental set-up is presented in §2. It depends on the fact that such an instability is known to be convective (Nicolas *et al.* 1994, 1996). The influence of the experimental parameters on the nonlinearly saturated wave is presented in §3. Then, in §4, we show how to relate the saturated wave-shape to the unknown solid viscosity and solid pressure functions appearing in the two-phase equations. The results concerning the solid

Set	d_s (μm)	ρ_s (g cm^{-3})
<i>A</i>	1220 ± 60	4.08 ± 0.01
<i>B</i>	928 ± 100	4.08 ± 0.01
<i>C</i>	685 ± 30	4.08 ± 0.01
<i>D</i>	1200 ± 90	2.48 ± 0.01
<i>E</i>	771 ± 40	2.55 ± 0.01

TABLE 2. Particle characteristics.

Fluid	<i>A</i> (% of glycerol)	μ_f (cP)	ρ_f (g cm^{-3})
<i>a</i>	0	0.9 ± 0.02	0.997 ± 0.002
<i>b</i>	35	3 ± 0.2	1.1 ± 0.03

TABLE 3. Fluid characteristics.

viscosity μ_s are presented in §5 and those concerning the solid pressure p_s in §6. Section 7 contains our discussion of the results.

2. Experimental techniques

2.1. Particles and fluids

Experiments were performed with different sets of glass beads having different densities ρ_s and diameters d_s . Characteristics of the particles are presented in table 2. Sets *A*, *B* and *C* were supplied by Cataphote (Jackson, MS, USA), set *E* by J.-C. Borgotti of Laboratoire Central des Ponts et Chaussées (Paris, France), and set *D* by Matrasur (Palaiseau, France). The beads were supplied presieved and were further carefully resieved between two close meshes. The bead diameter distribution was obtained from measurements of 300 beads with a charged coupled device camera and a digital imaging system composed of an acquisition board and of the public domain image processing NIH Image†. The distributions were all found to be approximately Gaussian with mean diameter d_s . The standard deviation was taken as the experimental error in the diameter. The particle density ρ_s was determined by measuring the volume variation when a known mass of particles was introduced into a known volume of water in a graduated vessel.

In order to examine the influence of the viscosity of the fluid, we used two fluids: pure water and a mixture of glycerine and water. The temperature of the fluids was maintained at $27 \pm 1^\circ\text{C}$ by using a thermostatically controlled bath as a fluid reservoir in the fluid circulating loop of the fluidized bed (see §2.2). Characteristics of the two fluids are displayed in table 3.

2.2. Apparatus

The fluidized bed apparatus, which is sketched in figure 1, was derived from that of Nicolas *et al.* (1996), itself derived from that of Ham *et al.* (1990). The fluidized bed was a straight and vertical cylindrical glass tube of height 1.8 m mounted on a rigid support structure. Different tubes having different inner diameters D were used in the experiments, as indicated in table 4. The bed to particle diameter ratio,

† Public domain NIH Image program, developed at the US National Institute of Health and available from the Internet by anonymous ftp from [zipper.nimh.nih.gov](ftp://zipper.nimh.nih.gov).

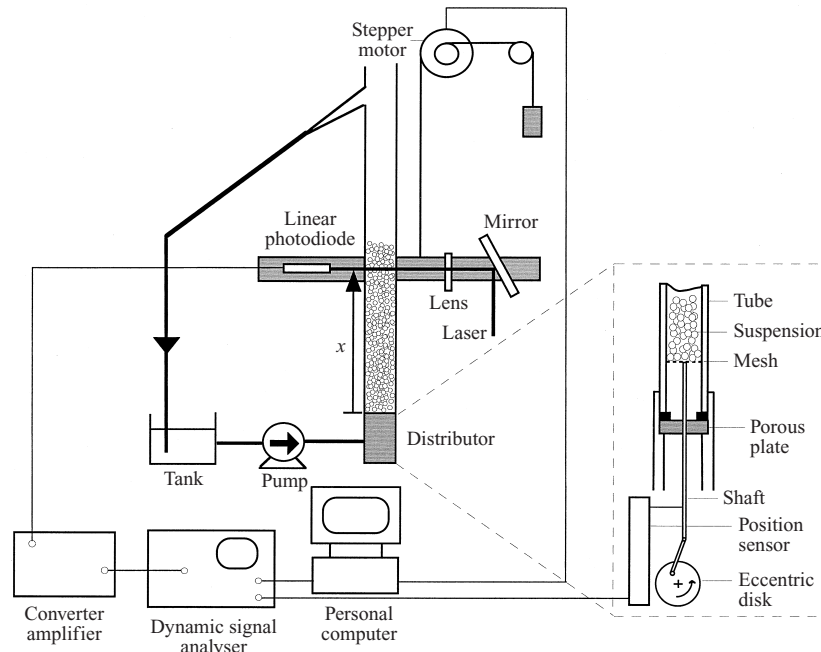


FIGURE 1. Sketch of the fluidized bed apparatus.

Tube	D (cm)
1	3.0 ± 0.02
2	1.5 ± 0.02
3	0.7 ± 0.02

TABLE 4. Tube characteristics.

D/d_s , was chosen to be smaller than 25 in order to ensure that the instability remains one-dimensional and larger than 10 in order to avoid the particle arching effect within the tube (see §3.1). This ratio falls into the ratio range used in the previous experiments of Ham *et al.* (1990) for which wall effects were considered negligible while maintaining a good resolution of the light attenuation technique (see §2.3). The different tubes were inspected to ensure that their cross-sections were round and constant along their lengths.

Fluid was circulated through the bed by a piston metering pump (Fluid Metering Inc. model QD, 1425 r.p.m), used to produce flow rates up to $7 \text{ dm}^3 \text{ min}^{-1}$. Soft tubing was placed upstream of the bed in order to isolate the bed from pump vibrations. Soft tubing also connected the overflow at the top of the bed and carried it to the reservoir. It provided an easy way of diverting the entire overflow into a beaker for gravimetric flow measurements.

The suspension was held by a piston composed of a mesh with holes smaller than the size of the beads. This piston could be either kept immobile or moved with a sinusoidal motion at a given frequency by an eccentric disk driven by a d.c. motor (see the blow-up in figure 1). The uniform distribution of the flow was provided by

Frequency	Relative power	Relative amplitude
f_0	1	1
$2f_0$	0.025	0.153
$3f_0$	0.018	0.136
$4f_0$	0.002	0.048

TABLE 5. Power spectrum of the displacement signal of the piston. The frequency f_0 is the forcing frequency.

a fixed porous plate located before the piston. The pores in the porous plate were small enough to ensure a large pressure drop. This piston-type distributor was used to study the response of the fluidized bed to a local harmonic forcing. When the piston moved upwards, it created a local compression of the fluidized particles, and when it moved downwards, it created a local deficit of particles. This local perturbation was then convected by the flow and spatially amplified along the fluidized bed (if the mode was unstable), see Nicolas *et al.* (1996). Since the piston was in fact a thin mesh, it did not induce significant variation of the flow rate.

The amplitude of the displacement of the piston had to be carefully selected. It had to be larger than the amplitude of the ‘natural’ noise which was always present at the distributor. On the other hand, if the amplitude (or the mean particle concentration) was too large, the motion of the piston created contacts between particles and therefore local close packing just above the piston, in particular for small bed to particle diameter ratio D/d_s . In the latter case, the beads may stay jammed in the tube owing to arching effects, which stops the propagation of the perturbation. Typically, in the present experiments, the amplitude of the piston was chosen to be $\approx 1.5d_s$. The motion of the piston was measured with the use of a linear displacement gauge (Novotechnic model T25) and an electronic circuit provided a reference phase signal used to trigger the concentration measurements (see §2.4). It should be mentioned that, because of the flexibility of the shaft holding the piston and the small size of the eccentric gear, the motion of the piston was not perfectly sinusoidal but presented few harmonics, as indicated in table 5.

2.3. Particle volume fraction measurements

The mean particle volume fraction, ϕ_0 , was estimated by measuring the fluidized bed mean height, h_0 . In a steady state regime of fluidization, the front between the fluidized particles and the clear fluid at the top of the bed was observed to exhibit fluctuations (due to the wave instability) around a fixed mean height. This mean height of the suspension, h_0 , was measured with a viewfinder mounted on a horizontal optical rail which could slide along the bed on two vertical rails. The position of the optical rail and therefore of the view-finder was determined with the use of a ruler attached along the bed with an accuracy of 0.5 mm. The mean volume fraction was then given by $\phi_0 = 4M_s/(\pi D^2 \rho_s h_0)$ where M_s is the weight of the particles. The mean particle volume fraction, ϕ_0 , was measured before and after any instability wave measurement. The relative error in ϕ_0 is $\approx 2\%$.

In order to determine the local particle volume fraction, $\phi(x, t)$, at time t and position x from the mean position of the piston-type distributor, measurements of the attenuation of light through the suspension were performed. The basic principle behind this light attenuation technique is that the amount of light attenuation by particles in a suspension is a function of the particle concentration (see for instance

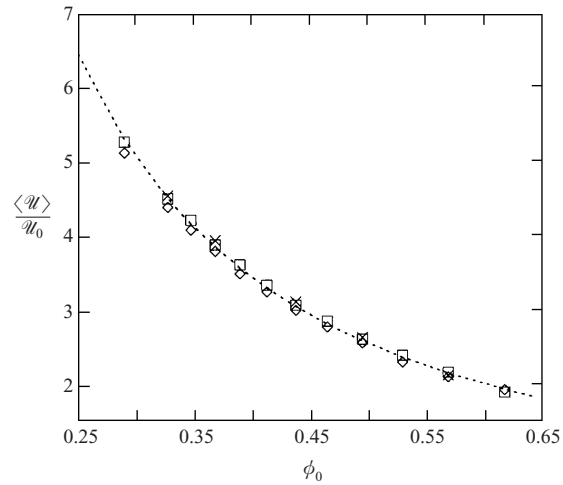


FIGURE 2. Calibration of the averaged signal, $\langle \mathcal{U} \rangle$, with the mean volume fraction, ϕ_0 at \diamond , $x = 5$ cm; \square , 10 cm; \times , 15 cm. The dotted curve corresponds to the best power law correlation, ϕ_0^ξ with $\xi = -1.35$ for combination 6.

Combination	Particles	Fluid	Tube	$\xi(\pm 0.1)$
1	A	a	1	-2.30
2	A	b	1	-2.15
3	D	a	1	-3.35
4	B	a	2	-1.80
5	B	b	2	-1.60
6	C	a	2	-1.35
7	C	a	3	-1.50
8	E	a	2	-1.60

TABLE 6. Value of ξ for all different combinations of particles, fluid and tube used in the present work.

the use of this technique in the case of fluidized beds by Anderson & Jackson 1969 and El-Kaissy & Homsy 1976, and in the case of sedimenting suspensions by Davis & Birdsell 1988). The light source was a 25 mW He-Ne stabilized laser (Spectra Physics 107B). The laser beam was incident at right angles on the bed glass tube and illuminated the tube with a 4 mm diameter round spot using a diverging lens.

A linear photodiode (Hewlett-Packard model 508-4220 PIN) was used to detect the transmitted light through the suspension. The photodiode was aligned opposite the laser beam along the same bed diameter. The lens and the photodiode were mounted on the optical rail which could slide along the bed. The motion of the rail was driven by a stepping motor which itself was monitored by a personal computer. The smallest available displacement corresponding to one step was 0.3 mm. The intensity signal from the photodiode was processed by a converter/amplifier electronic circuit which converted the micro-ampere current signal from the photodiode to a voltage signal, \mathcal{U} , for further processing.

The voltage signal was averaged over 160 s, a time much larger than the wave instability period. The averaged value $\langle \mathcal{U} \rangle$ was measured at a given position x as

a function of the mean particle volume fraction, ϕ_0 . The resulting plot which is presented in figure 2 is a monotonically decreasing function which was used to calibrate the light attenuation through the suspension. The best fit was found in each case to be a power law correlation: $\langle \mathcal{U} \rangle = \mathcal{U}_0 \phi_0^\xi$ with ξ depending on the beads, the fluid, and also the tube, see table 6.

However, owing to a small misalignment of the glass tube (and probably a small variation of the tube thickness), the light transmission through the tube without particles was not observed to be the same at different location along the tube, i.e. \mathcal{U}_0 varied with x . Therefore, $\langle \mathcal{U} \rangle$ was normalized by \mathcal{U}_0 at each position x and $\langle \mathcal{U} \rangle / \mathcal{U}_0$ did not vary along the tube, as shown in figure 2. For each position x , the local volume fraction was then given by

$$\phi(x, t) = \frac{\phi_0}{\langle \mathcal{U}(x, t) \rangle^{1/\xi}} \mathcal{U}(x, t)^{1/\xi}, \quad (2.1)$$

where the brackets note a temporal average over several periods.

2.4. Wave instability measurements

In order to obtain quantitative measurements of the wave instability, the recording of the signal \mathcal{U} over a few wave periods was synchronized with the piston-type distributor. A digital signal analyser (Hewlett–Packard model 3562A) in a triggering mode was used to record the signal \mathcal{U} at a given position x along the bed. In this triggering mode, time recording started when the forcing phase was zero (i.e. when the piston was in its average position and moving upwards). The signal analyser was controlled by the personal computer through an IEEE board. Each time recording was transferred to the personal computer and converted to concentration values using the calibration, see equation (2.1). The resulting concentration signal was then averaged over typically 30 or 100 recordings depending upon the desired accuracy of the measurements (30 for the study of the wave evolution, see §3.2, and 100 for the study of the saturated wave, see §3.3). This synchronized averaging technique provided the waveform of the mode which is correlated with the frequency of the forcing.

2.5. Wave velocity measurements

The wave propagation can also be visualized by backlighting the column with a neon light. A CCD camera captures a one-dimensional image of the tube and the digital imaging system is able to construct spatiotemporal plots from successive one-dimensional images. On such plots, see figure 3, clear lines correspond to low concentration regions of the fluidized bed moving upwards and the measurement of their constant slope gives the wave velocity c .

2.6. Experimental procedure

Once a weighted amount of particles was introduced into the bed, fluid was circulated through the bed at a flow rate sufficient to expand the bed to the top of the tube. The bed was operated in this expanded state for about 20 min to remove any small trapped air bubbles or impurities.

After the start-up procedure, the expansion behaviour of the bed was measured. The flow rate of the bed was lowered in different steps. At each step, the bed was allowed to come to a steady state with a constant height of the bed. The flow rate was then measured gravimetrically and the bed height measured. The flow rate examined ranged between the initial expanded state and a completely packed bed.

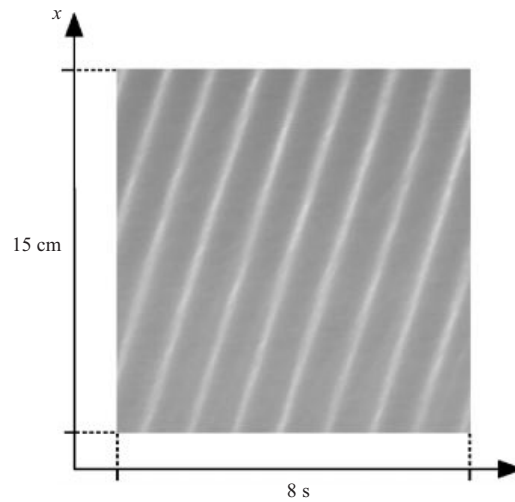


FIGURE 3. Spatiotemporal plot obtained with combination 2 and $\phi_0 = 0.540$. The wave is forced at 1 Hz. Only 15 cm of the bed, shot during 8 s, are shown.

Wave instability measurements were performed at a fixed flow rate (or particle volume fraction) and a given frequency of forcing. The wave mode correlated with the frequency of the forcing was measured along the bed, the use of the personal computer for controlling the signal acquisition and the motion of the optical rail ensuring reproducibility of the measurements.

3. Spatial evolution of the voidage wave instability

3.1. Fluidized bed expansion

As previously noted in the fluidized bed literature, see Didwania & Homsy (1981) and Ham *et al.* (1990) for instance, four different regimes were observed during the expansion of the bed. Typical expansion data showing superficial velocities q versus mean particle volume fractions ϕ_0 are presented in figure 4. The expansion curve can be fitted well by the empirical Richardson–Zaki relation $q = v_t(1 - \phi_0)^n$. The exponent n and terminal velocity v_t were measured by using this fit for the mean volume fraction range corresponding to the waves studied in § 3.3. The expansion characteristics are given in table 7 for all the different combinations of particles, fluid, and tube used in the present work.

Below the minimum fluidization velocity q_{mf} , the bed remained packed at the bottom of the tube, with a mean particle volume fraction ϕ_{mf} . This volume fraction corresponded to a random loose packing of the beads. With a gentle tapping of the tube, a random close packing was obtained, with a mean particle concentration ϕ_{cp} . This maximum value was below the classical value of a random close packing of monodisperse spheres (≈ 0.64) because the suspension is constrained by the small bed to particle size ratio.

For a fluid velocity slightly above q_{mf} , the top of the packing started to move, but the bottom of the suspension stayed still. The liquid then crossed the suspension of packed beads through preferential paths. This regime was called ‘worming’ fluidization, see Ham *et al.* (1990). The value of q_{mf} was taken to be the velocity at which the bed

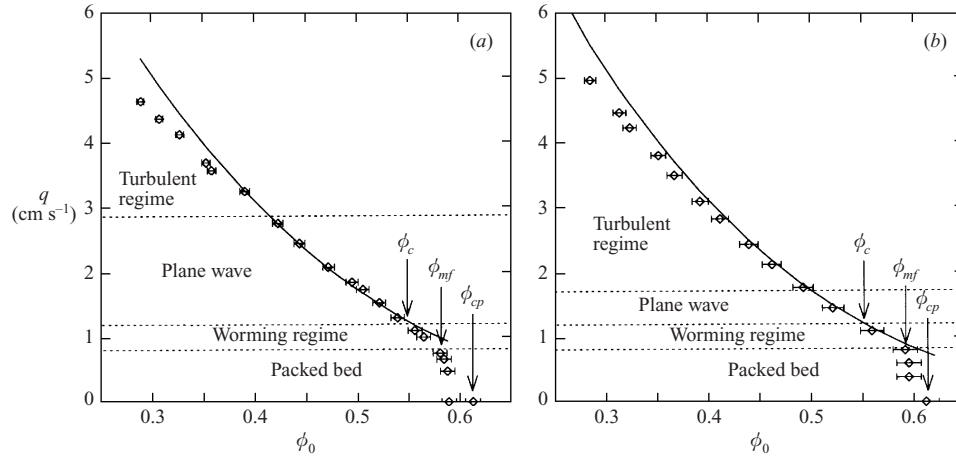


FIGURE 4. Expansion curve of the fluidized bed: (a) combination 7, $D/d_s = 10$; (b) combination 6, $D/d_s = 22$. The solid line corresponds to the Richardson–Zaki law.

Combination	Particles	Fluid	Tube	D/d_s	v_t (cm s ⁻¹)	n	ϕ_{cp}	ϕ_{mf}	ϕ_c
1	A	a	1	25	21.55 ± 0.35	2.43 ± 0.03	0.630	0.608	0.578
2	A	b	1	25	20.4 ± 0.25	3.18 ± 0.02	0.627	0.610	0.560
3	D	a	1	25	14.4 ± 0.20	2.58 ± 0.03	0.630	0.588	0.555
4	B	a	2	16	17.7 ± 0.30	2.84 ± 0.02	0.615	0.590	0.545
5	B	b	2	16	17.4 ± 0.40	3.65 ± 0.10	0.600	0.565	0.520
6	C	a	2	25	16.4 ± 0.40	3.25 ± 0.04	0.612	0.580	0.555
7	C	a	3	10	15.7 ± 0.20	3.18 ± 0.02	0.613	0.589	0.543
8	E	a	2	19	12.0 ± 0.20	3.30 ± 0.02	0.614	0.575	0.544

TABLE 7. Fluidized bed expansion characteristics. The experimental uncertainty on ϕ_{cp} , ϕ_{mf} and ϕ_c is ± 0.005 .

begins to expand and was measured by identifying the break in the expansion curve, see figure 4.

As the flow rate was increased, the whole suspension was fluidized and started to exhibit the primary voidage wave instability where a concentration plane wave propagated upwards along the bed at a flow rate q_c corresponding to a volume fraction ϕ_c . For the type of particles and fluids used in the present experiments, no stable regime of fluidization such as observed by Ham *et al.* (1990) was present.

For an even larger flow rate, the wavy instability no longer existed and the particles exhibited large and random displacements. This regime has been called the turbulent regime.

It should be stressed that instability threshold and range are strongly dependent upon aspect ratio D/d_s . When D/d_s is small (~ 10), as in combination 7 (see figure 4a), confinement effects tend to stabilize the plane wave. In this case, the ϕ_0 -range for which the waves are observed is much larger than in the cases of larger values of D/d_s (for instance for the case $D/d_s \sim 22$ shown in figure 4b). Also, for $D/d_s \sim 10$, if ϕ_0 was too large, the upward motion of the piston created close packing in the bottom of the dense suspension and the beads can become jammed in the tube owing to arching effects, which stops the propagation of the perturbation, as mentioned earlier. The forcing method was no longer efficient and the waves cannot be measured. Therefore,

Combination	ϕ_0	c (cm s ⁻¹)	ϕ_{max}	Amplitude	f_0 (Hz)	$Re(v_i d_s \rho_f / \mu_f)$
1	0.57	7.30 ± 0.15	0.606	0.104	1.4	287
1	0.558	7.95 ± 0.10	0.603	0.127	1.4	287
1	0.55	8.15 ± 0.10	0.598	0.126	1.4	287
2	0.548	5.60 ± 0.10	0.566	0.052	1.03	82
2	0.540	5.95 ± 0.05	0.563	0.061	1.00	82
2	0.538	5.90 ± 0.10	0.564	0.066	1.06	82
2	0.528	6.05 ± 0.20	0.555	0.062	1.07	82
3	0.545	4.96 ± 0.04	0.570	0.07	1.00	192
3	0.540	5.00 ± 0.05	0.564	0.064	1.05	192
3	0.535	5.25 ± 0.07	0.565	0.074	1.10	192
3	0.531	5.30 ± 0.07	0.561	0.074	1.10	192
4	0.527	5.95 ± 0.05	0.555	0.087	1.6	182
4	0.519	6.00 ± 0.05	0.551	0.094	1.8	182
4	0.512	6.15 ± 0.10	0.546	0.11	1.5	182
5	0.504	4.50 ± 0.04	0.522	0.045	1.3	54
5	0.499	4.60 ± 0.10	0.519	0.054	1.2	54
6	0.549	4.70 ± 0.15	0.575	0.082	1.1	125
6	0.549	4.30 ± 0.10	0.576	0.065	1.55	125
6	0.549	3.90 ± 0.10	0.568	0.035	2.2	125
6	0.534	4.70 ± 0.10	0.564	0.083	1.25	125
6	0.534	4.60 ± 0.10	0.565	0.078	1.62	125
6	0.525	4.90 ± 0.10	0.554	0.084	1.40	125
7	0.488	3.7 ± 0.1	0.522	0.082	2.1	120
7	0.496	3.8 ± 0.2	0.528	0.096	1.54	120
8	0.530	3.47 ± 0.03	0.548	0.077	1	103
8	0.521	3.59 ± 0.03	0.549	0.082	1	103
8	0.521	3.60 ± 0.03	0.548	0.077	1	103
8	0.521	3.64 ± 0.03	0.547	0.080	1.1	103
8	0.512	3.75 ± 0.10	0.545	0.087	1	103
8	0.511	3.80 ± 0.05	0.540	0.080	1	103
8	0.507	3.75 ± 0.05	0.541	0.082	1.25	103

TABLE 8. Saturated wave characteristics. The experimental uncertainty on ϕ_{max} and on the wave amplitude is estimated to be ± 0.003 . Within a given combination, the uncertainty on ϕ_0 is ± 0.003 , corresponding to the error on the measure of the height of the bed. When comparing two different combinations, we must also take into account the error on the total mass of beads and the density of the beads which leads to a global uncertainty of ± 0.01 .

in this case, waves were measured further above the instability threshold ϕ_c (see table 8). When D/d_s was larger (typically between 16 and 25, which is the case for all combinations except combination 7), transverse destabilizations of the plane wave occurred in earlier stages as the flow rate was increased. It was nonetheless possible to study the plane waves but the corresponding ϕ_0 -range was quite restricted, see figure 4(b). Plane waves were thus observed and measured in regions closer to the instability threshold ϕ_c .

3.2. Nonlinear evolution of the voidage wave instability

Since the instability is convective in nature as demonstrated by Nicolas *et al.* (1996), any perturbation created at the bottom of the bed ('natural' noise or controlled

perturbation) propagates and evolves along the bed. The behaviour of the fluidized bed was then analysed by investigating the response of the suspension to a localized and controlled perturbation produced by the forcing distributor (see §2.2). The spatial evolution of each forced mode was investigated independently. The synchronized average method described in §2.4 was used to separate the forced mode from the ‘natural’ noise. This ‘natural’ noise is indeed always present at the bottom of the bed, also grows along the height of the bed, and participates in the nonlinear behaviour of the wave.

For a given mean volume fraction, three types of behaviour were observed depending upon the forcing frequency f_0 . For large frequencies above a cutoff frequency, the wave amplitude decayed along the bed. Figure 5 shows the spatial evolution of such a stable mode. After a short length of propagation, the amplitude of this mode of high frequency vanished. It is important to notice that the decay of the stable mode amplitude is far from being exponential within the range of amplitudes which we could observe. The propagation of a neutral mode is shown on figure 6. Such a mode is propagating along the fluidized suspension without change of amplitude or shape. Finally, figure 7 shows an example of an unstable mode for which the amplitude is observed to grow and the shape to evolve. Once again, no range of exponential growth of the amplitude could be observed. The wave evolution is rapidly dominated by nonlinearities. We will focus on the unstable modes in the following sections of the paper.

The stability diagram for the combination 7 of table 7 summarizes the three types of modes and is given in figure 8 where the neutral curve separates two half-planes in the (ϕ_0, f_0) coordinates. The neutral curve $f_n(\phi_0)$ is a straight line. For large volume fraction, this line crosses the zero-frequency line at a volume fraction which is close to the value ϕ_c corresponding to the onset of the wavy instability (see §3.1). Stability diagrams were not collected for the other combinations of table 7 because the ϕ_0 ranges were very restricted. The present experiment focused on the nonlinear saturated waves described in the following section.

3.3. *Nonlinear saturation of the unstable modes*

The shape and amplitude of an unstable mode evolve along the bed. Close to the moving piston, the forced perturbation is symmetrical (with respect to the mean volume fraction) in shape, as can be seen on figure 7(a). At a short distance above the distributor, the wave loses its symmetry and its amplitude grows, as can be seen in figure 7(b,c). It then saturates as can be seen in figure 7(d,e). It is important to mention that the saturated amplitude of the mode is an intrinsic quantity. If the amplitude of the forcing at the bottom of the bed is smaller than the saturated amplitude, the mode amplitude grows to reach the saturated value. If the amplitude of the forcing is larger than the saturated amplitude, the mode amplitude decays to reach also the saturated value.

As can be seen in figure 9, which is typical of many further observations, the saturated wave can be described as a succession of concentration dips and plateaux and present a slight asymmetry. A summary of the characteristics of the saturated waves is presented in table 8 for different combinations of particles, fluids and beds as well as for different mean volume fractions ϕ_0 and forcing frequencies f_0 . In order to increase the measurement accuracy, 100 synchronized averages were performed to obtain the shape of the saturated waves. It should be mentioned also that for low forcing frequencies, as the unstable wave grows, a secondary minimum can occur and become important, see figure 10. It was verified that this secondary minimum

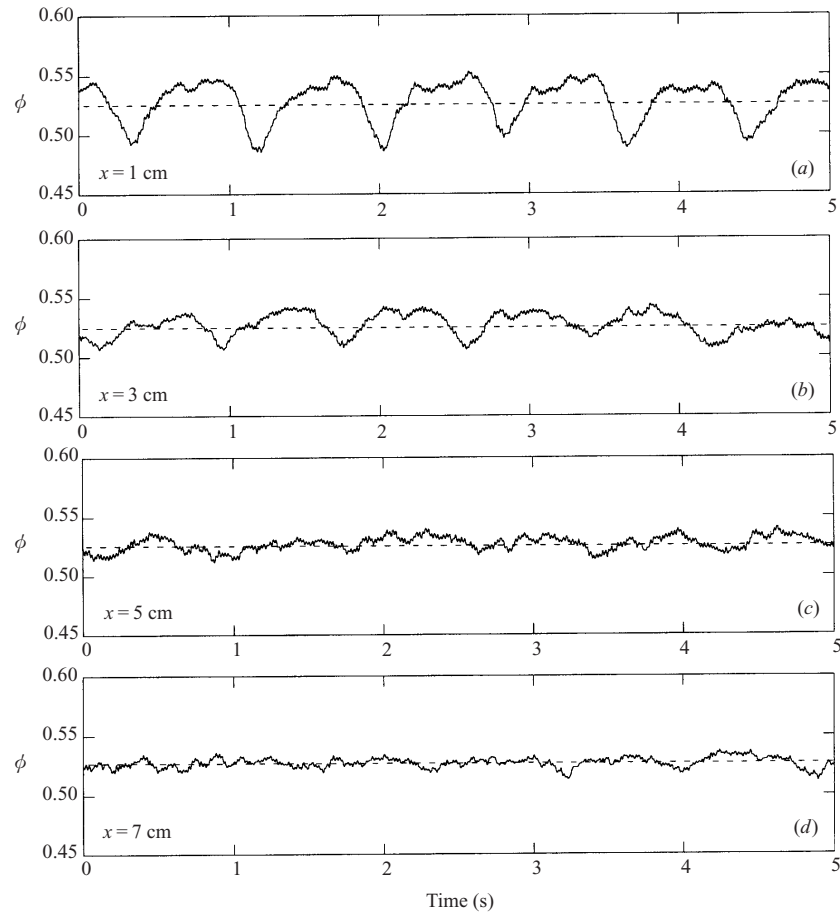


FIGURE 5. Spatial evolution of a stable mode. This stable mode was obtained when using combination 7 of particles, fluid and tube, with $\phi_0 = 0.524 \pm 0.002$ and $f_0 = 1.22$ Hz. The wave shape was measured at different positions x along the bed and obtained by averaging over 30 time sequences.

was due to the growing $2f_0$ mode produced by the imperfect moving piston (see table 5). When $2f_0 > f_n(\phi_0)$, this first harmonic is damped and does not produce any secondary minimum.

The phase velocity was measured by the digital image processing system, as already explained in §2.5. It does not seem to vary much along the bed, but spatio-temporal diagrams were nonetheless built from images near the top of the fluidized bed, where we knew for sure that the waves were fully saturated.

3.4. Experimental shape of the waves as a function of experimental parameters

The main characteristics of the saturated waves are presented in table 8. For a given set of particles, the shape of the saturated wave depends upon the values of experimental parameters, namely the mean particle concentration ϕ_0 , the forcing frequency f_0 and the fluid viscosity μ_f . It should be stressed that the value of the mean particle concentration is chosen in a range for which the wavy instability is observed naturally, i.e. without forcing, within the bed. This concentration is thus

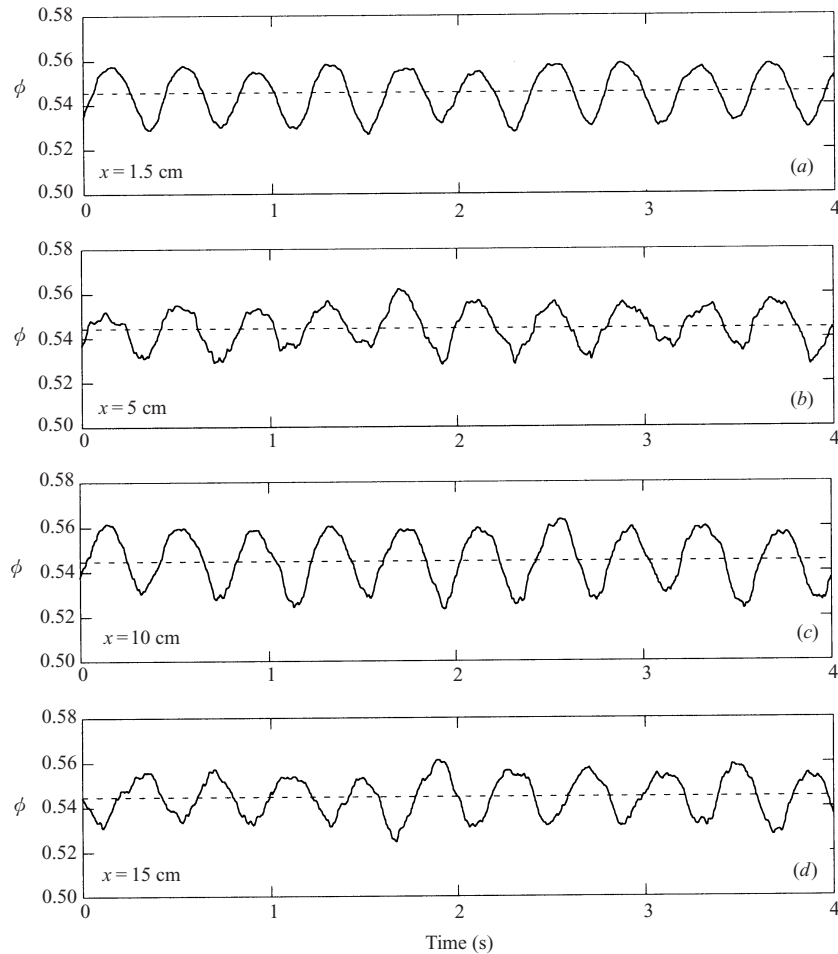


FIGURE 6. Spatial evolution of a neutral mode. This neutral mode was obtained when using combination 1 of particles, fluid and tube, with $\phi_0 = 0.545 \pm 0.005$ and $f_0 = 2.6$ Hz. The wave shape was measured at different positions x along the bed and obtained by averaging over 30 time sequences.

slightly lower than ϕ_c , but it has also to be greater than concentrations corresponding to turbulent regime. Consequently, the ϕ_0 -range for which waves can be measured is limited. Once the mean particle concentration is fixed by adjusting the flow rate, the forcing frequency f_0 is chosen. It has to be below the neutral frequency f_n (at the given ϕ_0) but also above $\frac{1}{2}f_n$, to avoid secondary minima as mentioned in the preceding section. Again, this leads to a limited range of forcing frequency (typically between 1 Hz and 2 Hz). The viscosity value was only changed by a factor of 3, see table 3, because the wave amplitudes were very small and difficult to detect for larger values (see the discussion below).

For a given frequency, changing ϕ_0 does not modify significantly the shape of the saturated wave. Figure 11 shows the shape of three of the saturated waves obtained with combination 2, for different ϕ_0 but with the same f_0 ; the wave amplitude is slightly larger at lower concentrations and its velocity higher (see table 8 for

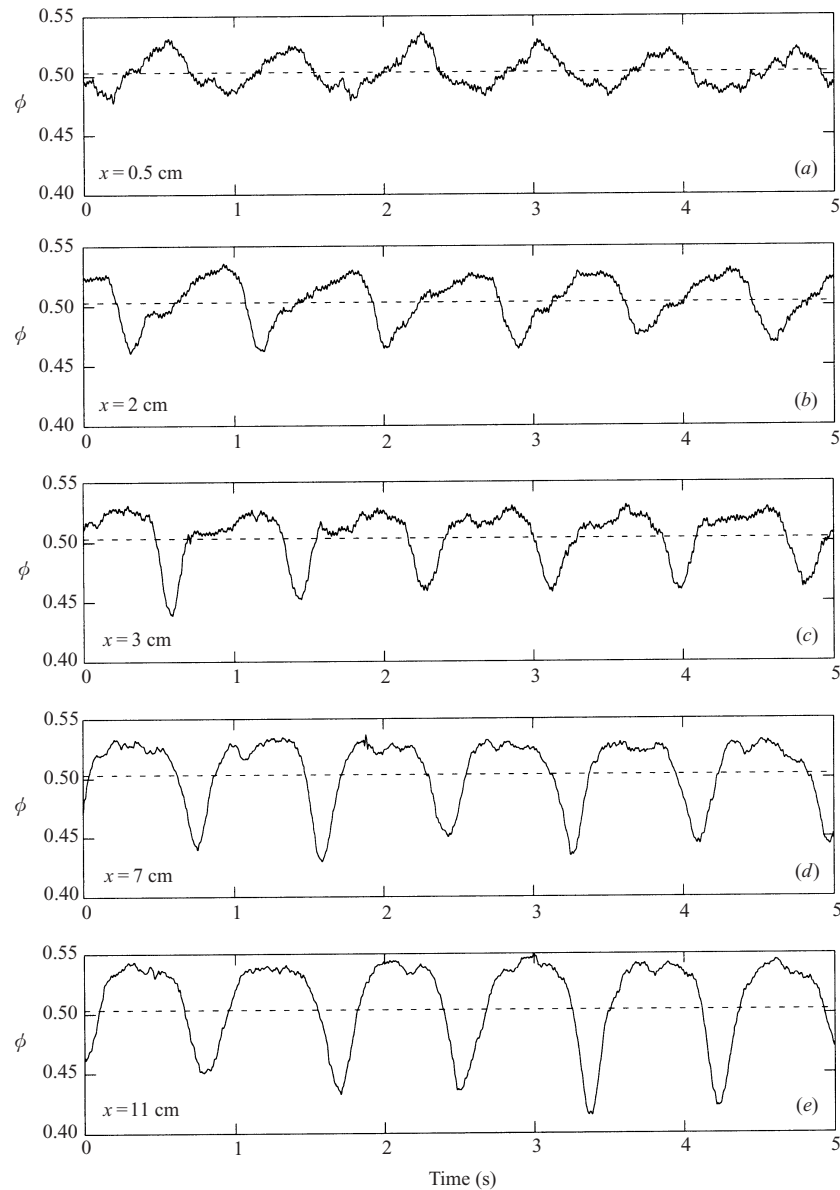


FIGURE 7. Spatial evolution of an unstable mode. This unstable mode was obtained when using combination 7 of particles, fluid and tube, with $\phi_0 = 0.503 \pm 0.002$ and $f_0 = 1.17$ Hz. The wave shape was measured at different positions x along the bed and obtained by averaging over 30 time sequences.

combination 3). Conversely, for a given mean particle concentration, changing the forcing frequency f_0 influences greatly the wave shape. As the frequency increases, the amplitude and wave velocity decrease, the wave becomes more and more symmetrical, and centred around the mean concentration. This can be seen in figure 12 which shows three of the saturated waves of combination 6, measured for different f_0 but with

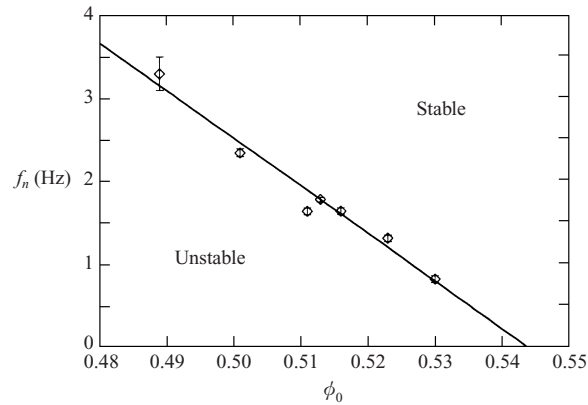
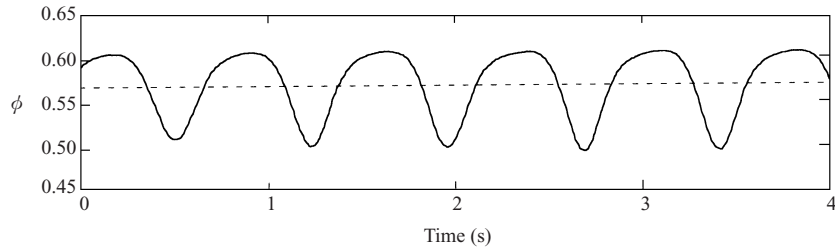
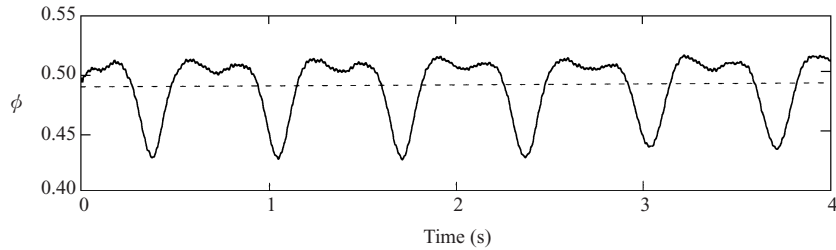


FIGURE 8. Stability diagram obtained for combination 7.

FIGURE 9. Saturated wave obtained for combination 7 with $\phi_0 = 0.57 \pm 0.005$ and $f_0 = 1.4$ Hz. This saturated wave was obtained by averaging over 100 time sequences.FIGURE 10. Wave showing a secondary minimum, obtained for combination 7 with $\phi_0 = 0.49 \pm 0.005$ and $f_0 = 1.5$ Hz. This saturated wave was obtained by averaging over 150 time sequences.

the same ϕ_0 . It is not surprising because, as $f_0 \rightarrow f_n$, the shape of the wave becomes closer to that of a neutral mode, that is, by definition, a symmetrical sinusoidal wave with an amplitude equal to that of the forcing.

Increasing the fluid viscosity (by a factor 3 in the present case) has two main effects. First, the instability threshold ϕ_c is slightly modified (see table 7). Waves are thus measured in a more dilute bed with fluid *b* than with fluid *a*. Secondly, it reduces the wave amplitude (by a factor 2 in the present case). Figure 13 shows two waves obtained with fluids *a* and *b*, respectively. It should be noticed that the forcing frequency is different for the two waves but, since it is far from the cutoff frequency

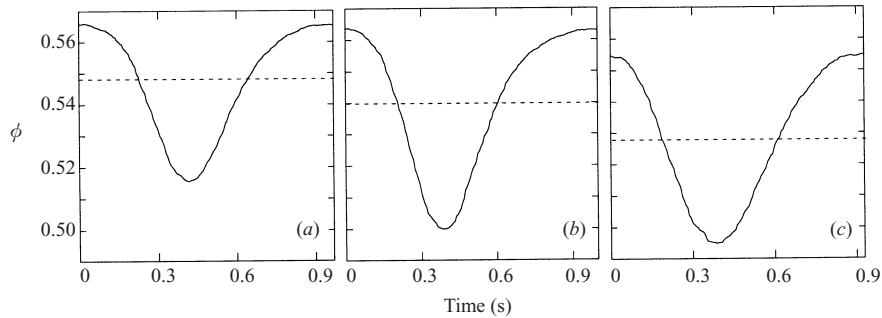


FIGURE 11. Influence of the mean particle concentration ϕ_0 on the shape of the saturated wave: (a) $\phi_0 = 0.548$; (b) $\phi_0 = 0.540$; (c) $\phi_0 = 0.528$. These waves were obtained with combination 2. Only one period of the wave is shown. The forcing frequency f_0 is ≈ 1.1 Hz for the three waves. The dashed line shows the mean particle concentration ϕ_0 .

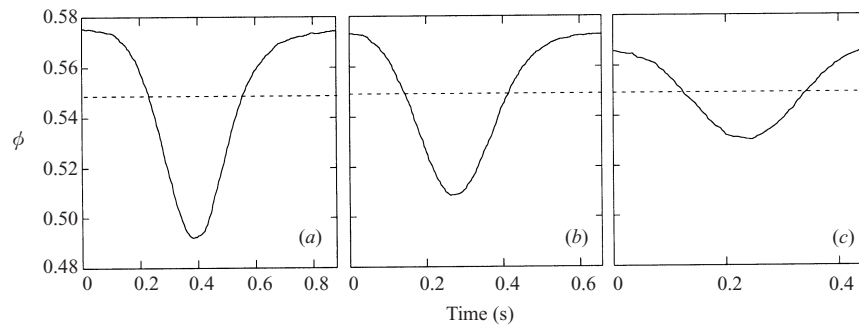


FIGURE 12. Influence of the forcing frequency f_0 on the shape of the saturated wave: (a) $f_0 = 1.1$ Hz; (b) $f_0 = 1.55$ Hz; (c) $f_0 = 2.2$ Hz. These waves were obtained with combination 6. Only one period of the wave is shown. The mean particle concentration ϕ_0 is 0.549 ± 0.003 for the three waves. The dashed line shows the mean particle concentration ϕ_0 .

f_n (≈ 2 Hz) in both cases, we can assume that the difference of amplitude between the wave of figure 13(a) and the wave of figure 13(b) is due to the difference in fluid viscosity only. It should be mentioned that when comparing figures 13(a) and 13(b), only the wave amplitude and c are modified (see table 8), the shape of the saturated wave remaining similar. It must also be noted that for fluid b , no state of stable homogeneous fluidization was observed. We also tried to use a more viscous fluid (a mixture of glycerin and water giving a viscosity $\mu_f = 5 \pm 0.2$ cP). A state of stable homogeneous fluidization was found in that case (for further details on the existence of stable fluidization with very viscous fluid or with light particles see Ham *et al.* 1990). Above the instability threshold ϕ_c , some voidage waves were observed, but they were of very small amplitude. It was, however, impossible to measure their shape precisely by averaging over a reasonable number of time sequences, because the signal to noise ratio was too small.

When changing the set of particles, the overall shape of the waves remains similar whereas amplitude of the waves and wave velocity c change, as can be seen in table 8. The remarks made above regarding the dependence of the saturated wave shape on ϕ_0 , f_0 , and μ_f are still relevant.

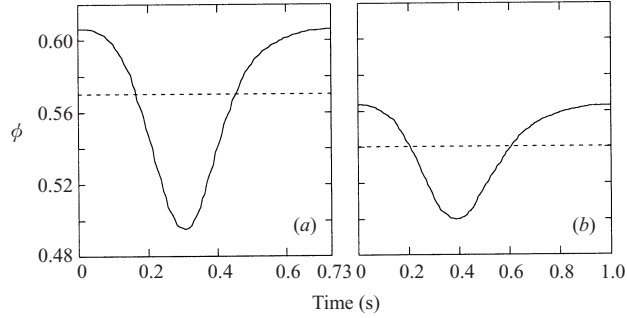


FIGURE 13. Influence of the fluid viscosity μ_f on the shape of the saturated wave: (a) wave of combination 1: $\phi_0 = 0.57$, $f_0 = 1.4$ Hz, $\mu_f = 0.9$ cP; (b) wave of combination 2: $\phi_0 = 0.54$, $f_0 = 1$ Hz, $\mu_f = 3$ cP. The dashed line shows the mean particle concentration ϕ_0 .

4. Nonlinear analysis of the saturated unstable waves

We now present the two-phase equations we used for the analysis of the experimental data. The fluidized bed is described as a mixture of two continuous phases. For simplicity, both phases have a Newtonian rheology. The goal of this analysis is the determination of the solid phase viscosity μ_s and of the derivative of the solid pressure $dp_s/d\phi$ from the shape of the saturated wave.

4.1. The saturated wave equation

We chose to use the model of Anderson & Jackson (1967), more recently described in Anderson, Sundaresan & Jackson (1995), as the basic equations. The fluid phase has local velocity $u(x, t)$, density ρ_f , viscosity μ_f , and pressure p_f . The solid phase is also described as a fluid, with local velocity $v(x, t)$, density ρ_s , viscosity μ_s , and pressure p_s . The phases are coupled by a drag force and an added-mass force of the fluid phase acting on the solid phase. Since the fluid is a liquid rather than a gas, the added mass term cannot be neglected in the present case.

The full three-dimensional equations are described in Anderson *et al.* (1995). For the purpose of the present study, we reduce the dimensionality to one. In that case, the two-phase equations have the following form:

$$\frac{\partial \phi}{\partial t} + \frac{\partial}{\partial x}(\phi v) = 0, \quad (4.1)$$

$$-\frac{\partial \phi}{\partial t} + \frac{\partial}{\partial x}[(1 - \phi)u] = 0, \quad (4.2)$$

$$\begin{aligned} \phi(\rho_s + \hat{C}\rho_f) \left(\frac{\partial v}{\partial t} + v \frac{\partial v}{\partial x} \right) - \phi\rho_f(1 + \hat{C}) \left(\frac{\partial u}{\partial t} + u \frac{\partial u}{\partial x} \right) + \frac{\partial p_s}{\partial x} \\ = \frac{4}{3} \frac{\partial}{\partial x} \left(\mu_s \frac{\partial v}{\partial x} \right) + \beta(u - v) - \phi(\rho_s - \rho_f)g, \end{aligned} \quad (4.3)$$

where (4.1) and (4.2) are the mass conservation equations and (4.3) is the momentum equation for the solid phase. We do not write the momentum equation for the fluid phase as it is not needed in the following nonlinear analysis of the waves.

Adding and integrating the two continuity equations gives the mean flow rate q

which is the experimental control parameter:

$$q = \phi v + (1 - \phi)u. \quad (4.4)$$

The first two terms on the left-hand side of equation (4.3) are inertial terms coming from the solid and fluid phases, respectively. The third term is the unknown solid pressure gradient. The parameter $\hat{C} = C(\phi)/(1 - \phi)$ is the reduced added mass coefficient. The added mass coefficient $C(\phi)$ takes the value $\frac{1}{2}$ for an isolated particle. Of course, there is a concentration dependence but it is not fully understood.

The first term on the right-hand side of equation (4.3) is the viscous term, with, at this stage, an unknown solid viscosity μ_s . The second term on the right-hand side represents the drag force of the fluid acting on the solid phase. The coefficient $\beta(\phi)$ is the drag coefficient that can be deduced from the Richardson–Zaki law:

$$\beta(\phi) = \frac{(\rho_s - \rho_f)g}{v_t} \frac{\phi}{(1 - \phi)^{n-1}}, \quad (4.5)$$

where the two parameters v_t and n are determined from the expansion curve of the fluidized bed (see § 3.1). The last term on the right-hand side of equation (4.3) is the weight corrected for buoyancy.

Crude estimates of the different terms in equation (4.3) show that the weight corrected for buoyancy balances drag within a few per cent. Taking $dp_s/d\phi \sim 1\text{--}100$ c.g.s., as suggested by Anderson & Jackson (1969) and Homsy, El-Kaissy & Didwania (1980), inertial and solid pressure terms can be estimated to be of comparable size. They represent less than 10% of the difference between drag and the weight corrected for buoyancy. Thus, the difference between drag and the weight corrected for buoyancy roughly equilibrates the solid viscous term.

If we now assume (as observed in the experiments) that a saturated wave travels in the fluidized bed at a constant velocity c , equations (4.1), (4.3) and (4.4) can be rewritten in a moving reference frame. The wave is stationary in this new reference frame with a space coordinate X defined by:

$$X = x - ct. \quad (4.6)$$

We also introduce the new velocities $u(X) = u(x, t) - c$ and $v(X) = v(x, t) - c$ and the volume fraction $\phi(X) = \phi(x, t)$. Using equations (4.1), (4.4) and (4.3), it is then possible to eliminate u and v successively and to write a single equation for the volume fraction ϕ . In the reference frame attached to the wave, the saturated wave equation has the form:

$$\frac{4}{3}c\phi_0 \frac{d}{dX} \left[\mu_s(\phi) \frac{d\phi}{dX} \frac{1}{\phi^2} \right] + F_1(\phi) + \left[F_2(\phi) - \frac{dp_s}{d\phi} \right] \frac{d\phi}{dX} = 0, \quad (4.7)$$

where

$$F_1(\phi) = \phi \rho_s \frac{g(\rho_s - \rho_f)}{\rho_s} \left[\frac{v_t(1 - \phi_0)^n - c(1 - \phi_0/\phi)}{v_t(1 - \phi)^n} - 1 \right], \quad (4.8)$$

and

$$F_2(\phi) = \rho_f \phi (1 + \hat{C}(\phi)) \frac{[v_t(1 - \phi_0)^n + c(\phi_0 - 1)]^2}{(1 - \phi)^3} + (\rho_s + \rho_f \hat{C}(\phi)) \left(\frac{c\phi_0}{\phi} \right)^2. \quad (4.9)$$

The function $F_1(\phi)$ contains the difference between drag and the weight corrected for buoyancy. $F_2(\phi)$ groups inertial and added mass terms. The first term in F_2 is much smaller than the second, representing at best 15% of the total.

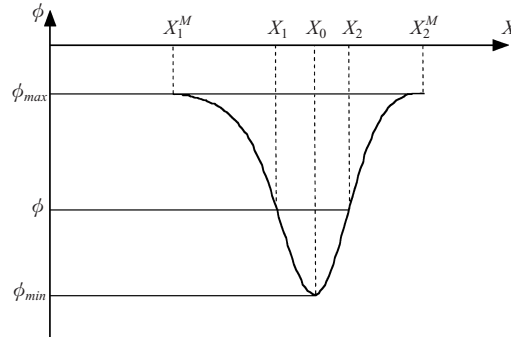


FIGURE 14. A saturated wave period plotted as a function of X . The quantities ϕ , ϕ_{max} , ϕ_{min} , X_0 , X_1 and X_2 introduced in §4.2 are shown.

4.2. Determination of μ_s and $dp_s/d\phi$

The two unknown functions of concentration, μ_s and $dp_s/d\phi$, can be determined from the shape of the wave $\phi(X)$ and its first derivative. The integration of equation (4.7) between two coordinates X_1 and X_2 such as $\phi(X_1) = \phi(X_2) = \phi$ (see figure 14) gives:

$$\frac{4\phi_0 c}{3\phi^2} \left[\left(\frac{d\phi}{dX} \right)_{X_2} \mu_s(\phi(X_2)) - \left(\frac{d\phi}{dX} \right)_{X_1} \mu_s(\phi(X_1)) \right] = - \int_{X_1}^{X_2} F_1(\phi(X)) dX. \quad (4.10)$$

This equation shows that the difference between the solid viscous stress at X_2 and X_1 balances the integral of the difference between drag and the weight corrected for buoyancy over the same interval.

The solid phase viscosity is thus given by:

$$\mu_s(\phi) = \frac{3}{4\phi_0 c} \frac{\phi^2}{(d\phi/dX)_{X_1} - (d\phi/dX)_{X_2}} \int_{X_1}^{X_2} F_1(\phi(X)) dX. \quad (4.11)$$

Using this formula, $\mu_s(\phi)$ can be computed in the range $\phi_{min} < \phi < \phi_{max}$ for each measured saturated wave. Once $\mu_s(\phi)$ is known, we can differentiate equation (4.7) to find $[F_2(\phi) - dp_s/d\phi]$ within the same range of concentration. Thus, our fully non-linear analysis of the shape of the saturated waves provides a determination of $\mu_s(\phi)$ and $dp_s/d\phi$ (under assumptions concerning $C(\phi)$ in order to compute $F_2(\phi)$), which are the two unknown functions of concentration introduced in the two-phase modelling.

Equation (4.10) requires a good accuracy in the calculation of the first derivative of $\phi(X)$. Despite the precision in the measurement of the shape of the wave provided by the averaging method, experimental results are too noisy to compute directly the first derivative of $\phi(X)$. Experimental results were therefore fitted by an analytical periodic function, provided by a nonlinear least-squares fit algorithm implemented in the MatLab software. As a fitting function we have chosen a periodic quartic B-spline over 10 subintervals. As an example of many further observations, figure 15 shows the good agreement between the experimental wave and the fitted curve. All the results presented in the next sections were obtained using the fitted analytical function.

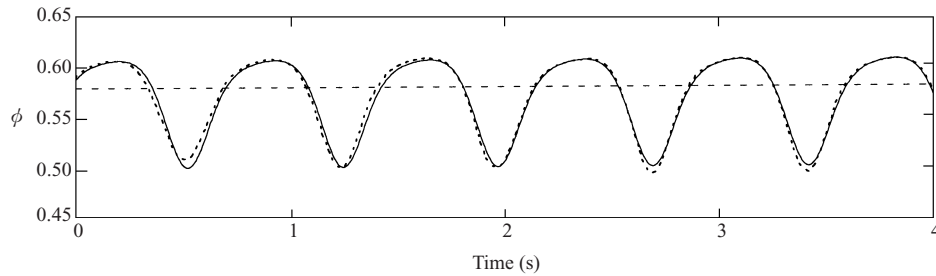


FIGURE 15. Example of a saturated wave fitted by a B-spline function. The saturated wave was obtained for combination 1 with $\phi_0 = 0.57 \pm 0.005$ and $f_0 = 1.4$ Hz. The dashed line is the experimental result and the solid line is the fitting B-spline function.

5. Determination of the solid phase viscosity μ_s

In this section, we present the results concerning the solid viscosity $\mu_s(\phi)$. For each of the measured saturated waves, we used formula (4.11) to compute $\mu_s(\phi)$. We hereafter study the influence of experimental parameters on $\mu_s(\phi)$.

5.1. Influence of ϕ_0 and f_0 on μ_s

Figure 16(a,b) shows the function $\mu_s(\phi)$ for waves shown in figures 11 and 12. For waves of figure 11, only the mean particle concentration ϕ_0 was changed, the wave frequency being roughly constant. Conversely, ϕ_0 was fixed and the forcing frequency f_0 was varied for waves of figure 12.

The solid viscosity $\mu_s(\phi)$ is found to be an increasing function of the particle concentration ϕ . The solid viscosity increases strongly as ϕ approaches ϕ_{max} . It is therefore more convenient to plot $1/\mu_s$ as a function of ϕ . This is done in figure 16(c,d) which shows the same results as in figure 16(a,b). The solid viscosity seems to vary as ϕ^{-1} , which was not obvious in figure 16(a,b) showing μ_s against ϕ . Note also the plot of $1/\mu_s$ against ϕ has the useful side effect of making the larger error bars at high ϕ appear smaller, because the relative error was not so large.

The solid viscosity does not seem to vary significantly with the mean particle concentration ϕ_0 , as can be seen on figure 16(a), at least for the limited range of ϕ_0 in which voidage waves were measurable. Differences for ‘low’ concentration between the wave at $\phi_0 = 0.528$ (circle in figure 16a,c) and the two others are displayed more clearly when we plot $1/\mu_s$ as a function of ϕ , see figure 16(c), but they are still within the large error bars. In the other cases studied, for example waves of combination 1 and 3 (see table 8), the differences have been also observed to be small and within error bars.

The solid viscosity does not seem to vary significantly with f_0 , in the range of frequencies examined. For waves of figure 16(b,d), the two curves for $f = 1.1$ Hz and $f = 1.55$ Hz are different, but it is not significant because of the large error bars involved. However, as can be seen in figure 16(d), the slope difference is much larger for the quasi-neutral mode at $f = 2.2$ Hz, but the data are still within the error bars of the two other curves. Concerning this last curve, we can wonder if we really measured a saturated wave as, when we approach the cutoff frequency f_n , the time (and thus the distance covered in the bed) taken by the wave to saturate should increase strongly. It is therefore possible that this saturated state was not reached in our bed of limited height. This could explain why results for this quasi-neutral mode are slightly different.

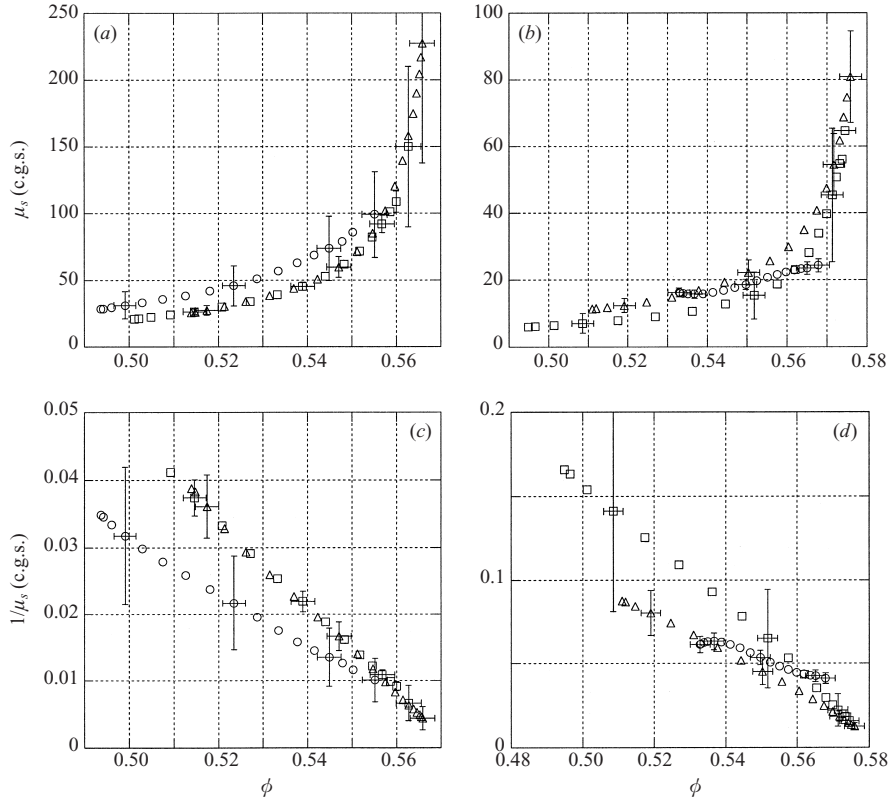


FIGURE 16. Influence of the mean particle concentration ϕ_0 and of the forcing frequency f_0 on μ_s . (a) μ_s plotted against ϕ for combination 2, at $f_0 = 1$ Hz; \triangle , $\phi_0 = 0.548$; \square , $\phi_0 = 0.540$; \circ , $\phi_0 = 0.528$. (b) μ_s plotted against ϕ for combination 6, at $\phi_0 = 0.549$; \square , $f_0 = 1.1$ Hz; \triangle , $f_0 = 1.55$ Hz; \circ , $f_0 = 2.2$ Hz. (c) $1/\mu_s$ as a function of ϕ , same curves as in (a). (d) $1/\mu_s$ as a function of ϕ , same curves as in (b).

The fact that the solid viscosity does not seem to vary with frequency supports the modelling of the stresses of the solid phase by a Newtonian viscous fluid without any elastic component of stress.

5.2. Influence of fluid viscosity on μ_s

We now consider the influence of the fluid viscosity μ_f on $\mu_s(\phi)$. The fluid viscosity μ_f has been increased by a factor 3 from combination 1 to combination 2. It must be stressed that the ϕ -range ‘probed’ in the present experiments, that is the typical interval $[\phi_{min}, \phi_{max}]$ for which μ_s can be computed owing to equation (4.11), is not the same for waves of combinations 1 and 2. As already mentioned, the instability threshold ϕ_c for fluid *b* is slightly smaller than that for fluid *a*. Therefore, the mean particle concentrations ϕ_0 for which saturated waves can be measured, are smaller for fluid *b* (see table 8). The interval $[\phi_{min}, \phi_{max}]$ being roughly centred around ϕ_0 , this results in a shift along the ϕ -axis between curves showing $1/\mu_s(\phi)$ for viscous fluid *b* and for fluid *a*, see figure 17(a). It is then difficult to compare directly the solid viscosity obtained in each case and to draw conclusions from the apparent difference between the two families of curves.

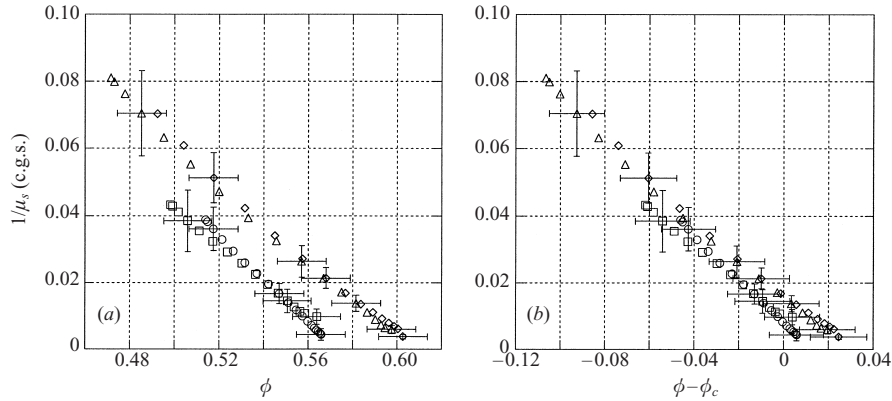


FIGURE 17. Influence of the fluid viscosity μ_f on μ_s . (a) $1/\mu_s$ plotted against ϕ ; (b) $1/\mu_s$ plotted against $\phi - \phi_c$; \circ , $\phi_0 = 0.548$; \square , $\phi_0 = 0.538$: combination 2 with $\mu_f = 3$ cP and $\phi_c = 0.560$. \diamond , $\phi_0 = 0.558$; \triangle , $\phi_0 = 0.55$: combination 1 with $\mu_f = 0.9$ cP and $\phi_c = 0.578$.

If we now plot $1/\mu_s$ as a function of $\phi - \phi_c$ instead of ϕ , all curves collapse into a single curve, as can be seen in figure 17(b). It then becomes clear that the solid viscosity does not scale with the fluid viscosity. The differences between the two families of curves in figure 17(a) can be interpreted as a shift of our measurement zone resulting from the shift in ϕ_c caused by the change in fluid viscosity. The collapse obtained when plotting $1/\mu_s$ as a function of $\phi - \phi_c$ means that the bed rheological behaviour, as far as μ_s is concerned, is controlled at a given ϕ by the distance to the instability threshold.

5.3. Influence of D/d_s on μ_s

In this section, we compare the solid viscosity for waves of combinations 6 and 7. Only the bed to particle diameter ratio D/d_s differs from combination 6 to combination 7, see table 8. The resulting curves are presented in figure 18. Once again, the ϕ -ranges for which $\mu_s(\phi)$ is computed are not the same for waves of combinations 6, 7 and the resulting shift along the ϕ -axis is large, see figure 18(a). This shift is not only due to the change in threshold ϕ_c (see table 7), but also to the fact that waves were measured ‘further’ above the instability threshold for combination 7 (as mentioned in §3.1). This latter point is not corrected if we plot $1/\mu_s$ as a function of $\phi - \phi_c$ and a significant shift between curves of combination 7 and curves of combination 6 remains. Therefore, we must plot $1/\mu_s$ as a function of $\phi - \phi_0$ for the shift to disappear, as can be seen in figure 18(b).

It must be emphasized that for all combinations, excepted combination 7, aspect ratio D/d_s was between 17 and 25 so that waves were measured near ϕ_c . The case of combination 7 is thus rather particular but important because it makes more obvious the relevance of cancelling shifts along the ϕ -axis before comparing the values of $\mu_s(\phi)$ for different combinations. However, it could also mean that for combination 7, the ratio D/d_s is too small and that our results are strongly influenced by wall effects.

5.4. Scaling law for μ_s

It remains for us to consider the influence of particle characteristics on $\mu_s(\phi)$. By comparing combinations 3 and 8, we can study the influence of the particle diameter d_s on $\mu_s(\phi)$. By comparing combinations 2 and 3, we can study the influence of particle

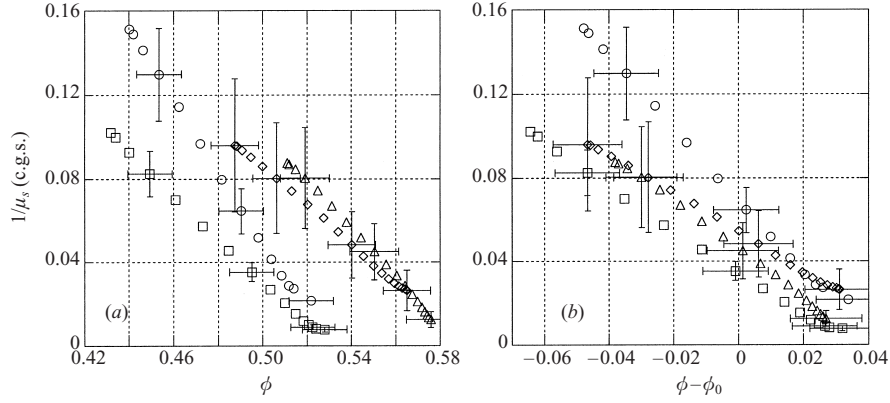


FIGURE 18. Influence of the bed to particle ratio D/d_s on μ_s . (a) $1/\mu_s$ plotted against ϕ ; (b) $1/\mu_s$ plotted against $\phi - \phi_0$. \circ , $\phi_0 = 0.488$; \square , $\phi_0 = 0.496$: combination 7 with $D/d_s \approx 10$. \triangle , $\phi_0 = 0.549$; \diamond , $\phi_0 = 0.534$: combination 6 with $D/d_s \approx 25$.

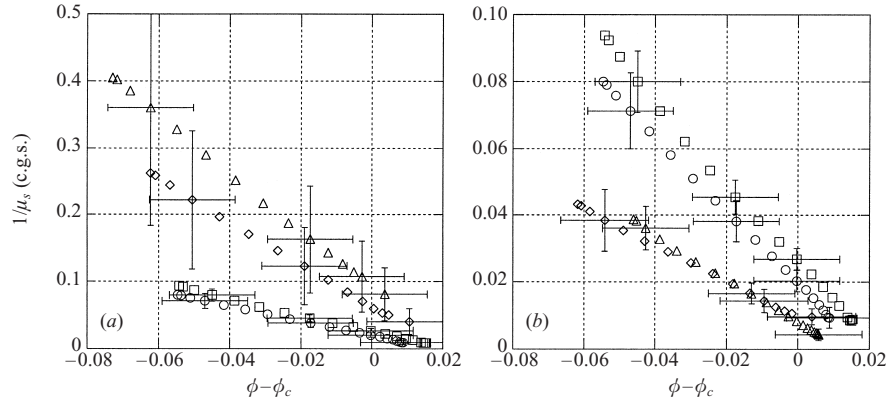


FIGURE 19. Influence of the characteristics of the beads on μ_s . (a) $1/\mu_s$ plotted against $\phi - \phi_c$; \square , $\phi_0 = 0.535$; \circ , $\phi_0 = 0.545$: combination 3 with $d_s v_t = 1.7$ c.g.s. and $\phi_c = 0.555$. \diamond , $\phi_0 = 0.530$; \triangle , $\phi_0 = 0.521$: combination 8 with $d_s v_t = 0.9$ c.g.s. and $\phi_c = 0.544$. (b) $1/\mu_s$ plotted against $\phi - \phi_c$; \square , $\phi_0 = 0.535$; \circ , $\phi_0 = 0.545$: combination 3 with $\rho_s v_t = 36$ c.g.s. and $\phi_c = 0.555$. \triangle , $\phi_0 = 0.548$; \diamond , $\phi_0 = 0.538$: combination 2 with $\rho_s v_t = 83$ c.g.s. and $\phi_c = 0.560$.

density ρ_s on $\mu_s(\phi)$. The difficulty is that the terminal velocity v_t also changes when ρ_s and/or d_s are changed. For example, for combinations 2 and 3, v_t is decreased by a factor of 50% while ρ_s is decreased by a factor of 60%.

We can see in figure 19(a) that, for a similar ϕ -range (which is ensured by plotting $1/\mu_s$ as a function of $\phi - \phi_c$), $\mu_s(\phi)$ is increased when $d_s v_t$ is increased for a given particle density ρ_s . Similarly, in figure 19(b), we can see that $\mu_s(\phi)$ is increased when $\rho_s v_t$ is increased for a given particle size d_s .

Several combinations of the bed can be constructed with the dimensions of viscosity. We have plotted μ_s made dimensionless by $\rho_s d_s v_t$ in figure 20(a) and by $\rho_f d_s v_t$ in figure 20(b). A good collapse into a single curve is obtained in both cases. Unfortunately, large experimental error-bars do not allow us to discriminate between these two scalings even though the scatter of the data seems smaller in

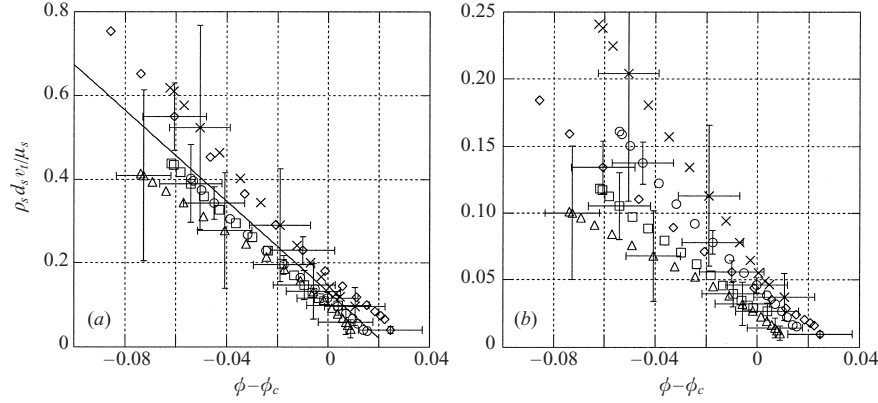


FIGURE 20. Scaling laws for μ_s : (a) $\rho_s d_s v_t / \mu_s$ as a function of $\phi - \phi_c$ for a representative sample of curves, the solid line shows the best fitting linear function for all these data; (b) $\rho_f d_s v_t / \mu_s$ as a function of $\phi - \phi_c$. \diamond , $\phi_0 = 0.558$, combination 1 with $\phi_c = 0.578$; \square , $\phi_0 = 0.538$, combination 2 with $\phi_c = 0.560$; \circ , $\phi_0 = 0.545$, combination 3 with $\phi_c = 0.555$; \triangle , $\phi_0 = 0.549$, combination 6 with $\phi_c = 0.555$; \times , $\phi_0 = 0.530$, combination 8 with $\phi_c = 0.544$.

figure 20(a). In the same way, scaling μ_s by $(\rho_s - \rho_f)d_s v_t$ or $(\rho_s \rho_f)^{1/2} d_s v_t$ would also provide similar good collapses.

To try to distinguish between these different possible scaling, we can refer to rheological measurements of stress in fluidized bed (for a good review, see Schügerl 1971). Effective viscosities measured in suspensions fluidized by air or a liquid are about the same size. This leads us to feel inclined towards a scaling involving the solid density *via* ρ_s or the difference $\rho_s - \rho_f$ rather than the fluid density ρ_f alone.

As a conclusion of this section, it should be stressed that the interpretation of our data was complicated by shifts along the ϕ -axis between curves corresponding to different combinations owing to fluid viscosity effects (see §5.2) or confinement effects (see §5.3). We resolved to correct these effects first, and then to compare curves giving $1/\mu_s(\phi)$. The solid viscosity seems to vary as ϕ^{-1} and to diverge for values of concentration between $\phi_c + 0.02$ and $\phi_c + 0.04$, see figure 20(a), which corresponds roughly to a random loose packing of the bed. In the limited range of f_0 , ϕ_0 and μ_f studied, we propose finally the best linear fit displayed in figure 20(a) as a scaling law for μ_s :

$$\mu_s(\phi) \approx 0.18 \frac{\rho_s d_s v_t}{\phi_{rlp} - \phi}. \quad (5.1)$$

The best linear fit gives the prefactor 0.18 and the value $\phi_{rlp} \approx \phi_c + 0.025$ for which μ_s diverges which can be considered as a random loose-packing concentration. Unfortunately, ϕ_{rlp} is not a well-defined physical quantity.

This scaling works for the results obtained with all combinations except combination 7. To take into account this last set of results, we should have introduced a dependence of the results with ϕ_0 . It is therefore a pity that the ϕ_0 -range probed for other combinations was so small that it was not possible to detect an hypothetical discrepancy between curves giving μ_s when ϕ_0 was varied. It would have then validated another kind of more complex scaling, involving ϕ_0 . However, as we have already mentioned, it is also possible that results obtained for set 7 are affected too strongly by wall friction and thus are not relevant.

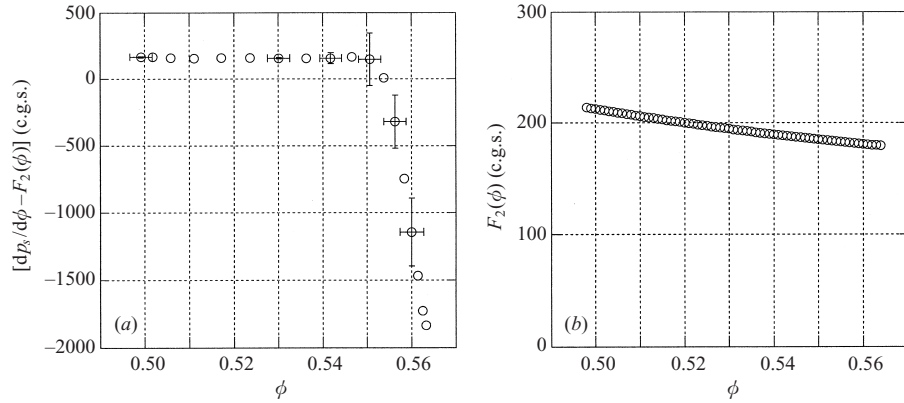


FIGURE 21. (a) $[dp_s/d\phi - F_2(\phi)]$ as a function of ϕ for the wave of combination 2 with $\phi_0 = 0.538$; (b) $F_2(\phi)$, computed with $C = \frac{1}{2}$, for the wave of combination 2 with $\phi_0 = 0.538$.

6. Determination of the solid pressure derivative $dp_s/d\phi$

The present nonlinear analysis of the saturated waves also provides some insight concerning $dp_s/d\phi$. As explained in §4.2, we can compute $[dp_s/d\phi - F_2(\phi)]$ for values of ϕ in the interval $[\phi_{min}, \phi_{max}]$. A typical curve is shown in figure 21(a). The quantity $[dp_s/d\phi - F_2(\phi)]$ is first constant for a large range of ϕ but, as ϕ approaches ϕ_{max} , the slope abruptly becomes negative and $[dp_s/d\phi - F_2(\phi)]$ decreases strongly as ϕ increases, when $0.55 < \phi < 0.564 = \phi_{max}$. This can also be seen owing to the following calculation. Multiplying equation (4.7) by $\mu_s(\phi) \times (d\phi/dX) \times 1/\phi^2$ and then integrating from X_1^M to X_2^M (see figure 14) leads to:

$$\int_{X_1^M}^{X_2^M} \mu_s(\phi) \left[F_2(\phi) - \frac{dp_s}{d\phi} \right] \left(\frac{d\phi}{dX} \frac{1}{\phi} \right)^2 dX = 0, \quad (6.1)$$

which proves that $[dp_s/d\phi - F_2(\phi)]$ must change its sign. The experimental curve of figure 21(a) indeed shows that the sign of this expression is first positive and then becomes negative. We can also see that for a perfectly symmetrical wave, we would have obtained $F_2(\phi) = dp_s/d\phi$, see equation (4.7), which means that the solid pressure gradient would compensate exactly the inertial terms in this hypothetical case. The slight asymmetry of the measured wave therefore means that $dp_s/d\phi$ is not exactly equal to $F_2(\phi)$ at all ϕ .

It is possible to compute $dp_s/d\phi$ by simply adding $F_2(\phi)$ to $[dp_s/d\phi - F_2(\phi)]$. Calculations have been made taking $C(\phi) = \frac{1}{2}$. A typical curve for $F_2(\phi)$ is shown in figure 21(b).

6.1. Influence of ϕ_0 on $dp_s/d\phi$

Figure 22(a) shows $dp_s/d\phi$ for three waves of combinations 2, shown in figure 11. Only the mean particle concentration ϕ_0 differs from one wave to another. For each curve, we encounter the same behaviour as in figure 21(a): $dp_s/d\phi$ is roughly constant for a large range of ϕ before decreasing when concentrations near ϕ_{max} are reached. The value of $dp_s/d\phi$ in the constant part is approximately the same for each curve. The quantity $dp_s/d\phi$ begins to decrease for $\phi = 0.53$ when $\phi_0 = 0.528$ (circles on figure 22a), whereas it begins to decrease for $\phi = 0.55$ when $\phi_0 = 0.548$ (diamonds on 22a). This small shift along the ϕ -axis is meaningful because it is not within

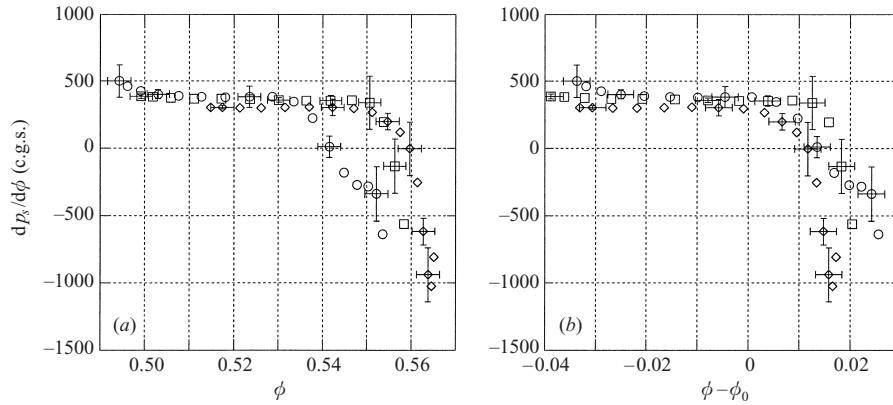


FIGURE 22. Influence of the mean particle concentration ϕ_0 on $dp_s/d\phi$: (a) $dp_s/d\phi$ for combination 2 as a function of ϕ ; (b) $dp_s/d\phi$ for combination 2 as a function of $\phi - \phi_0$. \diamond , $\phi_0 = 0.548$; \square , $\phi_0 = 0.538$; \circ , $\phi_0 = 0.528$.

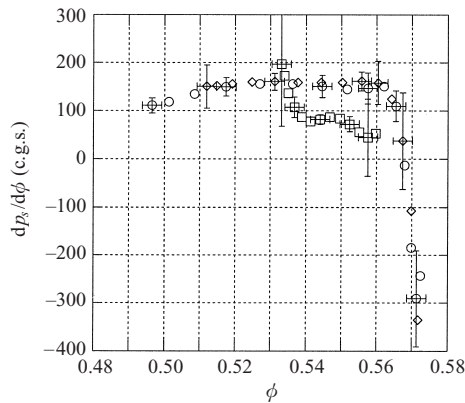


FIGURE 23. Influence of the forcing frequency f_0 on $dp_s/d\phi$: $dp_s/d\phi$ for combination 6 as a function of ϕ . \circ , $f_0 = 1.1$ Hz; \diamond , $f_0 = 1.55$ Hz; \square , $f_0 = 2.2$ Hz.

errors bars. This shift disappears if we now plot $dp_s/d\phi$ as a function of $\phi - \phi_0$, see figure 22(b). Owing to the relatively small ϕ_0 -range probed by our experiments, we were not able to confirm this result by measuring saturated waves and thus $dp_s/d\phi$ for mean particle concentrations lower than 0.528 which could have made the shift along the ϕ -axis greater. It is important to repeat that no noticeable differences were found in $\mu_s(\phi)$ for different ϕ_0 , see figure 16(a).

6.2. Influence of f_0 on $dp_s/d\phi$

Figure 23 shows $dp_s/d\phi$ for waves shown in figure 12. Only the forcing frequency f_0 differs from one wave to another. For the waves measured at $f_0 = 1.1$ Hz and $f_0 = 1.55$ Hz (circles and diamonds, respectively, in figure 23), the two curves are similar, with a decrease of $dp_s/d\phi$ when ϕ approaches ϕ_{max} . For the wave measured at $f_0 = 2.2$ Hz (square in figure 23), the data differ slightly from those of the two other curves. We have already suggested in § 5.1 that it could be due to the fact that the corresponding wave was not fully saturated when it was measured.

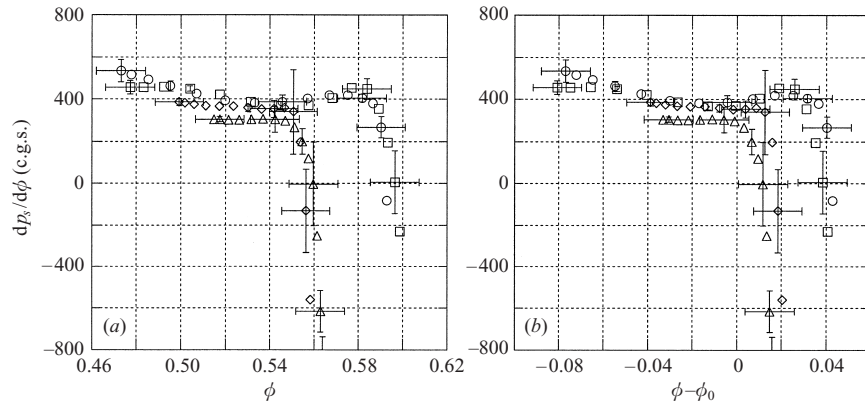


FIGURE 24. Influence of the fluid viscosity μ_f on $dp_s/d\phi$: (a) $dp_s/d\phi$ plotted against ϕ ; (b) $dp_s/d\phi$ plotted against $\phi - \phi_0$. \triangle , $\phi_0 = 0.548$; \diamond , $\phi_0 = 0.538$: combination 2 with $\mu_f = 3$ cP. \square , $\phi_0 = 0.558$; \circ , $\phi_0 = 0.55$: combination 1 with $\mu_f = 0.9$ cP.

6.3. Influence of μ_f on $dp_s/d\phi$

Figure 24(a) shows $dp_s/d\phi$ for waves of combinations 1 and 2. Only the fluid viscosity μ_f differs from combination 1 to combination 2. Each curve presents a decrease of $dp_s/d\phi$ when ϕ approaches ϕ_{max} . The value of $dp_s/d\phi$ in the constant part is approximately the same for each curve.

To compare the results obtained with fluid a with those obtained with fluid b , we have the same problem as that raised while dealing with the influence of μ_f on $\mu_s(\phi)$: the intervals $[\phi_{min}, \phi_{max}]$ differ with the fluid viscosity. Waves were obtained in a relatively more dilute bed with viscous fluid b and their amplitudes were half of those obtained with fluid a . Nonetheless, we have seen in § 5.2 that plotting $\mu_s(\phi)$ as a function of $\phi - \phi_c$ instead of ϕ (see figure 17), was sufficient to obtain a collapse of curves into a single one, showing that the apparent differences were mainly due to the influence of the fluid viscosity μ_f on the instability threshold ϕ_c (ϕ_c for combination 2 is lower than ϕ_c for combination 1).

However, in the present case, because we have seen in § 6.1 that there was a small influence of ϕ_0 on $dp_s/d\phi$, we decided to plot $dp_s/d\phi$ as a function of $\phi - \phi_0$ rather than $\phi - \phi_c$, see figure 24(b). Notice that plotting $dp_s/d\phi$ as a function of $\phi - \phi_c$ would have given the same kind of plot, regarding the relative position of each family of curves because waves were measured roughly at the same distance from the instability threshold ϕ_c in combinations 1 and 2. In fact, using $\phi - \phi_0$ instead of $\phi - \phi_c$ brings changes only regarding the relative position of curves of the same combination. In figure 24(b) showing $dp_s/d\phi$ as a function of $\phi - \phi_0$, only a small offset along the ϕ -axis nonetheless remains, which means that the change in fluid viscosity also brings a change in the amplitude of the waves.

6.4. Influence of D/d_s on $dp_s/d\phi$

We now plot $dp_s/d\phi$ for combinations 6 and 7. Only the bed to particle diameter ratio D/d_s differs in combinations 6 and 7. Figure 25(a) shows $dp_s/d\phi$ as a function of ϕ . The origin of the shift along the ϕ -axis between curves computed from waves of combination 6 and curves computed from waves of combination 7 has already been explained in § 5.3. The value of the constant part of function $dp_s/d\phi$ is roughly

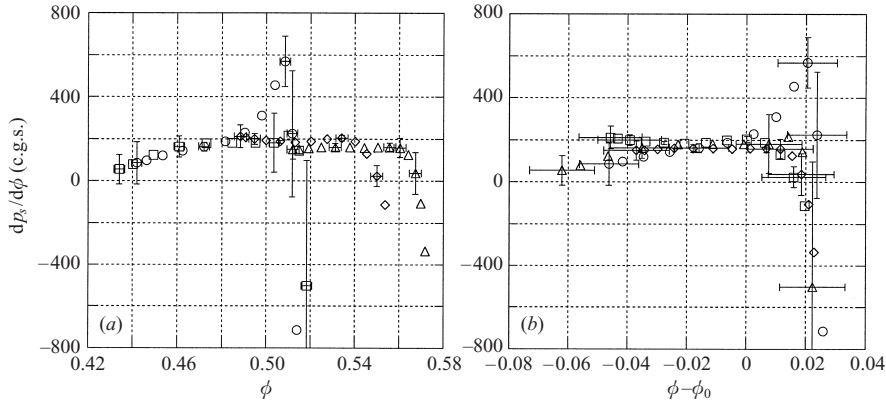


FIGURE 25. Influence of the bed to particle ratio D/d_s on $dp_s/d\phi$: (a) $dp_s/d\phi$ plotted against ϕ ; (b) $dp_s/d\phi$ plotted against $\phi - \phi_0$. \circ , $\phi_0 = 0.488$; \square , $\phi_0 = 0.496$: combination 7 with $D/d_s \approx 10$. \triangle , $\phi_0 = 0.549$; \diamond , $\phi_0 = 0.534$: combination 6 with $D/d_s \approx 25$.

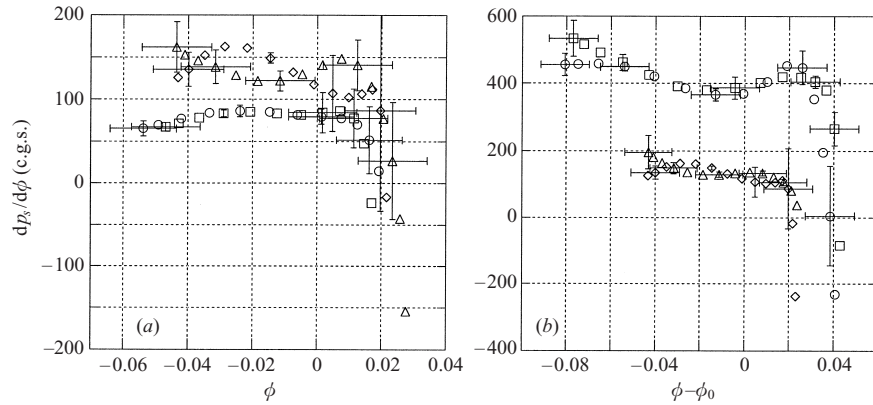


FIGURE 26. Influence of the characteristics of the beads on $dp_s/d\phi$: (a) $dp_s/d\phi$ as a function of $\phi - \phi_0$; \triangle , $\phi_0 = 0.535$; \diamond , $\phi_0 = 0.545$: combination 3 with $d_s v_t = 1.7$ c.g.s.; \square , $\phi_0 = 0.530$; \circ , $\phi_0 = 0.521$: combination 8 with $d_s v_t = 0.9$ c.g.s. (b) $dp_s/d\phi$ as a function of $\phi - \phi_0$; \triangle , $\phi_0 = 0.535$; \diamond , $\phi_0 = 0.545$: combination 3 with $\rho_s v_t = 36$ c.g.s.; \square , $\phi_0 = 0.558$; \circ , $\phi_0 = 0.550$: combination 1 with $\rho_s v_t = 88$ c.g.s.

the same for all curves. We obtain a good collapse into a single curve when plotting $dp_s/d\phi$ as a function of $\phi - \phi_0$, see figure 25(b).

6.5. Scaling laws for $dp_s/d\phi$

Now it remains to study the influence of particle characteristics on $dp_s/d\phi$. Figure 26(a) shows curves obtained with waves of combinations 3 and 8. The quantity $dp_s/d\phi$ is plotted as a function of $\phi - \phi_0$. It is clear that the value of the constant part of $dp_s/d\phi$ is greater when $d_s v_t$ is larger. In the same way, in figure 26(b), which shows curves obtained with waves of combination 1 and 3, we see that this value is greater when $\rho_s v_t$ is larger.

We thus plotted $dp_s/d\phi$ made dimensionless by $\rho_s v_t^2$ on figure 27(a) and by $\rho_f v_t^2$ on figure 27(b). These two graphs show that $dp_s/d\phi$ seems to scale with $\rho_s v_t^2$ or $\rho_f v_t^2$. Because of the scatter of the data, it is not possible to discriminate between these two

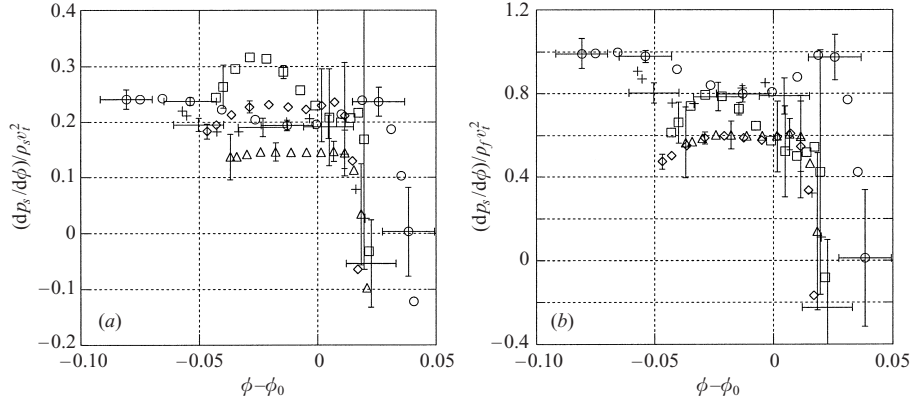


FIGURE 27. Scaling laws for $dp_s/d\phi$: (a) $(dp_s/d\phi)/\rho_s v_t^2$ as a function of $\phi - \phi_0$ for a representative sample of curves; (b) $(dp_s/d\phi)/\rho_f v_t^2$ as a function of $\phi - \phi_0$. \circ , $\phi_0 = 0.558$, combination 1; \square , $\phi_0 = 0.545$, combination 3; \times , $\phi_0 = 0.527$, combination 4; \triangle , $\phi_0 = 0.549$, combination 6; \diamond , $\phi_0 = 0.530$, combination 8.

scalings. In the same way, scaling μ_s by $(\rho_s - \rho_f)v_t^2$ would also provide a similar good collapse. In the limited range of f_0 , ϕ_0 and μ_f studied, we can therefore propose the following scaling laws for $dp_s/d\phi$, for most of the ϕ :

$$dp_s/d\phi \approx 0.2\rho_s v_t^2, \quad \text{or} \quad dp_s/d\phi \approx 0.7\rho_f v_t^2. \quad (6.2)$$

7. Discussion

By forming long-time averages synchronized with periodic forcing applied at the base of the fluidized bed, we have been able to observe the growth up the bed of one-dimensional voidage waves to their saturated finite amplitude. These saturated waves have a well-defined shape, with flat peaks of high particle concentrations and narrow troughs of low concentrations. Their variation with frequency and average particle concentration has been reported in § 3.4. These observations are all available to benchmark future new theories and computer simulations.

We have chosen to interpret the observations of the saturated voidage waves in terms of the simplest two-phase model of fluidized beds. We have thus measured the viscosity and pressure of the solid phase and found how they vary with particle concentration. It must be pointed out that these measurements were made over a limited range of parameters and only for saturated finite-amplitude one-dimensional voidage waves. It remains to be seen if they are applicable to a wider class, for instance three-dimensional flows.

Results for the viscosity of the solid phase, $\mu_s(\phi)$, were reported in § 5. The viscosity was found not to depend on the frequency of the periodic forcing, which means that the stresses should be characterized by a constant Newtonian viscosity rather than an elasticity or a more complex rheology. The solid phase viscosity was further found to depend little on the viscosity of the suspending fluid μ_f , the liquid flow rate q or equivalently the average particle concentration ϕ_0 , and the diameter of the tube D (except for combination 7 where the tube was narrow and for which wall-friction may have an effect). We found that the variation of the solid phase viscosity on the density ρ_s , diameter d_s and terminal velocity v_t of the particles and on the local

particle concentration could be approximated by the expression:

$$\mu_s(\phi) \approx 0.18 \frac{\rho_s d_s v_t}{\phi_{rlp} - \phi}. \quad (7.1)$$

This scaling law applies to the limited range of concentration in our experiments, $\phi > 0.5$, and indeed we would expect the solid phase viscosity μ_s to vanish as the concentration of the particles tends to zero. The evidence for the use of the particle density ρ_s in this expression instead of the density of the fluid ρ_f is not conclusive. We must recall here that our experiments are for liquid-fluidized beds with particles and liquid of similar density. In gas-fluidized beds, there would be a considerable difference between expression (7.1) and using the gas density ρ_f in place of the particle density ρ_s , with the latter option yielding more sensible values. We should also note here that the particle Reynolds number varies in our experiments over the range 20–200. We have not detected any simple variation with the Reynolds number, other than that used in the expression for the terminal velocity of an isolated particle v_t , but we certainly would expect a different behaviour at low particle Reynolds numbers.

The rapid increase in the solid phase viscosity as the concentration approaches the packing value ϕ_{rlp} explains the characteristic shape of the saturated voidage waves. When the particle concentration is equal to its mean value ϕ_0 , there is an exact balance between the drag on the particles and their weight. At higher concentrations, the drag wins and at lower concentration the weight wins, with an approximately linear variation of the imbalance with concentration over the small range of concentrations in our waves. It is the viscous stresses which principally equilibrate these slight imbalances between the weight and the drag. The same size of imbalance is equilibrated over a longer lengthscale at the high viscosity of the higher concentrations compared with the shorter lengthscale at the low viscosity of the lower concentrations; hence, the characteristic shape of the saturated voidage waves occurs with wide flat peaks of high concentrations and narrow troughs of low concentrations.

From our expression for the solid phase viscosity in a fluidized bed, we can also make a simple order-of-magnitude estimate of the wavelength of the saturated voidage waves. We equate the imbalance between the weight and the drag $(\rho_s - \rho_f)g\Delta\phi$ with the viscous term in the equation of motion $\mu_s v_t (2\pi/\lambda)^2$, where $\Delta\phi$ is the amplitude of the concentration variations and λ is the wavelength. Substituting our expression for the solid phase viscosity and the high-Reynolds-number estimate for the terminal velocity $v_t^2 \approx 0.8(\rho_s - \rho_f)gd_s/\rho_f$, we obtain:

$$\lambda \approx \frac{2.5 d_s}{\Delta\phi} \sqrt{\frac{\rho_s}{\rho_f}}. \quad (7.2)$$

The wavelength is expected to be a large multiple of particle diameter and to be slightly longer for heavier particles, as qualitatively observed in table 8. It should not depend upon frequency and be shorter for larger-amplitude waves (not clearly observed in table 8 owing to the short ranges of forcing frequency and amplitude). It is possible that this prediction of our simple order-of-magnitude estimate will be significantly modified by a more careful solution of the governing equation.

The solid phase pressure along with the inertial terms in the governing equation are small compared with the imbalances between the drag and the weight. Hence, the asymmetry in the form of the saturated voidage wave, for which they alone are responsible, is small. It was therefore more difficult to obtain accurate measurements of the solid phase pressure. Thus, while it appears that $dp_s/d\phi$ is constant over most

of the range of concentrations, the precise form at the highest concentrations remains unclear for our experiments. There is of course the possibility near to the maximum concentration that solid–solid contacts are forming a continuous network which would produce stresses not described properly by a solid phase pressure depending only on the particle concentration. While the smallness of the stabilizing pressure and destabilizing inertial terms is inconvenient experimentally, their smallness leads to a useful simplification in a theoretical study, in which the shape of the wave is first determined ignoring these small terms and then afterwards the saturated amplitude is found from the integral balance (6.1) between the stabilizing and destabilizing effects.

Experimentally, we found in §6 that the solid phase pressure did not depend on the frequency of the forcing. This means that a solid phase pressure varying with the particle concentration is a well-defined material property of a fluidized bed; at least, in the restricted range of our experiments. We also found that the solid phase pressure, like the solid phase viscosity, varied little with the viscosity of the liquid μ_f , the average particle concentration ϕ_0 , and the diameter of the bed (except for the very narrow bed in combination 7). The variation with the density ρ_s , diameter d_s , and terminal velocity v_t of the particles seems to be described by the expression:

$$dp_s/d\phi \approx 0.7\rho_f v_t^2, \quad \text{or} \quad dp_s/d\phi \approx 0.2\rho_s v_t^2, \quad (7.3)$$

over a range of most of the concentrations, with large negative values at the highest concentrations. Figure 27 does, however, display a large variation around the value 0.7, with values 0.5 and 0.9 suiting certain results better. It is unclear whether there is a systematic trend, say with the particle Reynolds number, between the different experiments which we have not detected, or whether the differences are just a reflection of the large experimental uncertainty in determining this small quantity. With the large variation between our results for the solid phase pressure, the choice between the alternative expressions $dp_s/d\phi \approx 0.7\rho_f v_t^2$ and $dp_s/d\phi \approx 0.2\rho_s v_t^2$ remains open. However, a strong dependence of the stabilizing term with ρ_s was observed by Ham *et al.* (1990).

Our experimental finding that $dp_s/d\phi$ is a positive constant for most concentrations before decreasing sharply to negative values at the highest concentrations is very different from all the expressions which have been proposed before in theoretical studies, see table 1. The previously proposed expressions have the pressure increasing monotonically, and mostly increasing sharply at the highest concentrations. As a consequence, our slightly asymmetric one-dimensional wave has a higher slope of concentrations when increasing in time compared with when decreasing, whereas previous theoretical studies had the opposite asymmetry (see for example Anderson *et al.* 1995). The traditional justification of these increasing expressions has been a consideration of the stability of the fluidized bed. Fluidized beds are more stable at higher concentrations[†]. In the competition between the stabilizing effects of pressure and destabilizing effects of inertia, it was therefore natural to expect the pressure to increase strongly at high concentrations. This argument for the pressure overlooked the behaviour of the destabilizing inertial terms. In order to explain the greater stability of concentrated beds, when the pressure term $dp_s/d\phi$ is constant as we have found, we must observe that the inertial terms can decrease as the concentration increases.

[†] Of course, at very high concentrations, the particles are in continuous contact, and under these conditions the particle pressure cannot be related to the local value of the concentration but instead is determined globally by the need to avoid further compaction of the bed.

This decrease accompanies the decrease in the kinematic wave speed $v_t \phi_0 n (1 - \phi_0)^{n-1}$ at higher concentrations.

As we have discussed above, the pressure term $dp_s/d\phi$ might be either $0.7\rho_f v_t^2$ or $0.2\rho_s v_t^2$. If the correct expression is the former, then the stabilizing pressure term would be proportional to the density of the fluid ρ_f while the destabilizing inertial term is proportional to the density of the particle ρ_s (plus an added mass term proportional to ρ_f) but with a smaller coefficient. In such circumstances we would speculate that there is a minimum density of the particles, around $1.5\rho_f$ for $n = 3$, for the destabilization to beat the stabilization at any concentration, i.e. fluidized beds of light particles would be stable.

In conclusion, we can say that while the simplest two-phase model of a fluidized bed might be misconceived from a theoretical point of view because simple expressions for the closures should not exist, it would appear that this simplest model is quite satisfactory for describing the one-dimensional voidage waves in the limited range of parameters that we have studied. It remains to be tested experimentally in more general flows, where for example an important role might be played by the large fluctuations in the bed which were averaged out by the sampling technique for the saturated wave.

We would like to thank R. Jackson for discussions during the course of this work. This work is part of the thesis of P.D. sponsored by the French Ministère de l'Éducation Nationale, de la Recherche et de la Technologie. It would not have been possible without the technical assistance of F. Ratouchniak, J.-C. Morellini and P. Cervetti.

REFERENCES

- ANDERSON, T. B. & JACKSON, R. 1967 Fluid mechanical description of fluidized beds. Equations of motion. *Ind. Engng Chem. Fundam.* **6**, 527–539.
- ANDERSON, T. B. & JACKSON, R. 1968 Fluid mechanical description of fluidized beds. Stability of the state of uniform fluidization. *Ind. Engng Chem. Fundam.* **7**, 12–21.
- ANDERSON, T. B. & JACKSON, R. 1969 Fluid mechanical description of fluidized beds. Comparison of theory and experiments. *Ind. Engng Chem. Fundam.* **8**, 137–144.
- ANDERSON, K., SUNDARESAN, S. & JACKSON, R. 1995 Instabilities and the formation of bubbles in fluidized beds. *J. Fluid Mech.* **303**, 327–366.
- BATCHELOR, G. K. 1991 The formation of bubbles in fluidized beds. In *Proc. Honoring John W. Miles on his 70th Birthday*. Scripps Institution of Oceanography, Ref. Series 91–24.
- DAVIDSON, J. F. & HARRISON, D. 1971 *Fluidization*. Academic.
- DAVIS R. H. & BIRDSELL K. H. 1988 Hindered settling of semidilute monodisperse and polydisperse suspensions. *AIChE J.* **34**, 123–129.
- DIDWANIA, A. K. & HOMSY, G. M. 1981 Flow regime and flow transitions in liquid-fluidized beds. *Intl J. Multiphase Flow* **7**, 563–580.
- EL-KAISSY, M. M. & HOMSY, G. M. 1976 Instability waves and the origin of bubbles in fluidized beds. Part 1: experiments. *Intl J. Multiphase Flow* **2**, 379–395.
- FANUCCI, J. B., NESS, N. & YEN, R.-H. 1981 Structure of shock waves in gas-particulate fluidized beds. *Phys. Fluids* **24**, 1944–1954.
- GLASSER, B. J., KEVREDIKIS, I. G. & SUNDARESAN, S. 1996 One- and two-dimensional travelling wave solutions in gas-fluidized beds. *J. Fluid Mech.* **306**, 183–221.
- GLASSER, B. J., KEVREDIKIS, I. G. & SUNDARESAN, S. 1997 Fully developed travelling wave solutions and bubble formation in fluidized beds. *J. Fluid Mech.* **334**, 157–188.
- HAM, J. M., THOMAS, S., GUAZZELLI, É., HOMSY, G. M., & ANSELMET M.-C. 1990 An experimental study of the stability of liquid-fluidized beds. *Intl J. Multiphase Flow* **16**, 171–185.

- HARRIS, S. E. & CRIGHTON, D. G. 1994 Solitons, solitary waves, and voidage disturbances in gas-fluidized beds. *J. Fluid Mech.* **266**, 243–276.
- HOMSY, G. M. EL-KAISSY, M. M. & DIDWANIA, A. 1980 Instability waves and the origin of bubbles in fluidized beds. Part 2: comparison with theory. *Intl J. Multiphase Flow* **6**, 305–318.
- JACKSON, R. 2001 *Dynamics of Fluidized Particles*. Cambridge University Press.
- NEEDHAM, D. J. & MERKIN, J. H. 1983 The propagation of voidage disturbances in a uniform fluidized bed. *J. Fluid Mech.* **131**, 427–454.
- MURRAY, J. D. 1965 On the mathematics of fluidization. Part 1. Fundamental equations and wave propagation. *J. Fluid Mech.* **21**, 465–493.
- NICOLAS, M., CHOMAZ, J.-M. & GUAZZELLI, É. 1994 Absolute and convective instabilities of fluidized beds. *Phys. Fluids* **6**, 3936–3944.
- NICOLAS, M., CHOMAZ, J.-M., VALLET, D. & GUAZZELLI, É. 1996 Experimental investigations on the nature of the first wavy instability in liquid-fluidized beds. *Phys. Fluids* **8**, 1987–1989.
- RICHARDSON, J. F. & ZAKI, W. N. 1954 Sedimentation and fluidization. Part 1. *Trans. Inst. Chem. Engrs* **32**, 35–53.
- SCHÜGERL, K. 1971 Rheological behavior of fluidized systems. In *Fluidization* (ed. J. F. Davidson & D. Harrison), chap. 6. Academic.

B.8 Experimental study of gravity-driven dense suspension jets

M. NICOLAS

Phys. Fluids **14** (10), 3570–3576 (2002).

Experimental study of gravity-driven dense suspension jets

Maxime Nicolas

IUSTI, Technopôle de Château-Gombert, 5 rue Fermi, 13453 Marseille cedex 13, France

(Received 12 April 2001; accepted 12 July 2002; published 5 September 2002)

This article presents experimental results from a study of a jet of dense suspension falling under gravity in a quiescent liquid bath of miscible liquid. The initial jet velocity v_0 scales with the square of the initial jet diameter. Four different flow behaviors are observed. The jet remains cylindrical and stable when viscous forces are dominant. A capillary-like instability with formation of blobs occurs when a Reynolds number based on the particle diameter and a free-falling velocity is over unity. The blobs are stable and settle without changing shape only for a blob Reynolds number below a critical number. Dispersion of the jet particles is observed when the particle Reynolds number is over 1, and an atomization behavior occurs when particle inertia is large compared to viscous forces, i.e., when the Stokes number of the particles is large compared to unity. © 2002 American Institute of Physics. [DOI: 10.1063/1.1504447]

I. INTRODUCTION

This work is part of the general study of granular matter immersed in a fluid, with interactions between grains through hydrodynamics and direct contact. In many industrial or natural situations, the volume fraction of solid particles is not homogeneous, but may vary from one point to another between zero (no particles at all) up to a maximum value for which the particles are in contact. This is the case, for example, when a powder is poured into a liquid before a mixing process or in a fluidization reactor in the bubbling regime. In such situations, an interface between the dense suspension and the clear fluid can be defined. This is not a classical interface at which there is interfacial tension, but a well-defined surface where particle fraction changes abruptly.

Few situations where the suspension is strongly inhomogeneous have been studied. One of them is the settling of a swarm or a cluster (often termed a “blob”) of solid particles in a large volume of liquid. Since Brinkman,¹ many works have focused on the viscous drag exerted by the fluid on the swarm.^{2,3} Adachi and co-workers⁴ computed the settling velocity of a dilute swarm and studied experimentally the break-up of dilute swarms. The break-up or dilution of blobs may be caused by a shear flow. Kao and Mason⁵ and Powell and Mason⁶ have experimentally determined the effect of shear flow properties on the dispersion of blobs of neutrally buoyant particles.

More recently, Nitsche and Batchelor⁷ have numerically studied the individual paths of particles in a dilute swarm undergoing breakup, and compared their results with an experiment at low Reynolds number but with a concentrated blob of particles. The settling of a dilute suspension blob and its break-up was also considered by Schaffinger and Machu.⁸

If the suspension is modeled as an effective fluid, the dispersion of a dense suspension injected in a large volume of clear fluid is a configuration analogous to a fluid-into-fluid jet. Several kinds of jets may be taken in consideration. The everyday experiment of the water jet exiting from a tap is

one. Under certain conditions, especially if the flow-rate is not sufficient, the jet breaks in droplets. This capillary instability is driven by the surface tension at the water/air interface and must be considered for any liquid into gas jet. When the flow-rate is very high, the drops undergo secondary breakup to create a fog or a mist. This phenomenon is atomization and depends strongly on the nozzle conditions (velocity profile of the jet and shape of the nozzle).^{9,10}

If a liquid is injected in another liquid, different behavior exists depending upon whether the liquids are miscible or not. Moreover, the viscosity of the outer liquid may be an important parameter.^{11,12}

The situation where the jet fluid is lighter than the outer fluid is also of interest. This is the case for plumes or diffusion flames. The relevant parameters are the Richardson number and the density ratio.^{13,14}

The goal of this article is to present an overview of the behavior of the gravity-driven jet of a dense suspension into a miscible liquid bath. We present an experimental study of jets of dense suspensions falling in a quiescent liquid. The dense suspension (roughly 60% particle volume fraction) is prepared as a random packing of spherical particles and is released from a cylindrical tube. Size and density of the particles, as well as the density and viscosity of the liquid, were varied. Under certain conditions, the jet is unstable and exhibits the formation of clusters, discrete groups of particles which are of concentration similar to the original dense suspension. For larger flow rates, the suspension of the jet is diluted by the flow and mixing with the clear liquid occurs.

After a presentation of the experimental setup (Sec. II) and of the relevant parameters (Sec. III), the experimental results are presented in Sec. IV. A correlation for the initial velocity of the jet is proposed (Sec. IV A) before the different jet regimes are presented (Sec. IV B). The dynamics of cluster formation and evolution are shown in Sec. IV C, and a discussion about the physical origin of the instability is presented in the last section.

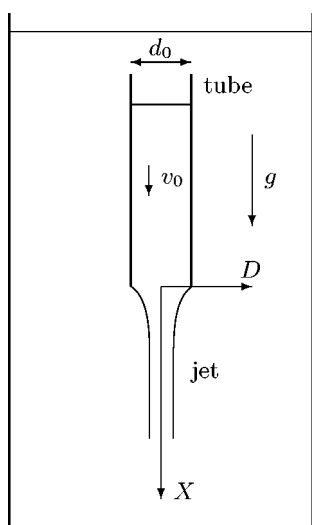


FIG. 1. Sketch of the experimental setup.

II. EXPERIMENTAL SETUP

The experimental setup is sketched in Fig. 1. The tank was of rectangular $10 \times 8 \text{ cm}^2$ cross section and 50 cm in height, made with glass plates. It was filled with 4 l of liquid. The suspension reservoir was a cylindrical glass tube held vertically on the upper part of the tank and was fully submerged, with its upper section 5 mm below the liquid surface. The lower orifice was closed by a thin moveable plate which could rotate around a vertical axis without disturbing the liquid. The tubes diameters d_0 were ranging from 4 to 8 mm. All the tubes were 20 cm in length. The error in verticality of the tube was kept below 0.5° .

Seven different sets of particles and four different liquids were used for the experiments. Particle and liquid characteristics are given in Tables I and II. A small amount of soap was added to water to prevent cohesion of the particles. The particle/liquid pairs were chosen to allow a wide range of jet velocity. Thirty different combinations of particles, liquid and tube diameter were used during the experiments.

The tube-to-particle diameter ratio d_0/d_p was varied from 15 to 38. No experiment could be made for $d_0/d_p < 15$ because of particles arching across the tube, which prevented a stationary flow of the suspension. One exception is the iron/water suspension jet where $d_0/d_p = 6$ without arches, apparently because of the large density of iron.

The suspension was prepared with the same liquid as the tank liquid. The suspension was first strongly stirred to re-

move air bubbles, and then was pipetted into the closed tube. The particles settled to form a random packing supported by the gate.

The initial volume fraction of particles ϕ_0 in the tube was measured for each set of particles. As no compaction process other than gravity was involved, the packing of particles in the tube was loose. With systematic measurements, we have found that the particle volume fraction can be correlated with the tube-to-particle diameter ratio through the empirical equation

$$\phi_0 = 0.62 - 0.3 \left(\frac{d_p}{d_0} \right). \quad (1)$$

The limit value of 0.62 is below the volume fraction of a random-close packing (roughly 0.64) because the packings in the tubes were loose and because of the relatively small value of d_0/d_p . For all experiments, the particle volume fraction was $0.57 < \phi_0 < 0.61$.

The tank was illuminated with white light from a slide projector, and a digital camcorder was focused below the tube to capture video images of the jets. As particles were reflective, the suspension appeared white on a black background. It must be noted here that all pictures presented in this article are printed with an inverted grayscale so that particles are dark on a white background. The acquisition rate was 25 frames per second. For each combination of particles, liquid and tube, a video sequence of a minimum of 125 consecutive frames was time averaged to obtain the envelope of the jet. The averaged image was thresholded and the average contour of the jet $\bar{D}(X)$ was then digitized.

During the fall of the suspension in the tube, it remained packed and the upper front stayed sharp. The velocity of the upper front was the same as the outlet velocity v_0 , i.e., the suspension flowed as a solid body during the fall inside the tube. This was checked by velocity measurements with a spatio-temporal plot along the jet axis. The spatio-temporal plot was obtained by recording the vertical line of pixels along the axis of the tube.

At the opening of the gate, the packed suspension accelerated until a stationary downward movement was attained, with a constant velocity v_0 . A slight acceleration also occurred when the height of the remaining suspension in the tube was of the order of a few tube diameters. For example, the time evolution of the height of the suspension of acrylic resin particles (D in Table I) in water is plotted in Fig. 2. It has been checked that the velocity of discharge was independent of the initial filling height of the tube, as in the unloading of a silo of dry granular media.¹⁵

TABLE I. Particles characteristics.

Code	Material	d (μm)	ρ_p (g cm^{-3})
A	Polystyrene	202 ± 16	1.05
B	Acrylic resin	212 ± 16	1.19
C	Leaded glass	214 ± 9	4.0
D	Acrylic resin	230 ± 21	1.19
E	Polystyrene	381 ± 39	1.05
F	Glass	193 ± 24	2.5
I	Iron	1000	7.96

TABLE II. Liquid characteristics. Kinematic viscosity and density are given for a temperature of 20°C .

Liquid	ν_f (cSt)	ρ_f (g cm^{-3})
Water	1	1
Silicone oil	5	0.92
Silicone oil	10	0.93
Silicone oil	20	0.95
Silicone oil	1000	0.97

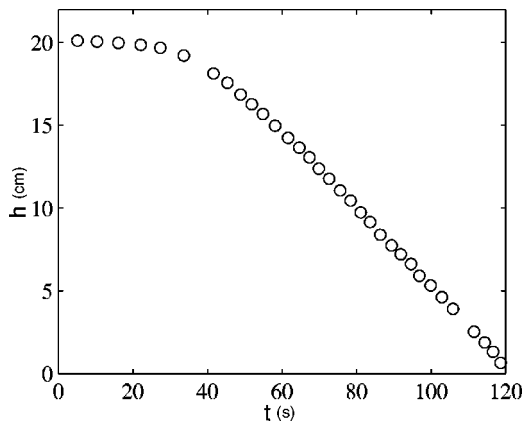


FIG. 2. Discharge of the tube for a suspension of acrylic resin particles (D in Table I) in water. The tube diameter was $d_0=6.95$ mm. Initial height was 20.1 cm.

III. DIMENSIONLESS PARAMETERS

The characteristic length of the system is the tube diameter d_0 , and the characteristic velocity scale is the velocity of the suspension at the outlet of the tube. Thus we introduce the non-dimensional position $X=x/d_0$ which is zero at the tube outlet, the jet diameter is $D=d/d_0$, and the non-dimensional velocity is $V=v/v_0$. If the particle volume fraction is constant during the flow, the mass conservation equation is written as

$$VD^2=1 \quad (2)$$

for $X \geq 0$.

As the suspension flow is driven by gravity, an important dimensionless group is the ratio of the clear liquid density ρ_f with the jet density ρ . The latter depends on the particle density ρ_p and the volume fraction ϕ_0 of the suspension. The density ratio parameter is written as

$$\alpha = \frac{\rho_f}{\rho} = \frac{\rho_f}{\phi_0 \rho_p + (1 - \phi_0) \rho_f}, \quad (3)$$

and ranges theoretically between 0 (heavy particles and high volume fraction) and 1 (neutrally buoyant particles or very dilute suspension). In the experiments, the density ratio was $0.201 < \alpha < 0.971$.

The nozzle velocity v_0 at the bottom outlet of the tube depends on ρ_p , ρ_f , the liquid kinematic viscosity ν_f , and the ratio between the particle mean diameter d_p and the tube diameter d_0 . As the suspension falls into a quiescent liquid of viscosity ν_f , the Reynolds number at the outlet of the tube is

$$R_0 = \frac{v_0 d_0}{\nu_f}, \quad (4)$$

where the subscript 0 indicates that this number is computed at the nozzle outlet ($X=0$). Taking the gravitational acceleration g into account, it is also possible to make the jet velocity dimensionless in the form of a Froude number

$$F_0 = \frac{v_0}{\sqrt{g d_0 (1 - \alpha)}}. \quad (5)$$

This number has the same significance as the Richardson number $R_i = 1/F_0^2$ widely used in the flames and plumes literature.^{13,14} Taking the particle diameter as the scaling length of the problem, one can define also a particle Reynolds number $R_p = (d_p/d_0)R_0$, and a particle Froude number $F_p = \sqrt{d_p/d_0}F_0$. At the scale of the particle, the ratio of gravity force to the viscous force is thus

$$M_p = \frac{R_p}{F_p} = \sqrt{\frac{d_p}{d_0}} \frac{R_0}{F_0}. \quad (6)$$

This number is analogous to a Reynolds number where the scaling velocity is a free-falling velocity $v_g = \sqrt{g d_p (1 - \alpha)}$. Last, the ratio of particle inertia to viscous force is characterized by a Stokes number

$$S = \frac{1}{9} \frac{\rho_p d_p v_0}{\nu_f \rho_f}. \quad (7)$$

IV. RESULTS

A. Initial velocity of the jet

As noted above, the initial velocity v_0 is governed by the physical parameters of the suspension and the friction against the inner wall of the tube. For each combination of particles, liquid and tube diameter, this velocity was observed to be constant in time and independent of the filling height. Modeling the suspension as an effective liquid of viscosity $\eta_s = \eta_r \eta_f$ (where η_r is the nondimensional relative viscosity), we can assume a balance between the shear force on the tube wall and the weight of the suspension:

$$2 \pi r \eta_s \left(\frac{\partial v}{\partial r} \right) = - \pi r^2 (\rho - \rho_f) g, \quad (8)$$

where $v(r)$ is the axial velocity profile and r is the radial coordinate. As the suspension is highly concentrated, the relative viscosity is large and the velocity profile is rather flat. After integration of (8), the mean suspension velocity in the tube is

$$v_0 = \frac{1}{32 \alpha \eta_r} \frac{(1 - \alpha) g d_0^2}{\nu_f}, \quad (9)$$

which can be written as

$$F_0 = \left(\frac{R_0}{32 \alpha \eta_r} \right)^{1/2}. \quad (10)$$

The initial velocity was measured for each particle/liquid/tube combination. The slowest jet was observed for acrylic resin particles (B in Table I) in viscous silicone oil ($\nu_f = 10^3$ cSt), while the most rapid jet was obtained for iron particles (I in Table I) in water. The Reynolds number defined by (4) ranged from 7×10^{-4} to 5×10^3 , whereas the Froude number defined by (5) ranged from 10^{-3} to 3.9. The Froude number is plotted versus the Reynolds number in Fig. 3, and the experimental data are compared with (10), plotted in solid line for η_r of the order of 100. The agreement is good on eight decades and the scattering of the experimental data around the theoretical curve may be explained by the uncertainty on the relative viscosity η_r , which is known to

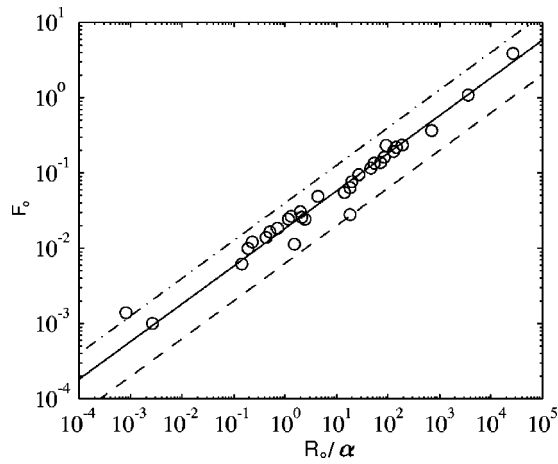


FIG. 3. Correlation between Froude (F_0) and Reynolds (R_0) numbers for different jet experiments. Upper dashed line is Eq. (10) computed with $\eta_r = 20$, the solid line (best fit) is for $\eta_r = 93$ and the lower dashed line is for $\eta_r = 800$.

be very sensitive to the particle volume fraction and the suspension configuration. The upper dashed line of Fig. 3 has been computed with $\eta_r = 20$ while the lower dashed line has been computed with $\eta_r = 800$.

B. Jet regimes

Four different flow regimes of the suspension jet have been observed: stable jet, unstable jet with blobs formation, spiral jet with dispersion and atomized jet.

It has been found experimentally that except for an M_p number below 1 (typically $R_0 < 10^{-3}$), all the suspension jets were unstable. Figure 4(a) shows a jet obtained with acrylic resin particles (B in Table I), silicone oil ($\nu_f = 10^3$ cSt) and a tube diameter $d_0 = 6$ mm, with $M_p = 9.5 \times 10^{-2}$, $R_0 = 7 \times 10^{-4}$. After a contraction of the jet diameter due to the acceleration of the suspension, it reached a constant value. Within experimental error, no change in the jet diameter was observed until the jet reached the bottom of the tank, 30 cm below the reservoir tube.

At $M_p \approx 0.2$, a slight variation of the jet diameter was observed, with a typical wavelength of $3 d_0$, and an amplitude of 10% of the jet diameter. Far from the tube, this instability resulted in the formation of stretched clouds of particles. This first kind of instability was more pronounced for larger M_p numbers. For example, Fig. 4(b) shows a jet for $M_p = 3.3$. In this regime, the jet exhibited a capillary-like instability. Jet diameter modulation occurred soon after the contraction length (one tube diameter), and increased in amplitude with increasing distance from the tube outlet. Eventually, the jet broke up into blobs of dense suspension separated by a thin column of particles. The formation and evolution of these blobs are presented in more detail in Sec. IV C.

As long as the particle Reynolds number was below 1, no dispersion of the jet was observed. Above this value, the jet was fast enough to allow the external shear flow to tear away the peripheral particles from the dense suspension. This is shown in Fig. 4(c), where $R_p = 3.9$. One can also see

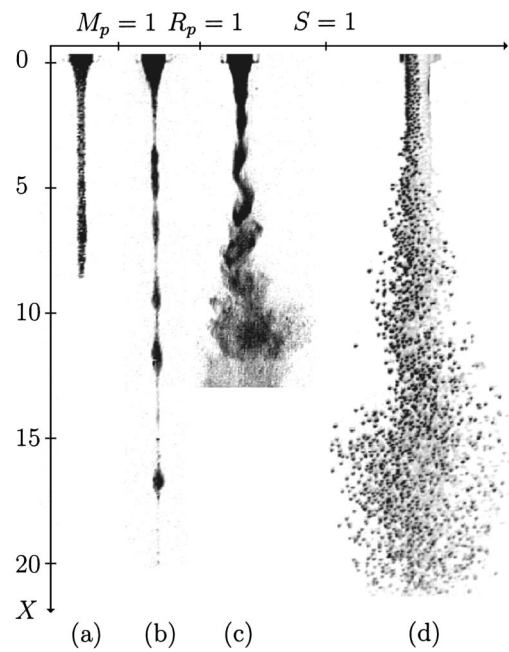


FIG. 4. Frame captures of various jet experiments: (a) acrylic resin particles (B), silicone oil ($\nu_f = 10^3$ cSt), $d_0 = 6$ mm, $R_0 = 7 \times 10^{-4}$, $M_p = 9.5 \times 10^{-2}$, $R_p = 2.5 \times 10^{-5}$, $S = 3.4 \times 10^{-6}$; (b) polystyrene particles (A), silicone oil ($\nu_f = 20$ cSt), $d_0 = 6$ mm, $R_0 = 0.22$, $M_p = 3.3$, $R_p = 7.3 \times 10^{-3}$, $S = 9 \times 10^{-4}$; (c) acrylic resin particles (B), water, $d_0 = 6$ mm, $R_0 = 130$, $M_p = 103$, $R_p = 3.9$, $S = 0.5$; (d) iron particles (I), water, $d_0 = 6$ mm, $R_0 = 5086$, $M_p = 531$, $R_p = 848$, $S = 750$. The horizontal scale indicates increasing dimensionless numbers from left to right. Vertical scale is the position below the tube outlet.

on this picture that the jet did not remain vertical, but followed a sinuous path ($X \approx 5$). Eventually, the suspension was diluted and the particles formed a cloud of dilute suspension ($X \approx 10$) before reaching the bottom of the tank. In this regime, soon after the contraction, the jet also exhibited a blob formation, but these blobs were too fast to reach a stationary state (see Sec. IV C for details). For a $R_p > 10$, the

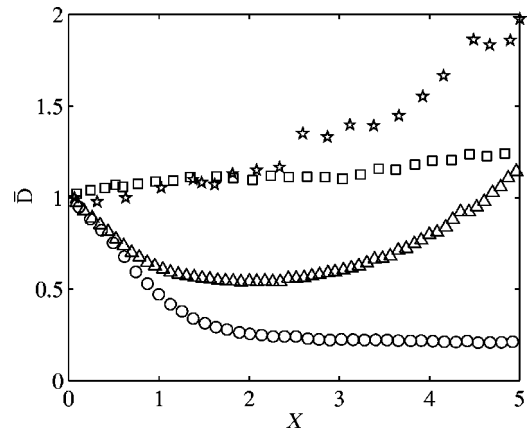


FIG. 5. Average contour of the jet $\bar{D}(X)$ for different jet behaviors: $R_0 = 0.22$, $M_p = 3.3$, $R_p = 7.3 \times 10^{-3}$ and $S = 9 \times 10^{-4}$ (circles), no dispersion of the jet; $R_0 = 170$, $M_p = 118$, $R_p = 4.5$ and $S = 0.6$ (triangles), dispersion of the jet; $R_0 = 1274$, $M_p = 221$, $R_p = 45$ and $S = 20$ (squares) and $R_0 = 5086$, $M_p = 531$, $R_p = 848$ and $S = 750$ (stars), atomization regimes.

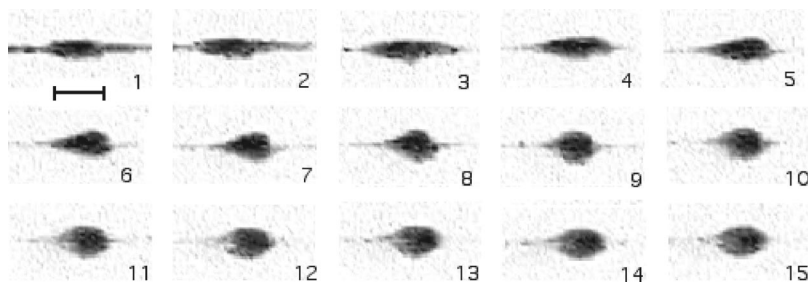


FIG. 6. Sequence of photographs of a single blob emanating of a jet of polystyrene particles (A in Table I) in silicone oil ($\nu_f=20$ cSt) with $R_0=0.22$ and $M_p=3.3$. Reynolds number of the blob is $R_b=5$, time interval between two snapshots is 0.4 s. The horizontal scale indicates the tube diameter $d_0=6$ mm.

jet did not produce blobs but was dispersed by its own sinuous movement.

In the previous observations of the jet behavior, the Stokes number defined by (7) remained below the unity. Another behavior was noticed for Stokes numbers larger than one. For such fast jets [Fig. 4(d), with $S=750$], no contraction of the jet diameter was observed. On the contrary, the dispersion of the jet occurred at the outlet of the tube. This behavior was similar to the atomization of fast liquid jets into a gas.

Figure 5 illustrates the average contour of the suspension jet for different regimes. In the blob regime without dispersion (circles), the jet averaged diameter \bar{D} decreases and reaches a constant value $D_\infty=0.25\pm 0.05$ for $X>3$. The mass conservation equation (2) has been checked for this case with jet velocity measurements. Corresponding dimensionless numbers are given in the figure caption. When dispersion occurs (triangles), the $\bar{D}(X)$ curve has a minimum and then increases because of the combination of the spiral movement of the jet and the dispersion of the suspension.

C. Blobs evolution

We focus in this section on the clusters of suspended particles which we term “blobs.” A capillary-like instability has been observed for $M_p\geq 1$ and $R_p\leq 1$. When the instability was fully developed, the jet broke up into blobs of dense suspension, separated by a thin column of one particle diameter [see Fig. 4(b)]. The “birth” of a blob is depicted in Fig. 6, a sequence of photographs of the same blob of polystyrene particles (A in Table I) in silicon oil ($\nu_f=20$ cSt), where downward direction is from left to right. The first snapshot (1) shows the blob centered at $X=6.9$. The shape is stretched, with an aspect ratio of 5 (ratio of vertical length on the horizontal length). The photographs 2–8 show a deformation of the blob: particles seem to gather together and to accumulate at the bottom of the blob. The aspect ratio decreases during this evolution from $X=7.5$ to $X=13.6$. Following photographs (9–15) show an almost stationary shape of the blob, with a final aspect ratio of 1.7 ± 0.1 for $13.6 < X < 22.6$.

The blob velocity was $v_d=16.9$ mm/s throughout the fall, and was independent of the shape (and aspect ratio) of the blob. The corresponding Reynolds number for the blob was $R_b=5$. The blob velocity is very close to the settling velocity of a solid sphere of diameter $0.65d_0$ (typical size of the blob perpendicularly to the gravity). Thus, the granular nature of the suspension blob does not seem to have any

observable effect on its velocity. Such a blob was observed to have a constant shape until it nears the bottom of the tank ($X=50$). Near the bottom, the blob was seen to evolve into a ring, itself evolving in a cascade of smaller rings, as seen in Fig. 7, a sequence of snapshots captured for another experiment. This ring formation has already been observed by Schafinger and Machu⁸ in the case of a dilute suspension.

Blobs were not isolated in a large volume of liquid but were vertically separated by a thin column of particles. This pattern was stationary. That means that each blob was losing particles behind whereas it was gaining some ahead. This is evidenced by the results shown in Fig. 8, a spatio-temporal diagram of an experiment with polystyrene particles (E in Table I) and silicone oil ($\nu_f=20$ cSt). The horizontal axis is time (in seconds) and the vertical axis is the pixel line centered on the axis of the jet for X between 7 and 19 (part of the developed blobs area). Black bold lines are blobs falling with a constant velocity. Thinner lines are isolated particles between two successive blobs. One can see on this diagram that some particles lost by a blob decelerate, then are again accelerated until they are caught by the following blob. The slopes of the bold lines are slightly different, which means that, eventually, two successive blobs will interact and merge. This merging occurred too close to the bottom of the tank to give a clear understanding of blob interaction.

In the dispersion regime ($R_p\geq 1$), the dispersion occurred only after some blobs of particles have been formed, just after the contraction of the jet diameter [as shown in Fig. 4(d)]. For example, an experiment with acrylic resin particles (B in Table I) and water produced a jet with $R_p=0.9$, creating rapid blobs with a typical velocity of 6.5 cm/s and a blob

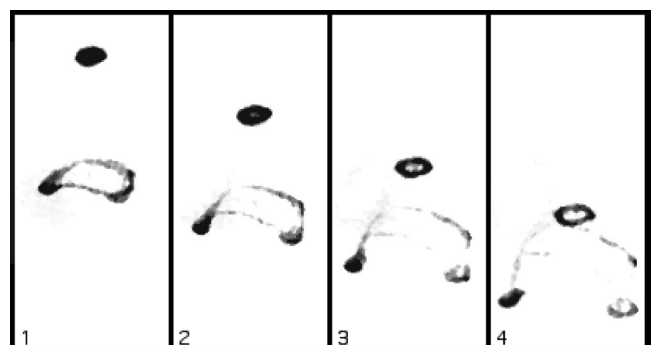


FIG. 7. Sequence of photographs of two blobs destabilizing into a ring at the bottom of the tank. This was obtained with acrylic resin particles (D in Table I), silicone oil ($\nu_f=20$ cSt), $d_0=5$ mm. The time interval between two snapshots is 0.4 s.

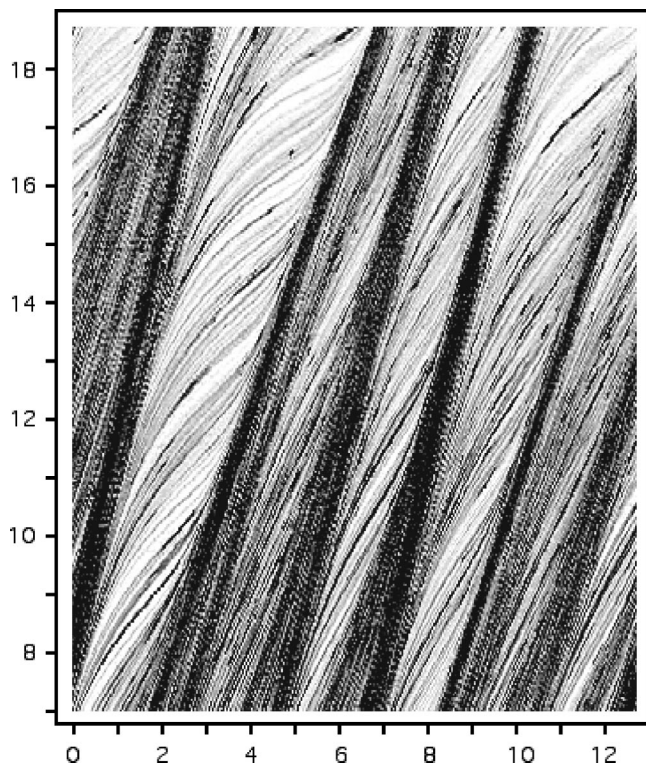


FIG. 8. Spatio-temporal plot of a jet in the blob regime obtained with polystyrene particles (E in Table I), silicone oil ($\nu_f=20$ cSt) and $R_0=0.18$, $M_p=4.5$. Vertical axis is position along the jet axis (in units of tube diameter) and horizontal axis is time (in seconds).

Reynolds number $R_b = 168$. Figure 9 shows a ten photograph sequence of such a blob. The initially stretched blob of particles curved during the fall, exhibiting a sinuous movement, and eventually was dispersed into a cloud of separated particles. No stationary movement of the blob could be observed for this regime. The transition between a stationary blob and a dispersible blob occurred for an R_b between 26 and 124, but no experimental data was available to reduce the uncertainty on the critical blob Reynolds number.

V. DISCUSSION AND CONCLUSION

The transitions between different flow behaviors are characterized by some dimensionless groups. The dispersion of the jet occurs when *liquid* inertia, at the scale of a particle, becomes dominant over the viscous force. The particle Reynolds number R_p is thus a good criterion to characterize the dispersion phenomenon, even if the dispersion occurs after an acceleration distance of the jet. When the *particle* inertia

is large compared to the viscous force ($S \gg 1$), the particle trajectories are decorrelated from the liquid flow field, and atomization occurs.

One of the major questions raised by these experimental results is the physical origin of the capillary-like instability, leading to the formation of blobs. It may exist also for $M_p \gg 1$ but may be hidden by the sinuous movement of the jet and the dispersion of the blobs.

In the case where M_p was below 1, the liquid was a viscous silicone oil ($\nu_f=1000$ cSt). In this configuration, the force needed to separate two particles initially in contact is infinite for perfectly spherical particles, and must be very large for real particles with rough surfaces. Therefore, the characteristic time to separate particles and the characteristic time of the instability may be larger than the settling time of the suspension until the bottom of the tank. No diameter variation was observed in this configuration, and we conclude that hydrodynamic “bonds” between adjacent particles are strong enough to keep the jet in a cylindrical shape.

The dense suspension can be seen as an effective liquid, with a viscosity depending on the particle volume fraction. This effective viscosity can be computed with various empirical relations, for example that proposed by Leighton and Acrivos:¹⁶ the ratio of the suspension viscosity to the clear liquid viscosity is computed by $\eta_r = [1 + 1.5\phi_0 / (1 - \phi_0 / \phi_{max})]^2$. In our case, the typical particle volume fraction is $\phi_0 \approx 0.61$ and the maximum volume fraction for the suspension out of the tube may be slightly larger than 0.62 when the suspension is out of the tube. If we choose $\phi_{max} \approx 0.63$, $\eta_r \approx 800$. This contrast of viscosity is large, and one may wonder whether it could be responsible for the jet instability.

In order to test this hypothesis, a liquid-into-liquid jet experiment was performed. Dyed glycerol was injected into salted water. The amount of salt was adjusted to have a density difference $\alpha_L = 0.968$. Glycerol was chosen because of its high viscosity (roughly 800 cSt) and its miscibility with water. The observed jet was cylindrical on all the length of the tank and very stable. The Reynolds number of the liquid jet was $R_L = 11.3$. The shape of the jet is compared to a suspension jet in Fig. 10. The suspension jet was made of polystyrene particles (A in Table I) into water, with a 6 mm tube. The density ratio was $\alpha = 0.97$ and the jet Reynolds number $R_0 = 13.8$, both almost equal to α_L and R_L . This comparison shows that the contrast of viscosity cannot explain the suspension jet instability. This instability is therefore intrinsic to the particulate structure of the jet.

The use of the dimensionless number M_p , scaling as the size of the particles to the power $\frac{3}{2}$, suggests that the

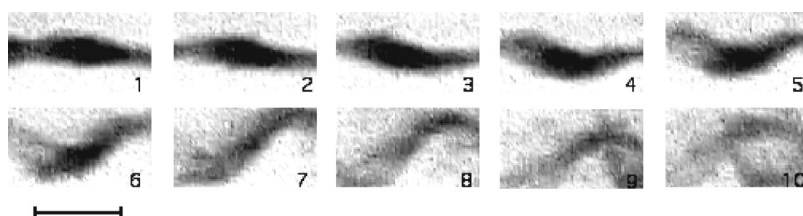


FIG. 9. Sequence of photographs of a single blob emanating of a jet of acrylic resin particles (B in Table I) in water ($R_0=16.3$, $M_p=58.5$). Reynolds number of the blob is $R_b = 168$. Time interval between two snapshots is 0.04 s. Tube diameter was $d_0 = 4$ mm.

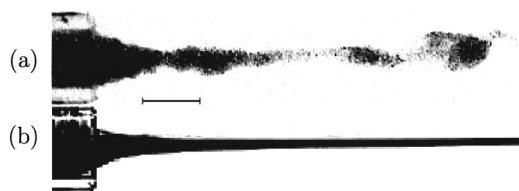


FIG. 10. Snapshot of a suspension jet (polystyrene particles A in water) with $R_0=13.8$ and $\alpha=0.97$ (a) and snapshot of a glycerol jet into salted water with $R_L=11.3$ and $\alpha_L=0.968$ (b).

capillary-like instability arises when the gravity force is dominant compared to the viscous force. Qualitatively, this could explain that for $M_p > 1$, the hydrodynamic bonds are not strong enough to stabilize the jet under diameter perturbations. But the small range of particle diameters used in the experiments can not help to conclude that M_p is the only relevant dimensionless group for the capillary-like instability. Indeed, the interstitial liquid pressure may play a role when the deformation of the jet occurs, and the flow of the liquid between the suspension and the clear liquid may hence be considered.

The effect of the particle volume fraction on the instabilities has not been investigated in this work, but a previous study of Schaflinger and Machu⁸ has shown that even for low volume fraction ($\phi_0 \approx 0.05$), a suspension column is unstable and produces blobs. Therefore, we conclude that the hydrodynamic interactions between particles in the suspension have to be taken in account in order to explain this capillary-like instability. The large volume fraction gradient at the interface of the jet is also a parameter of interest and may lead to an asymmetry of forces and stresses acting on the particles at the boundary of the jet. Further work is thus needed to explain this instability.

The behavior of gravity-driven dense suspension jets has been investigated experimentally. A broad range of Reynolds number has been studied. The main behaviors of the jets were a stable cylindrical jet for $M_p \lesssim 1$, an unstable jet with blob formation for $M_p \gtrsim 1$ and $R_p \lesssim 1$, an unstable jet with spiral movements and dispersion for $R_p \gtrsim 1$, and an atomized jet for $S \gg 1$. The velocity of the suspension in the tube res-

ervoir was seen to be independent of the filling height (like in a silo of dry granular matter), and was seen to scale as the square power of the tube opening.

ACKNOWLEDGMENTS

The author thanks M. Piot for help during the experiments, and O. Pouliquen and J. F. Morris for a critical reading of the manuscript. This work was supported by the French Ministère de la Recherche through a grant ACI "Écoulements granulaires en géophysique."

- ¹H. C. Brinkman, "A calculation of the viscous force exerted by a flowing fluid on a dense swarm of particles," *Appl. Sci. Res., Sect. A* **1**, 27 (1947).
- ²F. P. Bretherton, "Inertial effects on clusters of spheres falling in a viscous fluid," *J. Fluid Mech.* **20**, 401 (1964).
- ³C. K. W. Tam, "The drag on a cloud of spherical particles in low Reynolds number flow," *J. Fluid Mech.* **38**, 537 (1969).
- ⁴K. Adachi, S. Kiriyama, and N. Yoshioka, "The behavior of a swarm of particles moving in a viscous fluid," *Chem. Eng. Sci.* **33**, 115 (1978).
- ⁵S. V. Kao and S. G. Mason, "Dispersion of particles by shear," *Nature (London)* **253**, 619 (1975).
- ⁶R. L. Powell and S. G. Mason, "Dispersion by laminar flow," *AIChE J.* **28**, 286 (1982).
- ⁷J. M. Nitsche and G. K. Batchelor, "Break-up of a falling drop containing dispersed particles," *J. Fluid Mech.* **340**, 161 (1997).
- ⁸U. Schaflinger and G. Machu, "Interfacial phenomena in suspensions," *Chem. Eng. Technol.* **22**, 7 (1999).
- ⁹R. D. Reitz and F. V. Bracco, "Mechanism of atomization of a liquid jet," *Phys. Fluids* **25**, 1730 (1982).
- ¹⁰S. P. Lin and D. J. Kang, "Atomization of a liquid jet," *Phys. Fluids* **30**, 2000 (1987).
- ¹¹A. Reynolds, "Observations of a liquid-into-liquid jet," *J. Fluid Mech.* **14**, 552 (1962).
- ¹²J. C. Mollendorf and B. Gebhart, "An experimental and numerical study of the viscous stability of a round laminar vertical jet with and without thermal buoyancy for symmetric and asymmetric disturbances," *J. Fluid Mech.* **61**, 367 (1973).
- ¹³B. M. Cetegen, "Behavior of naturally unstable and periodically forced axisymmetric buoyant plumes of helium and helium-air mixtures," *Phys. Fluids* **9**, 3742 (1997).
- ¹⁴B. M. Cetegen and Y. Dong, "Experiments on the instability modes of buoyant diffusion flames and effects of ambient atmosphere on the instabilities," *Exp. Fluids* **28**, 546 (2000).
- ¹⁵R. L. Brown and J. C. Richards, *Principles of Powder Mechanics* (Pergamon, Oxford, 1970).
- ¹⁶D. Leighton and A. Acrivos, "Viscous resuspension," *Chem. Eng. Sci.* **41**, 1377 (1986).

ANNOUNCEMENTS

The 2003 François Naftali Frenkiel Award for Fluid Mechanics

The recipient of the 20th François Naftali Frenkiel Award for Fluid Mechanics is **Maxime Nicolas**, the Université de Provence (Marseille), for his paper “Experimental study of gravity-driven dense suspension jets,” which was published in *Physics of Fluids*, Vol. 14, 3570–3576 (2002). Professor Nicolas was presented with this award on 23 November 2003 at the annual meeting of the APS Division of Fluid Dynamics in East Rutherford, NJ. He received a check for \$1000 plus a scroll bearing the following citation:

For careful and original experimental observations of the modes of instability of jets of dense particles, determination of the parameters on which they depend, and insight into their physical mechanisms, the François N. Frenkiel Award for 2003 is awarded to Maxime Nicolas.

The purpose of this Award, which is named after Dr. F. N. Frenkiel, founder and longtime editor of *Physics of Fluids*, is to recognize significant contributions in fluid mechanics by young investigators. The Award is sponsored by the Division of Fluid Dynamics of the APS, and is given annually to a young author of a paper that has been published in *Physics of Fluids*, during the calendar year preceding the presentation. “Young” will normally be defined as being under 40 years of age. More than one author may be involved, and one author may be a thesis advisor sharing the Award if he/she is also under 40. The winner of this Award is selected by a committee, the chair of which is an associate editor of *Physics of Fluids*.



Maxime Nicolas received his Ph.D. in Physics of Liquids in 1997 at the Université Pierre et Marie Curie in Paris. His dissertation focused on the plane-wave instability occurring in liquid-fluidized beds, a doctoral work under the supervision of Dr. Elisabeth Guazzelli. He joined the Université de Provence (Marseille) in 1999 as Assistant Professor in the Mechanics and Energetics Department. His research interests are in the flow of concentrated solid particles, submarine avalanches, flow of particles in microchannels, heterogeneous sedimentation, with mainly an experimental approach.

François Naftali Frenkiel, who was born in Warsaw, Poland, on 19 September 1910, received his undergraduate education in Mechanical and Aeronautical Engineering at the University of Ghent, Belgium, and his Ph.D. in Physics from the University of Lille in France where he studied under the direction of Kampé de Fériet. He came to the States in 1947 and was associated successively with Cornell University, the U.S. Naval Ordnance Laboratory, the Johns Hopkins University Applied Physics Laboratory, and, from 1960 until his retirement, with the David W. Taylor Naval Ship Research and Development Center. In addition to being the founder and longtime editor of *Physics of Fluids*, he served on a large number of national and international committees, e.g., to name but a few, the International Union of Theoretical and Applied Mechanics, the U.S. National Committee on Theoretical and Applied Mechanics, and the Division of Fluid Dynamics of the American Physical Society of which he was the chairman and secretary on numerous occasions. He published extensively in the field of turbulent flows and pioneered the application of high-speed digital computing methods to the measurement of turbulence and the mathematical modeling of urban pollution. He was elected Fellow of the American Physical Society, the American Geophysical Union, and the American Association for the Advancement of Science. Dr. Frenkiel retired in 1981 and passed away on 9 July 1986, in Washington, D.C.

B.9 Fluctuating particle motion during shear induced granular compaction

O. POULIQUEN, M. BELZONS & M. NICOLAS
Phys. Rev. Lett. **91** (1) 014301 (2003).

Fluctuating Particle Motion during Shear Induced Granular Compaction

O. Pouliquen, M. Belzons, and M. Nicolas

Institut Universitaire des Systèmes Thermiques et Industriels (IUSTI), 5 rue Enrico Fermi, 13453 Marseille cedex 13, France

(Received 2 April 2003; published 1 July 2003)

Using a refractive index matching method, we investigate the trajectories of particles in three dimensional granular packing submitted to cyclic shear deformation. The particle motion observed during compaction is not diffusive but exhibits a transient cage effect, similar to the one observed in colloidal glasses. We precisely study the statistics of the step size between two successive cycles and observe that it is proportional to the shear amplitude. The link between the microscopic observations and the macroscopic evolution of the volume fraction during compaction is discussed.

DOI: 10.1103/PhysRevLett.91.014301

PACS numbers: 45.70.Cc, 05.40.Fb

Granular materials are often described as athermal systems [1,2]. For grains greater than a few microns, thermal fluctuations are negligible and play no role in the dynamics. A granular assembly can then be trapped in a metastable configuration and will not evolve unless an external perturbation such as vibration or shear is applied. The compaction of an initially loose granular sample represents a simple configuration to study the dynamics of athermal systems.

Two configurations have been experimentally investigated to study granular compaction. The first one consists of imposing vertical taps to a granular packing [3–6]. The second consists of imposing a periodic shear deformation to a sample contained in a box [7,8]. In both cases, when the amplitude of excitation is constant (the tap intensity or the shear amplitude), a slow logarithmic relaxation towards more compact states is observed [3,6,7]. In contrast to this slow dynamics, rapid changes in volume fraction can be observed when a sudden change in excitation is imposed [5,7]. The packing dilates (compacts) when the excitation amplitude increases (decreases). Moreover the system exhibits a short term memory, i.e., two packings at the same volume fraction but being prepared differently do not evolve the same way when submitted to the same excitation. The coexistence of a slow and a rapid dynamics and the observation of memory effects have motivated a number of numerical or theoretical models mainly based on the free volume concept and geometrical constraints [9–14]. However, to our knowledge, no link has been made between the macroscopic dynamics and the microscopic structure of the packing during compaction. Does the slow and rapid dynamics correspond to different grain rearrangements? What does the memory effect mean for the particle's position? In this study we address these questions by analyzing the individual motion of the grains during a cyclic shear compaction.

In thermal systems such as colloidal suspensions, the microscopic motion of the particles has been recently studied in detail. Using confocal microscopy, Weeks *et al.* [15,16] followed the three dimensional trajectories

of the particles in colloidal hard sphere suspensions. They have shown that near the glass transition the particles spend most of the time trapped in localized regions or “cages” and occasionally exhibit longer excursions. Considering the analogy often proposed between granular compaction and aging in glassy systems [2], one can legitimately wonder if similar microscopic behaviors are present in granular compaction.

The experimental setup is described in detail in [7] and presented in Fig. 1. Spherical glass beads ($d = 3$ mm in diameter) contained in a parallelepipedic box (7.7 cm wide, 10.2 cm deep, and typically 10.5 cm high) are submitted to a periodic shear by inclining the two side-walls. The top plate which applies a constant pressure on the packing is free to move vertically only. The measure of its vertical position gives the bulk volume fraction. All the experiments are carried out in a quasistatic regime and the only control parameter is the amplitude of the cyclic shear measured by the maximum inclination θ of the sidewalls.

The particles are tracked during compaction using an index matching method. The material is immersed in a mixture of 67% turpentine and 33% methylnaphthalene matching the glass refractive index of the beads. The

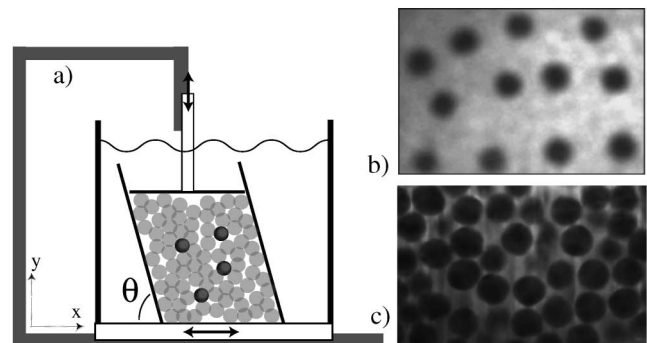


FIG. 1. (a) Experimental setup. (b) Picture of the packing full of index matching liquid with 12 colored tracers. The fuzziness allows a better accuracy for particle tracking. (c) Picture obtained with the laser sheet method.

packing is then transparent and it is possible to follow a few colored glass beads initially introduced in the packing [Fig. 1(b)]. The experimental procedure is as follows. The top plate being removed, the particles are gently poured in the container filled with the index matching liquid. Colored particles are then carefully introduced in the packing and the top plate is slowly put into contact with the beads. The mean initial volume fraction is typically 0.61. Once the packing is ready, the shear deformation is imposed: the sidewalls are successively inclined to an angle $+\theta$ then $-\theta$, then put back at the vertical position. After each cycle, we measure the volume fraction from the position of the top plate and we take a front picture of the packing. The tracers locations in the x - y plan are determined from the picture using a particle tracking algorithm. The location accuracy is $\pm 15 \mu\text{m}$.

In order to observe trajectory correlations between adjacent particles, another visualization method is developed. Fluorescent dye is added to the mixture (with some alcohol to help dilution) and the packing is lighted with a vertical thin laser sheet in the x - y plane. The particles then appear as black disks [Fig. 1(c)]. This method allows one to study short time correlation motion but does not allow one to follow particles in the long time, as they can move perpendicular to the laser plane and eventually leave it.

The first experiments are performed at a constant shear amplitude θ . An example of the particle motion obtained for $\theta = 5.4^\circ$ is presented in Fig. 2(b). The plot represents the stroboscopic trajectory, i.e., the successive positions of the particles measured after each shear cycle. Trajectories are first characterized by an overall decrease of the

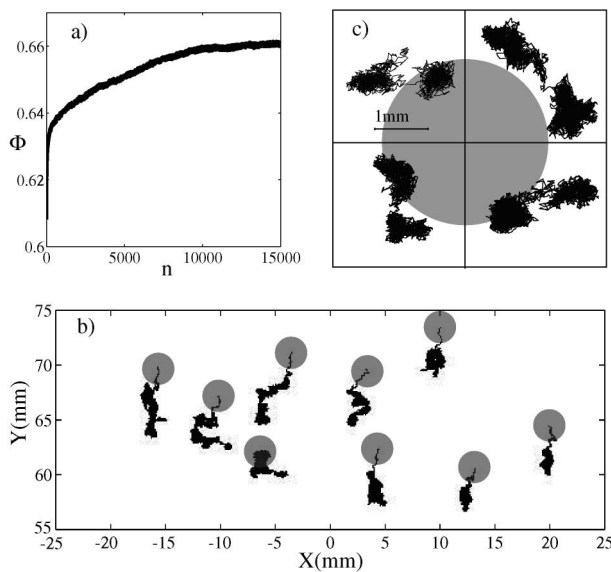


FIG. 2. Compaction for $\theta = 5.4^\circ$. (a) Volume fraction as a function of the number of cycles. (b) Examples of trajectories during 15 000 steps. The disks give the beads size and indicate the initial position of the tracers. (c) Examples of cages (trajectories plotted for time slots between 2500 and 5000 steps).

vertical coordinate as the number of cycles increases, reminiscent of the macroscopic compaction. The corresponding evolution of the volume fraction is plotted in Fig. 2(a). On top of this mean vertical displacement, one observes fluctuating motion characterized by ball-like regions as shown in the close-up of Fig. 2(c). This could reveal a caging process. The random motion of the particles seems to be trapped in a finite volume before escaping and being trapped again in another cage. Notice that the change of the cage corresponds to a displacement quite smaller than the particle diameter (about one-fourth). When compaction goes on, the time spent in a cage becomes longer and longer and the particles eventually move around a fixed position. The cage effect is reminiscent of what has been observed in colloidal glasses by Weeks *et al.* [15,16]. The main difference here is that the system is not time invariant and evolves towards more and more compact states. Cage properties change with time and particles experience only a few cage changes before being trapped in its final location (between 2 and 5). Thus, we have not been able to get significant statistics about cage sizes.

However, in order to investigate how the random motion evolves with compaction, we study the statistics of the displacement $\Delta r = \sqrt{\Delta x^2 + \Delta y^2}$ experienced by the particles between two successive cycles. The distribution of $P(\Delta r)$ obtained at various stages of the compaction process are plotted in Fig. 3, the step size being normalized by the standard deviation σ . One observes that the distribution is slightly larger than that obtained if the x and y displacements were distributed according to a Gaussian centered on zero (solid line in Fig. 3). This

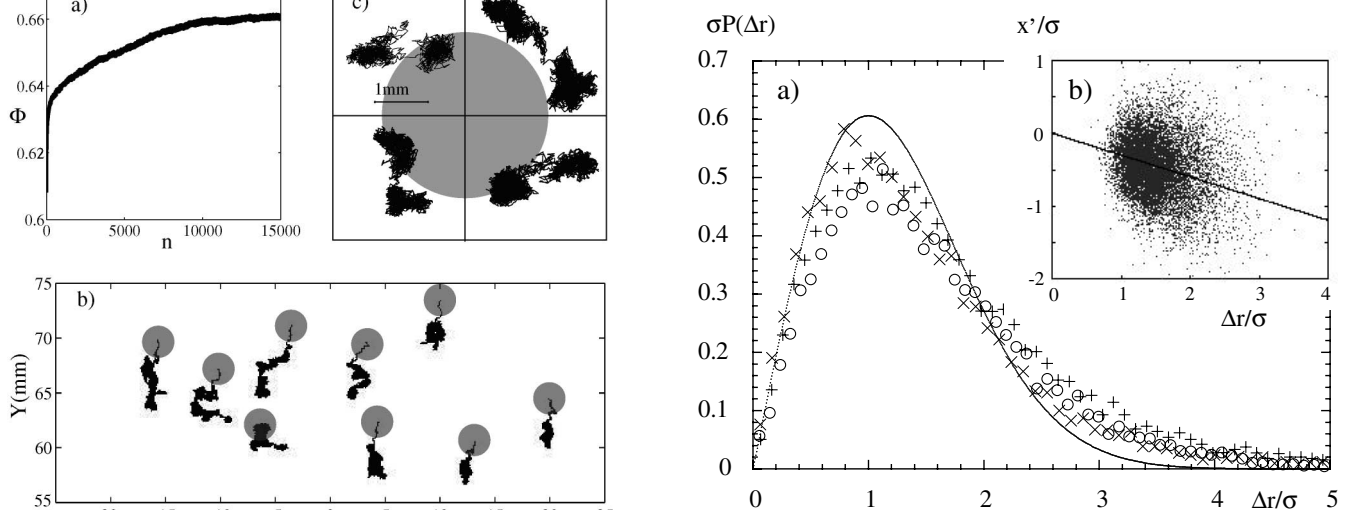


FIG. 3. (a) Normalized distribution $P(\Delta r)$ computed at different stages during compaction; σ is the standard deviation. $\theta = 8.1^\circ$; (O) distribution obtained for $1 < n < 1000$ ($\sigma = 72 \mu\text{m}$); (+) $4000 < n < 5000$ ($\sigma = 54 \mu\text{m}$); (\times) $9000 < n < 10000$ ($\sigma = 52 \mu\text{m}$). Solid line is the Gaussian distribution. (b) x' as a function of Δr (see text). The line is a linear fit.

observation is again very similar to the step size statistics observed in colloidal glasses [16].

Another analogy with colloidal glasses is observed when studying the correlation between two successive cycles: the random motion seems to be anticorrelated. When a particle moves in one direction, it has a great probability to move in the opposite direction the next step, which is reminiscent of a cage effect. This is shown in Fig. 3(b) where the component x' of the $n + 1$ th displacement along the direction of the n th displacement is plotted against the size Δr of the n th displacement. As in thermal colloidal glasses, x' is statistically negative, revealing anticorrelation.

With the granular compaction system not being invariant in time, we study how the step size distribution varies during compaction. The different curves in Fig. 3 correspond to the distribution at a different time in an experiment at $\theta = 8.1^\circ$ and show that the shape of the normalized distribution does not vary much with time. However, the mean value $\langle \Delta r \rangle$ varies during the compaction as shown in Fig. 4. The mean step size $\langle \Delta r \rangle$ is plotted as a function of the volume fraction Φ during experiments carried out for three different shear angles θ . In the three runs, the mean step displacement first decreases down to $\Phi = 0.63$ which corresponds roughly to 500 cycles and eventually reaches a constant value for dense enough packing. The asymptotic value depends on the shear amplitude and is smaller for small θ . An interesting observation is that once the packing is dense enough ($\Phi > 0.64$), the mean step displacement is only a function of θ independent of the history of the packing. This means that the same $\langle \Delta r \rangle$ is measured if the compaction is carried out at a constant θ or if the packing is first compacted under a shear amplitude θ_1 and then sheared at θ . This is shown in Fig. 5 where we plot $\langle \Delta r \rangle$

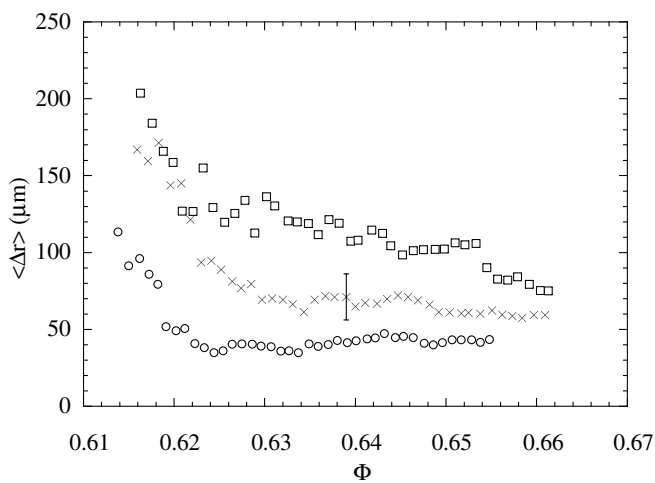


FIG. 4. Evolution of the mean step size $\langle \Delta r \rangle$ with Φ during compaction for $\theta = 2.7^\circ$ (O); $\theta = 5.4^\circ$ (X); $\theta = 8.4^\circ$ (□). The average $\langle \rangle$ means over 40 identical slots in Φ and over particles. Fluctuations from one particle to another due to heterogeneities in the packing and force network are given by the error bar.

014301-3

as a function of θ for many different experiments carried out at constant or nonconstant shear amplitude. The striking feature is the linear relation $\langle \Delta r \rangle = \beta \theta$ with $\beta = 8 \mu\text{m}/\text{deg}$. The higher the shear amplitude, the larger the random displacement between two cycles.

This linear relation between microscopic displacement and shear amplitude is reminiscent of the macroscopic observations of our previous study [7]. When a sudden change $\Delta\theta$ was imposed to the packing, a rapid (in less than 10 cycles) variation of volume fraction $\Delta\Phi$ was measured. $\Delta\Phi$ was found to vary linearly with $\Delta\theta$ independently of the packing history. One can wonder if a link exists between the microscopic random motion and the macroscopic behavior.

In order to investigate this link, experiments are performed where the shear amplitude is discontinuously varied. A typical run is presented in Fig. 6. The packing is first compacted at a fixed amplitude $\theta = 8.4^\circ$ for 10^4 cycles and then θ is varied from 10.2° to 0.6° by a step of 1.2° , the angle being kept constant during 1000 cycles. The corresponding volume fraction variation is plotted in Fig. 6(a). As expected from our previous study [7], successive increasing steps in volume fraction are observed. The typical microscopic behavior of a particle during this experiment is presented in Fig. 6(b). The volume explored by the particle during its random motion successively shrinks when the shear amplitude decreases because the mean step size $\langle \Delta r \rangle$ decreases with θ (Fig. 5). However, each time the shear angle changes, the other particles below the test particle experience the same decrease in their exploration volume. The result is a net downward motion observed when the angle changes. The observed volume fraction variation thus seems to result from the change in the volume randomly explored by the particles. This becomes clear when looking at the displacement of all the particles during a change in θ [Fig. 6(c)]. Thanks to the laser light visualization, we are able to follow each

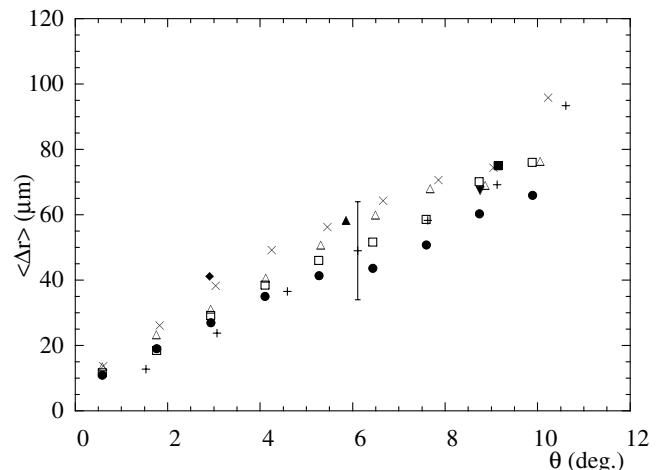


FIG. 5. Mean step size $\langle \Delta r \rangle$ as a function of shear angle θ . The different symbols correspond to different experiments with θ kept constant or changed stepwise.

014301-3

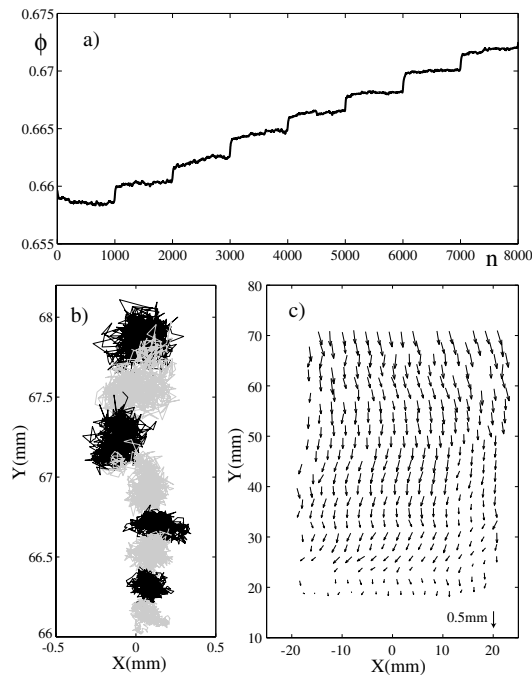


FIG. 6. (a) Volume fraction as a function of cycles when θ varies stepwise (see text). (b) Corresponding trajectory of one particle. Changes in color correspond to changes in θ . (c) Displacement field measured in the cell when θ changes from 10.4° to 1.4° .

particle in a plane when the shear angle changes from 10.4° to 1.4° . An homogeneous deformation is observed [Fig. 6(c)], as if when the angle decreases, all the particles deflate yielding a change in volume fraction. An estimation of the change in volume fraction can be made. Assuming that the random fluctuating motion of a particle occupies a volume of the order $(d + \langle \Delta r \rangle)^3$, the volume fraction is $\Phi = \Phi_0 \{d^3 / [d + \langle \Delta r \rangle(\theta)]^3\}$ where Φ_0 is a reference volume fraction. Knowing from Fig. 5 that $\langle \Delta r \rangle = \beta\theta$, a change $\Delta\theta$ in the shear amplitude induces a volume fraction variation $\Delta\Phi = -3\Phi_0\beta\Delta\theta$. A linear variation is predicted as observed in [7] and the predicted coefficient (taking $\Phi_0 = 0.7$) is $-3\Phi_0\beta = -0.56 \times 10^{-3} \text{ deg}^{-1}$ having the right order of magnitude compared to the value $-1.5 \times 10^{-3} \text{ deg}^{-1}$ measured in [7].

All the results presented up to now are obtained for monodispersed glass beads. In this case, the compaction occurs towards crystallization [7]. We have checked that the microscopic behavior does not qualitatively change when using a bidispersed material (mixture of 2 and 3 mm beads) which does not crystallize. Cages are still observed and the sudden change of volume fraction when changing the shear amplitude [8] is correlated to a change of the mean random step size. The crystal nature of the packing then does not qualitatively influence the dynamics of the system.

In conclusion a simple scenario can be proposed for the compaction process. We have seen that the particle's mo-

tion can be divided in two kinds: random motion within confined volumes or cages, whose extent is directly proportional to the shear amplitude, and occasionally longer exploration corresponding to a change of cage. We think that the slow dynamics of compaction observed in experiment at a constant amplitude may be attributed to the change in cages. This changes are irreversible and push the system towards more and more compact configurations. How cage deformations occur and what is the influence of one cage rearrangement on the next one are open questions. The cage changes certainly involve complex cooperative processes associated with modifications in the contact and force network which have not been studied here. However, we have shown that the rapid change of volume fraction observed when changing the amplitude is of a different nature: it is simply related to the change of the cage size, without important structural changes. This means that this variation of volume is reversible and can be recovered by coming back to the previous amplitude of excitation. The existence of these two processes which affect differently the packing volume fraction explains that memory effects can be observed.

We thank F. Ratouchniak for his technical assistance.

-
- [1] A. J. Liu and S. R. Nagel, *Nature (London)* **396**, 21 (1998).
 - [2] G. D'Anna and G. Gremaud, *Nature (London)* **413**, 407 (2001).
 - [3] J. B. Knight, C. G. Fandrich, C. N. Lau, H. M. Jaeger, and S. Nagel, *Phys. Rev. E* **51**, 3957 (1995).
 - [4] E. R. Nowak, J. B. Knight, E. Ben-Naim, H. M. Jaeger, and S. R. Nagel, *Phys. Rev. E* **57**, 1971 (1998).
 - [5] C. Josserand, A. Tkatchenko, D. Mueth, and H. Jaeger, *Phys. Rev. Lett.* **85**, 3632 (2000).
 - [6] P. Philippe and D. Bideau, *Europhys. Lett.* **60**, 677 (2002).
 - [7] M. Nicolas, P. Duru, and O. Pouliquen, *Eur. Phys. J. E* **3**, 309 (2000).
 - [8] M. Nicolas, P. Duru, and O. Pouliquen, in *Powder and Grains 2001*, edited by Y. Kishino (A. A. Balkema, Tokyo, 2001), pp. 17–19.
 - [9] A. Coniglio and H. J. Herrmann, *Physica (Amsterdam)* **225A**, 1 (1996).
 - [10] E. Caglioti, V. Loreto, H. J. Hermann, M. Nicodemi, and A. Coniglio, *Phys. Rev. Lett.* **79**, 1575 (1997).
 - [11] G. C. Barker and A. Mehta, *Phys. Rev. A* **45**, 3435 (1992).
 - [12] A. Barrat and V. Loreto, *Europhys. Lett.* **53**, 297 (2001).
 - [13] T. Bouteux and P. G. de Gennes, *Physica (Amsterdam)* **244A**, 59 (1997).
 - [14] J. Brey, A. Prados, and B. Sánchez-Rey, *Phys. Rev. E* **60**, 5685 (1999).
 - [15] E. R. Weeks, J. C. Crocker, A. C. Levitt, A. Schofield, and D. A. Weitz, *Science* **287**, 627 (2000).
 - [16] E. R. Weeks and D. A. Weitz, *Phys. Rev. Lett.* **89**, 095704 (2002).

B.10 Pore pressure relaxation during granular compaction

M. NICOLAS, M. BELZONS & O. POULIQUEN

Proceedings of the XXI ICTAM, 15–21 August 2004, Warsaw, Poland.

PORE PRESSURE RELAXATION DURING GRANULAR COMPACTION

Maxime Nicolas, Max Belzons, Olivier Pouliquen

IUSTI, UMR 6595 CNRS-Polytech Marseille, 5 rue Fermi 13453 Marseille cedex 13 France

Summary The compaction of a granular assembly immersed in a fluid implies complex interactions between viscous forces and grain contact forces. We present the study of the compaction under tapping of a granular packing fully immersed in water. In order to follow the interaction between the grains and the fluid, we measured the pore pressure at the base. A simple model is proposed to understand the time relaxation of the pore pressure.

INTRODUCTION

Powder compaction is an old subject that has recently attracted the attention of physicists as the prototype of non thermal disordered systems. The complex evolution of an initially loose granular packing submitted to external perturbations like vibration has been precisely studied [1, 2, 3]. In all the previous studies the role of the interstitial fluid is negligible. However, the fluid can play an important role in the compaction dynamics as shown for example by the liquefaction phenomena. Grains in a fluid can interact both by direct frictional contact and by viscous forces through the fluid. Dense granular packing in a fluid can then behave like a granular material or a suspension, and the transition between both behaviors is not clearly understood. An initially loose sand saturated with water can liquefy when submitted to vibration (an earthquake for example). As the material compacts, the fluid has to escape developing pressure gradients enough to carry the weight of the grains.

In this work, we investigate a simple configuration where both viscous and contact interaction are present. A granular packing fully immersed in water is compacted under vertical tapping. In order to determine the role of the liquid we measure the time evolution of the pore pressure under the packing during compaction.

EXPERIMENTAL SETUP

The experimental set up is presented in Figure 1. A rectangular box separated in two is fixed on top of an electromagnetic vibrating device. Both sides of the box are full of water, but grains are placed on one side only. The particles are $112 \pm 20 \mu\text{m}$ diameter spherical glass particles. A differential pressure sensor measures the water pressure difference between the two sides of the box and an accelerometer is attached at the bottom of the tank. Before the experiment starts, the granular material is stirred in order to create a suspension. We then wait until all the material is settled at the bottom of the container. The pressure difference between the two side is then zero, as the weight of the grains is carried by the box. We then impose a vertical controlled acceleration and measure the time evolution of the pressure. These signals are digitized at 10 kHz using an acquisition board.

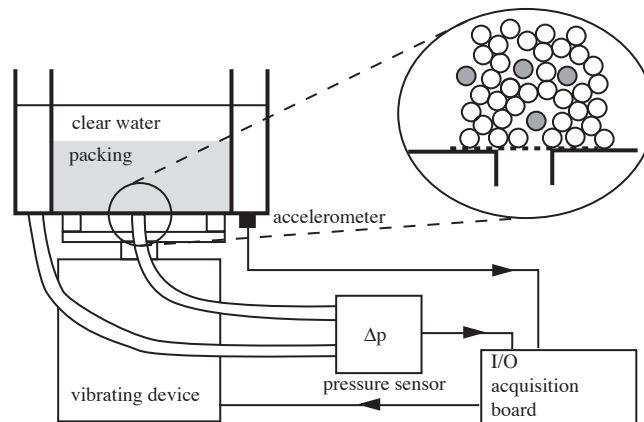


Figure 1. Experimental setup.

PORE PRESSURE MEASUREMENTS

A typical pore pressure relaxation is shown on Fig. 2 for a maximum acceleration of 19 m/s^2 and a « tapping time » of 250 ms. This relaxation is very close to an exponential relaxation and can be explained by a simple model. If we note h_c

the height of the packing in the most compact configuration, and h the height in a loose configuration, the pore pressure may be written as an hydrostatic pressure due do suspended particles in the packing (see insert of Fig. 1 for a schematic view) :

$$\Delta P = \phi \Delta \rho g (h - h_c) \quad (1)$$

where ϕ is the particle volume fraction and $\Delta \rho$ the density difference between the particles and the liquid.

This pressure induces a flow inside the deformable porous packing of permeability k . Using Darcy's law, the governing equation for the height is then

$$\frac{dh}{dt} = -\frac{k}{\eta} \phi_c h_c \Delta \rho g \frac{h - h_c}{h^2} \quad (2)$$

where η is the liquid dynamic viscosity and ϕ_c is the random close packing volume fraction. This model is in qualitative agreement with the experimental results and helps understand why pressure relaxation is a slow process compared to the typical time scale of the tapping.

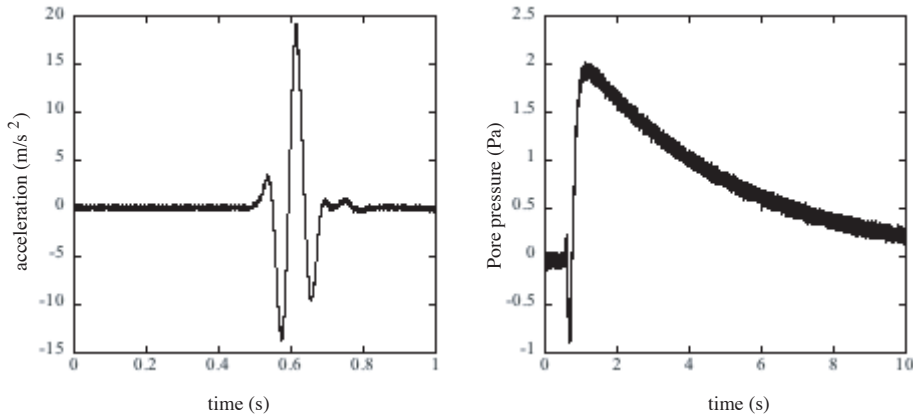


Figure 2. Acceleration (left) and pore pressure relaxation (right) versus time for a 2 cm high packing of 112 μm glass spheres.

CONCLUSIONS AND PERSPECTIVES

We show that the pore pressure inside a packing relaxes exponentially when the material is submitted to a rapid sollicitation such as a vertical tapping. If the time between two successive sollicitations is shorter than the typical relaxation time, then the pressure may build up until it balances the weight of particles, leading to liquefaction of the liquid/particles mixture.

References

- [1] Nowak E.R., Knight J.B., Ben-Naim E., Jaeger H.M., Nagel, S. Phys. Rev. E **51**, 3957 (1995).
- [2] Josserand C., Tkatchenko A., Mueth D., Jaeger H.M. Phys. Rev. Lett. **85**, 3632 (2000).
- [3] Nicolas M., Duru P., Pouliquen O. Eur. Phys. J. E **3**, 309 (2000).

B.11 Spreading of a drop of neutrally buoyant suspension

M. NICOLAS

Accepté à *J. Fluid Mech.*, sous presse (2005).

Spreading of a drop of neutrally buoyant suspension

By MAXIME NICOLAS

Groupe Écoulements de Particules, Institut Universitaire des Systèmes Thermiques Industriels, UMR 6595 CNRS-Université de Provence, 5 rue Fermi, 13453 Marseille cedex 13, France

(Received 1 February 2005 and in revised form 8 July 2005)

The spreading of suspension drops on a flat surface is studied using mixtures of liquid and density-matched particles. As expected from an energy balance model, the spreading factor is reduced with increasing particle volume fraction. This decrease is quantitatively understood through an effective viscosity coefficient. However, for large drop Reynolds number, the particles are not uniformly distributed into a spread drop but form an annulus. For higher impact velocities, a particle-induced break-up of the drop is observed.

1. Introduction

A great number of industrial processes rely on the understanding of the mechanics of the impact and spreading of liquid drops on a flat substrate. Since the pioneering work of Worthington, there have been numerous studies of drop spreading phenomena (see Rein 1993 for a review). Most of the studies, including viscous spreading models (Gu & Li 1998, 2000), are based on an energy balance model (presented in §2). Considering a drop of diameter d_0 impacting with a velocity U on a flat surface, the spreading diameter βd_0 is predicted to depend on the Reynolds number $Re_0 = \rho d_0 U / \eta$ and the Weber number $We = \rho d_0 U^2 / \sigma$ (ρ is the density of the liquid, η its dynamic viscosity and σ is the interfacial tension of the liquid with air). In the limit of a vanishing impact velocity, the spreading factor β depends only on the contact angle and the Bond number $Bo = \rho g d_0^2 / \sigma$ (Shikmurzaev 1997; Reznik & Yarin 2002). For a moderate impact velocity, the kinetic energy is dissipated by viscous forces and the drop reaches a static state after a finite spreading time. Some fingering patterns of the contact line may occur during this process (Thoroddsen & Sakakibara 1998). If the initial kinetic energy is too large to be dissipated by viscosity, splashing of the drop occurs.

Range & Feuillebois (1998) have shown that the value of the Reynolds number Re_0 at which splashing is first observed is strongly affected by the roughness of the plane on which the drops impinges. Moreover, when the Ohnesorge number $Oh = \sqrt{We} / Re_0$ is small, the viscosity is negligible and the critical Re_0 was found to be inversely proportional to Oh , with the constant of proportionality depending only on the roughness of the plate. At larger Oh , according to Stow & Hadfield (1981) and Mundo, Sommerfeld & Tropea (1995), this critical Re_0 becomes inversely proportional to $Oh^{0.8}$. This criterion can also be written as $We^{0.5} Re_0^{0.25} > K_0$, where K_0 is a constant depending on the surface roughness.

To date there has been no quantitative study of the deposition of a drop of suspension. However, some industrial processes use a mixture of a liquid solvent and

solid particles instead of a pure liquid. For example, an emerging application such as a particle-laden ink jet requires small-volume droplets of suspension impacting at high velocity (Seerden *et al.* 2001). Since this small-scale and fast-time phenomenon is quite difficult to observe, a scaled experiment should help to understand the influence of non-deformable solids on the drop spreading. We aim to describe the spreading of a particle-laden drop impacting on a flat surface. The suspension is made of particles with diameter d_p and density equal to that of the liquid. Assuming that the particles are initially uniformly distributed in the drop volume with a particle volume fraction ϕ , the drop viscosity $\eta\eta_r(\phi)$ can be estimated using an effective viscosity model such as the Krieger–Dougherty correlation. The relevant Reynolds number is thus modified and is written $Re = Re_0/\eta_r(\phi)$.

Our goal is to obtain some insight into the particle-laden drop impact phenomenon. A predictive model for the effect of the particles on the spreading factor is proposed and compared with experimental results. In our experiment we measure the spreading factor and the particle position distribution in the spread drop. Two particle configurations are observed: a uniform distribution for low Re_0 and annular distribution for higher Re_0 . A qualitative analysis is suggested. For a high impact velocity, break-up of the suspension drop may occur and can be described by a $We^{0.5}Re_0^{0.25} > K_0$ criterion. But unexpectedly, K_0 is seen to decrease when the particle volume fraction is increased.

2. Theoretical predictions

2.1. Mass and energy balance model

The spreading process involves inertial, viscous and gravity forces, the interfacial tension and the wettability of the liquid on the solid surface. Despite this large number of parameters, some predictions can be made using mass conservation and energy balance equations.

The first conservation equation is the mass or volume conservation. Whatever the shape of the spread drop (a flat disk or a spherical cap), its volume must be equal to the volume $\pi d_0^3/6$ of the spherical drop before impacting on the plane.

The second equation is a balance between energy before the impact and energy when the spreading is over. This is written

$$E_k + E_p + E_s = E'_k + E'_p + E'_s + W_d \quad (2.1)$$

where indices k , p and s denote kinetic, potential and surface energies respectively. The work of viscous dissipative forces during the spreading is W_d . The initial kinetic energy is $E_k = \frac{1}{2}\pi\rho d_0^3 U^2$. After the spreading, the kinetic energy is zero: $E'_k = 0$. For high-velocity drop impacts (i.e. $Re \gg 1$ and $We \gg 1$), since the kinetic energy overcomes the potential and surface energies, it is only balanced by the work of dissipative viscous forces.

The energy dissipated by viscous forces is commonly estimated as $\int_0^{t_s} \int_{\Omega} \Phi \, d\Omega \, dt$ where t_s is the time of spreading and Ω the volume of the drop. The spreading time t_s scales as d_0/U and Pasandideh-Fard *et al.* (1996) suggested $t_s = (8/3)(d_0/U)$ as a correct value. The volumic rate of dissipated energy Φ then scales as $\alpha\eta(U/L)^2$ with L the typical length over which the velocity varies and α a dimensionless number. Although this number may vary a little with the Reynolds number, we choose to keep it constant for simplicity. For high-viscosity liquids, viscous dissipation occurs in the whole drop volume and the mean thickness of the spread drop is $L = h = 2d_0/3\beta^2$ (Chandra & Avedisian 1991; Mao, Kuhn & Honghi 1997; Park *et al.* 2003). The energy

	ρ (g cm ⁻³)	η (g cm ⁻¹)	σ (mN m ⁻¹)	Material	d_p (μ m)	d_0 (mm)	d_0/d_p
L1P1	1.18 \pm 0.1	0.22 \pm 0.01	56.8 \pm 0.5	PMMA	636 \pm 24	4.7 \pm 0.2	7.4 \pm 0.5
L2P2	1.05 \pm 0.005	0.011 \pm 0.001	28.0 \pm 0.4	polystyrene	720 \pm 37	4.0 \pm 0.2	5.5 \pm 0.3
L2P3	1.05 \pm 0.005	0.011 \pm 0.001	28.0 \pm 0.4	polystyrene	381 \pm 39	4.4 \pm 0.1	10.5 \pm 1

TABLE 1. Characteristics of liquid, particles and drops of suspension.

dissipated by viscosity is then $W_d = \alpha\pi\eta U d_0^2 \beta^4$ and the energy balance equation (2.1) leads to

$$\beta = \left(\frac{Re}{12\alpha} \right)^{1/4}. \quad (2.2)$$

2.2. Effect of the particles on the spreading

The effective viscosity of a suspension is known to be larger than the viscosity of the liquid alone. This increase has been the subject of numerous studies since Einstein in 1905 and the effective viscosity of a suspension is formally written as $\eta_s = \eta_f \eta_r(\phi)$ where $\eta_r(\phi)$ is a monotonic function of the particle fraction. For a wide range of particle volume fraction, the Krieger–Dougherty model estimates the relative viscosity as $\eta_r = (1 - \phi/\phi_m)^{-n}$ where $\phi_m = 0.68$ is the random close packing volume fraction and $n = 1.87$. As stated in the introduction, the particle-laden drop Reynolds number is $Re_0/\eta_r(\phi)$, and assuming that (2.2) is valid, one should expect a spreading factor

$$\beta = \left(\frac{Re_0}{12\alpha} \right)^{1/4} \left(1 - \frac{\phi}{\phi_m} \right)^{n/4}. \quad (2.3)$$

And if we assume that the volume fraction is low ($\phi \ll \phi_m$), then

$$\beta \approx \left(\frac{Re_0}{12\alpha} \right)^{1/4} \left(1 - \frac{n}{4} \frac{\phi}{\phi_m} \right) \quad (2.4)$$

and the decrease of spreading due to particles is

$$\frac{d\beta}{d\phi} = -\frac{n}{4\phi_m} \left(\frac{Re_0}{12\alpha} \right)^{1/4} \quad (2.5)$$

which gives $d\beta/d\phi = -0.37Re_0^{1/4}$ for $\alpha = 1$. This expression is compared to experiments in §4.1.

3. Materials and experimental conditions

We used different liquids and particles to prepare the density-matched suspensions (see table 1). Liquid L1 was a water and glycerol mixture and liquid L2 was salted water. A small amount of surfactant (a liquid soap) was added to L2 to prevent particle aggregation. Both liquids were dyed using fluoresceine. Viscosity η was measured using a Rheomat RM 180 Couette rheometer and a Gilmont falling ball viscosimeter. Surface tension was measured with a ring tensiometer. All experiments and measurements were carried at $T = 23^\circ\text{C}$. When needed, pure liquid drop impacts were studied.

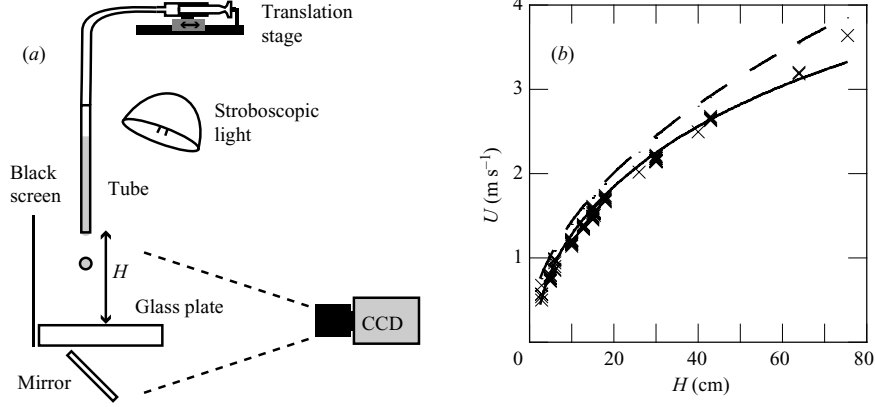


FIGURE 1. (a) Schematic diagram of the experimental apparatus. (b) Correlation between the height of release H and the impact velocity U . The dashed line is the free-fall velocity and the continuous line is the velocity obtained with $U = \sqrt{gH_0(1 - \exp(-2(H - \Delta H)/H_0))}$.

Figure 1(a) shows the experimental apparatus used to produce droplets at the outlet of a cylindrical tube and to photograph their fall and impact on a clean plate of glass at a distance H below. A 45° mirror placed below the glass plate was used to photograph the spreading while the CCD camera was focused on the vertical plane below the tube. A stroboscopic light produced 100 to 175 flashes per second while the camera shutter rate was 25 Hz. The flash duration was short enough to freeze the droplet motion during the fall or the spreading. A fast camera ($1000 \text{ frames s}^{-1}$) was also used to record the fast motion and the particle positions during the spreading.

Delivery of a single droplet was ensured by a home-made programmable pump based on a translation stage driven by a PC computer through a LabView interface. The tube had a 3 mm inner diameter and was 200 mm long. The velocity U of each droplet was measured between two successive snapshots just before the impact. The measured impact velocity was seen to be slightly different from the free-fall velocity $\sqrt{2gH}$ (see figure 1b). Since the droplet is larger than the capillary length, the droplet is not perfectly spherical and exhibits oscillations during the fall. Since the drag is not negligible, we assume a constant friction coefficient C_f (as suggested by Range & Feuillebois 1998), hence the impact velocity is $U = \sqrt{gH_0(1 - \exp(-2(H - \Delta H)/H_0))}$ where ΔH is the distance between the tube and the droplet at zero velocity, and $H_0 = 4\rho d_0 / (3C_f \rho_{air})$, in good agreement with the experimental results (see figure 1b).

Once the droplet is spread on the glass plate, we computed the spreading factor $\beta = \sqrt{2A_w / \pi d_0^2}$ by measuring the wetted area A_w on the image. If break-up of the drop occurred, the spreading factor was measured as the maximum diameter of the wetted area divided by d_0 . For each experiment, we measured the initial drop diameter d_0 , the spreading factor β , the number of particles N , the particle volume fraction $\phi = N(d_p/d_0)^3$ and the positions of each particle. We define $r = 2\sqrt{x^2 + y^2} / \beta d_0$ the dimensionless particle distance from the centre of impact.

In our experiments, the particle volume fraction was varied from 0 (pure liquid) to 0.45, leading to an effective viscosity $1 < \eta_r < 7.45$. The distance H between the tube and the glass plate was varied from 2.9 to 75.5 cm. The Reynolds number range was $79 < Re < 9907$, the Weber number was $24 < We < 1276$, the Ohnesorge number was $0.003 < Oh < 0.11$, and the Bond number was $3.5 < Bo < 8.0$.

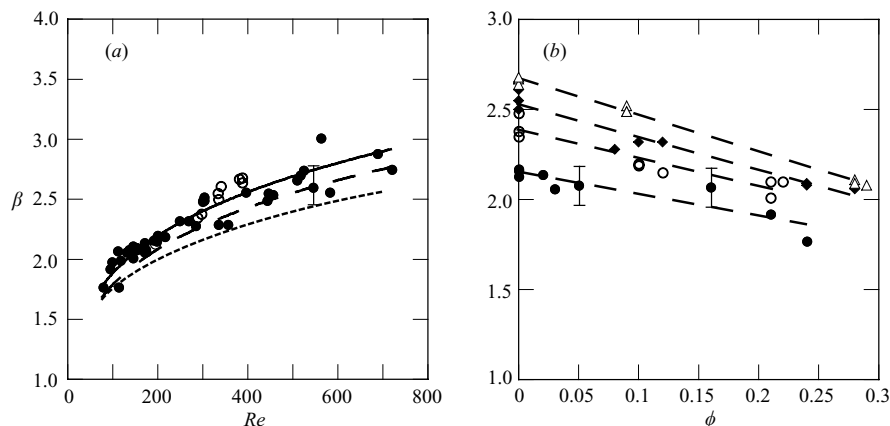


FIGURE 2. (a) Spreading factor vs. $Re = Re_0/\eta_r$ for pure liquid L1 (open circles) and suspension L1P1 (filled circles). Dotted line is the prediction due to Pasandideh-Fard *et al.* (1996), dashed line is (2.2) with $\alpha = 1$, and solid line is (2.2) with $\alpha = 0.89$. (b) Effect of the particle volume fraction on the spreading factor: $Re_0 = 188$ (filled circles), $Re_0 = 292$ (open circles), $Re_0 = 348$ (filled diamonds) and $Re_0 = 389$ (open triangles) for the suspension L1P1. The dashed lines are the best linear trends for each set of data.

4. Results

4.1. Spreading factor and transition to a break-up regime

Experiments with the most viscous liquid L1 were done with impact velocities ranging from 0.5 to 3.64 m s⁻¹. The particle volume fraction was up to 30%. No drop break-up was observed for these ranges of parameters. The average value of $Re/81\beta^4$ is 0.11 ± 0.02 , suggesting that viscous dissipation occurs in the whole volume of the drop. We compare in figure 2(a) our measurements with the spreading factor predicted by (2.2), and the prediction made by Pasandideh-Fard *et al.* (1996). The spreading factor ranges from 1.5 to 3 for a Reynolds number varying from 100 to 700. The model is in good agreement with the experimental results if the fitting parameter α is 0.89 (solid line). For comparison, the theoretical spreading factor is shown for $\alpha = 1$ (dotted line). This good agreement shows that the effective viscosity approach still holds even if the liquid film thickness h is smaller than the particle diameter d_p . This occurs as soon as the spreading factor β is larger than $\sqrt{2d_0/3d_p}$ which takes the value 2.2 for experiments L1P1. As expected, an increase in volume fraction increases the effective viscosity of the suspension and thus decreases the spreading factor. This trend is shown in figure 2(b) where we present four sets of results corresponding to four impact velocities. The error bars give an estimate of the experimental error in the spreading factor measurements. The decrease of β can be fitted well by a linear function, allowing measurement of $d\beta/d\phi$.

Results for the less viscous liquid (L2) are shown on figure 3. A first comment is that the size of the particles does not seem to play a strong role in the spreading. Secondly, β varies from 2 to 5 for a Reynolds number increasing from 500 to 10000. The agreement of experimental results with the β predicted by (2.2) is fairly good but the data show more scatter than those for the more viscous suspension. Nevertheless, we still observe a decrease of β with the particle volume fraction the (figure 3b), and $d\beta/d\phi$ can still be measured using a linear fit to the experimental data.

The decrease of the spreading factor due to particles $d\beta/d\phi$ is plotted in figure 4(a) and compared to the value predicted by (2.5). The results for all the particle/fluid

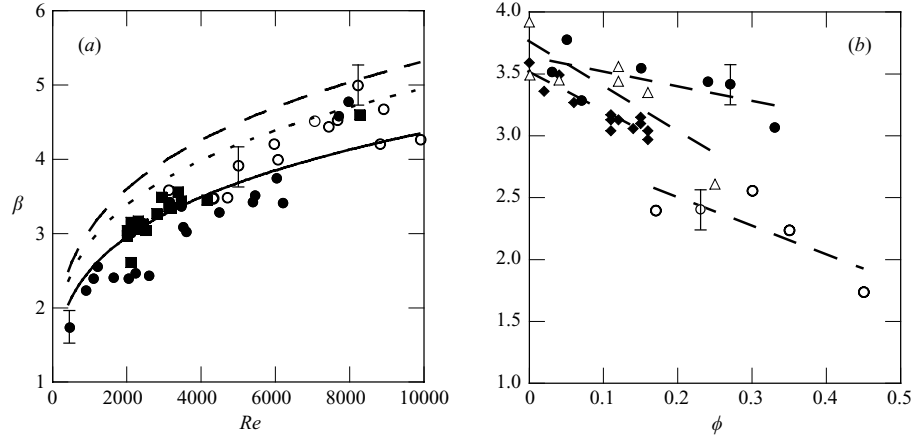


FIGURE 3. (a) Spreading factor vs. $Re = Re_0/\eta_r$ for pure liquid L2 (open circles), and suspensions L2P2 (filled squares) and L2P3 (filled circles). Solid line is the (2.2) for $\alpha = 1.57$, dashed line computed with $\alpha = 1$ and dotted line is computed with the expression given by Pasandideh-Fard *et al.* (1996). (b) Effect of particle volume fraction on the spreading factor: suspension L2P2 at $Re_0 = 3496$ (open circles) and $Re_0 = 6118$ (filled circles); suspension L2P3 at $Re_0 = 3326$ (diamonds) and $Re_0 = 4917$ (triangles). The dashed lines are the best linear trends for each set of data.

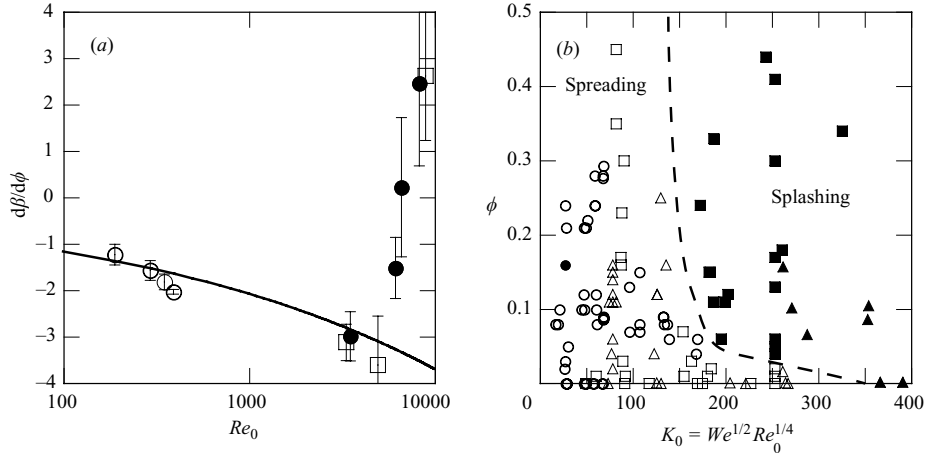


FIGURE 4. (a) Spreading reduction due to the particles L1P1 (open circles), L2P2 (filled circles) and L2P3 (squares). The continuous line is (2.5) computed with $\phi_m = 0.68$, $n = 1.87$ and $\alpha = 1$. (b) Map of the spreading/splashing regimes in the (K_0, ϕ) -plane: L1P1 (circles), L2P2 (squares) and L2P3 (triangles).

combinations follow the same curve. Despite the scattering of the experimental data for the viscous liquid L2, it shows a good agreement for $Re_0 < 5000$: $d\beta/d\phi$ is negative and scales as $Re_0^{1/4}$. For $Re_0 > 5000$, $d\beta/d\phi$ increases and eventually becomes positive for $Re_0 \gtrsim 6000$. In that range of Reynolds number, the particles do not reduce the spreading compared to the pure liquid impact, but on the contrary enhance the spreading. The resulting impact is no longer a circular contact line, but a rather distorted line or even several droplets formed by the break-up of the impacting drop.

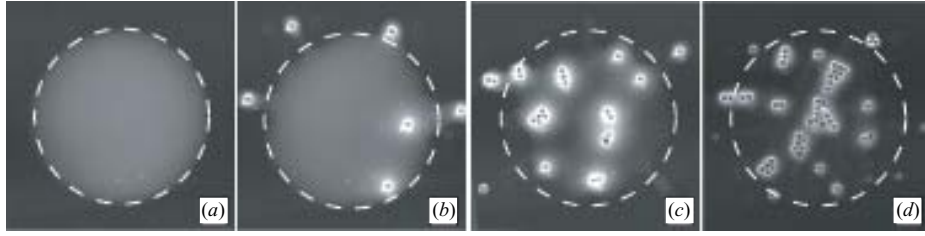


FIGURE 5. Photographs of droplets impacting at the same velocity $U = 2.15 \text{ m s}^{-1}$: (a) Liquid L2 without particles (b) Liquid L2 without particles at $\phi = 0.04$, (c) $\phi = 0.13$ and (d) $\phi = 0.30$. Pure liquid Reynolds number is $Re_0 = 8217$.

An example of such a break-up is shown on figure 5. The four photographs depict the effect of an increase of ϕ on the impact of a L2P2 suspension drop for the same $Re_0 = 8217$. Some particles are found outside the circle depicting the pure-liquid spread drop. In some cases, some particles were observed to move far from the impact point and eventually to leave the glass plate. All our observations are summarized in figure 4(b). Following Mundo *et al.* (1995), we attempt to describe the break-up regime using a critical number $K_0 = We^{0.5} Re_0^{0.25}$. This critical number seems to depend on the volume fraction: when ϕ increases, K_0 is unexpectedly decreased. This is in apparent contradiction with the energy balance model.

Finally, one can observe that the particles in the spread drop are grouped in clusters. This is due to surface tension effects because the liquid film thickness h is lower than the particle diameter. The particles deform the liquid/air interface and increase its surface energy. This is very similar to what happens in a raft of floating bubbles (Bragg & Nye 1947), where the interaction between two bubbles can be described by a potential analogue to the interaction potential between two atoms (Shi & Argon 1982). The attractive force between two particles at a liquid–gas interface has also been studied by Joseph *et al.* (2003).

4.2. Particle distribution in the spread drop

For each experiment we measured the dimensionless radial particle positions r and computed the probability $P_r(r)$ for a particle to be at a distance r from the spread drop centre. The probability density function (p.d.f.) of the position is $P(r, \theta)$ and must satisfy $\pi^{-1} \int_0^{2\pi} \int_0^1 P(r, \theta) r d\theta dr = 1$. Assuming that the spreading is axisymmetric, P does not depend upon θ , and $P = P_r/2r$. The maximum value of the p.d.f. $P(r)$ denotes the preferred position for the particles in the spread drop.

We show on figure 6(a, b) the particle positions and the probability P for the suspension L1P1 for a Reynolds number $Re_0 < 807$. The probability has a weak maximum for $r < 0.1$ and is nearly constant for $0.1 < r < 0.7$. As can be seen on figure 6(a) the particles seem randomly dispersed in a disk of radius $r \approx 0.7$. The probability density decreases strongly for $r > 0.7$ which is the signature of a depletion of particles near the boundary of the droplet.

The situation is quite different for suspensions made with a less viscous liquid. Figure 6(c, d) shows the particle positions and the p.d.f. for drops L2P3 with $Re_0 \approx 3350$. The maximum of the p.d.f. is for a radius $0.4 < r < 0.5$ and the depletion of particles occurs in the centre of the droplet ($r < 0.2$) as well as in the outer annulus ($r > 0.7$). This situation was also observed for higher Reynolds numbers ($Re_0 \approx 5000$) as well for the drops of suspension L2P2. Whatever the liquid and the particles,

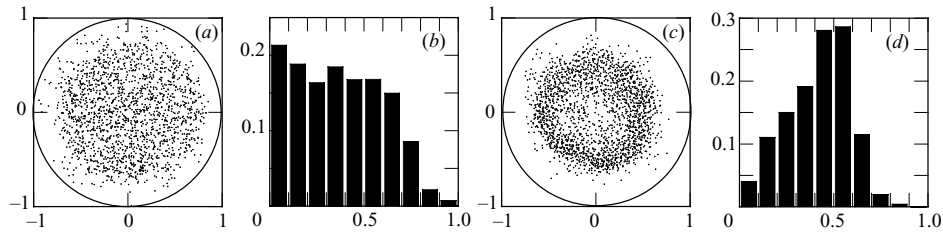


FIGURE 6. (a) Particle position distribution in the spread droplet and (b) radial probability P for L1P1, $140 < Re_0 < 807$ and $0.03 < \phi < 0.28$. (c) Particle position distribution in the spread droplet and (d) radial probability P for L2P3, $3184 < Re_0 < 3513$ and $0.11 < \phi < 0.16$. Data were collected from different runs.

it seems that there is no obvious dependence of the position distribution upon the particle volume fraction.

The annular distribution of particles for Reynolds numbers larger than 3000 may be explained by the oscillation of the liquid during the spreading. If the spreading is governed by viscous forces (low Re_0), all the momentum of the liquid is dissipated during the time needed to reach a steady contact line between the drop and the solid substrate. Conversely, if inertial forces are large enough, a fraction of momentum may remain after the contact line motion has stopped. A raised rim then forms at the periphery and the central liquid pool thins out. The rim is then pulled back towards the centre since the interfacial tension minimizes the liquid/air contact area. We suggest that the particles follow the liquid oscillations qualitatively, as they are density matched with the liquid. Moreover, if the local thickness of the liquid is lower than the particle diameter d_p , the interface is deformed and its motion may create a force acting on the particle. In the same manner, the periphery of the drop has a very low thickness and this prevents the particles getting close to the contact line, creating a depletion of particles for large r values ($r > 0.7$ from our results).

This assumption has been checked with the video recording large frame rate (1000 f.p.s.) of a drop spreading for a Reynolds number at which the annular distribution of particles occurs. We show on figure 7 the time evolution of the spreading factor $\beta(t)$ and the motion of one test particle on the same time scale. While the drop contact line stops growing 7 ms after the impact, the test particle still moves, reaches a maximum radial position at $t = 19$ ms, and then moves back to reach a steady position at $t = 48$ ms. The particles are thus observed to move after the spreading factor has reached a constant value.

5. Conclusion

We have studied the impact, spreading and break-up of a liquid drop containing solid density-matched particles. Using an effective viscosity model for the drop, the spreading factor scales as $Re^{1/4}$, and the effect of solid particles is quantitatively described. A uniform particle distribution in the spread drop is observed for $Re \lesssim 800$ and an annular distribution is observed for larger values of the Reynolds number. The periphery of the drop is always depleted of particles owing to interfacial forces acting on the particles. For a large impact velocity, break-up of the drop is observed. The break-up criterion takes the form $We^{1/2} Re_0^{1/4} > K_0(\phi)$ where K_0 decreasing when ϕ increases.

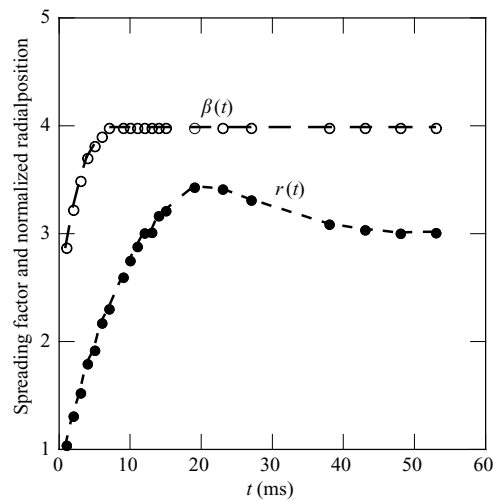


FIGURE 7. Time evolution of the spreading factor $\beta(t)$ (open circles) compared to the normalized radial position of a test particle (filled circles) for suspension L2P2. The Reynolds number was $Re_0 = 6500$ and the particle volume fraction was $\phi = 0.02$.

Some clusters of particles were also observed for the less viscous liquid. This feature demonstrates the interaction of the particles with the liquid/air interface, and this issue is surely connected with the unexpected transition from the spreading to the break-up regime. This might suggest a further study of the forces and stresses between a particle and an interface.

The author thanks É. Guazzelli for discussions and help.

REFERENCES

- BRAGG, L. & NYE, J. F. 1947 A dynamical model of a crystal structure. *Proc. R. Soc. Lond.* **190**, 474–481.
- CHANDRA, S. & AVEDIAN, C. T. 1991 On the collision of a droplet with a solid surface. *Proc. R. Soc. Lond. A* **432**, 13–41.
- FORD, R. E. & FURMIDGE, C. G. L. 1967 Impact and spreading of spray drops on foliar surfaces. *Wetting Soc. Chem. Industry Monograph*, pp. 417–432.
- GU, Y. & LI, D. 1998 A model for a liquid drop spreading on a solid surface. *Colloids Surface A* **142**, 243–256.
- GU, Y. & LI, D. 2000 Liquid drop spreading on solid surfaces at low impact speeds. *Colloids Surface A* **163**, 239–245.
- JOSEPH, D. D., WANG, J., BAI, R., YANG, B. H. & HU, H. H. 2003 Particle motion in a liquid film rimming the inside of a partially filled rotating cylinder. *J. Fluid Mech.* **496**, 139–163.
- MAO, T., KUHN, D. C. S. & HONGHI, T. 1997 Spread and rebound of liquid droplets upon impact on flat surfaces. *AIChE J.* **43**, 2169–2179.
- MUNDO, C., SOMMERFELD, M. & TROPEA, C. 1995 Droplet-wall collisions: experimental studies of the deformation and breakup process. *Intl J. Multiphase Flow* **21**, 151–173.
- PARK, H., CARR, W. W., ZHU, J. & MORRIS, J. F. 2003 Single drop impaction on a solid surface. *AIChE J.* **49**, 2461–2471.
- PASANDIDEH-FARD, M., QIAO, Y. M., CHANDRA, S. & MOSTAGHIMI, I. 1996 Capillary effects during droplet impact on a solid surface. *Phys. Fluids* **8**, 650–659.
- RANGE, K. & FEUILLEBOIS, F. 1998 Influence of surface roughness on liquid drop impact. *J. Colloid Interface Sci.* **203**, 16–30.

- REIN, M. 1993 Phenomena of liquid drop impact on solid and liquid surfaces. *Fluid Dyn. Res.* **12**, 61–93.
- REZNIK, S. N. & YARIN, A. L. 2002 Spreading of an axisymmetric viscous drop due to gravity and capillarity on a dry horizontal wall. *Intl J. Multiphase Flow* **28**, 1437–1457.
- SEERDEN, K. A. M., REIS, N., EVANS, J. R. G., GRANT, P. S., HALLORAN, J. W. & DERBY, B. 2001 Ink-jet printing of wax-based alumina suspensions. *J. Am. Ceram. Soc.* **34**, 2514–2520.
- SHI, L. T. & ARGON, A. S. 1982 The potential and force law between different-size bubbles in soap bubble raft. *Phil. Mag A* **46**(2), 255–274.
- SHIKHMURZAEV, Y. D. 1997 Spreading of drops on solid surfaces in a quasi-static regime. *Phys. Fluids* **9**, 266–275.
- STOW, C. D. & HADFIELD, M. G. 1981 An experimental investigation on fluid flow resulting from the impact of a water drop with an unyielding dry surface. *Proc. R. Soc. Lond. A* **373**, 419.
- THORODDSEN, S. T. & SAKAKIBARA, J. 1998 Evolution of the fingering pattern of an impacting drop. *Phys. Fluids* **10**, 1359–1374.

B.12 Submarine granular flows down inclined planes

C. CASSAR, M. NICOLAS & O. POULIQUEN

Phys. Fluids, **17**, 103301 (2005).

Submarine granular flows down inclined planes

C. Cassar, M. Nicolas, and O. Pouliquen

IUSTI, Université de Provence—Centre National de la Recherche Scientifique (CNRS), 5 rue Enrico Fermi, 13453 Marseille Cedex 13, France

(Received 2 December 2004; accepted 24 August 2005; published online 7 October 2005)

Submarine flows of granular material down a rough inclined plane are experimentally investigated. We focus on the dense flow regime when the whole sediment layer is flowing down the slope and when no deposition nor entrainment occurs. In this regime, steady uniform flows are observed for which we systematically measure the depth-averaged velocity, the thickness, and the excess pore pressure for different inclinations and different flow rates. The experimental measurements are analyzed within a theoretical approach inspired by recent results obtained for dry granular flows. The basic assumption of the model is that the constitutive law obtained in the dry case still holds for submarine flow, if one substitutes the inertial time scale coming into play in the rheology by a viscous time scale. The agreement between the measurements and the theory supports this assumption. © 2005 American Institute of Physics. [DOI: 10.1063/1.2069864]

I. INTRODUCTION

Flows of cohesionless granular materials have been the subject of an intense research activity during the recent years. Many studies concern dry granular flows, i.e., flows for which the interstitial fluid between grains does not play any role. The rheology is in this case controlled by friction and collisions between particles. Many different configurations have been investigated, such as grains flowing down a slope, on a pile, in a silo, etc. Progresses in our understanding of the rheology have been made recently by comparing the different flow configurations.¹ However, in some applications the fluid in which the granular material is immersed cannot be neglected, for example, when sand flows underwater. In this case the viscous interaction between the grains and the surrounding fluid plays a role and has to be taken into account in the rheological properties.

This problem is of importance in many industrial applications as well as in most of the geophysical events involving flow of soils. A debris flow is an example of a hazardous granular flow with a lot of water content.² A submarine avalanche occurring on a continental margin is another example.³ The flow of sediments can be triggered either by an earthquake, human activity, or when the sediment deposit is intrinsically unstable. The large amount of material (mud, sand, gravel, or rocks) that starts flowing underwater can create a tsunami⁴ and can run on very low slopes (a few degrees of inclination)³ damaging undersea cables, pipelines, etc.

Different approaches have been developed in the literature to describe mixtures of grains and fluids. A first approach encountered when modeling both subaqueous or aerial debris flows is to consider the flowing layer of material as a fluid with an empirical non-Newtonian rheology. The Bingham rheology is a frequent choice found in the literature^{5–7} to describe submarine flows. If such a choice can be suitable for pure mudflows, it is certainly less justified when noncolloidal particles are involved in the flowing mixture. In this case, the particles experience different kind of

interactions:^{8,9} hydrodynamic interactions due to the fluid motion, frictional interactions when contact occurs, collisions when strongly agitated, etc. A lot of effort has been devoted to the relatively dilute and viscous case when the suspension dynamics is mainly controlled by hydrodynamics interactions.^{10–12} Even in this simple case the rheology is nontrivial and characterized by a viscosity which diverges when increasing the volume fraction and by the development of normal stress effects.¹³ Attempts to take into account the other contact interactions have been developed.^{9,14}

However, most of the approaches to understand dense granular suspensions are based on dilute suspensions and try to infer how the behavior changes with an increasing volume fraction. In this paper we address the problem by starting from the other extreme case, i.e., the dry granular case where only contact interactions are present. As our knowledge about dry granular flows has been considerably improved during the last decade, it is worth to investigate how a fluid could modify flow properties in these systems and hence better understand the dynamics of grainfluid mixture.

The influence of the interstitial fluid on granular flows has been studied in different configurations. Prasad and Kytomaa have sheared granular suspensions starting from dense packing in Couette cells.¹⁵ They have shown that in the dense case the suspension essentially has a shear-rate-independent behavior. Muir *et al.*¹⁶ have investigated how the discharge of a silo can be influenced by the interstitial fluid. Jain *et al.*¹⁷ have shown that the major characteristic of a granular flow involving large and heavy beads in a rotating drum is unchanged when the drum is filled with liquid. In the present study, we will refer to the work carried out by Courrech du Pont *et al.*¹⁸ in the rotating-drum configuration. They have systematically studied the avalanche durations for different particle sizes, different densities, and different interstitial fluid viscosities. They have determined the relevant time-scales controlling the flow and were able to find the relevant dimensionless number characterizing the different flow regimes. We will show in this paper that the time-scale analysis

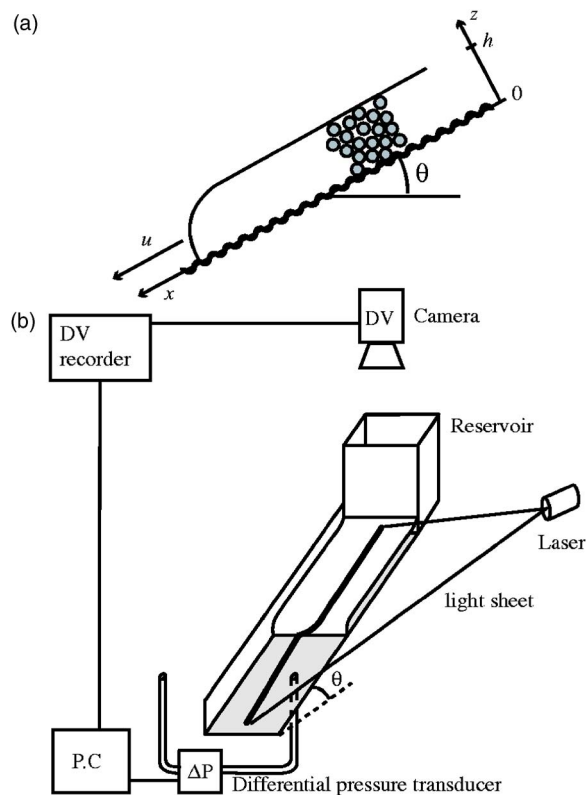


FIG. 1. (a) Sketch of the submarine inclined plane configuration. (b) Sketch of the experimental setup.

provided by their study of intermittent avalanches also applies to describe the continuous flow properties.

In this paper, we experimentally study submarine granular avalanches obtained in the inclined plane configuration [see Fig. 1(a)]: a layer of grains of controlled thickness flows down a rough surface inclined at a constant angle. The whole setup is immersed in a water tank. The experimental procedure is different from classical density current experiments, where a suspension is released on a slope in fresh water.^{19–21} In this case deposition occurs during the flow and entrainment of fresh water in the surge also exists. In our experiments, the avalanche is created from a dense packing where the grains are already in contact and the inclination angles are high enough such that the whole granular layer flows down the slope. It is similar to early experiments carried out by Allen.²² In this regime no deposition nor entrainment occurs. The flows we are studying are then reminiscent of the flows of dry granular materials down inclined plane that have been extensively studied and have provided a lot of information about the rheology of dry particles.¹ Our aim is to compare the immersed case with the dry case by investigating the different flow regimes and the properties of steady uniform flows. We also measure the interstitial pore pressure which gives an indication of the coupling that exists between the stresses carried by the particles and the stress developed by the fluid flowing through the porous media formed by the grains.^{2,23,24}

The experimental setup we use and the measurement techniques are presented in Sec. II. The different flow regimes and the flow characteristics of the steady uniform

flows are given in Sec. III. Section IV discusses how a simple constitutive law extended from the dry granular constitutive law can be proposed and the comparison between the prediction of this heuristic approach and experiments is shown in Sec. V. Finally, a summary and some conclusive remarks are given in Sec. VI.

II. EXPERIMENTAL SETUP

The sketch of our experimental setup is shown in Fig. 1(b). The setup is built from a 49-cm-long and 14-cm-wide PVC (vinyl polychloride) plate linked to a 1120 cm³ parallelepipedic reservoir. The opening of the reservoir is a slot of controlled height h_g . We note θ as the angle between the rough plane and the horizontal. The whole setup is fully immersed in a 150 liter glass tank ($L \times W \times H = 70 \times 40 \times 50$ cm) filled with water at ambient temperature. The plate is made rough by gluing with black sprayed paint one layer of the same particles as the flowing material. Flowing particles are spherical glass beads of density $\rho_p = 2.47 \pm 0.01$ g cm⁻³. Two different sizes are used, small and large particles with diameters $d = 112 \pm 20$ μ m and $d = 208 \pm 19$ μ m, respectively.

The flowing material is lighted with a He–Ne laser sheet at a small angle of incidence [see Fig. 1(b)]. When the flow occurs, the laser line is distorted, and its horizontal displacement, which is proportional to the flow thickness,²⁵ provides the granular layer thickness measurement. The flow is recorded using a digital video (DV) camera placed above the water tank. A typical image is given in Fig. 5(a). Images are analyzed using the image processing software NIH IMAGE (developed at the US National Institute of Health and accessible through internet). The movie gives measurements of the front velocity $u(t)$ with an accuracy of 2.5% and the flow thickness $h(x, t)$ with an accuracy of 6%.

The basal liquid pressure below the avalanche is measured as follows. A 5 mm pressure hose is drilled at 25 cm from the reservoir gate. The hole is covered with a 50 μ m metallic mesh to prevent particles from falling in the hose. A second pressure hose is placed beside the rough plane at roughly the same depth from the water surface. Both hoses are connected to a Druck LPM9845 differential pressure transducer with 5-mm-i.d. flexible tubes. The tubes are tightened to a metallic structure to prevent any vibration. A specific care is taken to avoid any air bubble in the pressure transducer body or in the tubes which could alter the pressure signal. The pressure transducer has a 0 ± 10 Pa range with an accuracy of ± 0.04 Pa. The pressure signal is digitized with a 16-bit digital acquisition board at a 100 Hz rate. With this device we can accurately measure how the hydrostatic liquid pressure is modified by the granular avalanches.

A typical experiment is done as follows. We first pour a mixture of water and particles in the immersed reservoir, the gate being closed, and wait for 5 min to ensure that the sedimentation of particles is complete. The gate of the reservoir is then opened gently to avoid surface waves in the tank. Pressure measurements and top view images are recorded during the whole emptying of the reservoir which lasts typically between 20 s and 4 min. Several experiments have

TABLE I. Experimental parameters. The particles are glass beads ($\rho_p=2470 \text{ kg/m}^3$) of diameters $d=112\pm 20 \text{ }\mu\text{m}$ (small) and $d=208\pm 19 \text{ }\mu\text{m}$ (large). The characteristics of air are $\eta=1.85\times 10^{-5} \text{ kg/m s}$ and $\rho_f=1.29 \text{ kg/m}^3$, and the characteristics of water are $\eta=10^{-3} \text{ kg/m s}$ and $\rho_f=10^3 \text{ kg/m}^3$.

Expt.	Particles	Fluid	Flow thickness	Inclination	St	r
W1	small	water	$3.2 < h/d < 40.5$	$22^\circ < \theta < 42^\circ$	$0.07 < \text{St} < 0.27$	2.48
A1	small	air	$6.2 < h/d < 60.3$	$23^\circ < \theta < 38^\circ$	$7 < \text{St} < 23$	69.2
W2	large	water	$2.1 < h/d < 25.8$	$24^\circ < \theta < 36^\circ$	$0.15 < \text{St} < 0.55$	2.48
A2	large	air	$4.3 < h/d < 30.1$	$24^\circ < \theta < 34^\circ$	$15 < \text{St} < 37$	69.2

been performed, with two particle sizes both in air and in water. The inclination angle was varied from 22° to 42° and the gate opening was varied from 2 to 8 mm. A summary of the various experimental conditions is given in Table I.

III. MEASUREMENTS

A. Different flow regimes

Different flow regimes are observed, depending on the two control parameters in our experiment: the inclination of the plane θ and the opening of the gate h_g . However, to analyze the data in terms of rheological properties, it is more convenient to use the thickness h of the flowing layer once the flow is developed, rather than the opening of the gate. The phase diagram for the small particles in water (experiment W1) is plotted in the (θ, h) plane in Fig. 2 [the insert is in the (θ, h_g) plane]. Three different regimes are distinguished: a regime where no flow is possible, a regime where steady uniform flows are observed, and a regime where an instability develops and the flow becomes wavy. Such a phase diagram is very similar to the one observed with dry granular material.²⁶

As in a dry granular flow,²⁵ the border between the static regime and the steady flow regime can be accurately mea-

sured by looking at the deposit remaining on the plane once the flow stops. The deposit thickness h_{stop} is the minimum thickness for which a flow is possible. The results are presented in Fig. 3 for both the submarine and aerial cases for the small particles. Within the error bars, the deposit thickness remains unchanged when the flow occurs either in water or in air. Whatever the gate opening, the deposit thickness depends only on the inclination angle and is thus a pure material property. However, no deposit is observed after an aerial flow for an inclination larger than $\theta \approx 38^\circ$, whereas after an immersed flow a small layer of particles remains on the plane even for a large inclination angle, up to 45° . We do not have any explanation for this difference which could be due to subtle cohesive effects.²⁷ It must be noticed that during the flow, a side observation of the flow shows that no static layer of particles exists.

Above the $h_{\text{stop}}(\theta)$ curve in the phase diagram, flows are possible. For large inclination (typically above 38°) and large opening of the gate, the flows are not steady. The front accelerates along the plane and a free-surface instability develops. The free surface experiences a wavy deformation which grows along the plane and can ultimately create a suspension flow (Fig. 4). This instability is certainly reminiscent of the long-wave instability observed in the dry case.²⁶ We have not studied this flow regime in detail yet.

In this study we rather focus on the steady uniform

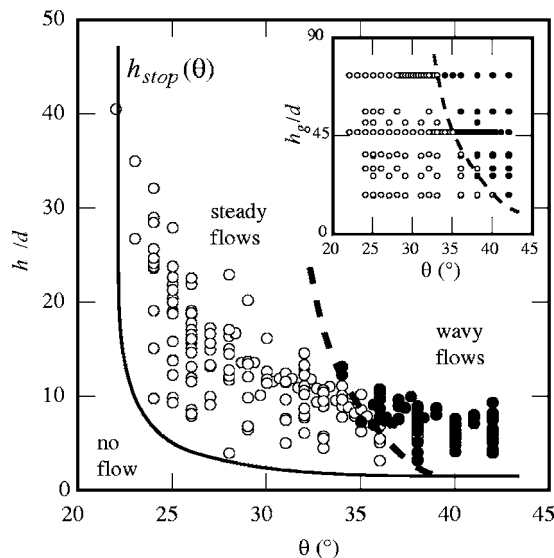


FIG. 2. Map of the different flow regimes in the $(\theta, h/d)$ plane for experiment W1. The open circles are the stationary flows and the filled circles are the wavy flows. The solid line is the $h_{\text{stop}}(\theta)$ curve and the dashed line is the qualitative boundary between the stationary and wavy flow regimes. The inset shows the same data in the $(\theta, h_g/d)$ plane.

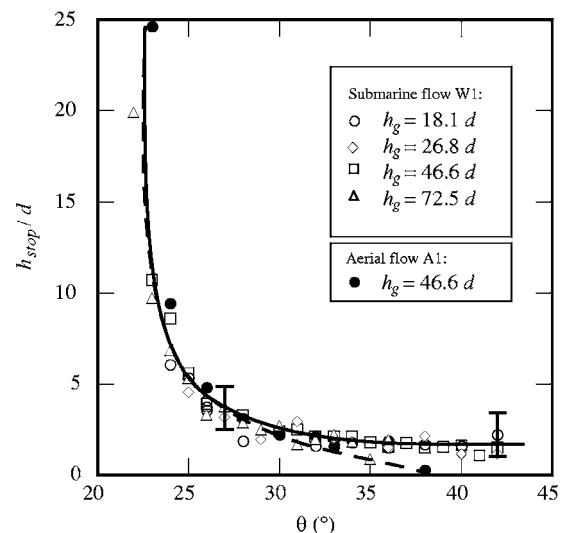


FIG. 3. Deposit thickness h_{stop} vs inclination angles in the subaqueous (W1) and aerial (A1) cases. The continuous and dashed lines show the qualitative trends for the submarine and aerial flows, respectively.

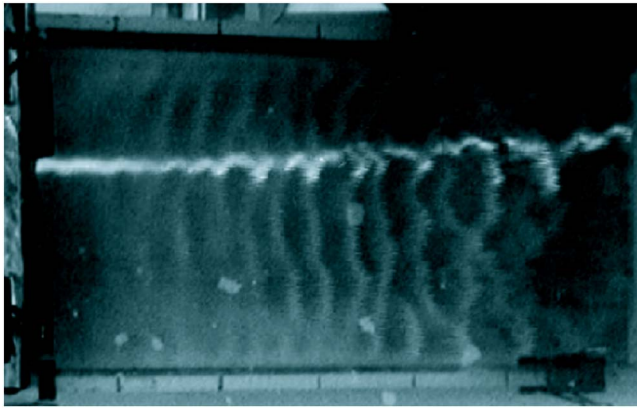


FIG. 4. Snapshot of a wavy flow (W1) for $\theta=42^\circ$ and $h_g=46.6d$. The particle reservoir is on the left of the picture (not shown) and the flow is from left to right. The bright distorted line is the reflection of the laser sheet on the flow surface.

flows, for inclinations ranging from 24° to 38° . Once the gate is opened, a well-defined front propagates down the slope at a constant velocity, as shown in Fig. 5(a). The curved shape of the front observed in Fig. 5(a) is certainly due to a non-homogenous feeding from the reservoir induced by friction on the walls. The measurements presented below are made in the center line, but the same velocity measurements carried out on the side change only by a factor less than 5%. In this range of inclinations the front rapidly reaches a steady shape and propagates down the slope without deforming, as shown in Figs. 5(b) and 5(c). The constant velocity of the front is shown in Fig. 5(b). Behind the front a steady uniform flow develops, with a flat surface and a uniform thickness h [Fig. 6(a)]. The thickness h remains constant during the whole emptying of the silo as shown in Fig. 6(b) where the thickness measured just above the pressure hose is plotted as a function of time. In Fig. 6(c) we also plot the basal interstitial pressure Δp_i measured during the experiment which stays also constant during the experiments. As the front keeps a stationary shape and the flow that develops behind is steady and uniform, one can conclude from mass conservation that the front velocity u is equal to the depth-averaged velocity of the fully developed flow.²⁵ We are then able to characterize the steady uniform flows at a given inclination θ and a given opening of the gate h_g by measuring the three following quantities: the mean thickness h , the mean velocity u , and the interstitial pressure Δp_i . We have systematically studied how these quantities vary when changing the control parameters θ and h_g .

B. Steady uniform flow properties

Figures 7(a) and 8(a) show how the mean velocity u varies as a function of the thickness for different plane inclinations θ for small and large beads, respectively. The typical immersed flow velocity is of the order of 1–50 mm/s for small particles and 1–70 mm/s for large particles. The flow is faster for thick flows and when the inclination is high. As a comparison, we have plotted in Figs. 7(b) and 8(b) the measurements obtained in the aerial case for the same beads. The velocity range is from 10 to 600 mm/s. Although the

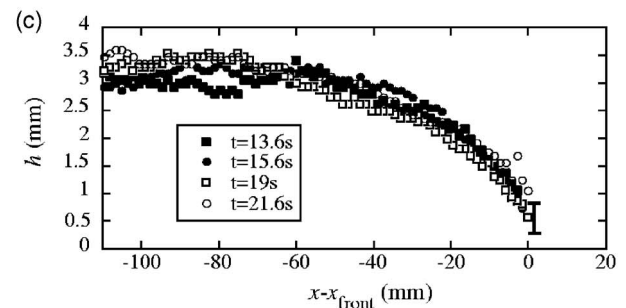
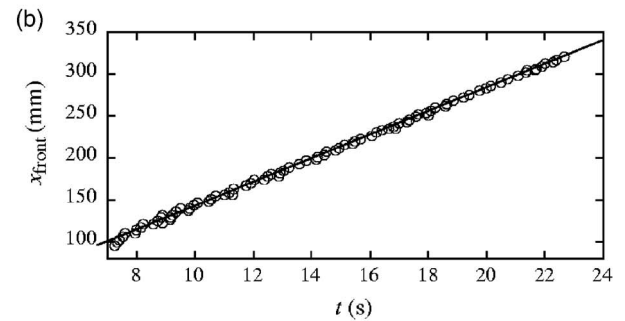
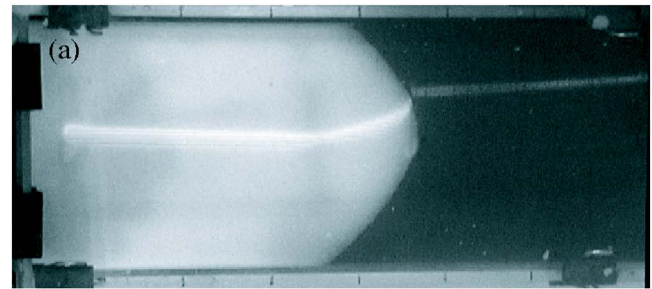


FIG. 5. Front propagation for configuration W1: (a) Snapshot of a submarine flow for $\theta=25^\circ$ and $h_g=72.5d$. The bright curve is the laser sheet. The particle reservoir is on the left of the picture (not shown) and the flow is from left to right. (b) Front position as a function of time for $\theta=26^\circ$ and $h_g=47d$. (c) Shape of the front at four different times for $\theta=26^\circ$ and $h_g=47d$.

variations are qualitatively the same in the aerial and in the submarine cases, the flow velocity is about ten times slower in water than in air, indicating a strong influence of the interstitial fluid. We will discuss the physical origin of this dependence in Sec. IV.

C. Excess pore pressure measurements

The excess pore pressure also depends on the control parameters. Figure 9 shows how Δp_i varies as a function of the flow thickness for different inclinations in submarine experiments for the two particle sizes we used (experiments W1 and W2). The first remark is that Δp_i is always positive, indicating that the fluid pressure below the avalanche is always higher than the hydrostatic pressure. No negative excess pore pressure has been measured in the steady uniform flows. The second remark is that the excess pressure is relatively low in the steady uniform regime compared to what one would expect in the case of a fully suspended flow. If all the particles were suspended, the liquid excess pressure measured below the flow would be²⁸ $\Delta p_i^{\text{susp}} = \Delta \rho g h \cos \theta$ with the

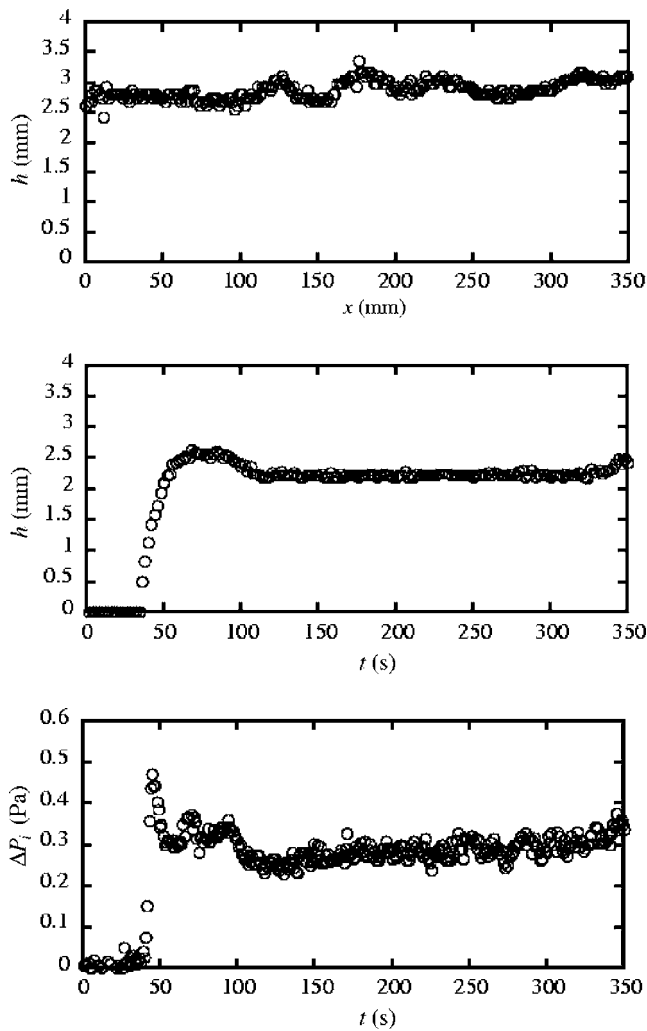


FIG. 6. (a) Free-surface profile at $\theta=26^\circ$ and $h_g=47d$. (b) Time evolution of the flow thickness h and (c) the excess pore pressure Δp_i above the pressure hose for $\theta=28^\circ$ and $h_g=56d$.

density difference defined as $\Delta\rho=\phi(\rho_p-\rho_f)$, where ϕ is the packing volume fraction assumed to be constant and equal to 0.55 in the following.

The maximum relative excess pressure $\Delta p_i/\Delta p_i^{\text{susp}}$ observed is about 25%. This means that in the steady uniform flows we observed, contact interactions between particles are important: at least 75% of the weight of the particles is carried by the contact network and not by the pore pressure. Higher values of the pore pressure have been measured but in the wavy flow regime only. The waves that developed at the free surface probably promote more and more particles into a suspension. The last remark is that the pressure seems to follow a roughly linear dependence with the thickness (Fig. 9).

D. Shear stress at the top of the flow

A source of dissipation in submarine avalanches could be the shear that develops between the clear fluid and the granular layer. In classical gravity current experiments, this shear promotes the destabilization of the interface and an entrainment process.¹⁹ In our experiments no entrainment is

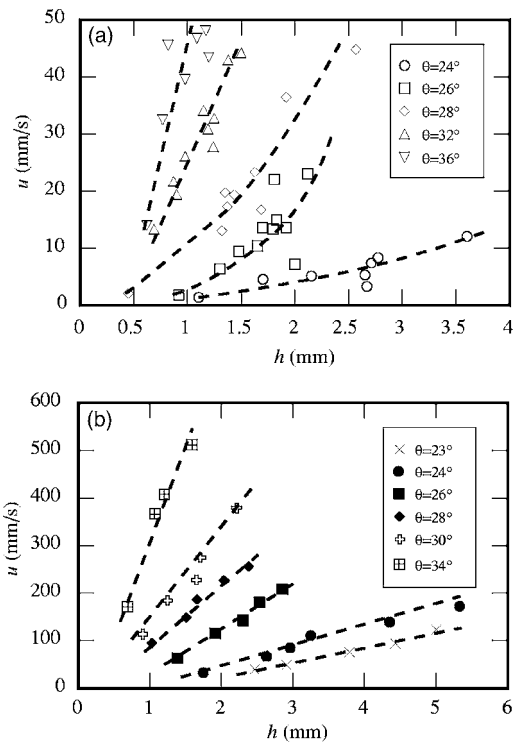


FIG. 7. Velocity measurements for submarine flows W1 (a) and aerial flows A1 (b). The dotted lines show the qualitative trend.

observed in the steady uniform regime. In order to quantify the influence of the shear, the clear fluid is seeded with tiny green fingerprint powder particles, and the tank is lighted with a vertical green laser sheet. Using two successive frames of a video recording, we compute the velocity field of the water flow above the granular layer. The shear rate $\dot{\gamma}_{\text{out}}$ just above the grains is found to be of the order of 4 s^{-1} . This implies that the outer shear stress is $\eta\dot{\gamma}_{\text{out}} \approx 4 \times 10^{-3} \text{ Pa}$, to be compared with the stress induced by the gravity $\Delta\rho gh \sin \theta$ which is typically of the order of 12 Pa for an immersed flow with $\theta=24^\circ$ and $h=3.2 \text{ mm}$ thick. As a result, we can conclude that the shear in the outer fluid has no influence on the flow and that the rheology is controlled by the internal deformation of the granular layer. Moreover, no fluid exchange occurs during the flow. When fluorescein dye is added to the interstitial liquid in the reservoir, no dye gets out of the granular layer flowing down the slope. The interstitial liquid is trapped inside the porous material formed by the assembly of the particles.

IV. TIME-SCALE ANALYSIS AND CONSTITUTIVE LAW

In this section we present a simple theoretical approach to analyze our data based on a constitutive law recently proposed to describe dry granular flows. The influence of the water is discussed in terms of time scales of the motion of a single grain. We first summarize the recent results obtained for the rheology of dry granular flows before presenting a generalization of the approach to the submarine case.

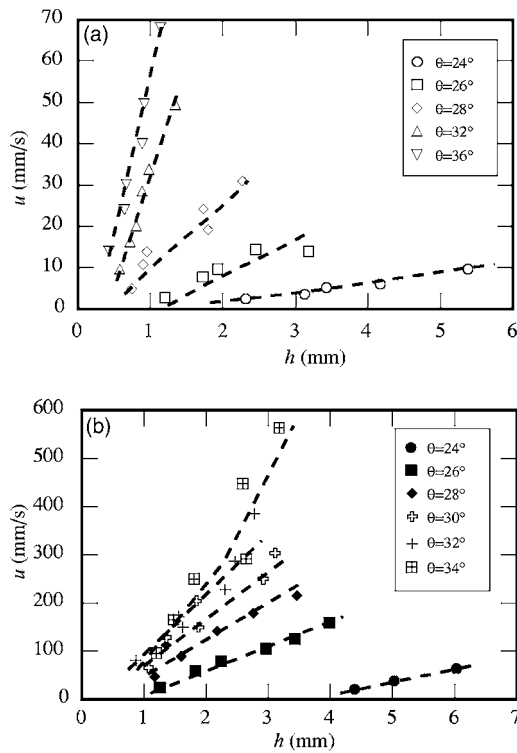


FIG. 8. Velocity measurements for submarine flows W2 (a) and aerial flows A2 (b). The dotted lines show the qualitative trend.

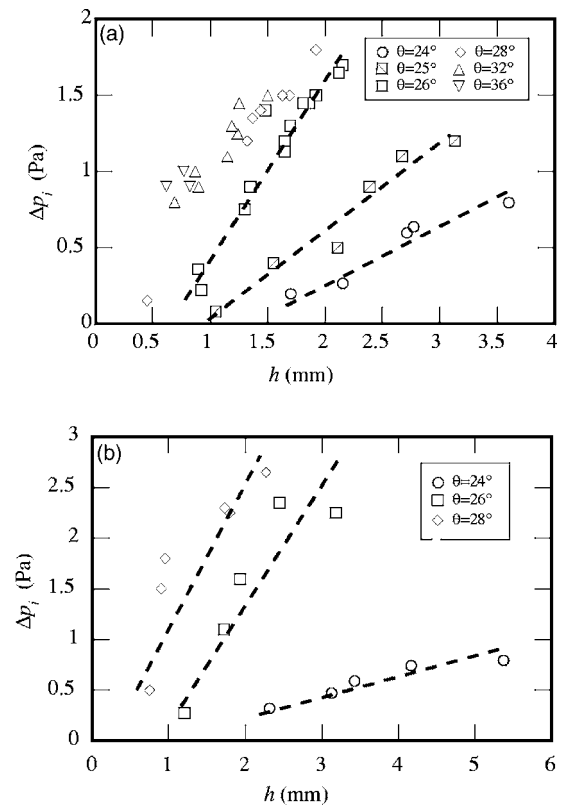


FIG. 9. Excess pore pressure vs thickness in physical units for submarine flows W1 (a) and W2 (b).

A. Previous results in dry granular flows

The flow of dry granular flows, when the interstitial fluid plays no role, has recently been the subject of numerous studies. Based on a dimensional analysis, a simple heuristic rheology has been proposed which correctly predicts many of the features observed in dense granular flows.^{1,29,30} Let us consider a granular material submitted to a simple shear with a shear rate $\dot{\gamma}$ and to a confining pressure P_g (Fig. 10). It has been shown with numerical simulations^{29,30} that the shear stress τ verifies the following friction law:

$$\tau = P_g \mu(I), \tag{1}$$

with a friction coefficient depending on a single dimensionless parameter I defined by

$$I = \frac{\dot{\gamma} d}{\sqrt{P_g / \rho_p}}. \tag{2}$$

As discussed in a recent collective paper,¹ an interpretation of the constitutive law can be given in terms of the relevant time scales controlling grain motion. Let us consider the motion of one grain during a simple shear, as plotted in Fig. 10. The grain first follows the mean deformation with a rate $\dot{\gamma}$ but eventually reaches an unstable position when passing at the crest over the particle just below. It is then rapidly pushed down in the next hole due to the confining pressure P_g . The time of fall can be estimated by a simple free fall of the particle of diameter d and density ρ_p under a force $P_g d^2$ over a distance d : $t_{fall} = d / \sqrt{P_g / \rho_p}$. The parameter I is interpreted as the ratio between this rapid time of rearrangement t_{fall} and the mean time $t_{\dot{\gamma}} = \dot{\gamma}^{-1}$ spent by the particle to move

from one hole to the next one. Notice that the dimensionless number I is the square root of the Savage number³¹ or Coulomb number⁹ defined as the ratio between the collisional stress and the total stress. Here, we keep the description in terms of I as we will see that the interpretation in terms of a time-scale ratio helps our understanding of immersed granular flows. If one neglect the time scale related to the elasticity of the particles, I is the only dimensionless number and the shear stress τ has to be proportional to the pressure P_g multiplied by a function of I , leading to the constitutive law (1).¹ Despite the limitation of such a simple description discussed in the collective work,¹ the friction law (1) succeeds in describing a plane shear flow,^{29,30} flows on inclined plane,^{1,25} and flows on a heap.³² It is then interesting to modify this simple picture introducing the influence of the interstitial fluid.

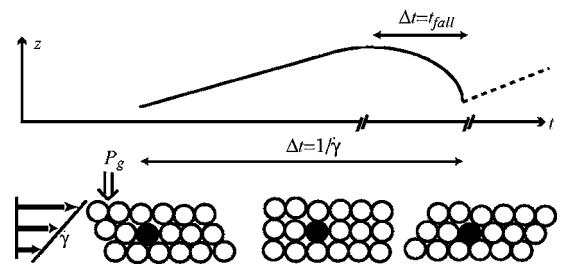


FIG. 10. Sketch of the motion of a grain $z(t)$ during a simple shear $\dot{\gamma}$ under a confining pressure P_g .

B. Times scales for submarine granular flows

In the simple picture presented above, the first influence of the fluid is to change the time scale. If one assumes the flow to be in a regime where the contacts between particles are still important, the motion of the grains in Fig. 10 is going to be the same in the presence of fluid or not, except that the time t_{fall} it takes to fall in the hole once the crest is passed could be affected by the fluid. This idea suggests that immersed dense granular flows can be described by the same constitutive law (1), using a modified dimensionless parameter I . Our purpose in the following analysis is to study the validity of this simple assumption.

In order to do that, we need to estimate the time t_{fall} in the presence of a fluid. We follow the work of Courrech du Pont *et al.* who analyzed the free fall of a particle under gravity¹⁸ but we consider that the particle is submitted to a confining pressure instead of the gravity. Let us write the equation of motion along the vertical direction of a particle submitted to the confining pressure P_g in a fluid of density ρ_f and viscosity η_f :

$$\frac{\pi}{6}\rho_p d^3 \frac{dv_p}{dt} = \frac{\pi}{4}P_g d^2 - F_d, \quad (3)$$

where F_d is the drag force due to the fluid. Depending on the particulate Reynolds number Re_p , the drag force can be either a pure viscous Stokes force ($\text{Re}_p \ll 1$) or an inertial force ($\text{Re}_p \gg 1$). We can now analyze the motion of the particle for the different cases.

- Dry granular regime: The drag force is negligible. The particle then follows a free-fall motion characterized by an accelerated motion. The time it takes for the particle to travel one diameter is then

$$t_{\text{ff}} = d\sqrt{2\rho_p/3P_g}.$$

- Viscous regime ($\text{Re}_p \ll 1$): In this case, the fall of the grain is hindered by a viscous drag force, and the displaced liquid has to flow through a porous medium of permeability $k = \alpha d^2$. Using Darcy's law, the pressure difference across the particle is then equal to $\eta_f dv_p/k$ and the drag force can be written as follows:

$$F_d = (\pi/4\alpha)\eta_f dv_p. \quad (4)$$

The estimation of the coefficient α is not easy as it depends on the size distribution of the particles³³ and on the fact that our porous medium is deformable. For spherical particles at volume fraction around 0.55 different estimates in the literature³³ give values in between 5×10^{-3} and 10^{-2} . Our medium being deformable, we have chosen in the following the highest value $\alpha = 0.01$. This choice will be discussed in Sec. V C. At short times, the grain first accelerates but because of the drag force, the grain eventually reaches a limit viscous velocity $v_{\infty v}$ in the characteristic acceleration time t_{av} given by

$$v_{\infty v} = P_g \alpha d / \eta_f,$$

$$t_{av} = \frac{2\rho_p \alpha d^2}{3\eta_f}.$$

If $t_{av} \ll t_{\text{ff}}$, the particle rapidly reaches its limit velocity and the time to travel a diameter is then given by $t_{\text{fall}} = d/v_{\infty v}$, otherwise $t_{\text{fall}} = t_{\text{ff}}$.

- Inertial regime ($\text{Re}_p \gg 1$): When the particulate Reynolds number Re_p is not small compared to unity, inertial effects must be taken in account. The drag force is equal to $F_d = (\pi/6)C_d d^2 \rho_f v_p^2$, where C_d is the drag coefficient which is nearly constant and equal to 0.4 for $10^3 < \text{Re}_p < 10^5$. In this case the grain will reach a limit velocity $v_{\infty i}$ in the characteristic time t_{ai} given by

$$v_{\infty i} = \sqrt{3P_g/2\rho_f C_d},$$

$$t_{ai} = \rho_p d (2/3\rho_f C_d P_g)^{1/2}.$$

If $t_{ai} \ll t_{\text{ff}}$, the particle rapidly reaches its limit velocity and the time to travel a diameter is then given by $t_{\text{fall}} = d/v_{\infty i}$, otherwise $t_{\text{fall}} = t_{\text{ff}}$.

In order to classify the different regimes, Courrech du Pont *et al.*¹⁸ introduced three dimensionless numbers: the Stokes number $\text{St} = t_{av}/t_{\text{ff}}$, the density ratio $r = t_{ai}/t_{\text{ff}}$, and the Reynolds number $\text{Re} = t_{av}/t_{ai}$:

$$\text{St} = \left(\frac{2}{3}\right)^{1/2} \frac{\alpha d \sqrt{\rho_p P_g}}{\eta_f}, \quad (5)$$

$$r = \sqrt{\frac{\rho_p}{\rho_f C_d}}, \quad (6)$$

$$\text{Re} = \frac{\text{St}}{r} = \frac{\alpha d}{\eta_f} \sqrt{\frac{2\rho_f C_d P_g}{3}}. \quad (7)$$

As shown by Courrech du Pont *et al.*, three regimes can be characterized depending on the value of the dimensionless numbers St and r (the Reynolds number being the ratio between both of them): a viscous regime ($\text{St} \ll 1$ and $\text{St} \ll r$) where the particle reaches the viscous limit velocity during its elementary motion, an inertial regime ($r \ll 1$ and $\text{St} \gg r$) where it reaches the inertial limit velocity, and a free-fall regime ($\text{St} \gg 1$ and $r \gg 1$) where it follows an accelerated motion. The three regions in the plane (St, r) are shown in Fig. 11.

In this analysis, we have computed the time t_{fall} a particle takes to fall into the hole as a function of the two parameters St and r and consequently we are able to propose constitutive equations for the three different regimes. In all cases the shear stress is proportional to the confining pressure [Eq. (1)] with a unique function $\mu(I)$ but with a time ratio I that depends on the regimes and is given by $I = \dot{\gamma} t_{\text{fall}}$:

- in the free-fall regime $\text{St} \gg 1$ and $r \gg 1$,

$$I = I_{\text{ff}} = \dot{\gamma} d \sqrt{\frac{2\rho_p}{3P_g}}; \quad (8)$$

- in the viscous regime $\text{St} \ll 1$ and $r \gg \text{St}$,

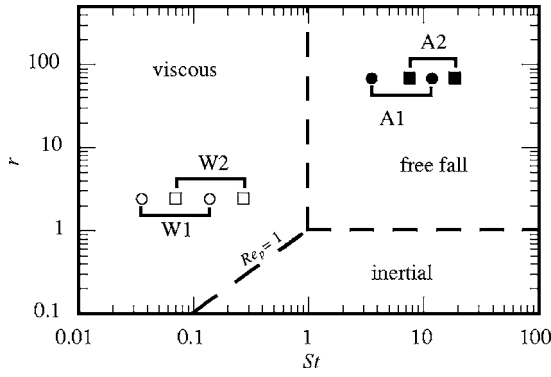


FIG. 11. Different flow regimes in the (St, r) plane based on the fall of one grain [after Courrech du Pont *et al.* (Ref. 18)]. The symbols show the extreme values reached for the experiments with glass beads $d=112 \mu\text{m}$ in air (A1, open circles) and in water (A2, filled circles) and with glass beads $d=208 \mu\text{m}$ in air (A2, open squares) and in water (W2, filled squares).

$$I = I_v = \frac{\dot{\gamma}\eta_f}{\alpha P_g}; \quad (9)$$

- in the inertial regime $St \gg r$ and $r \ll 1$,

$$I = I_i = \dot{\gamma}d \sqrt{\frac{2\rho_f C_d}{3P_g}}. \quad (10)$$

The strong assumption underlying the proposed constitutive laws is that the interstitial fluid only plays a role by changing the time scale of the microscopic rearrangements. In order to test the validity of this simple approach in our experiment, let us first derive the predictions for the flow down an inclined plane.

C. Predictions for flows down inclined plane

In the inclined plane configuration, if one assumes that the excess pore pressure is negligible, the momentum balance implies that the effective shear stress and effective normal stress for a steady uniform flow are $\tau = \Delta\rho g(h-z)\sin\theta$ and $P_g = \Delta\rho g(h-z)\cos\theta$, where $\Delta\rho = \phi(\rho_p - \rho_f)$ is the effective density of the granular medium. The ratio between the shear stress and the normal stress is then constant across the layer and equal to $\tan\theta$. As a result, if the material is described by a constitutive law (1), one obtains $\tan\theta = \mu(I)$, meaning that the parameter I does not vary across the layer and is independent of z . From the different expressions given in Eqs. (8)–(10), one can then derive the velocity profiles for a layer of thickness h flowing on a plane inclined at θ for the three different regimes:

- in the free-fall regime ($St \gg 1$ and $r \gg 1$),

$$u_x(z) = \frac{I_{\text{ff}}}{d} \sqrt{\frac{2\Delta\rho g \cos\theta}{3\rho_p}} [h^{3/2} - (h-z)^{3/2}]; \quad (11)$$

- in the viscous regime ($St \ll 1$ and $r \gg St$),

$$u_x(z) = \frac{I_v \alpha}{\eta} \Delta\rho g \cos\theta \left(h - \frac{z}{2}\right); \quad (12)$$

- in the inertial regime ($St \gg r$ and $r \ll 1$),

$$u_x(z) = \frac{I_i}{d} \sqrt{\frac{2\Delta\rho g \cos\theta}{3\rho_f C_d}} [h^{3/2} - (h-z)^{3/2}]. \quad (13)$$

In the viscous regime, the velocity profile (12) is half parabolic and is similar to the flow profile of a layer of a viscous Newtonian fluid down an inclined plane. In the other regimes, the velocity profile is Bagnold-like, as for a dry granular flow down a slope. In order to compare the prediction with the experimental data, we compute from these equations the depth-averaged velocity $u = 1/h \int_0^h u_x(z) dz$. For the three regimes we can then express the parameter I as a function of the three measured quantities u , θ , and h :

- in the free-fall regime ($St \gg 1$ and $r \gg 1$),

$$I = I_{\text{ff}} = \frac{5ud}{2h^{3/2}} \sqrt{\frac{2\rho_p}{3\Delta\rho g \cos\theta}}; \quad (14)$$

- in the viscous regime ($St \ll 1$ and $r \gg St$),

$$I = I_v = \frac{3u}{h^2} \frac{\eta_f}{\alpha \Delta\rho g \cos\theta}; \quad (15)$$

- in the inertial regime ($St \gg r$ and $r \ll 1$),

$$I = I_i = \frac{5ud}{2h^{3/2}} \sqrt{\frac{2\rho_f C_d}{3\Delta\rho g \cos\theta}}. \quad (16)$$

We are now able to test experimentally the theoretical approach. Having measured the three quantities u , h , and θ for different fluid conditions, we can plot for a given configuration the friction coefficient $\mu = \tan\theta$ as a function of the parameter I corresponding to the viscous, inertial, or free-fall regime, respectively. The first prediction is that the data for different inclinations and different thicknesses should collapse on a single curve $\mu(I)$. The second and most crucial prediction is that, because the function μ is fluid independent, the collapse should remain unchanged when changing the fluid condition, as long as the computation of the parameter I is changed according to the flow regime. We compare in Sec. V these predictions with our experimental results.

V. COMPARISON BETWEEN THEORY AND EXPERIMENTS

A. Friction law

The four different configurations we have studied using two sizes of particles in air or water are summarized in Table I where the range of Stokes numbers and r parameters are given. As shown in Fig. 11, it is clear that only two regimes are obtained in our experiments. The aerial granular flows belong to the free-fall regime, whereas the flows in water belong to the viscous regime. In order to do experiments in the inertial regime, one has to use larger particles.¹⁸ Unfortunately in our setup, the plane is too short to observe the fully developed uniform flows for particles larger than $300 \mu\text{m}$, we then have not been able to study the inertial regime.

From the data plotted on Fig. 7, we can compute with Eqs. (14) and (15) the corresponding I_{ff} number for the aerial experiment A1, and the I_v number for the subaqueous experi-

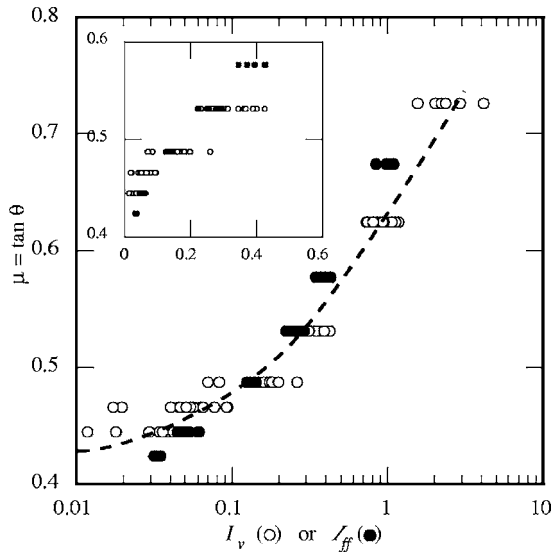


FIG. 12. Correlation between the viscous time ratio I_v (W1) or I_{ff} (A1) and the friction coefficient $\mu = \tan \theta$ for immersed flows W1 and aerial flows A1. The insert shows the same data in linear scale.

ment W1. The correlation between the effective friction $\tan \theta$ and these I numbers is shown on Fig. 12, where we have plotted on the same graph the results for the aerial and submarine flows for the small beads. A striking feature is that all the data obtained for different inclinations, different flow thicknesses, in water or in air, seem to collapse on a single curve in agreement with the theory. Despite the difference of more than an order of magnitude observed in the velocity measurement between the aerial and the submarine cases, the measurements collapse on the same curve when using the correct estimate for the dimensionless shear rate I . This result supports the assumption that the same friction law $\mu(I)$ applies for both aerial and submarine flows, the fluid changing only the time scale of particle rearrangements and thus the definition of I . The collapse is not perfect and the uncertainties in the measurements do not allow to conclude that the influence of the fluid is entirely captured by this approach. However, the superposition of the data obtained in air and water indicates that the main effect of the liquid is predicted.

The success of the approach is even more striking when plotting on the same graph all our measurements, obtained with different beads sizes, both in air and water (Fig. 13). Whatever the conditions and the bead diameters, the data seem to collapse on a single curve, which is well fitted by an analytical function of the form:

$$\mu(I) = \mu_1 + \frac{\mu_2 - \mu_1}{I_0 I + 1}, \quad (17)$$

where μ_1 , μ_2 , and I_0 are constant.

The friction coefficient tends to a minimum value μ_1 when $I \rightarrow 0$ and tends to a maximum value μ_2 at high shear rate. This expression of the friction law together with the expressions of the dimensionless parameter I given in Eqs. (8)–(10) provides a constitutive law that could be useful to describe more complex configurations.

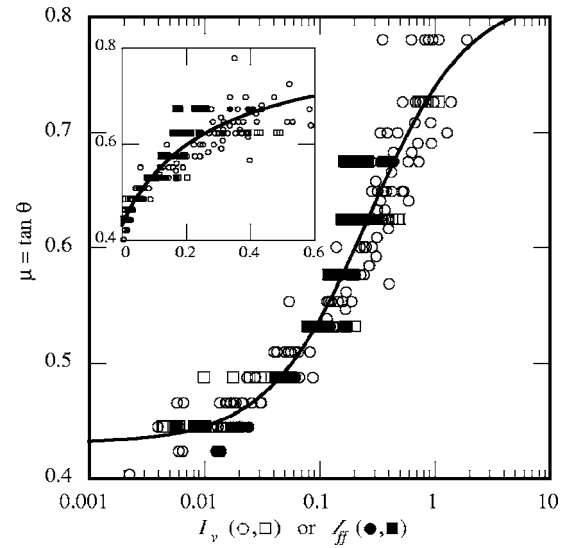


FIG. 13. Correlation between the viscous time ratio I_v (W1: open circles, W2: open squares) or I_{ff} (A1: filled circles, A2: filled squares) and the friction coefficient $\mu = \tan \theta$ for immersed flows W1 and W2 and aerial flows A1 and A2. The solid line is Eq. (17) with $\mu_1 = 0.43$, $\mu_2 = 0.82$ and $I_0 = 0.27$. The insert shows the same data in linear scale.

B. Excess pore pressure

Since the dimensionless parameter I successfully describes the flow properties and predicts the relation between θ , h , and u , one can analyze whether this approach can also give information about the excess pore pressure that develops during the flow. We have seen in Sec. III C that the excess interstitial pressure Δp_i increases linearly with thickness and increases with inclination angle. In order to see if these variations can also be captured through the single dimensionless shear rate I , we have plotted in Fig. 14 the relative pore pressure $\Delta p_i / \Delta \rho g h \cos \theta$ as a function of I_v for the two sets of beads in water. The pressure data collapse on a single curve showing that the parameter I_v also controls the magnitude of the excess pore pressure. The time-scale ratio I is clearly the relevant dimensionless parameter controlling submarine dense granular flows.

C. Discussion

The collapse of all the data on a single friction law strongly supports the assumption of our model stipulating that the major role of the fluid is to change the time it takes for a particle to fall into a hole. It is important to emphasize that the collapse is obtained with no fit parameter. The only parameter in the model which is not accurately determined is the parameter α introduced in the expression of the viscous drag force to take into account the interaction of the falling particle with its neighbors. In this study α has been estimated by computing the porosity of the surrounding porous medium, which is a first simple estimate. We have verified that changing α in the range from 0.008 to 0.015 does not strongly change the quality of the collapse. However, a more detailed study of the motion of one particle in the midst of others could help in better understanding and estimating the drag force.

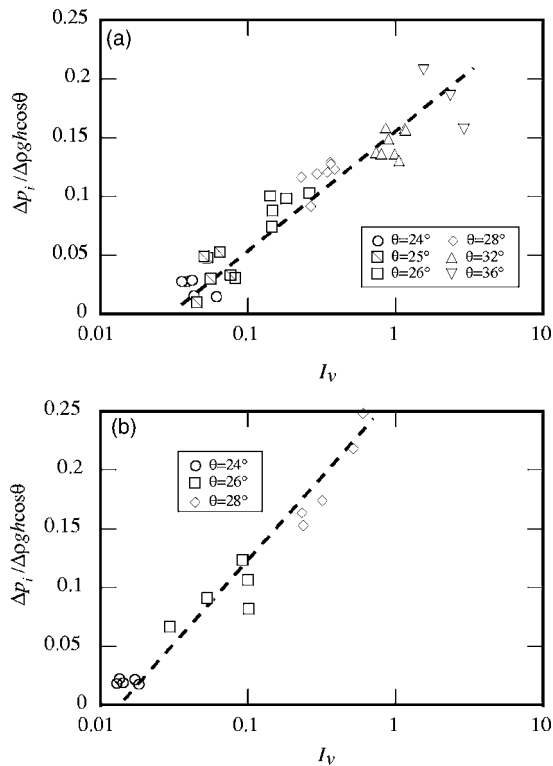


FIG. 14. Relative excess pressure $\Delta p_i / \Delta \rho g h \cos \theta$ as a function of I_v for submarine flows W1 (a) and W2 (b). The dotted lines show the qualitative trend.

Although the simple scaling arguments presented in this paper work surprisingly well to describe the rheology of the steady uniform flows, some limitations exist. First, the existence of a deposit and of a critical thickness h_{stop} below which no flow is possible is not predicted by the theoretical description, both in immersed and dry cases. Second, the role of the fluid is oversimplified. In our description, the complex coupling between the pore pressure and the grain motion is not taken into account. In writing the force balance, the granular stress applying on the particles is assumed to be the total weight of the particles. In the steady regime, this is a reasonable assumption, the measured excess pore pressure being always small. However, it is well known that for unsteady flows when a change in volume fraction occurs, a large excess pore pressure can develop and hence change the behavior of the flow.^{23,24} Despite this limitation, the scaling approach has shown that the pore pressure is controlled by the dimensionless shear rate I . This result gives new insights in the physical mechanisms controlling submarine granular flows and could help in developing more complete models coupling fluid motion and grains flow.

VI. SUMMARY AND CONCLUSIONS

In this paper, submarine flows of granular materials down rough inclined planes have been experimentally investigated. In the regime where steady uniform flows are observed, we have systematically studied the variation of the mean velocity and the pore pressure below the avalanche as a function of the two control parameters: the plane inclination and the layer thickness. The comparison with similar

experiments carried out in air shows that the liquid has a strong influence. For the glass beads we used, submarine flows are more than ten times slower than aerial flows. However, we are able to describe both cases in the same framework by modifying the recent rheological description proposed for dry granular material. In this description the constitutive law is a friction law. The coefficient of friction depends on the ratio of the time scale given by the mean shear rate and the time scale related to the rearrangements when a particle falls into a hole. We have transposed this picture to the submarine case by modifying the time scale of rearrangement to take into account the role of the fluid. The striking result is that this simple change of time scale is sufficient to describe both submarine and dry flows using the same friction law. We can then conclude that in the steady uniform regime, the mechanisms controlling the rheology remain the same with or without fluid, the major influence of the fluid on dense granular flows being a change on the microscopic time scale. This observation allows us to propose a constitutive law for submarine granular flows which is written as a friction Coulomb law with a coefficient of friction which depends on the shear rate and the fluid properties. This could be of interest for the description of geophysical events. Flows over complex topography such as submarine avalanches are often described using depth-averaged equations.^{6,34,35} However, in these approaches, the expression of the basal stress is not known and Newtonian, Bingham, or Coulomb rheologies are often used. The shear-rate-dependent friction law proposed here could represent an alternative.

However, one has to keep in mind that the constitutive laws found in this study are only valid for the steady uniform regime. When unsteady phenomena take place, for example, when the avalanche is triggered or when the flow stops, the coupling between the granular and the fluid is certainly more complex. It is known that in these transient regimes, a change of volume fraction occurs (for example, a dense granular material at the onset of flow will dilate), inducing fluid motions through the grains. The excess pore pressure associated with this fluid motion could then strongly modify the balance between the stress carried by the fluid and the stress carried by the grains, and thus alter the behavior of the flow.³⁴ Investigating this transient regime in small-scale experiments like the one used in this paper could provide interesting informations and seeds future studies.

ACKNOWLEDGMENT

The authors thank J. W. Vallance for his help during the early stage of this study.

¹G. D. R. Midi, "On dense granular flow," *Eur. Phys. J. E* **14**, 341 (2004).

²R. M. Iverson, "The physics of debris flows," *Rev. Geophys.* **35**, 245 (1997).

³F. Legros, "The mobility of long-runout landslides," *Eng. Geol. (Amsterdam)* **63**, 301 (2002).

⁴L. Jiang and P. H. LeBlond, "The coupling of a submarine slide and the surface water waves which it generates," *J. Geophys. Res.* **97**, 731 (1992).

⁵S. Assier Rzdakiewicz, C. Mariotti, and P. Heinrich, "Modeling of submarine landslides and generated water waves," *Phys. Chem. Earth* **21**, 7 (1996).

⁶J. Imran, G. Parker, J. Locat, and H. Lee, "1D numerical model of muddy

- subaqueous and subaerial debris flows," J. Hydraul. Eng. **127**, 959 (2001).
- ⁷M. Pastor, M. Quecedo, E. González, M. I. Herreros, J. A. Fernández Merodo, and P. Mira, "Simple approximation to bottom friction for Bingham fluid depth integrated models," J. Hydraul. Eng. **130**, 149 (2004).
- ⁸R. A. Bagnold, "Experiments on a gravity-free dispersion of large solid spheres in a Newtonian fluid under shear," Proc. Roy. Soc. A **225**, 49 (1954).
- ⁹C. Ancey, P. Coussot, and P. Evesque, "A theoretical framework for granular suspensions in a steady simple shear flow," J. Rheol. **43**, 1673 (1999).
- ¹⁰I. Jomha, A. Merrington, L. V. Woodcock, H. A. Barnes, and A. Lips, "Recent developments in dense suspension rheology," Powder Technol. **65**, 343 (1991).
- ¹¹U. Schaffinger, A. Acrivos, and K. Zhang, "Viscous resuspension of a sediment within a laminar and stratified flow," Int. J. Multiphase Flow **16**, 567 (1990).
- ¹²M. K. Lyon and L. G. Leal, "An experimental study of the motion of concentrated suspensions in two-dimensional channel flow. Part I. Mono-disperse systems," J. Fluid Mech. **363**, 25 (1998).
- ¹³I. E. Zarraga, D. A. Hill, and D. T. Leighton, "The characterisation of the total stress of concentrated suspensions of noncolloidal spheres in Newtonian fluids," J. Rheol. **44**, 185 (2000).
- ¹⁴J. A. G. Aragon, "Granular-fluid chute flow: Experimental and numerical Observations," J. Hydraul. Eng. **121**, 355 (1995).
- ¹⁵D. Prasad and H. K. Kytomaa, "Particle stress and viscous compaction during shear of dense suspensions," Int. J. Multiphase Flow **21**, 775 (1995).
- ¹⁶B. K. Muite, M. L. Hunt, and G. G. Joseph, "The effects of a counter-current interstitial flow on a discharging hourglass," Phys. Fluids **16**, 3415 (2004).
- ¹⁷N. Jain, J. M. Ottino, and R. M. Lueptow, "Effect of interstitial fluid on a granular flow layer," J. Fluid Mech. **508**, 23 (2004).
- ¹⁸S. Courrech du Pont, P. Gondret, B. Perrin, and M. Rabaud, "Granular avalanches in fluids," Phys. Rev. Lett. **90**, 044301 (2003).
- ¹⁹J. E. Simpson, *Gravity Currents in the Environment and the Laboratory*, 2nd Ed. (Cambridge University Press, Cambridge, 1997).
- ²⁰A. J. Hogg, H. E. Huppert, and M. A. Hallworth, "Reversing buoyancy of particle-driven gravity currents," Phys. Fluids **11**, 2891 (1999).
- ²¹A. J. Hogg and H. E. Huppert, "Spreading and deposition of particulate matter in uniform fluids," J. Hydraul. Res. **39**, 505 (2001).
- ²²J. R. L. Allen, *Sedimentary Structures, Their Character and Physical Basis* (Elsevier, Amsterdam, 1983), Vol. II.
- ²³R. M. Iverson and R. G. Lahusen, "Dynamic pore-pressure fluctuations in rapidly shearing granular materials," Science **246**, 796 (1989).
- ²⁴R. M. Iverson, "Differential equations governing slip-induced pore-pressure fluctuations in a water-saturated granular medium," Math. Geol. **25**, 1027 (1993).
- ²⁵Y. Forterre and O. Pouliquen, "Long-surface-wave instability in dense granular flows," J. Fluid Mech. **486**, 21 (2003).
- ²⁶O. Pouliquen, "Scaling laws in granular flows down rough inclined planes," Phys. Fluids **11**, 542 (1999).
- ²⁷S. Courrech du Pont, P. Gondret, B. Perrin, and M. Rabaud, "Wall effects on granular Heap stability," Europhys. Lett. **61**, 792 (2003).
- ²⁸J. J. Major, "Gravity-driven consolidation of granular slurries— Implications for debris-flow deposition and deposit characteristics," J. Sediment Res. **70**, 64 (2000).
- ²⁹F. Da Cruz, F. Chevoir, J.-N. Roux, and I. Iordanoff, "Macroscopic friction of dry granular materials," in *Transient Processes in Tribology, Proceedings of the 30th Leeds-Lyon Symposium on Tribology, Tribology and Interface Engineering*, 2-5 September 2003, Lyon, edited by A. Lubrecht and G. Dalmaz (Elsevier, Amsterdam, 2004), Vol. 4.
- ³⁰I. Iordanoff and M. M. Khonsari, "Granular lubrication: Toward an understanding between kinetic and fluid regime," ASME J. Tribol. **126**, 137 (2004).
- ³¹S. B. Savage, "The mechanics of rapid granular flows," Adv. Appl. Mech. **24**, 289 (1984).
- ³²P. Jop, Y. Forterre, and O. Pouliquen, "Crucial role of side walls for granular surface flows: Consequences for the rheology," J. Fluid Mech. (to be published).
- ³³F. A. L. Dullien, *Fluid Transport and Pore Structure* (Academic, San Diego, 1992).
- ³⁴R. P. Denlinger and R. M. Iverson, "Flow of variably fluidized granular masses across three-dimensional terrain. 1. Coulomb mixture theory," J. Geophys. Res. **106**, 537 (2001).
- ³⁵R. P. Denlinger and R. M. Iverson, "Flow of variably fluidized granular masses across three-dimensional terrain. 2. Numerical predictions and experimental tests," J. Geophys. Res. **106**, 553 (2001).

B.13 Dynamics of a sliding porous block: a toy model for submarine avalanches

C. CASSAR, O. POULIQUEN & M. NICOLAS
En préparation pour *Phys. Rev. E.*

Dynamics of sliding porous block: a toy model for submarine avalanches

C. Cassar, O. Pouliquen & M. Nicolas

IUSTI, Université de Provence - CNRS, 5 rue Enrico Fermi, 13453 Marseille cedex 13, France

(Dated: April 22, 2005)

The role of the interstitial fluid in granular flows is investigated through a toy model consisting in an immersed porous block sliding down a rough substrate. The roughness is modeled by a sinusoidal interface. We show that the up and down motion of the block moving over the sinusoidal substrate induces viscous forces through the porous media which dramatically influence the trajectory. The model is entirely defined by two dimensionless numbers: the Stokes number measuring the relative influence of gravity and viscous effects and the substrate angle θ . Depending on the values of these two parameters, three flow regimes are found: a contact regime, a ballistic regime, and a lubricated regime.

I. INTRODUCTION

The flow of granular material in interaction with a fluid is a topic of great interest for geophysical flows. Snow avalanches, submarine avalanches [1, 2], landslides, debris flows [3] or fault dynamics [4, 5] are typical examples where the fluid has a strong influence on the granular behavior. Hydrodynamic approaches often describe the mixture of solid particles and fluid as an effective fluid with a chosen rheology [6, 7]. However, such an approach appears to be oversimplified in some situations, as it does not precisely take into account the interaction between the particles and the fluid. The coupling between the deformation of the porous solid matrix formed by the grains and the fluid motion through this porous media is complex and may induce important variations of the interstitial fluid pressure, also called the pore pressure [4]. Depending on situations, this coupling may help or hinder the flow of the particles. For example, if the basal pore pressure is sufficiently large to support the material weight, the friction coefficient may drop to zero and this may lead to a strong increase of the flow velocity [8].

Mixture of grains and liquid have been the subject a many studies, mainly focused on the suspension regime, where the particles interact through hydrodynamics interactions and not through contacts. Recent studies have addressed the dense flow regime where particles are in contact and frictional forces are predominant. The influence of the interstitial fluid in this regime have been investigated in hour glasses [9], in rotating drums [10, 11] or on inclined planes [12]. However the coupling between grains and fluid is still not well understood.

One way to improve our understanding of granular flows is to consider a toy model and study the motion of a single layer sliding on top of a corrugated plate. Such an approach has been very fruitful for dry granular flows [16]. The detailed analysis of the motion of one grain rolling down a corrugated bottom has help understanding the source of dissipation and the basic mechanisms responsible to the hysteresis between flow and no flow in dry granular material [13–16]. The same kind of approach for flow in fluid could then give information about the role of the interstitial fluid.

The first study of this kind has been performed by Iversen and Lahusen [17]. They have experimentally measured the variation of the fluid pressure when two blocks made of glued rods slide one relatively to the other, the whole setup being immersed in fluid. They have shown that during the motion, negative and positive pore pressure alternatively develops corresponding to the motion of the top block on the bumpy surface made by the bottom one. A theoretical description taking into account the elastic behavior of the porous block have been proposed for this configuration [18]. A numerical approach of this system has been recently developed [19], showing that the level of pore pressure can be quantified by the Darcyan flow inside the porous media.

In this paper we present a simpler version of this problem for which a detailed analysis of the role of the fluid can be carried out and in which relevant dimensionless numbers can be discussed. We consider the motion of a porous media down an inclined plane (Fig. 1). Both the porous block and the plane have a sinusoidal shape to model the roughness between granular layers. When moving down the slope, the porous block follows the sinusoidal shape and then have an up and down motion which induces a flow through the porous media. The pressure gradient associated to this flow changes the normal force that applies at the contact between the block, and thus changes the friction force between the block and the substrate. Our aim is to study in detail this coupling to improve the understanding of the relation between the fluctuating motion of grains and the rheology of immersed granular material.

The model is presented in section (Sec. II). We then discuss the dry case in section III A before studying in detail the influence of the fluid in section III B. Discussions and conclusions are given in Sections IV and V.

II. THEORETICAL MODEL

A. Basic equations

We aim to describe the motion of a porous block sliding down a rough plane. The system is immersed in a

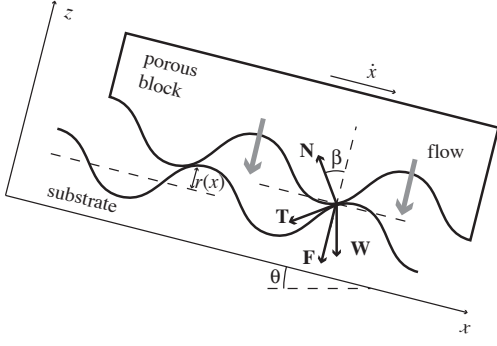


FIG. 1: Sketch of the system and forces acting on the porous block.

bath of fluid of viscosity η . The block is supposed to be infinitely long in the x direction. The roughness of both the substrate and the sliding block is described by a function $r(x)$ which is chosen sinusoidal of wavelength d : $r(x) = A d \sin(2\pi x/d)$, where A is the relative amplitude of the roughness. The contact between the block and the substrate is then a single point. Let us write the motion equation for a slice of block of size $d \times w \times H$ in the (x, y, z) reference frame, where $w = 1$ is a unit width. The mass of the block is $m = \phi d w H \rho_p$ where ρ_p is the density of the solid phase and ϕ is the solid fraction.

The motion of the porous block is governed by four forces: a gravity force $\mathbf{W} = m' \mathbf{g}$ with $m' = \phi \Delta \rho d w H$, which drives the block downwards, a normal reaction force \mathbf{N} perpendicular to the bottom surface, a tangential friction force \mathbf{T} , and a viscous force \mathbf{F} arising from the fluid motion through the porous block (See Fig.1). The Newton's equation is

$$m \begin{pmatrix} \ddot{x} \\ \ddot{z} \end{pmatrix} = \mathbf{W} + \mathbf{N} + \mathbf{T} + \mathbf{F}. \quad (1)$$

During the contact, the magnitudes of the normal and tangential friction forces are assumed to be related through a Coulomb's friction law

$$T = \mu_g N, \quad (2)$$

where $\mu_g = \tan \theta_g$ is the friction coefficient between the block and the substrate and is written as the tangent of the friction angle θ_g . The equation of motion (1) can be written as follows:

$$m \begin{pmatrix} \ddot{x} \\ \ddot{z} \end{pmatrix} = \begin{pmatrix} m' g \sin \theta - T_{eff} + F_x \\ -m' g \cos \theta + N_{eff} + F_z \end{pmatrix} \quad (3)$$

with an effective tangential force T_{eff} and an effective normal force N_{eff} , related through $T_{eff} = \mu(x) N_{eff}$ with a x -dependent friction coefficient

$$\mu(x) = \tan(\theta_g + \beta(x)). \quad (4)$$

We denote β the angle between the normal force and the z axis. This angle is related to the shape of the substrate through $\tan \beta = dr/dx$.

The next step is to model the hydrodynamic interaction \mathbf{F} between the block and the fluid. A detailed 3D description of the flow induced by the block motion in the open space and in the porous media is beyond the scope of this study. In the following we consider only the hydrodynamic force induced by the vertical motion of the block which induce a darcy flow through the porous media. Doing so, we neglect the shear stress linked to shear of the fluid in the open space. This assumption is certainly valid when the permeability of the porous media is low, i.e. when the stress due to flow in the porous media is much higher than shear stress due to shear. Under this assumption the viscous force is along z only $\mathbf{F} = F \mathbf{e}_z$ and using the Darcy law one can write that the pressure difference between the bottom and the top of the block is $\Delta p = (\eta/k) H u_f$, where k is the permeability and u_f is the filter velocity of the fluid through the porous medium simply equal to \dot{z} . The porous force is then $F = d w \Delta p$ and can be written as follows:

$$F = -\frac{\eta m}{k \phi \rho_p} \dot{z}. \quad (5)$$

When the block is in contact with the substrate, the block coordinates x and z are related through $z = r(x)$ and hence $\dot{z} = \dot{x}(dr/dx)$ and $\ddot{z} = \ddot{x}(dr/dx) + \dot{x}^2(d^2r/dx^2)$.

The combination of Eqs. (3) and (5) leads to a single differential equation for the block position

$$\ddot{x} \left(1 + \mu(x) \frac{dr}{dx} \right) = g \frac{\Delta \rho}{\rho_p} (\sin \theta - \mu(x) \cos \theta) - \mu(x) \left(\dot{x}^2 \frac{d^2 r}{dx^2} + \frac{\eta}{k \rho} \dot{x} \frac{dr}{dx} \right). \quad (6)$$

Introducing dimensionless variables $X = x/d$, $Z = z/d$ and $T = t/\sqrt{d \rho_p / g \Delta \rho}$, Eq. (6) becomes

$$\ddot{X} \left(1 + \mu(X) \frac{dR}{dX} \right) = \sin \theta - \mu(X) \cos \theta - \mu(X) \left(\dot{X}^2 \frac{d^2 R}{dX^2} + \frac{1}{St} \dot{X} \frac{dR}{dX} \right) \quad (7)$$

with a dimensionless parameter

$$St = \frac{k \phi}{\eta} \sqrt{\frac{g \rho_p \Delta \rho}{d}}. \quad (8)$$

This parameter can be interpreted as a Stokes number [10, 12] and gathers all the physical quantities describing the fluid and the porous block. The number St measures the relative importance of gravity over viscous forces. High values of St corresponds to the case where the fluid plays no role, obtained for low viscosity or high permeability. Conversely the motion in a highly viscous liquid or the motion of a low permeability porous block is depicted by low value of St . In the following

we focus on the difference between the dry case and the case with a fluid and will then discuss the dynamics in terms of St^{-1} instead of St , the dry case corresponding to $St^{-1} = 0$. A typical value of St^{-1} can be inferred from the flow of spherical particles down a rough plane. For $100 \mu\text{m}$ glass particles immersed in water and forming a porous medium of permeability 10^{-10} m^2 , $1/St \approx 30$ ($St \approx 0.03$). Changing the fluid to air gives $1/St \approx 0.5$ ($St \approx 2$).

Equation 7 is valid as long as the porous block is in contact with the substrate. However, the block can take off and 7 is no longer valid to describe its motion. This happens when contact normal force \mathbf{N} vanishes which is equivalent to say that N_{eff} vanishes. The contact condition then writes:

$$\dot{X}^2 \frac{d^2 R}{dX^2} + \ddot{X} \frac{dR}{dX} + \cos \theta + \frac{1}{St} \dot{Z} \frac{dR}{dX} \geq 0. \quad (9)$$

Without contact, the block follows a trajectory which is described by the dimensionless equations:

$$\begin{pmatrix} \ddot{X} \\ \ddot{Z} \end{pmatrix} = \begin{pmatrix} \sin \theta \\ -\cos \theta - St^{-1} \dot{Z} \end{pmatrix} \quad (10)$$

When the contact is renewed, the collision is considered to be fully inelastic, and the component of the velocity normal to the substrate at the point of impact is set to zero. If the collision occurs at time T , the velocity components $\dot{X}(T^+)$ and $\dot{Z}(T^+)$ along the x and z axis just after the collision are expressed as a function of velocity just before $\dot{X}(T^-)$ and $\dot{Z}(T^-)$:

$$\begin{pmatrix} \dot{X}(T^+) \\ \dot{Z}(T^+) \end{pmatrix} = \begin{pmatrix} \cos^2 \beta & -\cos \beta \sin \beta \\ -\cos \beta \sin \beta & \sin^2 \beta \end{pmatrix} \begin{pmatrix} \dot{X}(T^-) \\ \dot{Z}(T^-) \end{pmatrix} \quad (11)$$

where β is an angle defined by $\tan \beta = dR/dX$, the local slope of the substrate.

Equations of motion 7 and 10 with the contact condition 9 and the collision rule 11 completely define the dynamics of our system. We have performed numerical simulations of this system for various values of the St parameter and different inclinations.

B. Numerical method

Equations (7) for the contact flow or (10) for the flight flow were solved using a 4th order Runge-Kutta method. The temporal resolution δT is taken equal $\delta T = 1/300$ corresponding to the best accuracy/speed ratio during computation. The contact condition (9) is tested at each time iteration, and the solver switches from (7) to (10) when the contact is lost.

We performed the computations with two sets of initial conditions. The first set is a zero initial velocity with an unstable initial position, such as $X(0) = 1/4$. The porous block is initially at rest over a crest of the substrate. It then begin to slide down the first valley and can eventually reach a periodic trajectory or remain trapped in the

valley. The second set of initial condition we have studied in details consists in launching the block with an initial velocity U_0 . In this case the initial position we choose is the stable position $X(0) = \arccos(-\tan \theta/A)/2\pi - 1/2$ where the block is at the lowest height in the laboratory reference frame.

For both set of initial conditions we have performed simulations for different values of the Stokes number and different inclination. In each case we have computed the trajectories ($X(T), Z(T)$) and the velocity ($\dot{X}(T), \dot{Z}(T)$) and the mean velocity U defined as the time-averaged velocity over a wavelength.

III. RESULTS

We have simulated the above equations for different roughnesses conditions such that the maximum slope of the sinusoid ranges between 10 and 30 degrees. The results are qualitatively the same and in the following we present result obtained for a maximum local slope equal to 20° which correspond to $A = 1/16$. We first present result obtained for the dry case when the Stokes number is infinite, before studying in details the influence of the fluid.

A. Dry case: $St^{-1} = 0$

1. Dynamics with no initial velocity

When the block is released whitout initial velocity from a crest, three regimes are observed depending on the inclination. If the inclination is too low $\theta < \theta_{min}$, the block when released slides down the slope and stops in the valley. When inclination is too large $\theta > \theta_{max}$, the block accelerates, takes off, and never stops accelerating. The stationnary regime when the block reaches a periodic trajectory with a well defined mean velocity is observed between the two angles for $\theta_{min} < \theta < \theta_{max}$. The existence of this steady regime is due to the balance between the gain of potential energy due to the slope and the loss of energy due to the inelastic collision [16]. As a result, all the trajectories corresponding to a steady motion exhibit a sliding part and a free flight part as shown in Fig. 5(a). This is slightly different from the case that has been studied before of a single sphere on a bumpy plane made of particles (the tac-tac problem [16]). In this case the geometrical configuration of the bumpy plane allows collisions and thus dissipation without take off. Periodic trajectories without lost of contact are then observed contrary to the present model where the roughness is modeled by a simple sinusoidale shape.

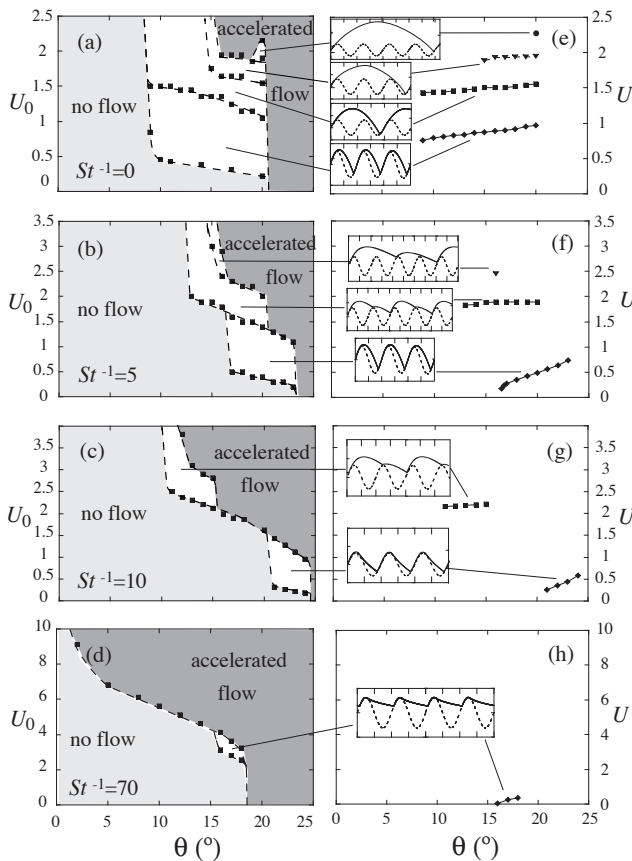


FIG. 2: (a)-(d) Domains in the (θ, U_0) plane corresponding to different trajectories observed when launching the block at velocity U_0 . The sketch of the corresponding periodic trajectories and the mean velocity are plotted in (e)-(h) for different value of St^{-1}

2. Dynamics with an initial velocity

For a given inclination θ , other time-periodic solutions can be achieved when the block is launched at a finite initial velocity and not just released from a crest. In order to investigate this dynamics, the block is placed at the position of zero slope in the valley and initiated at a velocity U_0 . Depending on U_0 and θ , different trajectories are observed corresponding to the jump over one or more wavelengths during the take off as sketched in Fig. 2 (e). The plane (θ, U_0) can then be divided in different attraction domains (Fig. 2 (a)). If the inclination is low or the initial velocity too small, the block stops after a transient motion and no flow is observed. At high inclination the block never reaches a periodic trajectory but accelerates along the plane. For an intermediate range of inclination, different trajectories are observed depending on the launch velocity. For a given θ , two different initial velocities will lead to the same periodic motion at the

same mean velocity U if they belong to the same domain of Fig. 2(a). To each domain corresponds an attractive branch $U(\theta)$ which is plotted in Fig. 2(e). Four domains have been observed corresponding to trajectories where the free flight of the block correspond to a jump over 1, 2, 3 or 4 crests before landing again.

In the following we now investigate the influence of the fluid on this dynamics by considering non zero St^{-1} parameter .

B. Role of the fluid: $St^{-1} \neq 0$

1. Dynamics with no initial velocity

For the case when the block is simply released from a crest with no initial velocity, the fluid influence is first to change the range of inclination for which the block moves down the slope at a constant mean velocity. As presented in Fig. 3 both the minimum and maximum angles of steady flows are higher with a fluid than in the dry case. But this influence is non monotonic. Starting from 10° for the dry case $St^{-1} = 0$, the minimal angle θ_{min} first increases up to 21° for $St^{-1} = 10$ then decreases down to 15° for $1/St = 100$. The maximal angle θ_{max} follows the same qualitative trend, as shown on Fig. 3. However an important observation is that the range of inclination for which steady flows are observed decreases by more than a factor two as soon as St^{-1} is greater than 20. This means that accelerated motion are facilitates when fluid is present, meaning that the dissipation seems to be less efficient to balance the gravity forces. We will discuss this point in more details in Section IV.

The corresponding mean velocities are plotted in Figs. 4 where Fig. 4(a) shows the variation of U with inclination for different value of St and Fig. 4(b) shows the variation of U with St for two inclinations. The velocity curves are almost undistinguishable for $St^{-1} \leq 0.1$, meaning that the fluid, if present, plays no role because of its low viscosity or a large permeability of the porous block. Thus the gravity is balanced only by the friction and the loss of energy during the collisions with the substrate. An effect of the fluid appears for $St^{-1} \geq 0.5$: the velocity strongly decreases. However, an interesting observation is that for a given inclination θ , the variation of U with St^{-1} is non monotonic. Velocity remains constant for $St^{-1} \leq 0.1$, dramatically decreases for $St^{-1} \geq 0.5$ then increases again. The fluid then seems to first hinder the flow for moderated values of St^{-1} but facilitates it for larger values.

A better understanding of the role of the fluid is given by the analysis of the trajectories. By contrast with the dry case where a single kind of trajectory is observed when the block is not launched, three different regimes exist with liquid depending on the value of St^{-1} and of the inclination as shown in Fig. 5). At low inclination and for $St^{-1} < 5$, a contact regime is observed, where the block remains in contact with the substrate during

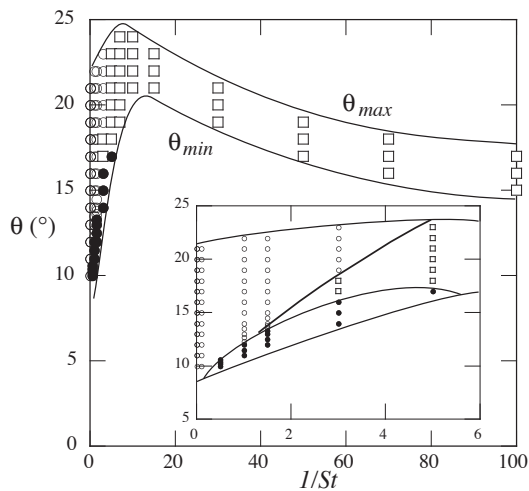


FIG. 3: Minimum and maximum angle for steady flows as a function of the inverse of Stokes number $1/St$. The symbols show the different flow regimes: flow with permanent contact (filled circles), ballistic trajectories (open circles) and lubricated flows (open squares).

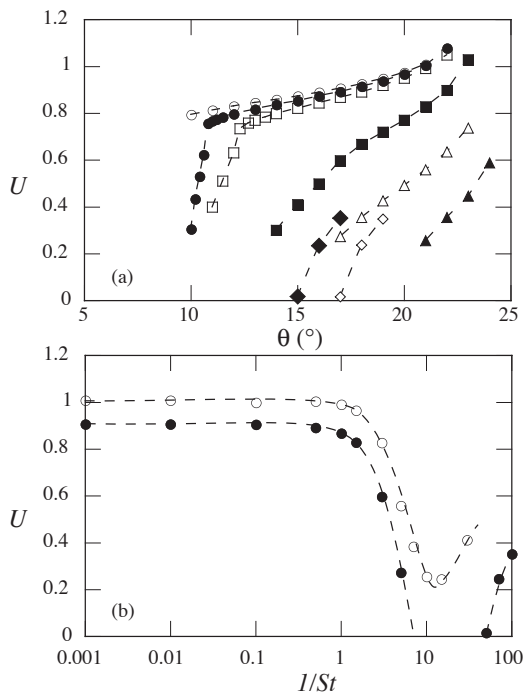


FIG. 4: (a) Mean velocity U of the porous block starting from rest as a function of θ for different values of $1/St$: $1/St = 0$ (open circles), $1/St = 0.5$ (filled circles), $1/St = 1$ (open squares), $1/St = 3$ (filled squares), $1/St = 5$ (open triangles), $1/St = 10$ (filled triangles), $1/St = 50$ (open diamonds) and $1/St = 100$ (filled diamonds). (b) Velocity as a function of $1/St$ for $\theta = 17^\circ$ (open circles) and $\theta = 17^\circ$ (filled circles).

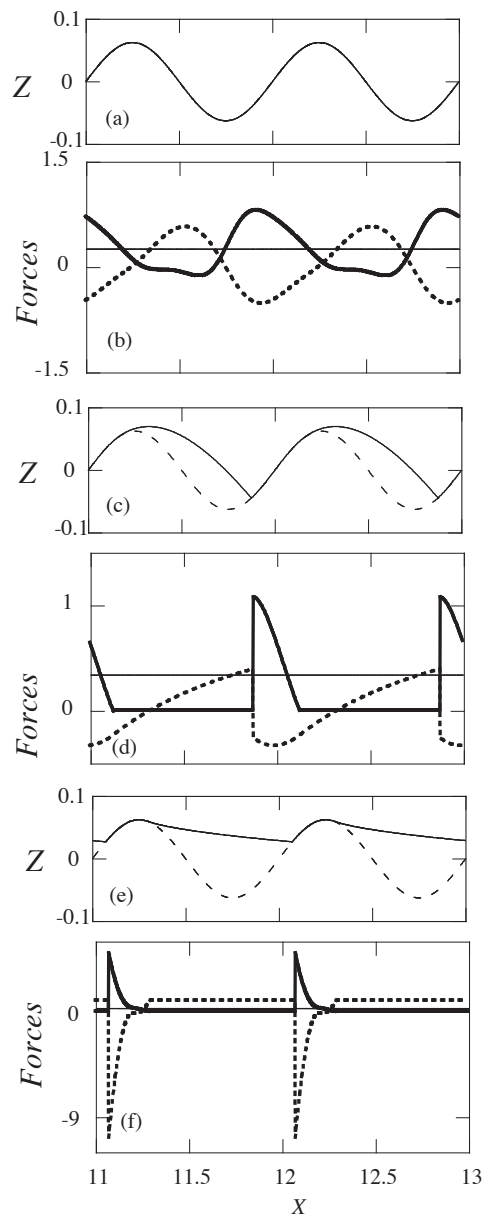


FIG. 5: (a) Block trajectory for contact regime (continuous line) over the substrate (dashed line) for $1/St = 3$ and $\theta = 15^\circ$ (b) Corresponding forces: gravity $\sin(\theta)$ (thin continuous line), effective friction $T_{eff}/m'g$ (thick continuous line), vertical viscous force $F/m'g$ (dashed line); (c) and (d): same as (a) and (b) for the ballistic regime, $1/St = 1$ and $\theta = 20^\circ$; (e) and (f): same as (a) and (b) for the viscous regime, $1/St = 50$ and $\theta = 18^\circ$.

the whole motion. This is in contrast with the dry case, where no steady motion was possible without take off. When the fluid is present, a coupling exists between the viscous force induced by the up and down motion of the block and the friction force resulting in a stabilization of the motion. The figure 5(b) shows the variation of the different forces along the trajectory in this regime. The gravity force is constant (thin continuous line). The viscous force normal to the slope varies along the trajectory and is negative when the block climbs up a bump and positive when going down (thick dashed line). The effective tangential friction force T_{eff} varies accordingly along the trajectories (thick continuous line).

At higher inclination but still low values of St^{-1} (less than 5), the trajectory is a ballistic one, similar to the one observed without fluid, see Fig. 5(c). The block takes off *before* the top of the bump. The take off is due to inertia and is nearly independent of the fluid. The presence of the fluid simply modifies the free flight trajectory by adding a vertical force (Fig. 5(d)).

For higher values of St^{-1} , the trajectory is lubricated i.e. characterized by a take off *after* the bump as sketched in Fig. 5(e). The loss of contact is no longer due to inertia but is due to the increase of the viscous force when the block accelerates down the slope and squeezes the fluid in the interstice. The viscous force eventually becomes high enough to balance the weight and the block loses contact. The variation of the viscous force is plotted in Fig. 5(f). It is constant during the flight when no contact exists, which means that the viscous force exactly balances the weight of the block and suddenly changes sign and increases in amplitude when the block lands on the back of the bump and starts climbing on it. The friction force follows this pressure change.

2. Dynamics with an initial velocity

The dynamics of the block when launched at a finite velocity also dramatically changes when the fluid interaction is present. The different domains of attraction in the plane (θ, U_0) are plotted for $St^{-1} = 5, 10$ and 70 in Fig. 2 (b)-(d). A first observation is that the number of periodic trajectories decreases when increasing the role of the fluid, such that for $St^{-1} = 70$ only one branch persists corresponding to a lubricated flow. The second information is that the size of the domain shrinks when increasing the role of the fluid. The range of inclination and of initial velocity for which the block reaches a periodic motion is smaller with fluid than in the dry case. The last but not most striking result concerns the size of the domain where accelerated motion is initiated. For high values of St^{-1} , and if the block is launched at a high enough velocity, it will accelerate forever, even at a very low inclination angle. The lubrication which is important in this regime seems to sustain the block in free flight long enough for the block to gain more potential energy than it can dissipate during the next collision and

contact.

IV. DISCUSSION

Despite the simplicity of the model, the dynamics of the porous block sliding down a wavy substrate appears to be complex. The fluid seems to have two antagonist effects. The first effect is to hinder the flow by introducing an additional dissipation. This effect takes place mainly when the block climbs on the back of the bump. The block then moves away from the substrate and the space between the two blocks sucks fluid. A negative viscous force then develops and presses the block against the substrate and thus increases the frictional dissipation. A second and opposite effect exists when the block moves down the hill after a bump. In this case, the fluid is expelled from the pores and the viscous force is positive. The fluid motion then lightens the block and decreases the friction force. In some cases we have shown that the pressure increases up to the point where it can sustain the block which no longer rubs on the substrate. Our results show that the balance between these two effects is far from being trivial. Both effects are always present during flows but depending on the value of the Stokes number, one or the other of these two effects can predominate. This explains the non monotonic influence of the fluid observed in the plots of the range of inclination (Fig. 3) or of mean velocity as a function of the Stokes number (Fig. 4). The hindering effect is more important for intermediate values of St^{-1} and for example leads to the possibility of a periodic trajectory without losing contact, although the contact is described by constant solid friction. On the other hand at high values of St^{-1} which correspond to high fluid viscosity or low permeability, the lubricated effect dominates, allowing accelerated motion at very low inclination.

A last important remark concerns the mean viscous force or equivalently the mean pressure gradient that applies on the flowing block. In our toy model, the viscous force is simply proportional to the z -component of velocity $F \propto \dot{Z}$. As a consequence, as soon as a periodic motion is reached, the time-averaged viscous force is zero, as it is simply given by the time integral of \dot{Z} over a period of time. In the steady regimes, the model then predicts no build up of pore pressure, even if the blocks take off. There exist phases where pore pressure is positive and phases where it is negative, but in average it will remain zero. This is no longer true in the accelerated regime. In this regime, the block jumps over more and more wavelength during its free flight and the contact time with the substrate is shorter and shorter, leading to an increase of the pore pressure. Within the framework of this toy model, the accumulation of pore pressure is then linked to accelerated motions.

V. CONCLUSION

In this paper we have studied a toy model of submarine avalanches made of a rigid porous block immersed in a fluid and sliding down a wavy substrate. Although the system is far from real submarine avalanches, it gives informations about the role the fluid. First we have been able to describe the coupling between the up and down motion of the block and the fluid motion. The wavy vertical motion of the block induced by the substrate roughness creates pressure forces that change the friction force at the contact between the porous material and the substrate. As a result the fluid has a non trivial effect along the trajectory. It increases the frictional dissipation in some part of the trajectory when the block moves away from the substrate, and decreases dissipation when the block approaches the substrate. A major result of this

study is that the relative importance of both effects is non trivial and depends on the Stokes number. When the viscosity of the fluid is low or the permeability is large, the presence of the fluid hinders the motion compare to the dry case. Conversely, the flow is lubricated at high viscosity or low permeability and if the block is launched at a sufficient velocity an accelerated motion along the plane could be sustained even at very low inclination angle. This result could be relevant to better understand the high mobility observed in some submarine landslide [2]. A last result that could be interesting for the dynamics of submarine avalanches concerns the pore pressure. Within the model, the pore pressure variations strongly influence the dynamics. However, its mean value remains zero when stationary flow are reached. This suggests that the pore pressure build up is essentially linked to transient phenomena.

-
- [1] L. Jiang and P. H. LeBlond, *J. Geophys. Res.* **97** 731 (1992).
 - [2] F. Legros, *Engineering Geology* **63**, (3-4), 301 (2002).
 - [3] R. M. Iverson *Rev. Geophysics* **35**, 245 (1997).
 - [4] J. W. Rudnicki and C. H. Chen, *J. Geophys. Res.* **93** 4745 (1988).
 - [5] P. Segall and J. R. Rice, *J. Geophys. Res.* **100**, 239 (1995).
 - [6] J. Imran, G. Parker, J. Locat and H. Lee, *J. Hydr. Engrg.*, **127**, 959 (2001).
 - [7] M. Pastor, M. Quecedo, E. Gonzalez, M. I. Herreros, J. A. Fernandez Merodo and P. Mira, *J. Hydr. Engrn* **130** 149 (2004).
 - [8] D. Mohrig, K. X. Whipple, M. Hondzo, C. Ellis and G. Parker, *GSA Bulletin* **110**, 387 1998.
 - [9] B. K. Muir, M. L. Hunt and G. C. Joseph, *Phys. Fluids* **16**, 3415 (2004).
 - [10] S. Courrech du Pont, P. Gondret, B. Perrin and M. Rabaut, *Phys. Rev. Lett.* **90**, 044301 (2004).
 - [11] N. Jain, J. M. Ottino and R. M. Lueptow *J. Fluid Mech.* **508**, 23 (2004).
 - [12] C. Cassar, M. Nicolas and O. Pouliquen *Phys. Fluids* to be published.
 - [13] F. X. Rigidel, R. Jullien, G. H Ristow, A. Hansen and D. Bideau *J. Phys* **4**, 261 (1994).
 - [14] S. Dippel, G. G. Batrouni and D. E. Wolf, *Phys. Rev. E* **54**, 6845 (1996).
 - [15] C. Ancey, P. Evesque and P. Coussot *J. Phys.* **16**, 725 (1996).
 - [16] L. Quartier, B. Andreotti, S. Douady and A. Daerr, *Phys. Rev. E* **62**, 8299 (2000).
 - [17] R. M. Iverson and R. G. LaHusen, *Science* **246**, 796 (1989).
 - [18] R. M. Iverson, *Mathematical Geology* **25**, 1027 (1993).
 - [19] A. Musso, F. Federico and G. Troiano, *Comp. and Geotech.* **31**, 209 (2004).